Centro Brasileiro de Pesquisas Físicas
Programa de Doutorado

Thales Menezes de Oliveira

The search for magnetic monopoles with Missing Transverse Energy and the luminosity monitoring with the ZCounting method in CMS Experiment

Rio de Janeiro/RJ

2025

The search for magnetic monopoles with Missing Transverse Energy and the luminosity monitoring with the ZCounting method in CMS Experiment

Thales Menezes de Oliveira

Tese de Doutorado apresentada no Centro Brasileiro de Pesquisas Físicas como parte dos requisitos para a obtenção do título de Doutor em Física.
Orientador: Carsten Hensel
Coorientador: Albert Alfons de Roeck

Rio de Janeiro/RJ

2025

"THE SEARCH FOR MAGNETIC MONOPOLES WITH MISSING TRANSVERSE ENERGY AND THE LUMINOSITY MONITORING WITH THE ZCOUTING METHOD IN CMS EXPERIMENT"

THALES MENEZES DE OLIVEIRA

Tese de Doutorado em Física apresentada no Centro Brasileiro de Pesquisas Físicas do Ministério da Ciência Tecnologia e Inovação. Fazendo parte da banca examinadora os seguintes professores:

gov.br Documento assinado digitalmente
CARSTEN HENSEL
Data: 04/11/2025 12:36:33-0300
Verifique em https://validar.iti.gov.br

Carsten Hensel - Orientador/CBPF

Marco Aurelio Lisboa Leite – USP

gov.br Documento assinado digitalmente
MURILO SANTANA RANGEL
Data: 26/10/2025 16:50:04-0300
Verifique em https://validar.iti.gov.br

Murilo Santana Rangel - UFRJ

gov.br Documento assinado digitalmente
MARCELO GAMEIRO MUNHOZ
Data: 28/10/2025 10:18:35-0300
Verifique em https://validar.iti.gov.br

Marcelo Gameiro Munhoz - USP

gov.br Documento assinado digitalmente
THIAGO RAFAEL FERNANDEZ PEREZ TOMEI
Data: 03/11/2025 12:38:09-0300
Verifique em https://validar.iti.gov.br

Thiago Rafael Fernandez Perez Tomei - UNESP

Rio de Janeiro, 15 de outubro de 2025.

Agradecimentos

I would first like to thank my parents, Claudio and Denise, for making it possible for me to embark on this path. I am grateful for all the guidance provided, which helped me improve as a person and in the development of my studies, from the beginning of my bachelor's degree at the State University of Rio de Janeiro (Universidade do Estado do Rio de Janeiro) until the conclusion of my doctorate. Without their constant support, this journey would not have been possible. Therefore, this thesis and the entire journey that accompanied it are dedicated to them and to my entire family, but, in particular, to them.

I also dedicate this thesis to my wife, Mariana Soeiro. From the very beginning of my journey, as a high school student learning about particle physics and the Standard Model, until this moment, you have always been by my side, sharing this path, which was only made possible thanks to your presence in my life.

I would liked to express my deepest gratitude to my supervisors, Dr. Carsten Hensel and Dr. Albert de Roeck, for the excellent supervision and essential support in carrying out this work. Their constant encouragement, as well as the opportunities provided, were fundamental to my professional and personal growth along this path, especially the international collaboration experience. I thank them for this text now being available to the academic community.

During the development of this work, I had the opportunity to interact with colleagues such as Andreas Meyer, David Walter, Patricia Telles, David Anthony Petit, Thomas Reis, among others. To all of you, my gratitude for all the discussions, which were essential throughout my journey. Among these, a special acknowledgement goes to Norraphat Srimanobhas, for the discussions on the analysis work regarding the search for magnetic monopoles, which were crucial for the development of this thesis work and for the analysis within the CMS Experiment itself.

Finally, I express my gratitude to the Conselho Nacional de Desenvolvimento Científico e Tecnológico (CNPq) and the Coordenação de Aperfeiçoamento de Pessoal de Nível Superior (CAPES), for the funding received during the years of my doctorate, as well as for the time I was able to spend at the European Organization for Nuclear Research (CERN) in Geneva.

Abstract

This thesis presents two complementary investigations within the CMS experiment at the Large Hadron Collider (LHC): a precision study of luminosity monitoring using Z boson production, and a dedicated search for magnetic monopoles which are hypothetical particles that, if discovered, would profoundly reshape our understanding of fundamental physics. The ZCounting study establishes a self-calibrating, data-driven method for measuring and monitoring the integrated luminosity based on Z boson yields. This approach offers advantages in long-term stability and cross-year consistency, particularly important as the LHC moves toward higher luminosity and pileup conditions. The method's robustness, linearity, and independence from external calibrations are evaluated using early Run 3 datasets.

The core of the thesis is a comprehensive search for magnetic monopoles in proton-proton collisions at $\sqrt{s} = 13$ TeV. Motivated by Dirac's original, the analysis targets monopoles with unit magnetic charge ($g_D = 1$) and TeV-scale masses, within the expected reach of the CMS detector. Signal simulations span multiple production mechanisms, such as Drell–Yan and photon fusion, across spin-0 and spin-1/2 scenarios. Due to their extremely high magnetic charge, monopoles cause severe saturation in the CMS pixel detector and produce highly localized energy deposits in the ECAL, resembling "spike-like" signatures. These atypical features, particularly in the ECAL, trigger rejection mechanisms designed to suppress noise, significantly reducing the efficiency of standard CMS triggers.

For this analysis, two dedicated search strategies were developed to address the unique experimental challenges posed by magnetic monopoles. The first strategy leverages `SinglePhoton` triggers, capitalizing on the topological similarities between monopoles and high-energy photons. The second strategy interprets the rejection of monopole-like signals by the trigger system as contributing to missing transverse energy (MET), making it accessible through `PFMET` triggers. Both approaches rely on powerful discriminating variables: $dE/dx_{\texttt{Significance}}$ from the tracker, which captures the unusually high ionization, and f_{51} from the ECAL, which characterizes the compact energy deposition. Given the unusual nature of the signal and the limitations of simulation-based background modeling, a data-driven approach is used for background estimation.

The final results, based on the full Run 2 dataset and currently in a blinded stage, establish the most stringent expected limits to date on magnetic monopole production within the CMS experiment. This work advances the experimental sensitivity to these elusive particles while also enhancing the precision toolkit for high-luminosity LHC operations through Z boson-based luminosity monitoring.

Key-words: CMS Experiment, LHC, Beyond Standard Model, Magnetic monopoles, Highly Ionizing Particles, Luminosity measurement, Z boson counting

Resumo

Esta tese apresenta dois tópicos complementares desenvolvidos no Experimento CMS do *Large Hadron Collider* (LHC): um estudo sobre o monitoramento da luminosidade a partir da produção de bósons Z e a busca dedicada por monopólos magnéticos, partículas hipotéticas que, se descobertas, transformariam a nossa compreensão da física fundamental. O método denominado ZCounting estabelece uma abordagem baseada em dados para medir e monitorar a luminosidade integrada a partir da contagem do número de bósons Z. Esse método é caracterizado pela sua estabilidade de longo prazo e consistência entre diferentes anos do período de tomada de dados, especialmente relevantes à medida que o LHC caminha para condições de maior luminosidade e *pile-up*. A robustez, linearidade e independência de calibrações externas desse método são avaliadas usando os primeiros conjuntos de dados do Run 3.

O foco da tese consiste na busca por monopólos magnéticos em colisões próton-próton a $\sqrt{s} = 13$ TeV. Motivada pela proposição original de Dirac, a análise foca em monopólos com carga magnética unitária ($g_D = 1$) e massas na escala de TeV, dentro do alcance do detector CMS. As simulações de sinal abrangem os principais mecanismos de produção, como Drell–Yan e a fusão de fótons, considerando os estados de spin 0 e spin 1/2. Devido à sua carga magnética extremamente elevada, os monopólos causam uma saturação considerável no detector de pixels do CMS e produzem depósitos de energia altamente localizados no ECAL, semelhantes a "picos" de ruído. Essas características atípicas, especialmente no ECAL, ativam mecanismos de rejeição projetados para suprimir contribuições de ruído, o que reduz significativamente a eficiência dos *triggers* padrões do CMS para tais eventos.

Para esta análise, duas estratégias foram desenvolvidas. A primeira explora semelhanças com fótons de alta energia, utilizando *triggers* do tipo `SinglePhoton`, enquanto a segunda interpreta a rejeição do sinal considerada como contribuição de energia transversal perdida (MET), permitindo uma busca por meio de *triggers* `PFMET`. Ambas as estratégias utilizam observáveis — como o $dE/dx_{\texttt{Significance}}$, capturando a sua alta capacidade de ionização, e f_{51} caracterizando o padrão comapcto de energia. Devido À peculiar natureza do sinal, um método baseado em dados é utilizado para a estimativa de eventos de fundo.

Os resultados finais, derivados do conjunto completo de dados do Run 2, sem a consideração da região de sinal, estabelecem os limites esperados mais restritivos até hoje para a produção de monopólos no experimento CMS. Este trabalho expande os limites da sensibilidade experimental a monopólos magnéticos, ao mesmo tempo em que contribui para o conjunto de ferramentas de precisão necessário para a operação em alta luminosidade por meio do monitoramento da luminosidade baseado em bósons Z.

Palavras-chave: Experimento CMS, LHC, Física além do Modelo Padrão, Monopólos magnéticos, Partículas altamente ionizantes, luminosidade, contagem de bósons Z

List of Figures

List of Tables

Summary

1 Fundamentals of particle physics

The Standard Model of particle physics (SM) is the prevailing theory for describing all known fundamental particles and interactions known to date. In this chapter, a summary of the *Standard Model* (SM) is provided, where a more detailed description can be found in Refs. [1, 2, 3, 4, 5, 6, 7, 8]. The SM is also known to be an incomplete theory, as topics such as gravitation, dark matter, and neutrino masses, among many others are not addressed by this model. In particle collision experiments, rigorous tests of the SM are performed to investigate some of these open questions. In particle collision experiments, rigorous tests of the SM are performed to investigate some of these open questions.

The *Standard Model* (SM) of particle physics has been in development since the 1960s. It consists of a Quantum Field Theory (QFT) for describing the dynamics of elementary particles and their interactions. In such a framework, a particle can be interpreted as an excited state of its underlying quantum field. The elementary particles described by the SM can be divided into fermions, vector bosons, and scalar bosons.

The fermions follow the Fermi-Dirac statistics, which, according to Pauli's exclusion principle, means that two particles with the same quantum numbers cannot exist in the same quantum state. Therefore, the fermions with the same quantum number must be separated from each other, forming the known matter of the Universe. Fermions can be divided into quarks and leptons, with leptons further classified as charged leptons and neutrinos. The second type of particles in the SM are the bosons, which obey the Bose-Einstein statistics, allowing two or more bosons to occupy the same quantum state.

The fundamental interactions in the Standard Model (SM) are described by gauge theories, with their mediators being spin-1 vector bosons. These forces include the electromagnetic, strong, and weak interactions. The four types of vector bosons are the gluons (mediators of the strong force), the photon (mediator of the electromagnetic force), and the $W^{\pm}$ and Z bosons (mediators of the weak force). The only spin-0 scalar boson in the SM is the Higgs boson, which is associated with the Brout-Englert-Higgs mechanism. The particle content of the SM is summarized in Figure 1.

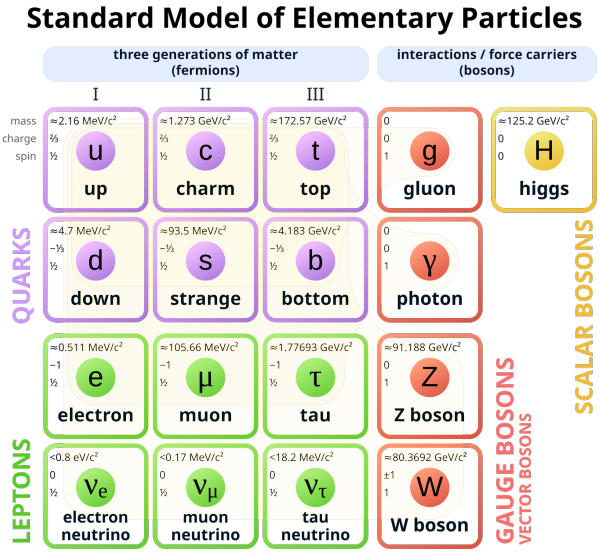

Figure 1 – Elementary particles described by the Standard Model of particle physics, with measured mass [9], spin denoted as scalar boson (spin 0), fermion (spin 1/2), or vector boson (spin 1), and electric charge.

Gauge theory:

The equation of motion for a field Φ is obtained from the principle of the least action.

$$\frac{\partial S[\Phi]}{\partial \Phi} = 0, \tag{1.1}$$

where $\mathcal{S}$ is a functional that depends on the field that can be written as

$$S[\Phi] = \int \mathcal{L}\Big(\Phi(x_\mu), \partial_\mu \Phi(x_\mu), x_\mu\Big)\, dx_\mu. \tag{1.2}$$

The interactions in the Standard Model (SM) are described through the local internal symmetries of $\mathcal{L}$, where the `SU(3)` symmetry represents the strong interaction. At high energy scales, the `SU(2)` $\times$ `U(1)` symmetry represents the electroweak interaction, while at low energy, the `SU(2)` symmetry is spontaneously broken leading to the split of the electroweak interaction into electromagnetic and weak interactions. An internal symmetry, which is also known as *gauge symmetry*, corresponds to a transformation that acts on the quantum field that leaves physical observables unchanged.

The bosons that mediate the fundamental interactions are known as gauge bosons, which are required to restore the symmetry after a transformation of the fermion fields. According to Noether's theorem, each continuous symmetry of the Lagrangian $\mathcal{L}$ corresponds to a conserved quantity [10]. These conserved quantities are identified with charges

to which the gauge bosons couple. These charges serve as additional quantum numbers for the particles.

Free fermion fields:

Under Lorentz transformation, the fermions are represented by two-component fields known as spinors, which can be represented by two different states, depending on their spin. The right-chiral (or right-handed) state is characterized by spin +1/2, while the left-chiral (or left-handed) by spin -1/2. Since the *Quantum Electrodynamics* (QED) was found to be invariant under parity transformations, fermions in QED are described as having both left and right chiral components. The two chiral states of the fermion can be expressed as

$$\Psi = \begin{pmatrix} \psi_L \\ \psi_R \end{pmatrix} \tag{1.3}$$

which is a four component field.

The Lagrangian of a free fermion field can be written as:

$$\mathcal{L}_{\text{Dirac}} = -m\overline{\Psi}\Psi + i\overline{\Psi}\gamma^{\mu}\partial_{\mu}\Psi, \tag{1.4}$$

which is invariant under the parity transformation, where $\bar{\Psi} = \Psi^{\dagger}\gamma^{0}$ is the Dirac adjoint and γ^{μ} are the Dirac gamma matrices.

1.1 Strong interaction

The *Quantum Chromodynamics* (QCD) is the quantum field theory that describes the strong interactions between the color-charged particles, which comprise the six quarks and eight gluons. The six quark flavors correspond to the up u, charm c, and top t known as the "up-type" quarks, and down d, strange s, and bottom b, the "down-type" quarks. The up-type quarks have an electric charge of +2/3 and down-type quarks of -1/3. Each quark carries one of three possible color charges, while antiquarks carry the corresponding anti-color charges. The massless gluons form a color octet and carry both a color and an anti-color charge. This structure allows interactions between the fields themselves, making QCD a non-Abelian gauge theory. As a result, the strong interaction is described by both quark-gluon couplings and gluon self-interactions.

In Figure 2, the measurements of the strong interaction coupling constant α_s as a function of different energy scales Q. It is worth noting the decrease of the interaction strength with the momentum transfer, commonly called the "running" of α_s. At the QCD scale of $\Lambda_{QCD} \approx 200$ GeV [11], due to high values of α_s at energies below the Λ_{QCD}, colored

particles can not exist as free particles. This leads to the phenomenon of confinement, in which quarks are bound into color-neutral states called hadrons.

At high energies, where α_s becomes small, quarks behave as if they are free particles—a phenomenon known as asymptotic freedom. In this regime, the matrix elements calculations can be approximated with a perturbative expansion in terms of α_s.

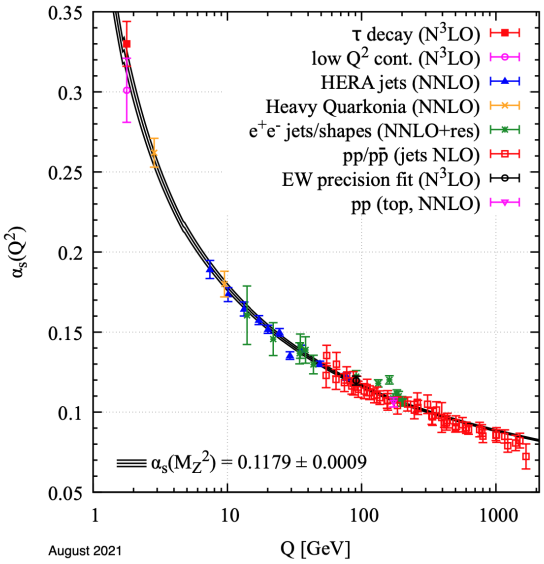

Figure 2 – Summary of measurements of the constant α_s as a function of the energy scale Q. The respective degree of QCD perturbation theory employed in the measurement of α_s is indicated, *next-to-leading* (NLO), *next-to-next-to-leading* (NNLO), NNLO+res., NNLO matched to a resummed calculation, and *next-to-NNLO* (N^3LO).

In high-energy interactions, the created quarks and gluons produce a shower of additional quarks and gluons via the strong interaction. As the energy of these particles drops below a certain threshold, they combine into color-neutral hadrons in a process known as "hadronization", which results in a collimated stream of hadrons called a "jet", which carries the energy and momentum from the initial parton. A detailed description of the jets is provided in Section 3.4.2.3.

1.2 Electroweak interaction

Unlike Quantum Electrodynamics (QED), the weak interaction is not invariant under parity transformation (P-violation), which was contrary to the assumptions [12]. After further experiments, it was established that the P-violation was maximal for weak interaction, where only left-chirality fermions participate in the weak interaction.

The weak and electromagnetic forces are unified under a single framework, the electroweak interaction (EW). This theory was developed by Glashow [13], Salam [8], and

Weinberg [7]. The electroweak scale, of about 246 GeV, defines the energy regime where this unified interaction is valid. Below this scale, the underlying symmetry is spontaneously broken, resulting in the separation into distinct weak and electromagnetic interactions. This symmetry breaking is described by the Higgs mechanism, which is discussed later in this chapter.

Before symmetry breaking:

Before the symmetry breaking via the Higgs mechanism, the electroweak (EW) theory is described by a $\mathtt{SU(2)} \times \mathtt{U(1)}$. The corresponding charges of the `U(1)` and `SU(2)` symmetries are the hypercharge Y_W and the third component of the weak isospin T_3, respectively. The electric charge Q is then defined as a linear combination of these two quantities, given by the Gell-Mann–Nishijima equation [14, 15]:

$$Q = \frac{Y_W}{2} + T_3 \tag{1.5}$$

Due to the description of the P-violating nature of the weak interaction, the `SU(2)` transformation acts only on fermions with left chirality, which are organized into weak isospin doublets L. In contrast, right-chiral fermions do not transform under the `SU(2)` group and are treated as weak isospin singlets R. Since neutrinos are considered massless and interact only via weak interaction, they are included only in the left-chiral fermion doublets.

The Higgs mechanism:

Within the `SU(2)` symmetry, mass terms for the vector boson fields are not allowed, and fermions within an isospin doublet are constrained to have equal masses. However, from the experimental results, it is well established that this symmetry must be broken at low energies. The mechanism that explains this spontaneous symmetry breaking—and enables the generation of mass terms for the vector bosons is the Higgs–Brout–Englert mechanism [5, 3].

The Lagrangian of the Higgs field can be written as

$$\mathcal{L}_H = (D_\mu \Phi^\dagger)(D^\mu \Phi) - V(\Phi) \tag{1.6}$$

$$V(\Phi) = -\rho^2 \Phi^\dagger \Phi + \lambda (\Phi^\dagger \Phi)^2 \tag{1.7}$$

where $\Phi = (\Phi^+, \Phi^0)^T$ is an isospin doublet composed of two complex scalar fields, and $V(\Phi)$ is the Higgs potential.

The real parameter λ is the Higgs quartic coupling, which must be positive to ensure the stability of the EW vacuum. The parameter ρ^2 defines the minimum of $V(\Phi)$ for a given positive value of λ, as illustrated in Figure 3. At very high energies, ρ^2 takes on a negative value, resulting in a single minimum configuration of the Higgs potential $V(\Phi)$, with $\Phi_{\text{min}} = (0, 0)^T$.

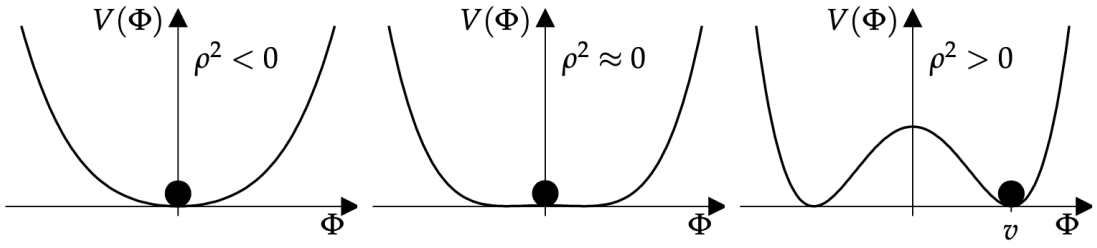

Figure 3 – The one-dimensional Higgs potential profile. The left plot corresponds to the potential before the symmetry breaking, the central plot to the critical energy, and the right plot illustrates to the potential after the symmetry breaking.

With the changes of the values of the parameters λ and ρ^2, an infinite number of minima arise for every real value of ϕ, given by

$$\Phi_{\text{min}} = e^{i\phi} \left(0, \sqrt{\rho^2/2\lambda}\right) \tag{1.8}$$

However, the selection of one of the minima results in the spontaneous breaking of the `SU(2)` symmetry. Since the underlying physics remains invariant under the choice of vacuum, a specific minimum can be selected without loss of generality. A common choice is:

$$\Phi_{\text{min}} = e^{i\phi} \left(0, v/\sqrt{2}\right)^T \tag{1.9}$$

with the vacuum expectation value of $v = \sqrt{\rho^2/\lambda}$.

An expansion around the minimum could be made, leading to

$$\Phi = e^{i\Theta_i \frac{\sigma_i}{2}} \begin{pmatrix} 0 \\ \frac{v+H}{\sqrt{2}} \end{pmatrix} \longrightarrow \begin{pmatrix} 0 \\ \frac{v+H}{\sqrt{2}} \end{pmatrix} \tag{1.10}$$

showing the transition to unitary gauge, where the Goldstone bosons are "gauged away".

A particular transformation, the unitary gauge, is chosen to absorb the three free parameters Θ_i, leaving a single physical Higgs field H. For the new ϕ in the Lagrangian of Equation 1.6, a non-diagonal mass matrix for the vector boson fields results from the mass eigenstates of the original fields. Diagonalizing this matrix yields the physical mass eigenstates, which are given by:

$$\begin{pmatrix} W_\mu^+ \\ W_\mu^- \end{pmatrix} = \begin{pmatrix} \frac{1}{\sqrt{2}} & -\frac{i}{\sqrt{2}} \\ \frac{1}{\sqrt{2}} & \frac{i}{\sqrt{2}} \end{pmatrix} \begin{pmatrix} W_\mu^1 \\ W_\mu^2 \end{pmatrix} \tag{1.11}$$

$$\begin{pmatrix} A^\mu \\ Z^\mu \end{pmatrix} = \begin{pmatrix} \cos\Theta_W & \sin\Theta_W \\ -\sin\Theta_W & \cos\Theta_W \end{pmatrix} \begin{pmatrix} B^\mu \\ W_\mu^3 \end{pmatrix} \tag{1.12}$$

where Θ_W is the Weinberg angle, also known as the weak mixing angle, which relates the fields of the `U(1)` and `SU(2)` groups.

The weak mixing angle determines the relationship between the masses of the Z and W bosons, which are given by $m_Z = m_W/\cos\Theta_W$. The angle Θ_W is a free parameter of the SM, and it is also related to the coupling constants g and g', as well as to the electromagnetic charge e. The massive Z_μ and $W_\mu^\pm$ boson fields mediate the neutral and charged current interactions through the Z and $W_\pm$ bosons. The masses of the weak bosons and the Higgs boson are given by:

$$m_Z = \frac{1}{2} v \sqrt{g^2 + g'^2}, \tag{1.13}$$

$$m_W = \frac{1}{2} v g, \tag{1.14}$$

$$m_H = \sqrt{2\lambda}\, v^2. \tag{1.15}$$

The large masses of the Z and W bosons are responsible for the short-range interaction character of the weak interaction, translating to short lifetimes of less than 10^{-24} s. These bosons decay into all three generations of leptons and quarks, except for the top quark. The decay fraction into quarks is the largest, due to the presence of three color charges for each quark flavor.

In the limit where the masses of the decay products are much smaller than the mass of the gauge boson, the gauge bosons can couple to all charged leptons with the same strength, a property called lepton universality. However, there are pieces of evidence for the violation of lepton universality, measured in decays of the B^+ mesons into K^+ in association with lepton pairs [16]. In these decays, for the ratio between the branching fractions into electrons and muons, a tension of 3.1 standard deviations from the SM prediction can be observed, opening the possibility for *Beyond Standard Model* (BSM) contributions.

Quantum Electrodynamics:

The *Quantum Electrodynamics* (QED) is the QFT that describes the electromagnetic interaction between the electrically charged fermions (quarks and leptons) mediated

by the photon. The three charged leptons ℓ^- are the electron e^-, the muon μ^-, and the tau lepton τ^-, with an electric charge of -1 and no color charge, and the corresponding antileptons ℓ^+ with an electric charge of +1. Since the massless photon has no electric charge, the electromagnetic interaction can be described only by fermion-photon couplings.

The strength of the electromagnetic interaction α_{EM} increases slowly as the momentum transfer decreases. The $\alpha_{\mathrm{EM}} \approx 1/137$, defined at zero momentum transfer, is known as the fine-structure constant. At higher energies, such as the mass scale of the Z boson, it increases to $\alpha_{EM} \approx 1/129$. Since α_{EM} is significantly smaller than unity, the cross-section calculations for QED processes can be reliably performed using perturbative expansions.

The weak interaction is the only fundamental interaction that involves all fermions, quarks, leptons, and neutrinos. It is mediated by the $W^{\pm}$ and Z bosons, which have masses of 80.4 GeV and 91.2 GeV, respectively. The $W^{\pm}$ boson carries an electric charge, while the Z boson is electrically neutral.

The neutrinos carry neither an electric charge nor a color charge, and there is one neutrino ν_ℓ for each charged lepton flavor ℓ. In the context of the SM, the neutrinos are considered massless particles, although the observation of neutrino oscillations requires neutrinos with a small but nonzero mass [17, 18].

In the Standard Model, neutrinos are treated as massless particles. However, the observation of neutrino oscillations provides clear evidence that neutrinos possess small but nonzero masses [17, 18].

Since the large mass of the mediators, the weak interaction is a short-range force at energy scales smaller than the mediator masses. Its interaction strength is much weaker than that of the electromagnetic or strong forces.

The mediation of the interaction between fermions and anti-fermions of the same flavor is provided by the Z boson, while the $W^{\pm}$ mediates the charged weak interactions, which is the only interaction in the SM where the change of flavor of particles can be changed. The W bosons couple to a neutrino and a lepton, or an up-type and a down-type quark. Additionally, W and Z bosons couple to each other, and because the W boson's electric charge, they also couple to photons.

The couplings of the W bosons defined the three generations of fermions present in the SM. Such generations are defined as follows. The first generation is composed of the electron-neutrino, the electron, the up quark, and the down quark. The second generation is composed of the muon-neutrino, the muon, the charm quark, and the strange quark. At last, the third generation comprises the tau-neutrino, the tau lepton, the top quark, and the bottom quark. These generations are ordered by mass: particles in the second generation are heavier than those in the first, while particles in the third are heavier still.

The W boson couples only to leptons and neutrinos of the same generation, and preferably to quarks of the same generation.

The reason for the existence of exactly three fermion generations in the Standard Model remains an open question.

However, there are no pieces of evidence for particles of a fourth generation. In particular, precision measurements of the Z boson width at the *Large Electron-Positron Collider* (LEP), effectively exclude a fourth neutrino generation [19].

The flavor mixing between quarks in charged weak interactions is described by the Cabibbo-Kobayashi-Maskawa (CKM) matrix [20, 21, 22]. The matrix elements $|V_{\alpha\beta}|$ ($|V_{\alpha\beta}|^2$) quantifies the transition probability between the up-type flavor α and the down-type flavor β, with special attention the terms of the main diagonal, which are dominant between the quarks of the same generation. Thus, couplings between quarks of different generations and a W boson are significantly suppressed, especially for couplings that involve a third-generation quark.

Because the charged weak interaction is the only fundamental interaction that allows flavor-changing decays of elementary particles, the CKM matrix plays a central role in determining the decay patterns and lifetimes of third-generation fermions.

From a global fit to experimental results sensitive to the CKM matrix elements, the absolute values of the nine elements are found to be:

$$V_{\mathrm{CKM}} = \begin{pmatrix} |V_{ud}| & |V_{us}| & |V_{ub}| \\ |V_{cd}| & |V_{cs}| & |V_{cb}| \\ |V_{td}| & |V_{ts}| & |V_{tb}| \end{pmatrix} = \begin{pmatrix} 0.97367 \pm 0.00032 & 0.22431 \pm 0.00085 & 0.00382 \pm 0.00020 \\ 0.221 \pm 0.004 & 0.975 \pm 0.006 & 0.0411 \pm 0.0012 \\ 0.0086 \pm 0.0002 & 0.0415 \pm 0.0009 & 1.010 \pm 0.027 \end{pmatrix} \tag{1.16}$$

Due to the almost diagonal structure of the CKM matrix, it is convenient to also express it as an expansion in terms of a small parameter $\lambda = \sin\theta_c = 0.225$, where θ_c is the Cabibbo angle. This approach is known as the Wolfenstein parameterization [23], allowing the matrix to be written in terms of four parameters λ, A, ρ, and η, making it easier to identify the CP-violating term for the Standard Model.

$$V_{\mathrm{CKM}} = \begin{pmatrix} |V_{ud}| & |V_{us}| & |V_{ub}| \\ |V_{cd}| & |V_{cs}| & |V_{cb}| \\ |V_{td}| & |V_{ts}| & |V_{tb}| \end{pmatrix} = \begin{pmatrix} 1 - \lambda^2/2 & \lambda & A\lambda^3(\rho - i\eta) \\ -\lambda & 1 - \lambda^2/2 & A\lambda^2 \\ A\lambda^3(1 - \rho - i\eta) & -A\lambda^2 & 1 \end{pmatrix} + \mathcal{O}(\lambda^4) \tag{1.17}$$

The Wolfenstein's parameters are obtained through a global fit with constraints from the SM [9].

$$\lambda = 0.22501 \pm 0.00068, \qquad A = 0.826^{+0.016}_{-0.015},$$
$$\bar{\rho} = 0.1591 \pm 0.0094, \qquad \bar{\eta} = 0.3523^{+0.0073}_{-0.0071}$$

1.2.1 Fermion masses

The coupling between the Higgs field and fermion fields can be included in the Lagrangian without breaking the `SU(2)` symmetry, which is described by the Yukawa interaction. Although originally developed for the explanation of the strong force through the exchange of spin-0 bosons [24], Yukawa interactions account for fermion mass generation following spontaneous symmetry breaking. The Higgs-fermion coupling terms take the form:

$$\mathcal{L}_{\text{Yukawa},f} = -\lambda_f \left(\overline{L} \Phi r + \text{h.c.} \right) \tag{1.18}$$

where λ_f is a coupling constant the *h.c.* is the hermitian conjugate.

After spontaneous symmetry breaking, the Higgs field acquires a nonzero vacuum expectation value, which generates mass terms for the fermions through the Yukawa interaction. Since the Higgs-Yukawa coupling has a linear relation with the fermion masses, the strength of the coupling increases with the mass of the fermion.

1.3 Physics beyond the Standard Model

The Standard Model (SM) of particle physics has been remarkably successful in the prediction and description of particle physics phenomena known to date. In the context of high-energy colliders experiments, it provides a robust framework that is continuously probed, with no significant deviations observed to this day. However, outside of collider experiments, there are clear pieces of evidence for the existence of physics phenomena that cannot be described by the SM. Thus, a model of particle physics with extensions of the SM is required, where among such phenomena, neutrino oscillations and dark matter can be mentioned.

The spontaneous conversion of neutrino flavors into each other, also known as neutrino oscillations, has been observed in dedicated neutrino experiments [17, 18]. A theoretical description of such oscillations requires that the neutrinos have a nonzero mass, which contradicts the SM expectation. Current cosmological observations constrain the neutrino masses to be very small, in the order of $\Sigma m_\nu < 0.12$ eV [25]. This has motivated extensions of the SM that incorporate neutrino mass terms. Moreover, the remarkable difference in the mass scale of the top quark mass and the neutrinos, which is about twelve

orders of magnitude, leads to additional questions about the underlying fundamental physics mechanisms responsible for fermion mass generation and points to the existence of new physics beyond the SM [26].

The astrophysical observations from Zwicky [27] indicate that the ordinary matter, which will later be described by the SM, only accounts for a fraction of the matter content of the Universe. According to the most recent cosmological measurements [25], which includes the dynamic of galaxies and the *Cosmic Microwave Background Radiation* (CMBR), the energy composition in the Universe is approximately: 69% of dark energy, 26 % of dark matter, and only about 5% of ordinary (baryonic) matter. Dark matter can be understood as gravitationally interacting matter, even with some considerations about its weak interaction possibilities. Several extensions of the SM propose new elementary particles that can be understood as dark matter candidates, such as *Weakly Interacting Massive Particles* (WIMPs) and axions. The dark energy component is required for the explanation of the accelerating expansion of the Universe, where it could be understood as a negative-pressure component. First inferred from Type Ia supernova observations [28], the dark energy could be modeled as a cosmological constant (Λ) within the ΛCDM framework, commonly known as the standard model for cosmology.

The observable structure of the Universe is composed almost entirely of matter, with little evidence for a significant presence of antimatter [29]. This imbalance is commonly referred to as baryonic asymmetry, and it could be explained by processes that violate the conservation of baryonic numbers, as well as charge conjugation (C) and charge-parity (CP) symmetries. The necessary conditions for generating such an asymmetry were outlined by Sakharov in 1967 [30]. These Sakharov conditions require: (1) baryon number violation, (2) C and CP violation, and (3) a departure from thermal equilibrium. All three conditions are necessary for the generation of the matter–antimatter asymmetry in the early Universe.

The *Grand Unified Theory* (GUT) was proposed to provide a common description of the strong and electroweak interactions, building on the successful unification of the electromagnetic and weak interactions. From an extrapolation of the energy dependence of the interaction strengths, the grand unification would be expected to occur at an energy scale of $\Lambda_{\mathrm{GUT}} \approx 10^{16}$ GeV. Considering a further unification with gravity as the four fundamental forces could lead to a "Theory of Everything" (TOE). However, since the gravitational interaction strength is much smaller than the other interactions, its impact on particle physics interactions would only be noticeable at energies above the Planck scale of $\Lambda_{\mathrm{Planck}} \approx 10^{19}$ GeV. A theory for the description of gravity in the QFT context is referred to as quantum gravity [31].

To provide possible explanations for such phenomena, several new physics models, or simply extensions of the SM, have been proposed. One of the most notable examples is supersymmetry (SUSY), which introduces a new symmetry that relates fermions and

bosons [32]. Many of these models predict new elementary particles at diverse energy scales, some of which could be within reach of current collider experiments such as the Large Hadron Collider (LHC). However, due to the absence of experimental evidence for new physics at the LHC, the search for deviations from SM expectations in precision measurements of SM observables gains importance in the search for new physics. A powerful and promising approach is the SM effective field theories (SMEFT) [33, 34, 35], which extends the SM by the inclusion of all possible higher-order couplings between the SM fields. This allows for a model-independent interpretation of precision measurements and enables constraints on potential new physics contributions.

2 Theoretical foundations of magnetic monopoles at CMS Experiment

In this first chapter, the role of magnetic monopoles in classical electromagnetism and Maxwell's equations is briefly described. The theoretical motivations for the monopoles, including Dirac and Schwinger quantizations, as well as their possible realization in the *Grand Unified Theories* (GUT) context, are also discussed.

From an experimental context, there have been many methods developed to search for such particles, considering both naturally occurring and collider-produced candidates. Previous particle collider experiments have focused on their characteristics as *Highly-Ionizing Particles* (HIPs) and their interactions with matter. The construction of the *Large Hadron Collider* (LHC) at *Organisation Européenne pour la Recherche Nucléaire* (CERN) allows the possibility to probe these particles for collider-produced methods. With its unprecedented collision energies, the LHC allows probes of monopole masses up to the multi-TeV scale, currently the highest energy range accessible for such searches.

2.1 Magnetic monopoles in electromagnetism

In classical electrodynamics, Maxwell's equations reveal an inherent asymmetry between electric and magnetic fields, due to the non-observation of a magnetic monopole. Because isolated magnetic charges have never been detected, they are excluded from the equations, resulting in this asymmetry.

In the absence of magnetic monopoles, Maxwell's equations can be written through the composition of the Gauss's law for electricity by 2.1 and magnetism by 2.2, Faraday's law by 2.3, and Ampère's law by 2.4.

$$\nabla \cdot \vec{E} = \frac{\rho}{\epsilon_0} \tag{2.1}$$

$$\nabla \cdot \vec{B} = 0 \tag{2.2}$$

$$\nabla \times \vec{E} = -\frac{\partial \vec{B}}{\partial t} \tag{2.3}$$

$$\nabla \times \vec{B} = \mu_0 \vec{J} + \mu_0 \epsilon_0 \frac{\partial \vec{E}}{\partial t} \tag{2.4}$$

where ρ is the electric charge density, ϵ_0 is the permittivity of free space, μ_0 is the permeability of free space, $\vec{J}$ is the electric current density, $\vec{E}$ the electric field, and $\vec{B}$ the magnetic field.

From Gauss's law for electricity, the divergence of the electric field originates from the distribution of an electric charge density (ρ), allowing the electric field lines to originate from this particular point in space. In contrast, from Gauss's law for magnetism, it can be observed that the magnetic field doesn't diverge, indicating that magnetic field lines form closed loops and do not originate from any point in space. This reflects the absence of magnetic charges (monopoles). Experimental evidence supports this since no magnetic monopoles have ever been observed. As a result, electric charge and current densities remain the main sources of both electrical and magnetic fields.

The consideration of a magnetic monopole would introduce a magnetic charge density $\vec{\rho}_m$ and a magnetic current density given by $\vec{J}_m$, restoring the symmetry in Maxwell's equations, leading to a modified version of such equations.

$$\nabla \cdot \vec{E} = \frac{\rho}{\epsilon_0} \tag{2.5}$$

$$\nabla \cdot \vec{B} = \mu_0 \rho_m \tag{2.6}$$

$$\nabla \times \vec{E} = -\frac{\partial \vec{B}}{\partial t} - \mu_0 \vec{J}_m \tag{2.7}$$

$$\nabla \times \vec{B} = \mu_0 \vec{J} + \mu_0 \epsilon_0 \frac{\partial \vec{E}}{\partial t} \tag{2.8}$$

The introduction of the magnetic monopole would make Maxwell's equation symmetric for both electric and magnetic fields under the duality transformation.

$$\begin{pmatrix} \vec{E} \\ c\vec{B} \end{pmatrix} = \begin{pmatrix} \cos\xi & \sin\xi \\ -\sin\xi & \cos\xi \end{pmatrix} \cdot \begin{pmatrix} \vec{E}' \\ c\vec{B}' \end{pmatrix} \tag{2.9}$$

$$\begin{pmatrix} c\rho_e \\ \rho_m \end{pmatrix} = \begin{pmatrix} \cos\xi & \sin\xi \\ -\sin\xi & \cos\xi \end{pmatrix} \cdot \begin{pmatrix} c\rho'_e \\ \rho'_m \end{pmatrix} \tag{2.10}$$

where ξ corresponds to the transformation parameter.

A duality transformation shows that the electric charge density and current are symmetric concerning the magnetic charge density and current under such transformation. The original Maxwell's equations can be recovered for the definition of the transformation angle $\xi = 0$. This symmetry achieved by the duality transformation raises fundamental questions about the individual distinction between electric and magnetic charges.

2.2 Dirac Magnetic Monopole

In 1931, Paul Dirac published a paper proposing the existence of magnetic monopoles within the framework of quantum mechanics, where it is shown that such particles

could provide a clear explanation for the charge quantization [36]. In his approach, by the behavior of an electric charge q in the vicinity of a magnetic charge g, the electric charge quantization could be described in a theory with the presence of magnetic monopoles. In 1948, the theory of the magnetic poles was also established by Paul Dirac [37], creating the theory of Dirac's string.

The Dirac quantization condition states that if a magnetic charge exists, then electric charge must be quantized, opening the possibility for the existence of a magnetic monopole type of particle. The construction of the magnetic monopole in quantum theory following Dirac's work can be summarized in the *gauge transformation*, and the introduction of the *Dirac's string*. Assuming the electric and magnetic fields described by the equations 2.11 and 2.12, due to the gauge invariance of electromagnetism, it is expected that such equations remain invariant under transformations of the form shown in Equations 2.13 and 2.14. This framework provides the foundation for incorporating monopoles into quantum theory while preserving consistency with the principles of gauge invariance.

$$\mathbf{B} = -\nabla\phi - \frac{1}{c}\frac{\partial \mathbf{A}}{\partial t} \tag{2.11}$$

$$\mathbf{B} = \nabla \times \mathbf{A} \tag{2.12}$$

$$\mathbf{A}' = \mathbf{A} + \nabla\Lambda \tag{2.13}$$

$$\phi' = \phi - \frac{\partial \Lambda}{\partial t} \tag{2.14}$$

Since the vector potential $\vec{A}$ does not correspond to a physical observable, the selection of such a potential is arbitrary and does not influence the observable physical quantities of the electric and magnetic fields, given by $\vec{E}$ and $\vec{B}$, respectively.

In quantum mechanics, a similar evaluation can be performed starting with the Hamiltonian of a charged particle q in an electromagnetic field.

$$H = \frac{1}{2m}\left(\vec{p} - q\vec{A}\right) + q\phi \tag{2.15}$$

where $\vec{p}$ is not gauge invariant.

The canonical momentum defined by

$$\vec{p}_{\text{canonical}} = m\vec{v} + q\vec{A} \tag{2.16}$$

which, under a gauge transformation can be written as

$$\vec{p}_{\text{canonical}} \rightarrow \vec{p}_{\text{canonical}} + q\nabla\Lambda \tag{2.17}$$

showing the change in the momentum by the gauge choice.

On the other hand, considering the kinetic momentum as the real physical observable, which can be described by:

$$\vec{p}_{\text{kinetic}} = m\vec{v} = \vec{p} - q\vec{A} \tag{2.18}$$

which, under a gauge transformation, can be written as

$$\vec{p}_{\text{kinetic}} \rightarrow \vec{p}_{\text{kinetic}} + q\nabla\Lambda - q\nabla\Lambda = \vec{p}_{\text{kinetic}} \tag{2.19}$$

denoting the gauge invariance of the kinetic momentum.

The electromagnetism is gauge invariant both from the classical and quantum mechanics approaches, provided that magnetic monopoles are absent from Maxwell's equations.

$$\vec{E}(\vec{r}) = \frac{1}{4\pi\epsilon_0}\frac{q}{r^2}\hat{r}, \tag{2.20}$$

where r is the distance from the source charge q.

In a similar manner, the magnetic field $\vec{B}$ of a magnetic charge g is described as

$$\vec{B}(\vec{r}) = \frac{\mu_0 g}{4\pi r^2}\hat{r}, \tag{2.21}$$

In quantum mechanics, electromagnetic interactions are described using scalar and vector potentials. The magnetic field is derived from the vector potential $\vec{A}$ through the equation:

$$\vec{B}(\vec{r}) = \nabla \times \vec{A} = \frac{\mu_0 g}{4\pi r^2}\hat{r}, \tag{2.22}$$

where a possible solution is the magnetic vector potential in the form of

$$\vec{A}(\vec{r}) = \frac{\mu_0 g(1-\cos\theta)}{4\pi r \sin\theta}\hat{\phi}, \tag{2.23}$$

where θ and ϕ are the polar and azimuthal angular coordinates, respectively.

This vector potential by Equation 2.23 represents the magnetic field of a point-like source of magnetic charge overlaid on the field of an infinitely long, thin solenoid extending from $z = -\infty$ to the origin, where the magnetic monopole is located. This potential becomes undefined at $\theta = \pi$, introducing a singularity known as the Dirac string.

Such a string can be imagined as a curved line that extends from one pole to the other located at infinity, carrying an opposite charge. In classical electrodynamics, this singularity does not lead to physical inconsistencies, since the magnetic field is the physical observable. For an infinitely long and thin *Dirac string*, it becomes invisible for any electrodynamic interaction.

However, in the framework of quantum mechanics, the presence of the Dirac string has observable consequences. When a point-like electric charge q is present, the vector potential affects the wavefunction. This interaction introduces a measurable phase shift in the wavefunction, which leads directly to the Dirac quantization condition. The resulting shift in the wave equation due to the electric charge can be evaluated from:

$$\Delta\Phi = \frac{q}{\hbar}\int_s \vec{A}\cdot d\vec{l} = \frac{\mu_0 gq}{4\pi\hbar}\lim_{\theta\to\pi}(1-\cos\theta)\int_0^{2\pi} d\phi = \frac{\mu_0 gq}{\hbar} \tag{2.24}$$

For the electric charge to remain unaffected, the shift from the equation 2.24 should be a non-negative integer multiple of 2π.

$$\frac{\mu_0 gq}{\hbar} = 2\pi n \rightarrow qg = \frac{2\pi nn}{\mu_0} \tag{2.25}$$

Under this approach, the *Charge Quantization Condition* can be derived. The right-hand side of the Equation 2.25 establishes that the electric charge is always a non-negative integer multiple of the magnetic charge. For n = 1 in the right-hand side of the Equation 2.25 and rewriting it in terms of the fine structure constant $\alpha = \mu_0 e^2/4\pi\hbar$, the smallest quantum of magnetic charge (g_D) is given by:

$$g = \frac{ne^2}{2\alpha q}(\text{for } n=1, q=e) \rightarrow g_D = \frac{e}{2\alpha} = 68.5e \tag{2.26}$$

where e is the charge of electron, observed as the smallest isolated unit of electric charge.

The result obtained in the equation 2.26 establishes the equivalence of the Dirac magnetic charge and the electric charge by a factor of 68.5. Consequently, a relativistic magnetic monopole with a minimum magnetic charge would have an ionization capacity about 4700 times greater than a particle with a single electric charge. Similarly, the strength of the magnetic Coulomb force between two elementary single charges is about 4700 times that of the electrostatic force between two elementary electric charges.

Such a remarkable ionization capacity will be observed as a large energy loss per unit of length, due to ionization, serving as a key property for its exploration in particle collider experiments.

2.3 The Schwinger monopole

The extension of the magnetic monopoles theory from Dirac was performed by Julian Schwinger, by the study of the monopole relativistic invariance [38]. From his study, the vector potential, which presents a solution for the field of the magnetic monopoles, can be described by:

$$\vec{A}(\vec{r}) = \frac{\mu_0 g}{4\pi r}\text{cotan}(\theta)\hat{\phi}, \tag{2.27}$$

From this definition, depending on the choice of vector potential can lead to alternative quantization conditions, other than the one proposed by Dirac in Equation 2.26. In some formulations, the minimum magnetic monopole charge would be twice the Dirac charge.

In 1969, Schwinger hypothesized a particle with an electric and magnetic charge, the so-called Dyons [38]. In this case, the quantization condition is given by

$$e_1 g_2 - e_2 g_1 = n \tag{2.28}$$

where we have two dyons with electric and magnetic charges (e_1, g_1) and (e_2, g_2).

The Dirac quantization condition also constrains the allowed electric charge for the dyons, where many of the theoretical arguments made for monopoles could be extended to the dyons, where some gauge models predict the existence of both monopoles and dyons. Such dyons are expected to be heavier than electrically neutral monopoles. Consequently, they can decay to monopoles via a process such as Dyon$^{\pm} \rightarrow M + e^{\pm} + X$, where X represents any other final-state particles.

2.4 Monopole-Photon coupling

The strength of the coupling between the photon and the electron is characterized by the fine structure constant α, and it can be employed for the definition of the monopole-photon coupling by the replacement of the electric charge e by e $\rightarrow$ g = ng_D/c

$$\alpha_m = \frac{\mu_0 g_D^2 c}{4\pi\hbar c} n^2 \tag{2.29}$$

The result for the monopole-photon coupling constant indicates is approximately 4 orders of magnitude greater than the fine structure constant. Considering n = 1, the coupling constant is $\alpha_m \approx 34$. This strong coupling strength has important implications for both the production of monopoles and their interactions with matter, indicating that

monopoles would be highly ionizing and strongly interacting particles—distinct from any known Standard Model particle.

2.5 Monopoles in Grand Unified Theories

The *Grand Unified Theories* (GUT) are characterized by the free production of all gauge bosons, all interactions have the same strength, and quarks can transform into leptons as easily as they change colors, manifesting the grand SU(5) symmetry. At an energy of about 10^{15} GeV, the SU(5) symmetry breaks down to originate the SU(3) and SU(2) $\times$ U(1) symmetries, the strong and electroweak interactions. At about 10^2 GeV, the SU(2) $\times$ U(1) symmetry becomes broken, reflecting the separation of electroweak interaction into the distinct weak and electromagnetic interactions. This picture of the unification of interactions also incorporates the variation in the strengths of charges, depending on the distance from which they are acted upon.

Unlike Dirac's monopole, several *Grand Unified Theories* (GUT), theories predict the existence of magnetic monopoles. Depending on the different grand unification scale M_X, varying ranges for the monopole mass can be predicted. The quantization of charge, as a result of the existence of monopoles, arises in the GUT models where the U(1) group is embedded into a higher rank non-Abelian group. Such a process is similar to the Standard Model, where the $\mathrm{SU(2)}_L \times \mathrm{U(1)}_Y$ symmetry breaks down to electromagnetism $\mathrm{U(1)}_Y$, which results in the origin of electroweak monopoles. However, in the framework of spontaneous symmetry breaking, the monopole solutions are not allowed [39, 40].

In 1974, studies by t'Hooft [41] and Polyakov [42] established a magnetic monopole solution generated by an SU(2) gauge symmetry breaking to U(1), within the framework of the Georgi-Glashow model [43]. In this broken phase, the theory has a spherically symmetric solution with a magnetic charge equal to the Dirac charge.

This 't Hooft-Polyakov monopole is not point-like and has a finite mass of the order of the Grand Unification scale. Additionally, in contrast with the Dirac monopole, the 't Hooft-Polyakov monopole theory does not necessitate the introduction of a source of magnetic charge; rather, it is due to the topological charge from the vacuum expectation value of a field. The absence of any singularity in the description of the 't Hooft-Polyakov monopole makes it mathematically preferable to the Dirac monopole.

The GUT models predict the magnitude of the monopole mass to be in the order of 10^{14} to 10^{16} GeV heavy stable elementary particle. However, such a high energy scale is not available at the actual and foreseen particle colliders, where the *Large Hadron Collider* (LHC) and the *Future Circular Collider* (FCC) can be mentioned.

2.6 Electroweak monopoles

Magnetic monopole solutions also exist within the framework of electroweak theory. Notably, such monopoles would be expected to have a mass set by the electroweak (EW) scale.

The electroweak monopoles obey Schwinger's charge quantization condition, which implies a minimum magnetic charge of $2g_D$. The mass for such monopoles is not well defined, as it is for Dirac and GUT monopoles. However, the theory developed by Cho and Maison [44], contradicts the earlier works where such solutions were not admitted by Weinberg-Salam models. In this lower-mass regime, the gauge electroweak monopoles could be present in cosmic rays, but may even be produced at the LHC. The proposition of the CKY model by Cho, Kimm, and Yoon constrained the mass of the electroweak monopole between 4 and 10 TeV. The generalization of the CKY model to be compatible with the LHC measurements of the $H \to \gamma\gamma$ further constrained the electroweak monopole mass to below 5.5 TeV [45]. Such mass ranges could be achieved in the current particle colliders and the foreseen FCC.

2.7 Searches for magnetic monopoles

The prediction of magnetic monopoles in GUT models has significantly increased interest in their experimental detection, leading to the development of several detection techniques. Exploiting the production of a high ionization signature due to the passage of monopoles through the matter leads to a range of techniques and methods for possible detection. Besides the high ionization signature, the magnetic monopoles are expected to be accelerated in the presence of a magnetic field, leading to the exploitation of anomalous tracks in detectors as an alternative avenue for detection.

The searches for magnetic monopoles can be performed based on the natural occurrence and on the production of such monopoles on particle colliders. A brief overview of the natural occurrence of cosmic searches for magnetic monopoles will be provided, since the focus of this work is the search for magnetic monopoles in the context of particle colliders, the latter will receive a more detailed overview.

2.7.1 Direct Detection Methods

Direct detection methods rely on the fact that monopoles can become bound in matter or leave detectable traces as they pass through a material. These methods exploit the extremely high ionization capacity of the monopoles, equivalent to that of a particle with approximately 68.5 times the electric charge of an electron. Such a signature is

characterized by a large energy deposit along the particle's path, with all the kinetic energy trapped inside the material.

2.7.1.1 Monopole bound in matter

The binding energies of monopoles in nuclei are estimated to be significantly higher than the binding energies of the atoms in solids or electrons to atoms. Due to the strong magnetic field associated with a monopole, it may cause disruptions in nuclear structure, potentially allowing the monopole to form bound states with protons and neutrons. This effect is particularly relevant in materials commonly used in beam pipes, such as beryllium and aluminum [46].

In induction-based searches, if a trapped magnetic charge is present in a sample, its passage through a superconducting coil will induce a measurable current. This current persists even after the sample has moved through the coil, as a consequence of the magnetic flux change caused by the monopole.

When a monopole passes through the coils, a nonzero net change in the current is produced, giving a current "step" characteristic of a magnetic charge. This effect can be observed from even one monopole in a macroscopic sample due to the long-range nature of the associated magnetic field. This change in current is detected and measured by a *Superconducting Quantum Interference Device* SQUID, which converts the current step into a corresponding voltage signal.

2.7.1.2 High ionizing active detection

Another method that can be employed for the detection of magnetic monopoles in matter is the application of a strong magnetic field on the sample where the monopole is trapped, allowing its extraction [47]. Detectors such as semiconductor trackers, drift chambers, and scintillators are designed to measure the energy loss dE/dx for these particles. A monopole passing through such a detector leads to a unique signature that can be exploited. A fast-moving monopole loses a significant amount of energy through ionization by the production of energetic δ-rays. This process can be observed and measured from the amount of collected charge, allowing the incident particle to be considered as a highly ionizing particle.

2.7.1.3 Heavy etching on nuclear tracker detector

The *nuclear track detector* (NTD) device is employed for the detection of highly ionizing particles, making them especially valuable for the search for magnetic monopoles in cosmic searches and high-energy particle colliders. These detectors are typically placed around interaction points, where they can record the passage of ionizing particles through permanent damage to the detector material. This damage occurs due to the displacement

of lattice atoms, and it enables the measurement of the particle's energy loss per unit length dE/dx.

The usage of the NTDs technique in cosmic rays searches for monopoles and high electric charge objects yields possible evidence of fast-moving magnetic monopoles [48].

2.7.1.4 Anomalous tracks in magnetic field

As previously discussed, magnetic monopoles are accelerated along magnetic field lines, unlike electrically charged particles, which experience a force perpendicular to the field. Tracking detectors placed in magnetic fields are typically used to measure the momentum of charged particles by analyzing the curvature of their paths.

However, the standard tracking reconstruction algorithms are designed to provide measurements for particles with only electric charges, which do not comprise magnetic monopoles or any other magnetically charged particles.

For such particles, it is expected that due to their interaction with the magnetic field, anomalous tracks followed by a trajectory in a different plane will be produced in particle detectors. In the context of the CMS experiment, where a solenoid magnet provides a magnetic field in the z-axis, it is expected to record measurements for circular tracks in the x-y plane with straight tracks in the r-z plane, considering ordinary electrically charged particles.

However, due to their magnetic charge, monopoles would respond differently to the magnetic field, resulting in non-helical trajectories or curved tracks in the r–z plane, providing a distinct signature for detection. For the consideration of a magnetically charged particle, the curved tracks are expected in the r-z plane, described by a parabola trajectory, with straight tracks in the x-y plane.

The trajectory developed by the magnetic monopole in the r-z plane isn't a perfect parabola due to the intense production of the δ-rays along its trajectory [49]. It is expected that the standard track reconstruction algorithms identify the magnetic monopole track with a very low efficiency. This limitation motivates the development of a dedicated tracking algorithm, which will be described in Sections 6.2 and 6.3.

2.7.2 Cosmic Searches

The cosmic searches for the magnetic monopoles are based on the GUT prediction of the creation of the magnetic monopoles in a similar abundance to the baryons in the early Universe, with its posterior dilution explained by the cosmological inflation theory [50].

The magnetic monopoles in the cosmic context could include the very heavy GUT

monopoles as well as lighter primordial monopoles which survived the cosmological inflation [51]. These monopoles can be characterized by their relative velocity $\beta = v/c$, which is in the order of $\beta = 10^{-3}$. This behavior is due to its acceleration either by the gravitational attraction of the heavy GUT monopoles or by the galactic magnetic fields for the lighter monopoles. In both scenarios, this low-velocity monopole provides a weak interaction signature for the detection methods relying on its high ionization capacity.

Among the searches for cosmic magnetic monopoles, the underground general detector MACRO [52], the array of track detectors at high altitude SLIM [53], and the radio interferometer ANITA [54] can be mentioned.

Additionally, there is also a group of experiments for neutrino detection that can act as magnetic monopole detectors, where ANTARES [55], IceCube [56], and Super-Kamiokande [57] are among such experiments. No observation of cosmic magnetic monopoles has been achieved by such detectors, where limits on the cosmological flux for different mass and speed hypotheses were set.

2.8 Searches at Electron-positron colliders

2.8.1 Collider Searches

For the magnetic monopoles search in particle colliders, two approaches can be employed. The first is focused on detecting monopoles trapped inside the matter, called the induction technique, and the second is focused on the exploitation of its characteristic highly ionizing signature. The second method is employed for the search for magnetic monopoles in the actual particle collider and detector experiments located at the LHC.

2.8.1.1 Electron-Positron colliders

Searches for magnetic monopoles at colliders started with CERN's *Intersecting Storage Rings* (ISR) and the *Super Proton–Antiproton Synchrotron* (SppS). Both experiments employed plastic track detectors and an extraction method that employed the exposure of a material to the magnetic field of the solenoid to detect any induced currents. These searches targeted beam dumps exposed to 300 GeV and 400 GeV proton beams [58, 59].

Exploring e^+e^- collisions from *The Cornell Electron Storage Ring* (CESR) and *Positron-Electron Tandem Ring Accelerator* (PETRA), the experiments CLEO and *Two Arm Spectrometer SOlenoid* (TASSO) experiments searched for magnetic monopoles by targeting their distinct non-helical trajectories in magnetic fields. It is expected that the monopoles are accelerated in the direction of the magnetic field, rather than bending in its perpendicular plane, the usual behavior for charged particles.

At a second stage, the experiments LEP1 and L6-MODAL [60] employed NTDs, which are capable of detecting high ionization signatures around the interaction region, studying the range of charges between 0.9 and 3.6 g_D, for monopole masses up to 45 GeV. With no monopole tracks observed, the MODAL experiment set limits on the monopole cross-section using the benchmark Drell-Yan production mechanism. From the OPAL experiment at LEP2 collisions with $\sqrt{s} = 206.3$ GeV, set new upper limits for the monopole production cross-section for $|g| = g_D$ with masses up to 102 GeV, assuming the Drell-Yan production mechanism.

The usage of the NTDs around the interaction region was also applied at other e^+e^- colliders, such as PEP [61], PETRA [62] and TRISTAN [63].

2.8.1.2 Hadron colliders

Searches in the Tevatron were performed using 35.7 pb^{-1} of luminosity with $\sqrt{s} = 1.96$ TeV proton-antiproton collisions. The *Collider Detector at Fermilab* (CDF) employed a time-of-flight system, while the E882 experiment used the induction technique to search for stopped monopoles in the beryllium pipe and other parts of the detector [64]. The *Omni-Purpose Apparatus at LEP* (OPAL) searched for magnetic monopoles at the LEP2 e^+e^- collider with $\sqrt{s} = 206.3$ GeV, through the observation of back-to-back particles with anomalously high ionization energy loss in the tracking chambers [65]. The *Hadron–Electron Ring Accelerator* (HERA) with its H1 experiment performed the search for monopoles using lepton-hadron scattering, employing the induction technique for the monopole detection [66].

Recent searches for magnetic monopoles have been performed at the LHC by the *Monopole and Exotics Detector at the LHC* (MoEDAL) [67] and ATLAS [68], studying proton-proton collisions with the highest center-of-mass energy available to date. The MoEDAL experiment searches for monopoles trapped inside the matter, while the ATLAS Experiment, similar to what has been performed at CMS, exploits high ionizing signatures, exploring masses up to 4 TeV. For the production of magnetic monopoles in collider experiments, two production modes are considered by MoEDAL [67, 69, 70, 71], the Drell-Yan and photon fusion, which will be described in Section 5.1.

For the Run I studies, ATLAS explored the pair-production of monopoles via the Drell-Yan mechanism for magnetic charges ranging between 0.5 and 2 g_D and electric charge range of $20 \leq |z| \leq 60$, considering masses between 200 GeV and 2500 GeV, for $\sqrt{s} = 7$ TeV and $\sqrt{s} = 8$ TeV [72, 73]. For such measurements, a combination of parameters from the *Transition Radiation Tracker* (TRT) and the liquid argon (LAr) electromagnetic calorimeter was employed.

In the absence of an observation of magnetic monopoles, the upper limits on the experimental production cross-section can be computed. Such limits indicate the expected

maximum value for the cross-section under the experimental parameters of the search, allowing the comparison of results from different experimental approaches. A summary of such upper limits can be observed in Figure 4.

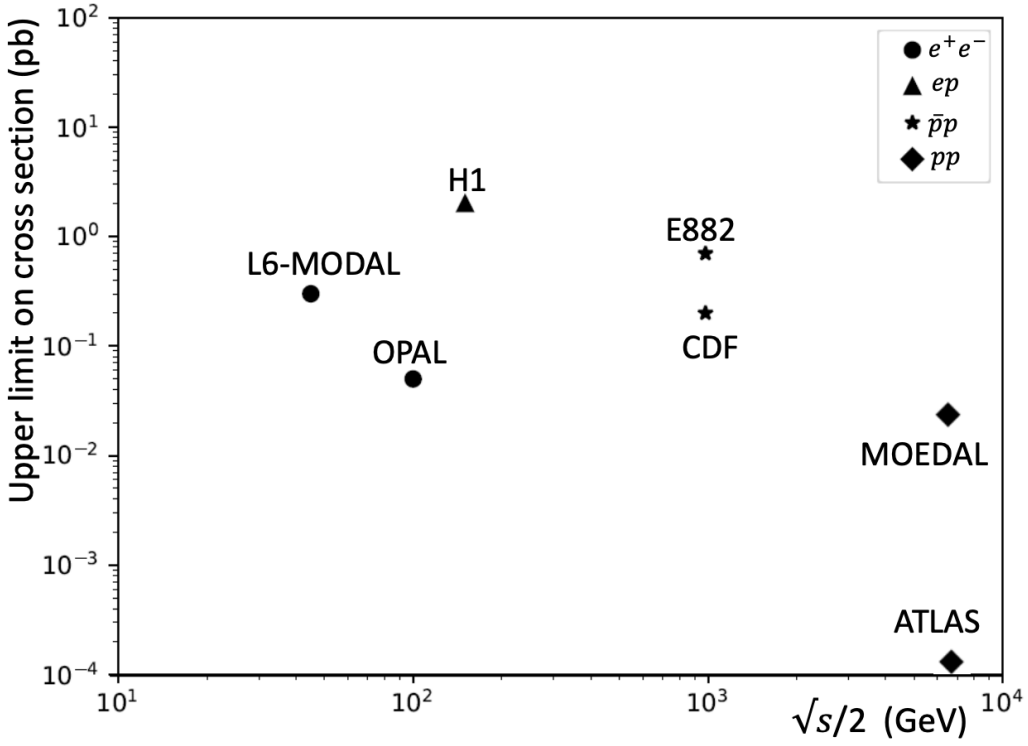

Figure 4 – Upper limits on the production cross-sections of magnetic monopoles combining results from various collider-based experiments.

2.9 Creation of HIPs at the LHC

For the results produced in this work, two pair-production mechanisms are considered as benchmark models. The Drell-Yan (DY) pair-production mechanism consists of a quark-antiquark annihilation mediated by virtual photons, which decays into a HIP-anti-HIP pair. The Photon Fusion (PF) mechanism is included for the first time in the search for magnetic monopoles in the CMS Experiment and consists of a pair of photons radiated from the colliding protons, which fuse and produce a monopole-anti-monopole pair. Through such mechanisms, fermionic (spin-1/2) and bosonic (spin-0) monopoles can be produced, both of which are considered in this thesis. Such mechanisms could also be employed for searches of *High Electric Charge Objects* where the Drell-Yan can be mediated by either the photon or a Z boson. Since the magnetic monopoles do not interact via the weak force, the monopole production via Drell-Yan can not be mediated by the Z boson. The HIPs can be produced with masses up to 4 TeV in LHC proton-proton collisions with $\sqrt{s} = 13$ TeV, considering the benchmark mechanisms [74]. Additionally, such HIPs can be produced with velocities around $\beta = v/c > 0.1$ and a Lorentz factor of $\gamma < 100$.

2.10 Interaction with matter

The electromagnetic interaction of a particle with electric and/or magnetic charge is given by the Lorentz force:

$$\vec{F} = q(\vec{E} + \vec{v} \times \vec{B}) + g(\vec{B} + \vec{v} \times \vec{E}) \tag{2.30}$$

From Equation 2.30, it can be seen that a magnetic monopole or any particle with magnetic charge g, with a relative velocity β, in the presence of the electric field $\vec{E}$, would experience a force with magnitude $gc\beta e$. Considering the Dirac magnetic charge equivalence of $g_D = 68.5$, this implies that a monopole would experience a force nearly two orders of magnitude greater than that on an electron under the same electric field $\vec{E}$. Furthermore, the strength of the magnetically charged particle coupling to the electromagnetic interaction is several thousand times that of the electrically charged particle. In particle collider physics, the responsible mechanisms of energy loss of a particle in matter are ionization, bremsstrahlung, and pair production. For monopoles, ionization becomes the most significant due to their extreme coupling strength.

2.10.1 Ionization

The ionization process occurs through the interaction of electrically charged particles with the atoms that constitute the matter. The energy loss per unit length, also known as

stopping power, is given by the Bethe-Bloch formula [75]:

$$-\frac{dE}{dx} = \frac{4\pi e^4 z^2 N_e}{m_e c^2 \beta^2}\left[\ln\left(\frac{2m_e c^2 \beta^2 \gamma^2}{I}\right) - \beta^2 - \frac{\delta}{2}\right] \tag{2.31}$$

where z is the electric charge of the traveling particle in units of e, N_e is the electron density of the material, $m_e c^2$ is the electron rest energy, I is the mean ionization energy of the material, and δ is the density effect correction.

For particles with magnetic charge g, a separate formula is needed for the description of the ionization-stopping power. Since the magnitude of the force between the magnetic monopoles and the electron field is given by β, the parameter for the electric charge z is replaced by $gc\beta$ in the original Bethe-Bloch formula given by Equation 2.31. Such a formula was developed by Steven Ahlen [76], describing the stopping power of magnetic monopoles due to ionization. Such a formula can be observed in Equation 2.32, and it considers both the high-momentum transfer and the low-momentum transfer. The first is characteristic of close interactions, and it is achieved by the introduction of the term $k(g)$ given by Equation 2.33, known as the KYG correction [77]. The low-momentum transfer for long-distance interactions through the Bloch correction $B(g)$ given by Equation 2.34, which originates from low-energy collisions.

$$-\frac{dE}{dx} = \frac{4\pi e^2 g^2 N_e}{m_e c^2}\left[\ln\left(\frac{2m_e c^2 \beta^2 \gamma^2}{I}\right) + \frac{k(g)}{2} - \frac{1}{2} - \frac{\delta}{2} - B(g)\right] \tag{2.32}$$

$$k(g) = \begin{cases} 0.406, & \text{if } |g| \leq 1\, g_D, \\ 0.346, & \text{if } |g| \geq 1.5\, g_D, \end{cases} \tag{2.33}$$

$$B(g) = \begin{cases} 0.248, & \text{if } |g| \leq 1\, g_D, \\ 0.672, & \text{if } |g| \geq 1.5\, g_D, \end{cases} \tag{2.34}$$

It is worth noticing that both equations for the energy loss for electrically and magnetically charged particles, given by Equations 2.31 and 2.32 respectively, show a direct proportion to the square of the charge. Evaluating the Equation 2.31 for a charge $|z| = 1$ and the Equation 2.32 for a magnetic monopole with $|g| = 1g_D$ yields an energy loss by the monopole to be four orders of magnitude larger than these of an electrically charged particle with $|z| = 1$.

In the Figure 5, the ionizing stopping power of a Heavy Electrically Charged Objects (HECO) particle with charge $|z| = 68.5$ and a magnetic monopole with charge $|g| = 1g_D$ is illustrated. It is worth noticing the decrease of the energy loss with the increase of β for the HECOs by the Bethe-Bloch formula, while for the magnetic monopoles, the large

energy deposits tend to occur at higher speeds following a $1/\beta^2$ dependence by the Ahlen formula.

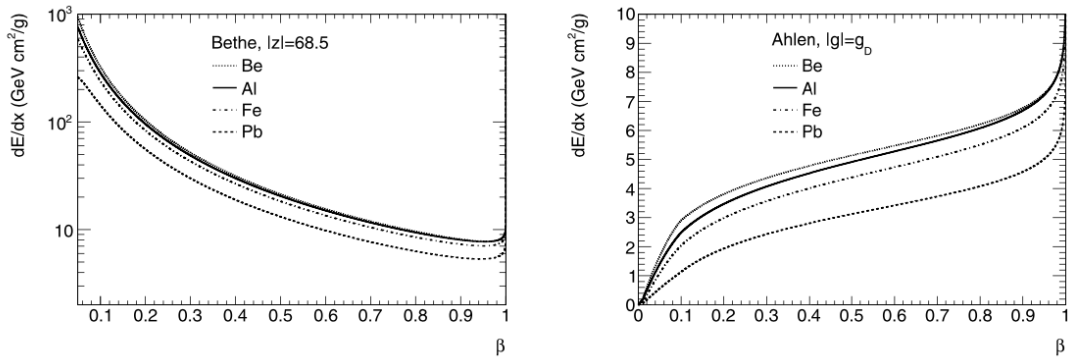

Figure 5 – The calculated ionization energy loss dE/dx as a function of velocity β for HIPs in various materials. In the left plot, a particle with electric charge $|z| = 68.5$, and for the right plot, a particle with magnetic charge $|g| = 1g_D$ is considered. The Equations 2.31 and 2.32 were employed.

2.10.2 Bremsstrahlung

Charged particles also lose energy through the Bremsstrahlung mechanism, where photons are emitted from the acceleration of such particles by the electric field of another particle. The amount of energy loss of a magnetic monopole depends on the material, the mass, and the Lorentz factor of the monopole. The mass of HIP becomes an important factor when comparing energy loss due to Bremsstrahlung and through ionization.

2.10.3 Pair production

The influence of the magnetic field of fast magnetic monopoles ($\gamma \gg 1$) can induce a transverse electric field, from the equivalent photon approximation, where the field would be similar to a beam of photons [78]. Such photons can decay into electron-positron pairs when interacting with matter. However, the energy loss through such a mechanism is only relevant for ultra-relativistic particles, which is not the case for HIPs produced at collider experiments.

In Figure 6, the three described energy-loss mechanisms are shown for a HIP with 1 TeV of mass as a function of the Lorentz factor γ. It is expected that the HIPs and consequently the magnetic monopoles would be mostly produced for $\gamma < 10$, making the ionization the dominant mechanism of energy loss by two orders of magnitude.

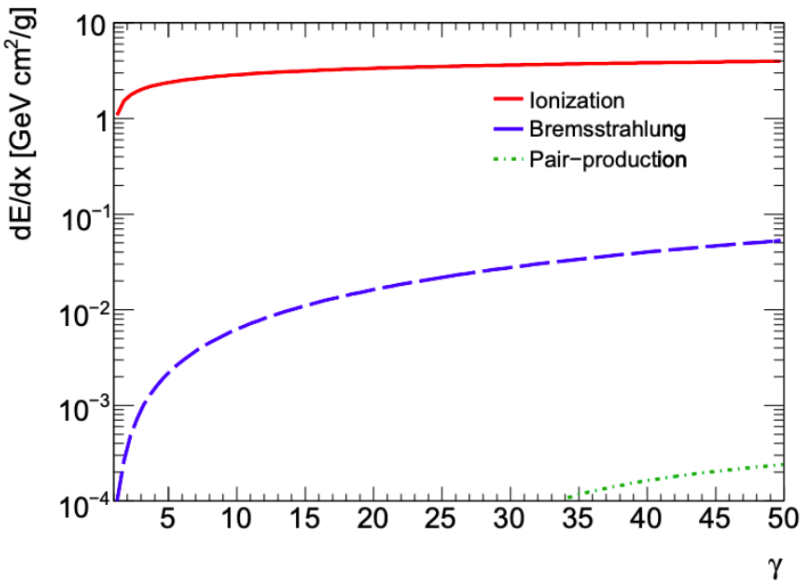

Figure 6 – The energy loss per unit distance (dE/dx) for a magnetic monopole of mass 1000 GeV and magnetic charge of $|g| = 1g_D$ traversing Argon. Three energy loss mechanisms are shown: ionization (solid-red line), bremsstrahlung (dashed-blue line), and pair-production (dotted-green line). [79]

3 The CMS Experiment at the LHC

3.1 The Large Hadron Collider facility

The *Large Hadron Collider* (LHC) [80] consists of a circular particle accelerator, built at the *European Organization for Nuclear Research* (CERN) in Geneva between 1998 and 2008, which brings protons, or lead ions into head-on collisions. The LHC is placed in a circular tunnel with a circumference of 26 659 m, which was previously occupied by the *Large Electron-Positron Collider* (LEP), a machine that was under operation from 1989 to 2000, with a maximum energy reached of 209 GeV. Large particle colliders are ideally placed in underground tunnels due to the external radiation shielding provided by the bedrock and the absorption of the ionizing radiation produced by the collider.

The energy available to the production of new particles in the collisions is the center-of-mass energy, which is denoted as the Mandelstam variable $\sqrt{s}$, which is obtained from the particle four-momenta p_1 and p_2, by the equation $s = (p_1 + p_2)^2$. For the collisions of two proton beams, the center-of-mass energy is simply the sum of the energy from the two beams, while for fixed-target experiments the energy available is proportional to $\sqrt{E_{\text{beam}}}$.

It was developed to provide an environment with high center-of-mass energy ($\sqrt{s}$) for its collisions, to allow study of Standard Model (SM) processes and to explore or constrain scenarios involving Beyond Standard Model (BSM) physics. For the proton-proton collisions, the center-of-mass energy is given by twice the value of the beam energy, which is, at this moment, $\sqrt{s} = 13.6$ TeV, for Run 3. A sketch of the LHC accelerator complex with its experiments and detectors can be observed in Figure 7.

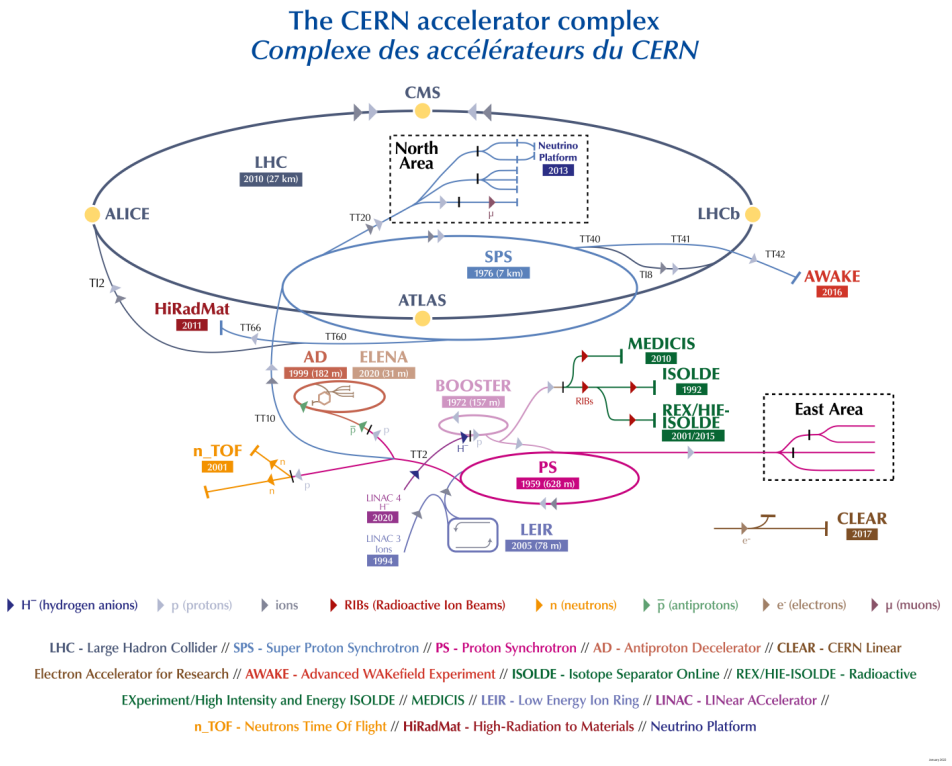

Figure 7 – The CERN's accelerator complex. [81]

The motivation for achieving high collision energies lies in the strong dependence of production cross-sections on the center-of-mass energy $\sqrt{s}$. For most processes of interest, such as the production of Z and $W_{\pm}$, and Higgs bosons, the production rate at the LHC increases with $\sqrt{s}$, as illustrated in Figure 8. The comparison of the production cross-section for these specific processes (σ_W, σ_Z) with the top curve which represents the total inelastic pp cross-section (σ_{tot}), it becomes clear that they represent only a small fraction of all inelastic interactions. This highlights the rarity of electroweak and Higgs boson production events relative to the dominant inelastic background at the LHC.

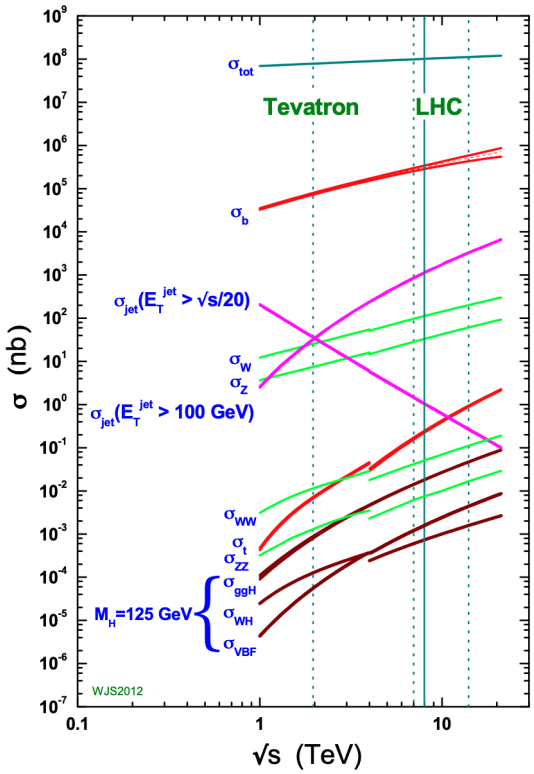

Figure 8 – The predicted total inelastic pp interaction cross-section (σ_{tot}) and production cross-section for several specific processes as a function of the center-of-mass energy $\sqrt{s}$[82].

For the collisions, two separate beams containing bunches of protons are circulated in opposite directions in the accelerator. For each beam pipe, eight superconducting cavities generate electromagnetic potential with an accelerating power of 5 MV m^{-1} with a frequency of 400 Hz. Such cavities are cooled down to 4.5 K and are responsible to accelerate and tighten the bunches. For bending the particles along the circular trajectory, dipole magnets provide 7.74 T of magnetic field are employed. For the focusing of the beam, superconducting quadrupole magnets are used, working on a temperature of 1.9 K. A vacuum pressure of 10^{-13} atm is ensured to avoid gas atoms.

3.1.1 Architecture

For the creation of the proton beams, hydrogen atoms are first accelerated with the *LINAC4* to an energy of 160 GeV. In a second stage, the protons are then accelerated to 2 GeV using the *BOOSTER* accelerator. Before the injection at the LHC, the proton beams are accelerated to energies of 26 GeV and a stage later, 450 GeV, by the *Proton-Synchrotron* (PS) and *Super Proton-Synchrotron* (SPS), respectively. At the ring of the LHC, the beam achieves its final energy collision. The two beams are accelerated in two separate rings, realized with a twin-bore magnet design, and crossed at four interaction points (IPs), where at each point a detector is placed. The LHC is designed to be filled with 2808

bunches per beam with around $1.2 \cdot 10^{11}$ protons each, with a bunch spacing of 25 ns. For a successful fill and the stability of the beams, it can circulate in the machine for more than ten hours, while the intensity of the beam gradually decreases due to the consumption of the protons in the collisions and other smaller particle losses. Each fill ends with the often called beam dump when a set of magnets deflects the beam to a separate tunnel that ends with water-cooled graphite blocks. After this beam duping process, the LHC needs to be refilled again, where a *fill* can be defined as the smallest unit of data-taking with a constant beam setup.

The four large experiments situated at the interaction points are ALICE, ATLAS, CMS, and LHCb. The *A Large Ion Collider Experiment* (ALICE) [83] is designed for the primary investigation of heavy-ion collisions. The extremely high temperatures for such collisions allow the experiment to study the quark-gluon plasma, a state present in the very beginning of the Universe [84]. The *Large Hadron Collider beauty* (LHCb) [85] is an asymmetric detector with a focus on the precision measurements of b hadron properties. In the LHCb, evidence of the lepton universality violation was found in B_+ meson decays with a significance of 3 standard deviations [16]. The *A Toroidal LHC Apparatus* (ATLAS) [86] and the *Compact Muon Solenoid* (CMS) [87] are general-purpose experiments. Both experiments have a very similar physics program, with the investigation of a wide range of physics processes, allowing for cross-checks and a combination of results. The most recognizable mutual achievement by the ATLAS and CMS experiments was the discovery of the Higgs boson with a mass of about 125 GeV in 2012 [88, 89]. Three smaller experiments are placed in the LHC complex, where the *Large Hadron Collider forward* (LHCf), for cosmic rays studies, the *Monopole and Exotics Detector* (MoEDAL), and *TOTal Elastic and diffractive cross section Measurement* (TOTEM) can be mentioned. A sketch of the LHC accelerator complex with its experiments and detectors can be observed in Figure 7.

3.1.1.1 Magnets and beam control

The 1232 dipole magnets of the LHC generate a magnetic field strong enough to keep the 6.5 TeV protons beam along the circular accelerator path. These magnets are superconducting electromagnets, each measuring 15 meters in length, weighing 35 tonnes, and capable of producing an 8 T magnetic field. The magnet coils are made from niobium–titanium (NbTi) superconducting cable.

The LHC is composed of eight powered independent sections, where the dipole magnets of each sector are connected in series inside the cryostat. To achieve superconductivity, the magnets are cooled down to 1.9 K temperature with superfluid helium, due to its high thermal conductivity.

To account for the repelling of the positively charged protons, the 392 quadru-

pole magnets are employed to constrain the height and width of the beam, keeping it collimated. In the LHC, the magnets are combined in one horizontally focusing and one vertically focusing quadrupole magnet, with higher-multipole magnets placed between them, providing additional control and focusing of the beam. The effect of the magnet system is to maintain the protons oscillating around the center of the vacuum tube, where near the interaction point, inner triple magnets are then used to squeeze the beam from a transverse size of ≈ 20 μm to ≈ 200 μm

3.1.1.2 Radio frequency cavities and beam acceleration

The protons are accelerated by 16 radio frequency cavities, which provide a strong gradient of 5 MV/m and are responsible for maintaining the longitudinal structure of the beam. The electric field inside the cavities oscillates at 400 MHz frequency, to not provide additional acceleration for protons with the already required energy. Radio frequency cavities are placed inside four cylindrical modules to cool up to 4.5 K, and operated in the superconducting state, to mitigate possible losses.

3.1.1.3 Fill structure and luminosity

The LHC beam consists of thousands of bunches of protons, typically 10 cm long, where the minimum distance between two subsequent bunches, often called bunch spacing, is 25 ns, which corresponds to 7.5 m. The bunch spacing could also determine the bunch crossing frequency, which is 40 MHz for the consideration of 25 ns bunch spacing.

The number of bunches in fill and the number of protons per bunch depend on the filling scheme employed for the beam injection from the SPS to LHC. In typical filling schemes, the bunches are arranged in bunch trains, separated by a series of empty trains. These empty trains are required for the correct control of the beam dumping process, giving the required magnets to deflect the beam, to ramp up their magnetic fields.

An important quantity in collider experiments is the average number of events of a specific process (N), that are produced in a given time interval. Such quantity can be defined as the product between the cross-section σ for the specific process and the instantaneous ($\mathcal{L}(t)$) or the integrated luminosity (L), which can be expressed by the Equation 3.1. The instantaneous luminosity is an intrinsic characteristic of a particle detector and it corresponds to the measurement of the collision rate per unit area. It quantifies how many particles are available for collisions in a given amount of time, and it can be defined by the Equation 3.2. For a high statistical significance for the physics analysis, the instantaneous luminosity should be as large as possible.

$$N = \sigma\mathcal{L} = \sigma \int \mathcal{L}(t)dt \tag{3.1}$$

$$\mathcal{L}(t) = \frac{N_b n_1 n_2 f}{A_{\text{eff}}} \tag{3.2}$$

From the Equation 3.2, the N_b is the number of bunches per beam, n_1 and n_2 consists the number of protons per bunch in either of the beams, f is the frequency of circulation and the A_{eff} consists in the overlap area between the two bunches in the collision, or the effective area of the collision. To decrease the effective beam area A_{eff}, and thus increase the instantaneous luminosity, a highly focused beam should be employed. However, this also raises the likelihood of multiple simultaneous proton–proton collisions, referred to as pile-up (PU). In that sense, the precise measurement of the instantaneous luminosity is crucial for the precise measurements of the LHC.

At the LHC, the data-taking period alternates with maintenance and upgrade dedicated periods, where the accelerator is shut down. The LHC started operations with several years of data-taking from 2009 to 2013 in the Run 1, including pp collisions at $\sqrt{s} = 7$ and 8 TeV, with a correspondent integrated luminosity of $\mathcal{L} = 29.4$ fb^{-1} delivered for the CMS and ATLAS.

For the Run 2 data-taking between 2015 and 2018, the heavy-ion collisions program was included in the pp collisions at $\sqrt{s} = 13$ TeV. Collisions between lead ions (PbPb) and between lead and protons (pPb and Ppb) at different energies can be mentioned from such a program. Peak luminosities values reached $\mathcal{L}(t) = 2 \cdot 10^{-34}\text{cm}^{-2}\text{s}^{-1}$. The integrated luminosity delivered for the CMS Experiment for each year is illustrated in the left plot of Figure 9, and amounts to a total value of $\mathcal{L} = 164$ fb^{-1}. The distribution of the number of pileup interactions for each year in Run 2 can be found on the right side of Figure 9.

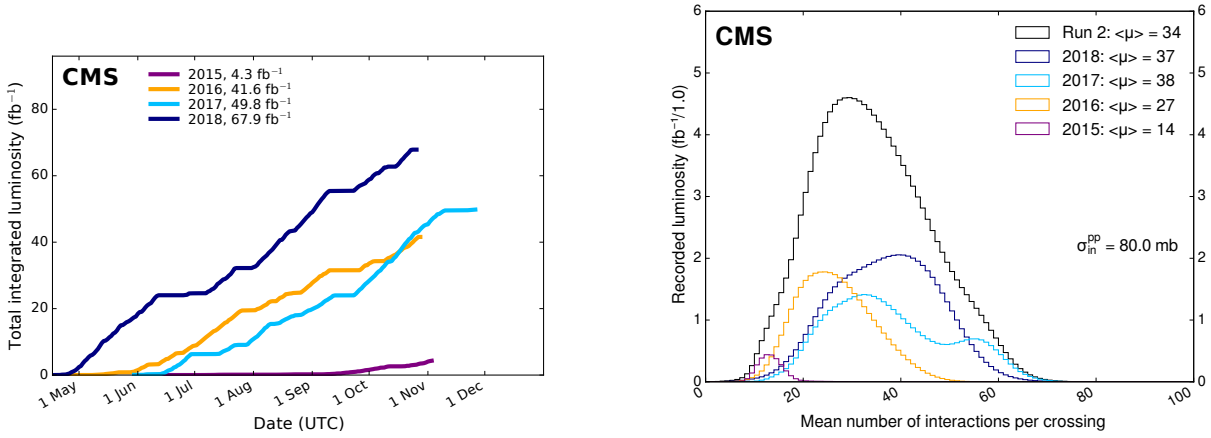

Figure 9 – In the left plot, the cumulative integrated luminosity is delivered as a function of the months of the year for Run 2 [90]. On the right, the spectrum of pileup interactions in each year of the Run 2 [90]

.

The current Run 3 data-taking period which started in 2022 is scheduled to finish in 2026. With the same instantaneous luminosity from Run 2, the current delivered

luminosity amounts to $\mathcal{L} = 196.4$ fb^{-1} with average pileup interactions reaching $< \mu > = 57$. The distribution of the number of pileup interactions for each year in Run 2 can be found on the right side of Figure 10.

Beyond 2026, a shutdown for major upgrades in the accelerators and experiments is expected to the foreseen *High Luminosity LHC* (HL-LHC) [91]. An instantaneous luminosity of $\mathcal{L}(t) = 5 \cdot 10^{-34}$ cm^{-2}s^{-1} could lead to increase the integrated luminosity by a factor of 10, reaching up to $\mathcal{L} = 3000$ fb^{-1}.

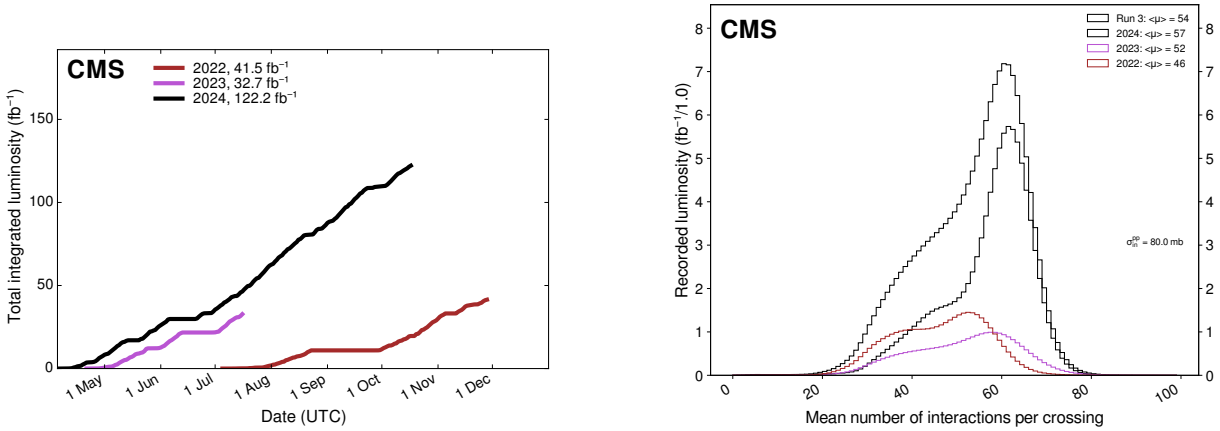

Figure 10 – In the left plot, the cumulative integrated luminosity delivered as a function of the months of the year for the Run 3 [90]. On the right, the spectrum of pileup interactions in each year of the Run 3 [90]

.

3.2 The Compact Muon Solenoid detector

The CMS detector is a general-purpose experiment situated at Point 5 (IP5) of the CERN (LHC) in Cessy, France. Its primary objective is to study proton-proton (pp) collisions, which occur at center-of-mass energies of up to 13.6 TeV. To achieve this broad research program, the detector is designed to accurately measure and distinguish all particles produced in these collisions, maximizing both spatial and momentum resolution, while enclosing the interaction as much as possible. The CMS detector has been built for many years of data-taking, ensuring its robustness and resilience against radiation damage. Its design follows a cylindrical concept, centered on the interaction point, with multiple layers concentrically arranged around the beam pipe. For the completion of the design, layers of endcap disks at both sides of the barrel increase the coverage at low angles concerning the beam pipe.

The CMS detector has a length of 21 m and a diameter of 15 m, with a weight of 14 000 tons, with many detector layers placed inside the strong solenoid magnet. The solenoid with a diameter of 6 m and length of 12,5 m produces a magnetic field strength of 3.8 T in the inner detector layers. An external iron yoke surrounds the solenoid, guiding the magnetic field with 2T through the outer detector layers. The CMS experiment is notably more compact than the ATLAS experiment.

The CMS detector is designed to measure fundamental particles including electrons, muons, photons, and both neutral and charged hadrons. Each subdetector within CMS provides complementary measurements of specific particle properties. The combination of these measurements enables precise identification of particle types.

The structure of the CMS detector is illustrated in Figure 11, where the protons are set to collide in the interaction point at the geometrical center of the detector. After traversing the beryllium beam pipe, the particles produced in these interactions encounter several layers of different subdetectors, which surround the interaction point, forming an onion-like structure. The detector employs a cylindrical geometry: the barrel region consists of detector layers wrapped around the beam axis, while the endcaps are composed of circular disks.

From the interaction region, the incident particles first reach the inner tracker. Here, their trajectories are bent by the magnetic field, allowing for the reconstruction of their paths and thus the measurement of the electric charge and momentum of charged particles. In the Electromagnetic Calorimeter (ECAL), electrons and photons are absorbed with the measurement of their energy. Similarly, hadrons are absorbed by the Hadronic Calorimeter (HCAL) for energy measurement. To ensure maximal detector hermeticity, forward calorimeters are positioned in the forward region, close to the beam pipe.

For the minimization of the energy losses before particles reach the calorimeters, the

superconducting coils are strategically placed outside these calorimeter systems. Beyond the coils, layers of steel return yoke are responsible for keeping the strong magnetic field contained inside the detector volume and also provide mechanical support for the whole structure. Finally, muons, having traversed both calorimeters, reach the dedicated muon chambers where their trajectories are precisely measured. A schematic cross-sectional view of the CMS detector can be observed in Figure 12.

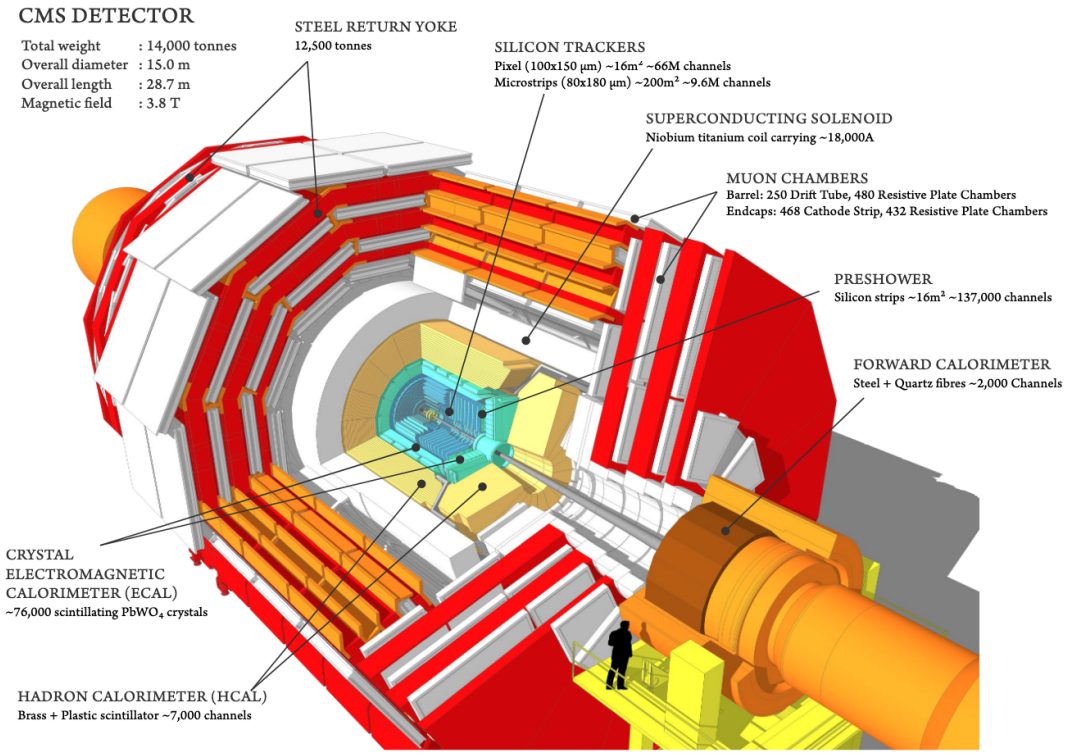

Figure 11 – An illustration of the CMS detector [92].

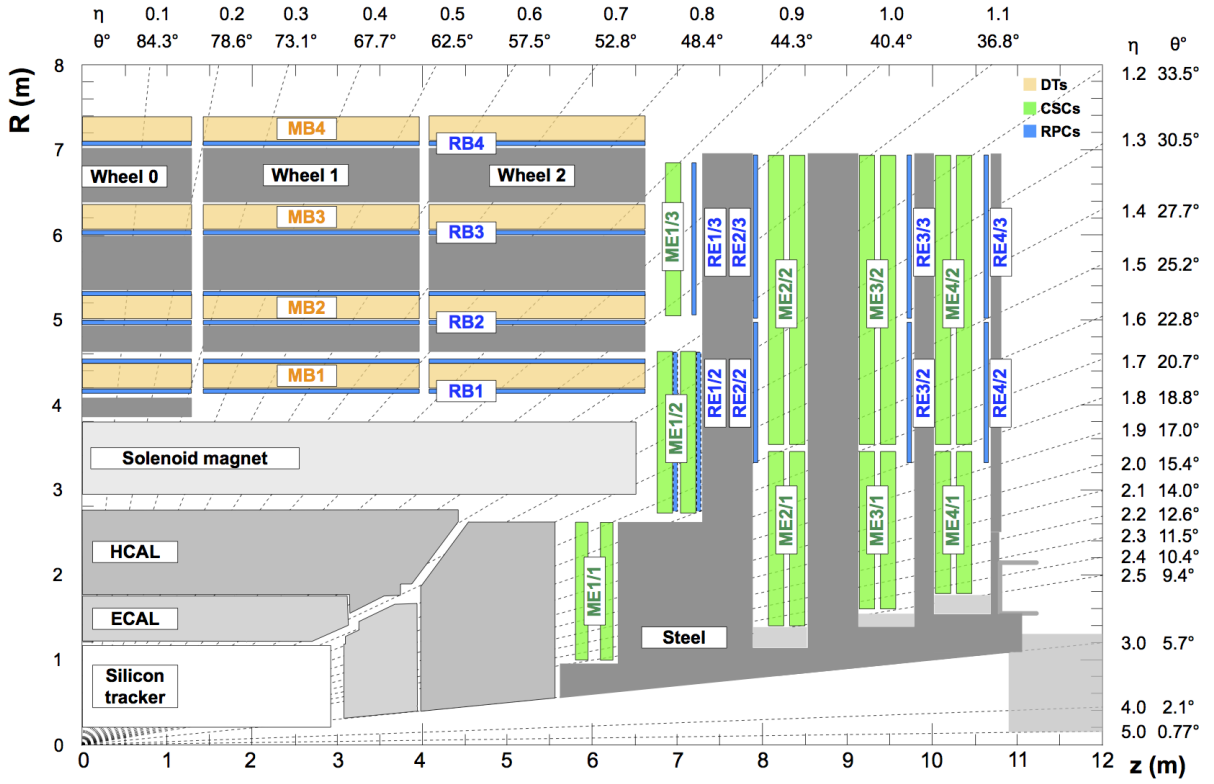

Figure 12 – An R-z cross-section of a quadrant of the CMS detector with the axis parallel to the beam pipe and the radius (R) increasing upward. [93].

3.2.1 Coordinate system

The CMS detector employs a right-handed coordinate system centered at the nominal interaction point. In this configuration, the x-axis is chosen to point to the center of the collider ring, the y-axis points upwards perpendicular to the collider plane, and the z-axis is chosen in the direction of the beam pipe. To account for the azimuthal symmetry of the detector, a spherical coordinate system is employed with the azimuthal angle ϕ defined in the (x,y) plane, and the polar angle ϕ is measured relative to the z-axis. For a particle with energy E and momentum $\vec{p}$, the rapidity y and pseudorapidity η are defined as:

$$y = \frac{1}{2}\ln\frac{E+p_z}{E-p_z} \approx \eta = \frac{1}{2}\ln\frac{|\vec{p}|+p_z}{|\vec{p}|-p_z} = -\ln\tan\left(\frac{\theta}{2}\right). \tag{3.3}$$

The approximate equality $y \approx \eta$ holds exactly for massless particles. Since the longitudinal momenta (p_z) are unknown for individual collisions, the rapidity is a useful quantity, since rapidity intervals Δy are invariant under Lorentz boosts along the beam pipe direction.

Quantities like transverse energy (E_T) and transverse momentum (p_T) refer to the plane perpendicular to the beam direction, i.e., the (x,y) plane. In the transverse

plane, the vector sum of the transverse momenta of all final-state particles is conserved. A non-zero net transverse momentum or energy can be attributed to undetectable particles, primarily neutrinos, escaping the detector. Therefore, the missing transverse momentum ($\vec{p}_T^{\,\text{miss}}$), with magnitude ($E_T^{\text{miss}}$), is defined as the negative sum of the momenta of all measured particles.

The missing transverse momentum ($\vec{p}_T^{\,\text{miss}}$) is defined as the negative of the vector sum of the transverse momenta of all measured particles. Its magnitude $E_T^{\text{miss}} = |\vec{p}_T^{\,\text{miss}}|$, represents the amount of transverse energy carried away by undetected or invisible particles.

3.2.2 Superconducting solenoid

The superconducting magnet of the CMS Experiment is the largest ever built, with 12.5 m in length and 6 m in diameter. It generates a powerful 3.8 Tesla magnetic field, storing 2.6 GJ of energy at full current [94]. This strong field is crucial for precise measurements of the momentum of charged particles by bending their trajectories due to the magnetic field. The magnetic flux is returned through a 12500-tonne steel yoke, which consists of five barrel wheels and two endcaps, each comprising three disks. A schematic view of the CMS solenoid is presented in Figure 13, while Figure 14 shows a photograph taken during its assembly in the SX5 cavern.

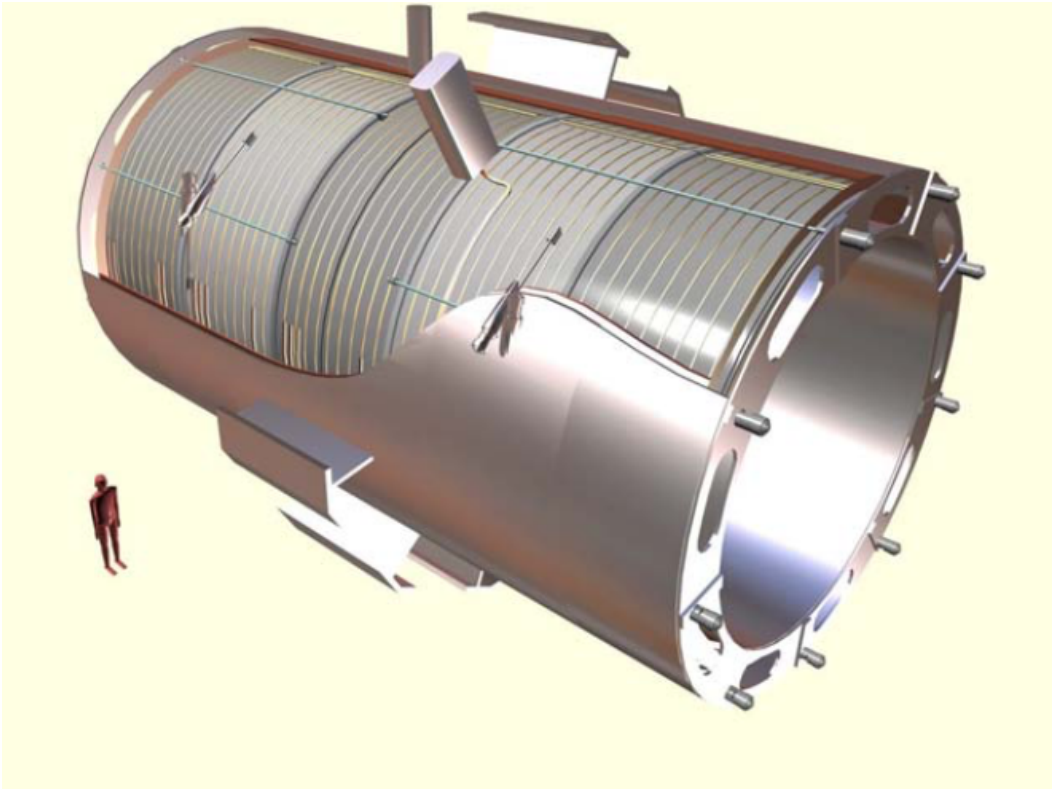

Figure 13 – General artistic view of the 5 modules which composes the cold mass inside the cryostat.

Figure 14 – The cold mass mounted vertically before integration and insertion in the vacuum chamber.

3.2.3 Silicon tracker

The tracking system is the innermost part of the detector, located at a distance of 30 mm from the beam pipe. It achieves precise reconstruction of charged particle trajectories by measuring their "hits"within the detector. The structure of the tracker system is illustrated in Figure 15 with its corresponding material budget in Figure 16. From the curvature of the tracks within the magnetic field, the momentum of the particle can be accurately determined. The part closest to the interaction point is equipped with fine-granularity pixel detectors, while the large bulk of the tracker consists of larger silicon strips. The reconstructed tracks can be associated with the primary vertex (PV) of the hard interaction in pp collisions or secondary vertices (SVs) from decays of heavy particles. The identification and rejection of pileup interactions are obtained through the reconstruction of the PV, while the SVs can be used to select events with τ leptons, b hadrons, or other long-lived particles.

It is expected a flux of around 10 million particles per square centimeter per second, which means that the tracker material should be radiation resistant, considering the operation for many years. The tracker must possess excellent spatial and temporal resolution to distinguish between hits from different particles and consider interactions at each 25 ns. Finally, the material that composes the track can not be too dense, since it

allows multiple scattering from the incoming particles and the early electron-positron pair conversion from the photons.

To meet these stringent requirements, both the pixel and silicon strip trackers utilize doped, layered semiconductor silicon technology. Multiple barrel and endcap layers are installed to achieve coverage up to $|\eta| < 2.5$ [95]. When a charged particle traverses these layers, it knocks out electrons within the detector material, generating an electrical field and a small electric pulse. This pulse is then amplified and detected by the readout electronics. For the construction of the silicon inner tracking system, two types of detectors are used: pixel and strip elements.

The pixel elements consist of small elements with the size of 100 μm $\times$ 150 μm, allowing a single hit resolution of about 10 μm (transverse) and 20-40 μm (longitudinal) [96]. The pixel detector comprises four barrel layers positioned between 29 mm $< r <$ 160 mm and three endcap disks located at 291 mm $< |z| <$ 516 mm. The inclusion of a fourth barrel layer enhances tracking redundancy for more accurate measurements, while the usage of carbon fiber and graphite compounds reduces the material budget.

The silicon strip element sizes, from the innermost to the outermost layers, range from 10 cm $\times$ 80 μm to 25 cm $\times$ 205 μm in length (η) and width (ϕ). Ten barrel layers are placed around the pixel detector up to a distance of 1.1 m. In the endcaps, three small and nine large disks are located on each side. The greater distance of these layers from the collision point results in a lower particle flux, which permits the use of larger segments and fewer readout electronics compared to the pixel detectors.

The silicon strip tracker is composed of four subsystems: the Tracker Inner Barrel (TIB), with four-barrel layers, the Tracker Outer Barrel (TOB), with six-barrel layers, the Tracker Inner Disks (TID) with three disks, and the Tracker EndCaps (TEC) with nine disks. Most of the strip modules in the barrel region are aligned with the z-axis, providing information on the radial coordinate (r) and the azimuthal angle (ϕ). In the endcaps, they are aligned radially, providing on z and ϕ, where a small tilt of 100 mrad, enables the measurement of a third spatial coordinate.

The tracker system offers excellent momentum resolution for charged hadrons, achieving better than 1% for particles with transverse momentum $p_T > 20$ GeV.However, this resolution degrades with increasing momentum, reaching approximately 5% at 1 TeV. For high-energy particles, which typically reach the calorimeters or muon chambers, the measurement of their momenta can be complemented by information provided by other subdetectors.

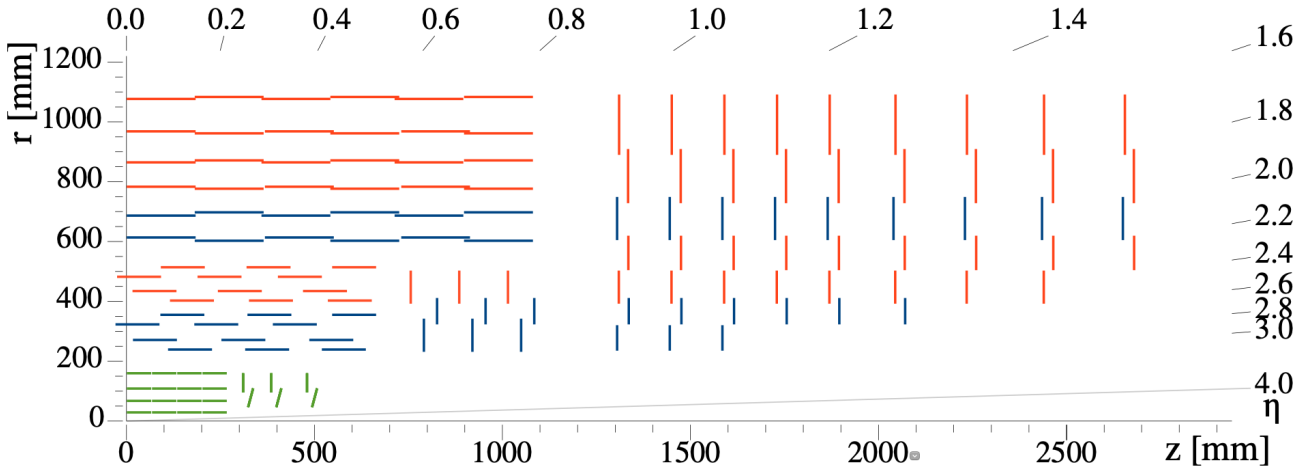

Figure 15 – Sketch of one quarter of the Phase-1 CMS tracking system in the r-z plane, with the pixel upgrade of 2016/2017 [97]. The pixel detector is shown in green, while the red and blue segments correspond to single-sided and double-sided strip modules.

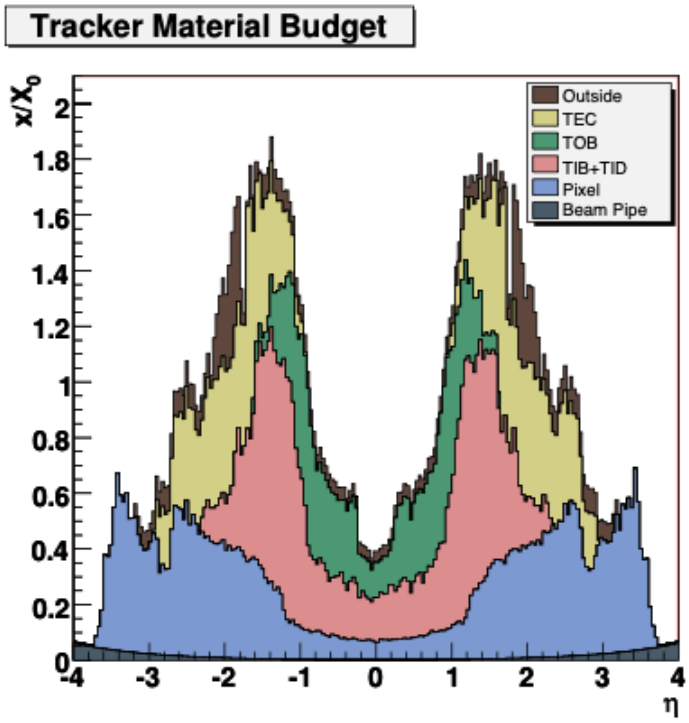

Figure 16 – Inner tracker material's budget total thickness is expressed in units of interaction lengths as a function of the pseudorapidity η.

3.2.4 Electromagnetic calorimeters

The silicon tracks are surrounded by the Electromagnetic Calorimeter (ECAL). The ECAL is responsible for the measurement of the electromagnetically interacting particles, such as photons and electrons. The ECAL is designed to provide excellent identification and energy resolution for these particles [98]. It is built from a single layer of lead tungstate ($PbWO_4$) crystals, which serve as both the absorber and scintillating material, as illustrated in Figure 17.

The ECAL is composed of a barrel, covering $|\eta| < 1.479$, which is segmented into 360 crystals in the ϕ direction, and 170 crystals in the z direction, corresponding to 61200 crystals in total. The ECAL crystals are grouped into 36 supermodules, each corresponding to 10 degrees ϕ and containing four modules with dedicated readout electronics. The configuration of crystals and modules is illustrated in Figure 18. In the barrel, each crystal is 23 cm long, with a segmentation of approximately 0.02×0.02 in the (η, ϕ) plane, which corresponds to the transverse size of electromagnetic showers in $PbWO_4$).

The ECAL endcaps are situated 3.15 m away from the interaction point, where each disk is composed of 7324 crystals, each 23 cm long, arranged in a rectangular grid. These endcaps extend the ECAL's coverage to $|\eta| < 3.0$. The crystals are arranged in 5 $\times$ 5 blocks known as super crystals, which share a common readout. Scintillation light produced in the crystals is collected by vacuum phototriodes (VPTs).

When charged particles interact with the detector material, it acts as an absorber, causing the emission of photons through bremsstrahlung. These photons can then undergo conversion, producing electron-positron pairs. This sequence of interactions leads to the development of an electromagnetic shower composed of photons, electrons, and positrons. Simulations indicate that approximately 98% of the energy from electromagnetic showers (up to 1 TeV) is absorbed by the ECAL. The remaining fraction ends up in the HCAL, while for hadrons, a small fraction of their energy is absorbed, due to the nuclear interaction length of $\lambda_I \approx 1$.

Concerning the development of the electromagnetic shower, the Molière radius and radiation length X_0 should be mentioned. The Molière radius characterizes the transverse width of an electromagnetic shower. The radiation length, X_0, is defined as the average distance over which an electron's energy is reduced to 1/e of its initial value, while photons, on average, undergo pair conversion after 7/9 X_0.vThe lead tungstate ($PbWO_4$) material has an exceptionally high density of 8.28 g/cm^3, which produces a Molière radius of 2.2 cm and a short radiation length of $X_0 = 0.89$ cm. Due to its high atomic number, the electrons and photons have a very high probability of interacting with the crystal material. The ECAL has a thickness of 23 cm in the barrel and 22 cm in the endcap, providing lengths of 26 X_0 and 25 X_0, respectively.

The lead tungstate ($PbWO_4$) also functions as a scintillator, emitting low-energy photons as the excited atoms return to lower energy states. This scintillation light is then detected by photodiodes attached to the end of each crystal. In the absence of radiation damage, the $PbWO_4$ crystals are optically transparent as glass, and the scintillation light reaches the photodiodes with minimal losses.

The material has a short excitation time, where approximately 80% of the scintillation light is emitted within 25 ns, which is within the duration of a single bunch crossing. Avalanche photodiodes (APD) collect the scintillation light from the crystals, where the amount collected is proportional to the energy deposited by the incident particle that initiated the particle shower.

The ECAL's simple structure and high density enable its compact design, allowing it to fit entirely within the solenoid magnet. The configuration of calorimeters where the absorbing and scintillating processes are done by the same material is referred to as homogeneous calorimeters.

In the endcaps, a preshower calorimeter is positioned in the forward region of the detector ($1.653 < |\eta| < 2.6$), situated between the tracker and ECAL. These preshower detectors are sampling calorimeters with passive layers for the absorption of the electromagnetic shower and active layers for the detection of the shower. Each of the two disks contains a lead absorber, where electromagnetic showers are initiated, and silicon strip sensors to measure the shower's energy. The high resolution of the preshower is employed for the identification of neutral pions decaying into a pair of photons, where this pair can be wrongly identified as one energetic photon.

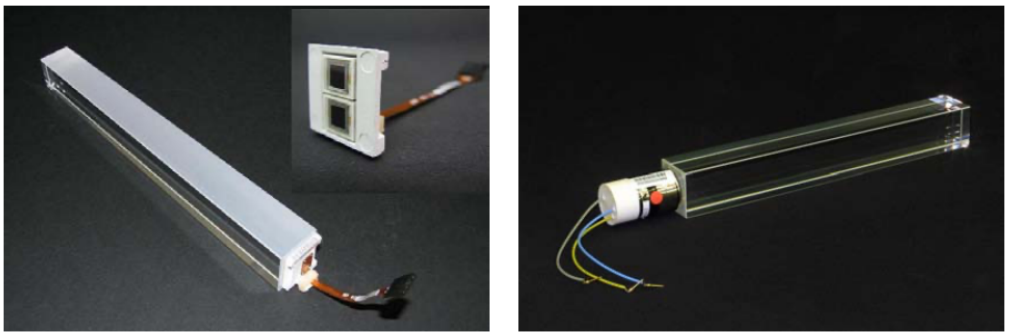

Figure 17 – The lead tungstate ($PbWO_4$) crystals with photodetectors attached. In the left figure is a barrel crystal with the APD capsule, and in the right figure, an endcap crystal.

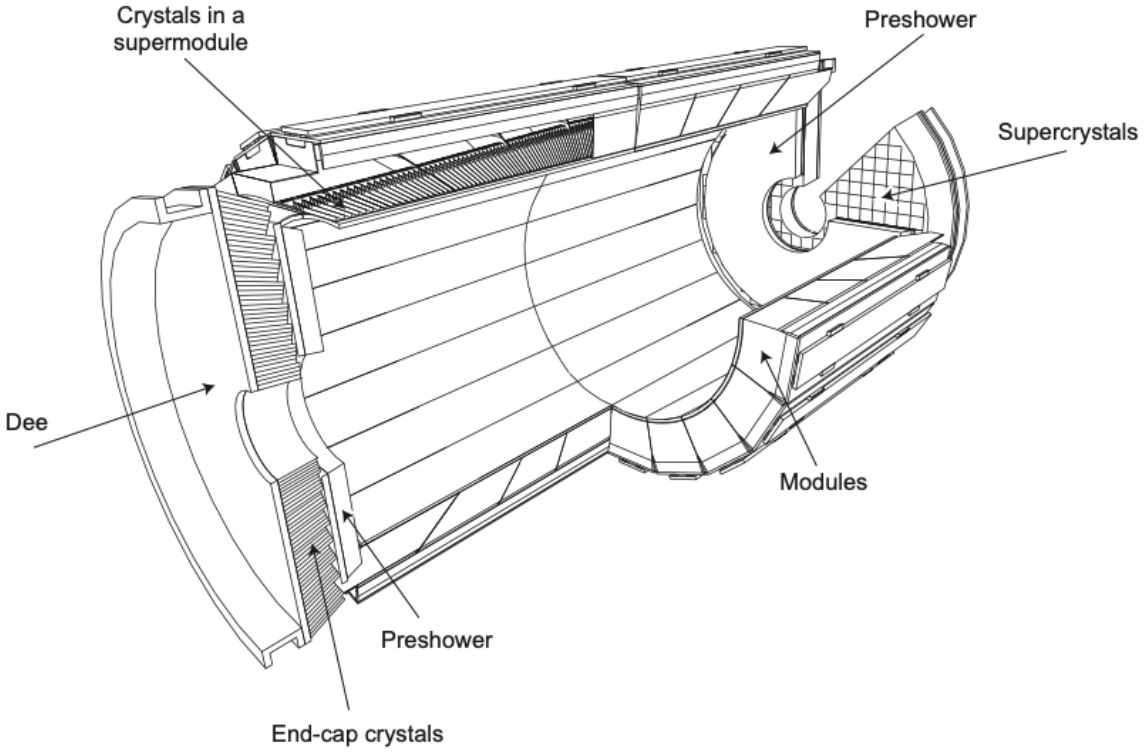

Figure 18 – Schematic layout of the CMS electromagnetic calorimeter (ECAL). The $PbWO_4$ crystals are organized in modules and supermodules in the barrel, and into supercrystals in the endcaps. The preshower detectors provide additional sensitivity in the endcaps.

3.2.5 Hadronic calorimeters

The hadrons are typically not fully absorbed by the ECAL. After traversing it, they interact with the Hadronic Calorimeter (HCAL), which hermetically surrounds the ECAL, allowing the precise measurement of the energy of hadronic jets. This configuration is also important for the measurement of the total energy of the system and for determining the missing transverse energy. The HCAL is designed to stop all incident particles, with the exception of muons, which are detected in the muon chambers, and neutrinos or other weakly interacting particles that do not interact within the CMS detector.

The HCAL consists of a sampling calorimeter, with alternating layers of absorber and active, or scintillating, materials. The flat brass absorbers are sandwiched by plastic scintillator material, with additional steel plates providing further absorption capability, while stabilizing the structure. The incoming particles initiate hadronic showers during the interaction with the absorber material. The light produced by the scintillating material is then transported via optical fibers to photodiodes for the readout. Since the hadrons typically start showering already in the ECAL, the combination of the signal from both calorimeters is important for the correct estimation of the hadron energy.

The structure of the hadronic calorimeter is depicted in Figure 19. It is composed of a barrel calorimeter (HB) covering the central region up to $|\eta| < 1.3$. It is divided into 36 azimuthal wedges, containing 14 brass plates parallel to the z axis, while thick steel plates are placed in the front (back) of the system. Its plastic scintillator layers contain 16 η segments with dedicated readouts. The HB is complemented by an outer HCAL layer (HO), installed outside of the solenoid coil. It contains one layer of absorber iron equipped with scintillators, placed near the innermost layer of the return yoke. The HCAL endcaps (HE) cover the range of $1.3 < |\eta| < 3.0$. Both the HB and HE are installed inside the magnetic solenoid coil, meaning that the trajectories of charged particles are bent by the magnetic field before they reach the HCAL.

In the barrel, the HB provides a granularity of approximately 0.087×0.087 (η, ϕ), which becomes coarser as a function of $|\eta|$, reaching 0.17×0.17 in the endcaps. Despite this variation, the granularity remains sufficient to distinguish between energy deposits from neutral and charged hadrons, particularly as the latter are affected by the bending magnetic field.

The total thickness of the total calorimeter system, including the magnetic coil, at its thinnest point ($|\eta| = 0$) corresponds to 11.8 λ_I. While the HE provides a thickness of approximately 10 λ_I, the HB offers only 5.82 λ_I at its thinnest point. Consequently, the probability of hadrons passing through the HCAL and reaching the muon chambers is very small, though not entirely negligible.

To ensure the coverage up to $|\eta| < 5.2$ for jet detection at the forward region, two forward calorimeters (HF) are placed in $z \pm 11.2$ m from the nominal interaction point. Since a higher dose of radiation is expected in the HF region, Cherenkov detectors are used in place of the scintillators. For charged particles, the Cherenkov light produced is transported to the readout system, using Quartz fiber as active material due to its radiation hardness. The HF offers $\eta \times \phi$ resolution of 0.175×0.175, and the amount of material corresponds to ≈ 10 nuclear interaction lengths.

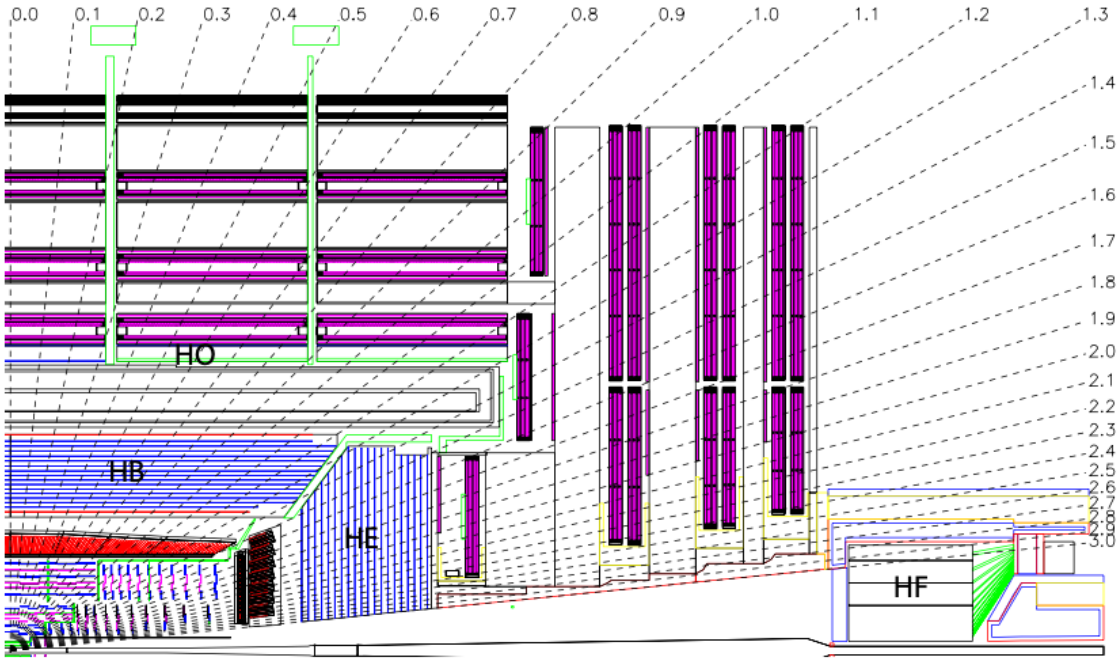

Figure 19 – The longitudinal view of the CMS detector with the locations of the hadron barrel (HB), endcap (HE), outer (HO), and forward (HF) calorimeters. In purple, the muon systems are presented.

3.2.6 Muon system

The muons can be understood as weakly interacting particles with a lifetime of 2.2 μs, without a significant energy deposition in the tracker and calorimeter systems [9]. The muon detector system is the outermost component of the CMS detector. It is located outside the solenoid magnet, placed between the layers of the iron return yoke, covering a range up to $|\eta| < 2.4$. The muon system is composed of three types of chambers, all of which use gas as an active medium, arranged in layers called muon stations.

The barrel region defined by $|\eta| < 1.2$ contains four layers of aluminum *drift tubes* (DT). In the endcaps, with the coverage of $0.9 < |\eta| < 2.4$, four layers of *cathode strip chambers* (CSC) are employed. For the improvement of the efficiency in the regions between the barrel and the endcaps, four layers of *resistive plate chambers* (RPC) complement both the DTs and CSCs.

The drift tubes (DTs) are detector elements filled with a mixture of ionizable gas, composed of 85/15% of argon and CO_2. Each tube contains a positively-charged wire at its center. When a muon traverses the gas, it can knock electrons out of the gas atoms, moving to the wire in the electric field. As the drifting electrons are accelerated by the field, the gas is further ionized, with the creation of an avalanche of secondary electrons, producing an electric signal that can be measured. The drift time, typically a few hundred nanoseconds, is dependent on the distance between the muon's path and the wire.

The CMS muon system incorporates 250 DT chambers, distributed across five barrel wheels, as shown in Figure 20. A fraction of the DTs is oriented parallel to the z-axis, measuring r and ϕ coordinates, while others are installed orthogonally, providing measurements of r and z coordinates. The resolution for the estimated distance between the muon track and the anode wire is around 200-800 μm, considering both arrangements of chambers.

The CSCs have a similar operation to the DTs but contain a higher number of electrodes for signal collection, which can be characterized by their good radiation hardness and fast response time. The CSCs are gas containers equipped with layers of negatively-charged cathode strips and positively-charged anode wires, interchanged between each other. The cathode strips are installed radially, providing measurements of the r and ϕ coordinates, while the anode wires provide an estimate for the z coordinate.

There are 540 CSC chambers in the CMS endcaps, where each chamber contains six anode wires, as illustrated in Figure 21. These CSCs use a mixture of argon, CO_2 and CF_4 gases in the proportion 40/50/10%. Due to their higher electrode density, the CSCs achieve superior spatial resolution for reconstructed hits in comparison with the DTs, in the order of 100 μm.

As schematically illustrated in Figure 22, the RPCs enclose a gaseous mixture between two resistive plates. A voltage is applied across this volume via the outer surfaces of these plates. Then, the ionization of gas is provided by an avalanche of electrons, which are collected by the anode plate. In total, 1056 RPC chambers are placed in the four layers in both the barrel and endcap regions. These chambers utilize an active gas mixture of 95.2/4.5/0.3% mixture of freon ($C_2H_2F_4$), isobutane (C_4H_1O) and sulfur hexafluoride ((SF_6)). Given their fast time resolution of approximately 1 ns and spatial resolution of around 1 cm, RPCs are primarily employed in the trigger system.

The *gas electron multiplier* (GEM) is employed for further redundancy of the muon system, improving reconstruction and trigger efficiency. This technology is well suited for the expected increase in the particle flux in the forward region of the future LHC operations. The GEM detectors are located in three stations ranging from $1.6 < |\eta| < 2.8$, increasing the previous coverage. Incoming muons ionize the chambers filled with an argon CO_2 gas mixture, enabling their detection. The GEMs are already operational for Run 3 data-taking, with further upgrades planned during the long shutdown following Run 3.

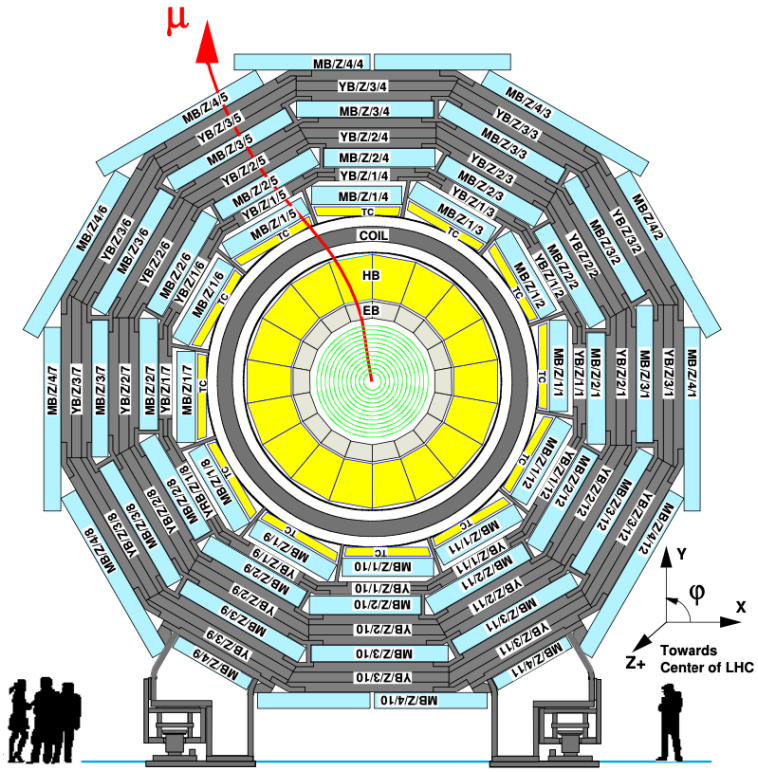

Figure 20 – Layout view of the CMS barrel muon drift tubes (DT) chambers in one of the 5 wheels. The wheels are identical except for the wheels -1 and +1, which are shorter, due to additional cryogenic structures.

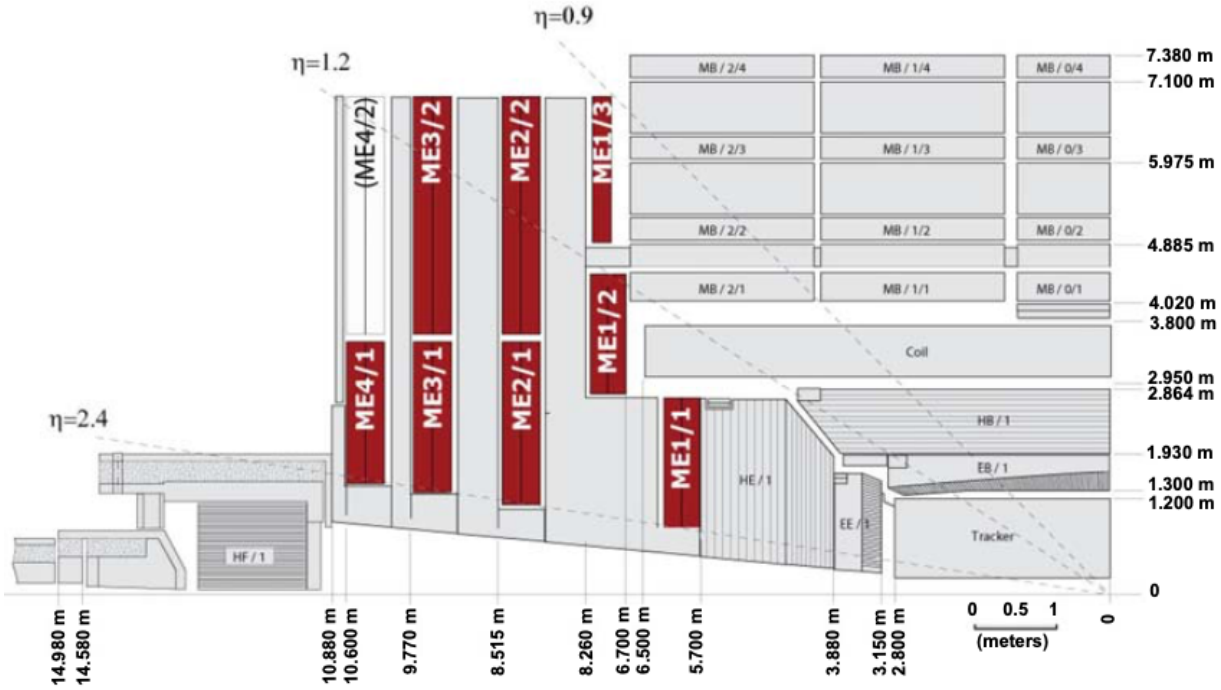

Figure 21 – Schematic quarter view of the CMS detector, where the cathode strip chambers (CSC) of the endcap muon system are highlighted.

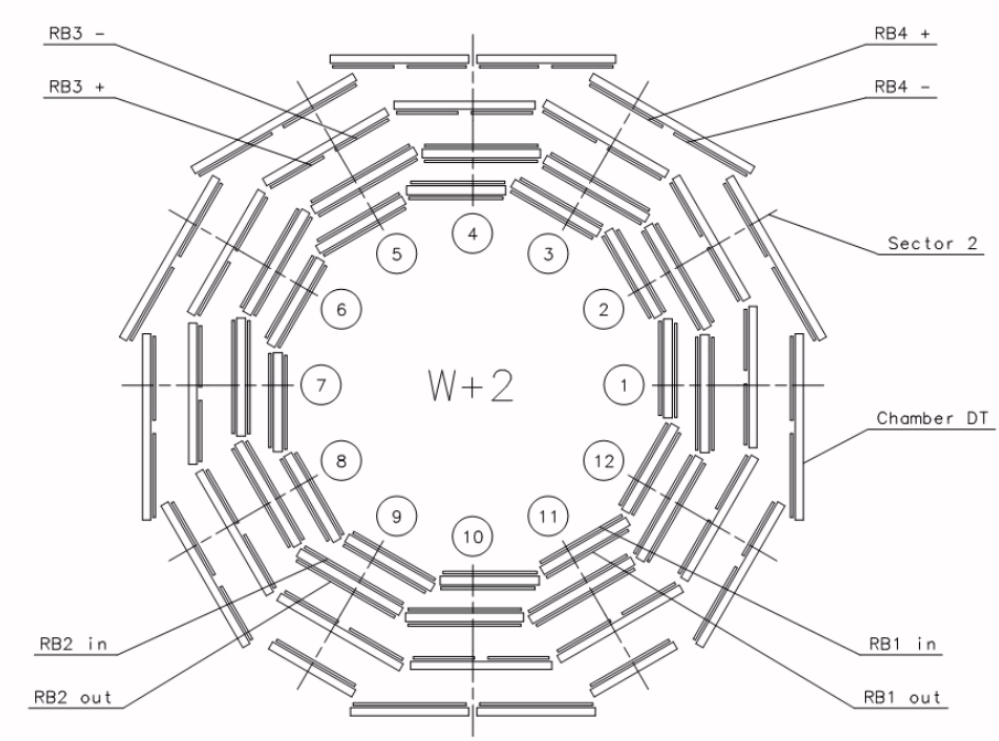

Figure 22 – Schematic layout of one of the 5 barrel wheels of the resistive plate chambers (RPC), which are labeled -2, -1, 0, +1, and +2, respectively.

3.2.7 Online event selection

In the CMS detector, signals are associated with a single event, originating from one 25 ns bunch crossing, are read out, filtered, and compressed by the data acquisition (DAQ) system. Each event requires approximately 1 MB of storage. Since the DAQ processes events at the collision rate, storing all produced events would demand around 40 TBs per second, which is currently unfeasible. Furthermore, most collisions result from Quantum Chromodynamics (QCD) interactions of lesser interest; only a tiny fraction of events contain data valuable for physics analysis. Consequently, CERN stores only a few hundred petabytes (PBs) across large data centers worldwide.

The solution to this storage challenge is the development and employment of a trigger system, which is designed to monitor collisions in real-time, identifying events with interesting physics. At every 25 ns bunch crossing, the trigger system can decide whether the event is accepted or discarded. The triggering procedure is also referred to as *online selection* of events, in contrast to the *offline selection* where a subset of recorded events is selected for further analysis.

The trigger system of an experiment defines its physics reach, as the types of events saved for subsequent analysis are entirely dependent on its configuration. A reliable and properly functioning trigger system is therefore a critical component of any collider experiment. Once an event is discarded by the trigger, it cannot be recovered.

In modern collider experiments, the trigger system is typically implemented in several layers. Each level discards part of the events, sending the accepted ones to the next levels, for further, more detailed inspection. This approach allows the trigger algorithms to increase their complexity at each level, with the first level providing the quickest decisions with less complex information. In the CMS Experiment, a two-tiered trigger system is employed [99, 100], where the *Level-1 trigger* (L1T) is completely hardware-based, selecting the events that will be fully readout, providing decisions every 4 μs, with a maximum output rate of 100 KHz. Events accepted by the L1T are then passed to the *High-level trigger* (HLT), which is a software-based filtering system. The HLT reconstructs the events using a standard CMS offline event reconstruction software, reducing the event rate to 1 kHz, and allowing its permanent storage. A diagram of the trigger and DAQ systems of the CMS experiment is presented in Figure 23.

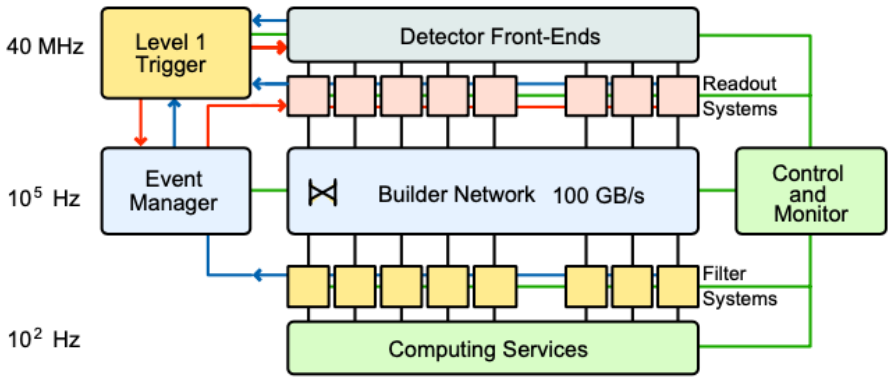

Figure 23 – An overview of the CMS trigger and data acquisition (DAQ) system. The hardware-based Level-1 trigger receives data from the detector frontends and readout systems, to select the events. After the complete information from all subdetectors is processed and combined, the High-Level Trigger (HLT) selects the events that will be permanently stored.

3.2.7.1 Level-1 Trigger

The Level-1 Trigger (L1T) provides low latency decisions at each 4 μs, reducing the initial 40 MHz collision rate to 100 kHz. Since the readout of the full event at a 40 MHz rate would be too resource-consuming, the L1T takes input only from the ECAL, HCAL, and the muon chambers. From these subdetectors, simpler "trigger primitives"are constructed, as processing the full information would take too long to be processed. The architecture of the CMS Level-1 Trigger is illustrated in Figure 24.

The data from the calorimeters are then combined to identify detector signals that are compatible with the hypothesis of an electron, photon, τ lepton, or missing transverse energy. Similarly, potential muon candidates are identified from the combination of the information provided by the muon detectors.

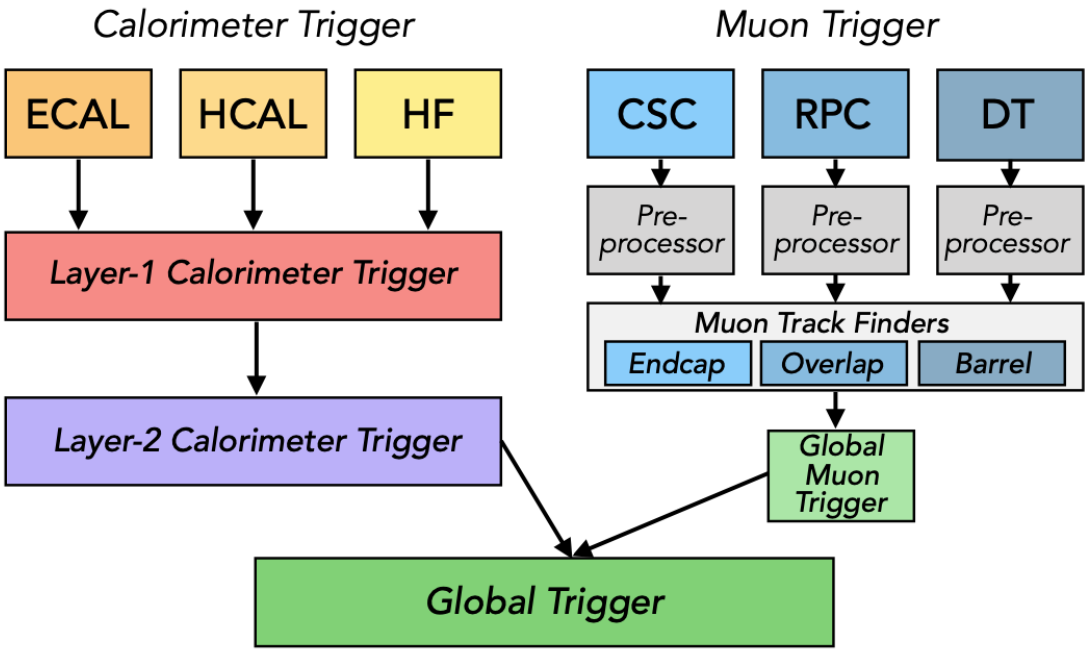

Figure 24 – Architecture of the CMS L1 trigger in Run 2 [101].

3.2.7.2 The Level-1 *Spike* Killer Algorithm

Despite the unique signature of monopole candidates within the ECAL, it is exactly this signature that poses a great obstacle in the analysis. These *spike* [102] signatures can be characterized as anomalous signals, with energies exceeding 100 GeV, resulting from direct strikes on the Avalanche Photodiodes (APDs). They manifest as isolated energy deposits within a single ECAL barrel crystal [103], caused by the ionization of silicon. These anomalous deposits have an inconsistent shower shape when compared to an ordinary electromagnetic shower. Furthermore, "spikes"are also understood to be associated with particles produced in proton-proton collisions that yield a large missing transverse energy (MET).

However, a *spike* killer algorithm or, more precisely, the *Fine-Grained Veto Bit* (*sFGVB*) algorithm, has been developed and built into the L1 trigger to reject events with large MET contributions associated with those *spikes*.

Figure 25 illustrates the functioning of the sFGVB algorithm. The algorithm starts with the scan of a strip, a 5×1 crystal rectangle, where each channel is compared against a threshold. If only one channel within the strip exceeds this threshold, the strip is assigned a value of 0 and identified as a *spike*. Whereas, when more than one channel is above the threshold, a value of 1 is attributed to the channel, and it is marked as an EM shower.

Following these scans and index assignments, the zero-valued sFGVB results (potential spikes) are then compared against the threshold of the ECAL trigger tower, defined as a 5×5 crystal square that forms a readout unit in the ECAL. For trigger towers

with transverse momentum greater than 12 GeV, the energy deposition is marked as an ECAL *spike* and then it is removed. The *sFGVB* algorithm has the capability of rejecting more than 95% of *spike* candidates, where this efficiency can be further improved with an additional implementation in the HLT. Furthermore, the offline rejection of *spike*-like events is built into the HLT-level. The *Swiss-Cross* topological variable, in addition to the production of the *spikes* before the collision, has been implemented in the HLT to improve the cleaning efficiency to around 99%, removing the *spikes* that passed through the L1 trigger.

From a broader perspective, it is possible to conclude that the monopole search analysis suffers a great impact of both online and offline *spike* killer algorithms. As data must pass through both the Level-1 (L1) and High-Level Trigger (HLT) systems, the distinct ECAL signatures of monopole candidates are often misidentified as ECAL "spikes"and subsequently removed by these triggers. This leads to a substantial reduction in the available statistics for monopole searches.

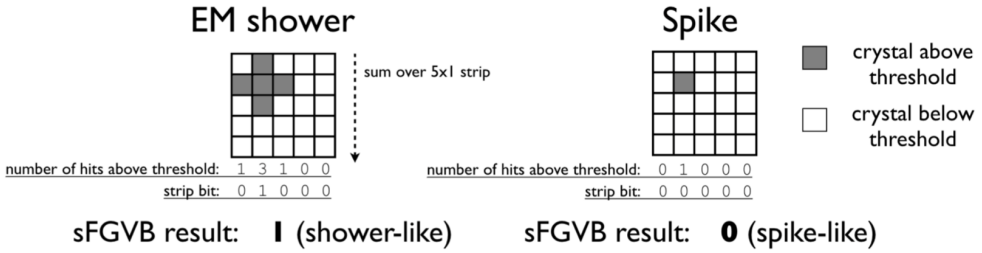

Figure 25 – Operation of the *sFGVB* algorithm on a *spike* candidate (right) and EM shower candidate(left) [102]

3.2.7.3 High Level Trigger

In the second stage, the *High-Level Trigger* (HLT) is a fully software-based trigger system designed to reduce the event rate to 1 kHz, enabling offline storage of the events. The HLT receives full event data, as read out from all CMS subdetectors, at a maximum rate of 100 kHz. It performs a rapid reconstruction of these events, making a trigger decision for each within a few hundred milliseconds.

Although the architecture of the HLT is different from the L1T, the HLT also contains a trigger menu with hundreds of different seeds, often called trigger paths. Unlike the L1T, the HLT benefits from the track information, due to a longer processing time. The tracks are then reconstructed following an iterative procedure, where the most resource-consuming ones are limited to the regions of interest, indicated by the presence of calorimeter jets of other tracks.

Furthermore, the HLT leverages full event information by through a simplified version of the Particle Flow (PF) reconstruction algorithm, which is also used in the

offline event reconstruction (see Section 3.4.1). The algorithm version used at the HLT is modified to allow event reconstruction within 200 ms of processing time per event. The data processing steps are performed from the simplest and fastest modules to filter the majority of events earlier. The processing of calorimeter information is done first, and as soon as the event fails one filtering step, the whole reconstruction is halted completely. In this approach, the slow PF full reconstruction is performed for a tiny fraction of events.

During Run 2, the HLT contained approximately 400 trigger paths, which relied on HLT-level Particle Flow (PF) candidates such as muons, electrons, photons, and both neutral and charged hadrons. These PF candidates are then clustered into jets to reconstruct other higher-level HLT objects, including tau leptons and b-quark jets. The employment of tracker information enables the discrimination between electrons and photons in the HLT, allowing the development of specific trigger paths. Both trigger levels can have a prescale p, to which only a fraction $1/p$ of events are selected by this trigger. Such a procedure is adjusted during the data-taking to allow the collection of events from processes with large cross-sections, providing great value for detector calibration and validation.

3.2.8 Computing and data sets

During the data-taking period, the data collected by the experiments are organized in different periods containing a certain amount of LHC fills with similar conditions, which can be then split in multiple runs. A single run is characterized by a specific configuration of detector and trigger settings, with any change in these conditions leading to the start of a new run. Each run is subdivided into luminosity blocks, typically lasting about 23 seconds.

The produced raw data with the full information of the detector hits and energy deposition is then further processed by an offline reconstruction chain. The raw data is written on tape for permanent storage for possible new detector calibrations performed in a later stage.

The data processing is performed at the *Worldwide LHC Computing Grid* (WLCG) [104]. The WLCG consists in multiple data centers that can be classified in different Tiers. The CERN computer centered is considered the *Tier 0*, with a dedicated 10 Gbit/s connection and representing around 20% of the total computing resources of the WLCG. The data is then sent out from CERN to 13 called *Tier 1* around different academic institutions in Europe, Asia, and North America, via dedicated optical fiber links with 10 Gbit/s bandwidth. Connected to this *Tier 1* structure, there are more than 150 *Tier 2* data centers with different sizes and resources located in various universities and institutes around the world.

3.3 Event simulation at the CMS Experiment

The computer simulation of collision events and the detector response is an integral part of the methodology employed in modern particle physics. The methods developed allow for detailed and accurate simulations, with a computationally expensive drawback. These methods are used to cover several orders of magnitude in energy and momentum of the particles.

The results produced by the simulations are used in several stages of experimental particle physics research. They can be employed for the design of new experiments and the upgrades of the already existing ones. It can also be employed for the derivation of signal hypotheses and feasibility studies. Similarly, the simulated events can provide methods to estimate background contributions from the often-called irreducible background processes that are difficult to measure from data without signal contamination. Additionally, comparisons between data and simulation of kinematic distributions are often useful for the validation of the analysis methods.

As briefly discussed in Section 3.1, the cross section for rare processes of interest,

such as magnetic monopole production, is many orders of magnitude smaller than the total inelastic proton–proton cross section. As a result, generating large samples of such events through the simulation of generic proton–proton interactions is computationally infeasible. Instead, event generation for such rare processes begins directly with the hard interaction of interest. Then, the outgoing particles are evolved forward in time, while the incoming particles are evolved backward to reconstruct the initial state of the interaction.

The workflow employed for the production of simulated proton-proton events can be divided into four components. The hard process is generated using perturbative QCD, followed by the evolution of the parton showers, the hadronization of the produced partons, and the modeling of secondary interactions of the partons in the protons. For the modeling of the detector response of the experimental apparatus, the generated events are processed through a simulation of the detector, which is discussed in Section 3.3.2.

3.3.1 Event generation

The general-purpose `Pythia` [105] and `HERWIG` [106] provide different tools for the performance of the four steps of event generation. In some cases, the modeling of the hard process can be performed by `MadGraph 5` [107] or `POWHEG` [108], commonly used to produce parton-level events. The outputs can be then transferred to the general-purpose software for the subsequent steps. A common event generation process chain could also include the *Les Houches Event* (LHE) [109] file format, which is used to describe parton-level events, providing them as input to the general purpose software for the parton showering and hadronization processes.

3.3.1.1 Hard process

For hard processes, Quantum Chromodynamics' (QCD) asymptotic freedom enables a perturbative treatment, allowing the hard interaction to be described by Feynman diagrams. The amplitude of the diagrams can then be obtained by the terms from the corresponding diagrams that describe the process up to a chosen order in perturbative QCD, typically leading order (LO) or next-to-leading order (NLO). The squared amplitude, or matrix element, is then used to determine the differential cross-section, from which the distributions of kinematic variables can be derived. The total cross-section is obtained from the integration over the differential cross-section, allowing the determination of the correct normalization of the simulated sample. This total cross-section is dependent on the center-of-mass energy available at the collision.

The general-purpose generators such as `Pythia` contain a selection for LO matrix elements for different processes of the SM and its extensions. The tools `MadGraph 5` can be used to generate events at LO, while for the NLO events, the `MadGraph5_aMC@NLO` [110] can be used.

The cross-section is evaluated through the estimation of high-dimensional phase space integrals. For such evaluation, Monte Carlo techniques are employed in the event simulation to an extent, resulting in the often-called Monte Carlo events. During the integration over the phase space, cuts can be introduced for the phase space parameters to take into account the detector acceptance, or to avoid divergences in the cross-section.

3.3.1.2 Parton distribution functions

In proton-proton collisions, the behavior of the partons' center-of-mass energy during the hard interaction is described by parton distribution functions (PDFs). A PDF f(x,μ) quantifies the probability of finding a specific type of quark or gluon carrying a fraction x of the incoming proton's total momentum when probed at an energy scale μ. While the scale dependence of PDFs can be theoretically determined, their functional form is governed by the non-perturbative physics within the proton, so it needs to rely on experimental data.

The choice of the PDF affects the total cross-section of the process and the kinematic distributions of the final-state objects. Then, the PDF can be applied in the simulation of parton showers and secondary parton interactions.

During the LHC Run 2, the set of PDFs used was the `NNNPDF3.0`, which was widely used in event generation. These functions are based on a large variety of experimental results from different experiments and energy scales. In the Figure 26, an example of the `NNNPDF3.0` parton densities is presented.

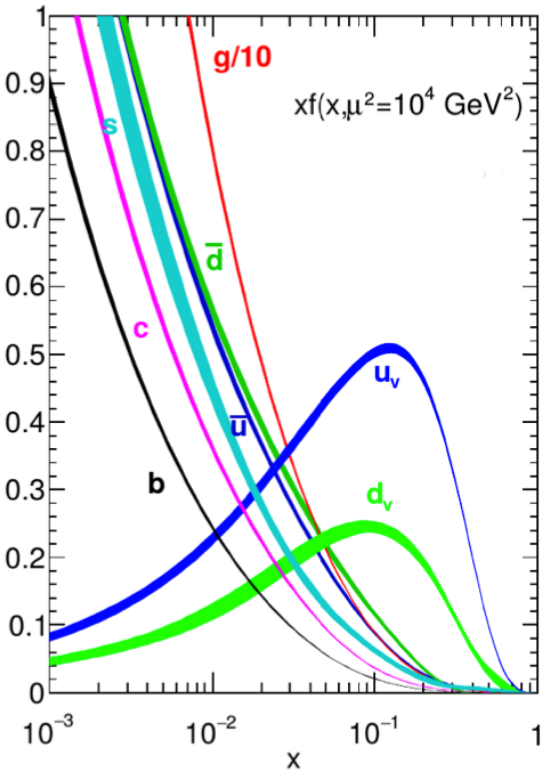

Figure 26 – Example of the NNNPDF3.O parton distribution functions, shown as a function of x [9].

3.3.1.3 Parton showering

Analogous to how charged particles emit bremsstrahlung radiation in Quantum Electrodynamics (QED), colored partons can radiate gluons in Quantum Chromodynamics (QCD). However, due to the non-Abelian nature of QCD, the gluons can also radiate gluons, a phenomenon not observed with photons in QED. This process initiates a cascade of partons that undergo continuous scattering, annihilation, and new particle production.

For the modeling of such showers, approximate results from perturbative QCD are applied for the shower creation in a probabilistic manner. Such processes can be interpreted as a Markov chain, allowing their efficient implementation with Monte Carlo techniques.

During the parton showering step, initial-state partons undergo backward evolution towards the incoming protons. This process effectively reverses time, evolving from high momentum transfer scales μ down to lower scales to characterize the partons within the incoming protons before the collision. Conversely, the final-state partons evolve forward in time, from the high μ scale of the collision gradually down to a scale where the hadronization takes place, due to the non-perturbative confinement. The parton showering can be implemented by different generators. The `HERWIG` uses angular-ordered showers, which accurately account for soft gluon emissions, while `Pyhtia` starts with the higher-p_T

order. The two orderings are considered to be effectively equivalent.

3.3.1.4 Hadronization

When the momentum transfers reach the ≈ 1 GeV scale, perturbative QCD is no longer applicable, and the event's subsequent evolution is described by the hadronization process. Such models are inspired by QCD, but they cannot be derived from theory due to its nonperturbative nature. The models for hadronization describe the confinement of the final-state partons in colorless hadrons and the interaction of the initial-state partons with the remaining protons of the incoming beam. These models are treated in a color-connected system that hadronizes collectively, with free parameters to be tuned to match the experimental results.

The hadronization process is often modeled using massless relativistic strings, which represent quark-antiquark pairs. These strings can split into two when the distance between the quarks reaches a certain point. Both `HERWIG` and `Pyhtia` software packages can be used for hadronization models, though they employ different approaches. `Pyhtia`'s model is based on a potential between two quarks that increases linearly with their separation, effectively stretching a color string between them. In contrast, `HERWIG`'s model is based on the formation of clusters by partons, which then decay into stable hadrons.

3.3.1.5 Secondary parton interactions

The total proton-proton cross-section is dominated by soft QCD events. However, soft secondary interactions can also occur between the partons of the colliding protons, where scattering and multiparticle production processes can be mentioned.

For low momentum transfers, with the impossibility of relying on the perturbative QCD, nonperturbative multiple-parton interaction models and diffraction models are employed to describe these secondary interactions. The final-state particles that are not produced in the hard process are referred to as the underlying event, which can also be subject to hadronization.

3.3.2 Detector Simulation

The geometry and material of all components of CMS are described in detail by the `GEANT4` toolkit [111], including both the active detector elements and the passive material such as cables and cooling systems. The generator-level particles, from simulated events, are then propagated through the simulation to account for the effects of magnetic fields, bremsstrahlung, photon conversions, and scattering, among other processes, with Monte Carlo simulation in a stochastic procedure. The simulated events are treated in the same manner as the data events concerning its reconstruction. The detector-level particles are

then obtained from generated signatures like energy deposits and hits in the detector's elements, and it also used as inputs for the readout and trigger emulation.

3.3.3 Pileup modeling

The simulation of pileup events is performed by mixing separately simulated *minimum bias* events, which primarily consist of soft QCD interactions. To achieve this, a sample of *minimum bias* events is generated using Pythia and processed through the full detector simulation chain based on `GEANT4`. The resulting simulated energy deposits are then superimposed on those from the primary hard-scattering events.

The mean number of interactions per bunch crossing ($< N_{PU} >$) is determined either from the distribution observed in real data, if available, or from an expected distribution if the simulation precedes data collection. For each generated event, the $< N_{PU} >$ value is sampled from the first distribution, and the amount of pileup in the specific event is sampled from a Poisson distribution with the mean value set to the chosen value of $< N_{PU} >$.

3.4 Event reconstruction at the CMS Experiment

The event reconstruction in the CMS Experiment relies on the *ParticleFlow* algorithm [112], where the reconstructed objects by PF are employed in the CMS analyses. Traditionally, each type of particle is reconstructed individually, with the combination of different pieces of information from various subdetectors. In contrast, the PF algorithm aims for a global event description, integrating all particles of the event, with an optimized combination of the full information of different systems. The fundamental concept of the PF algorithm is illustrated in Figure 27, while a display of a PF-reconstructed event can be observed in Figure 28.

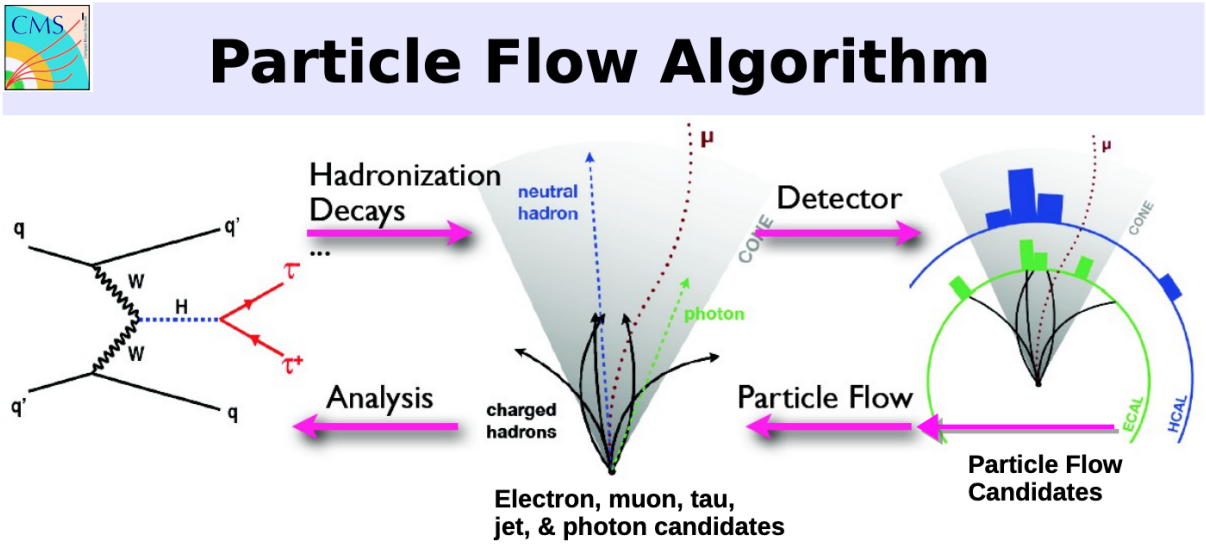

Figure 27 – The CMS *ParticleFlow* (PF) algorithm. The diagram shows how collisions lead to particle decay and final state particles, which leave tracks and energy deposits in the CMS detector. The detector information is then used to build the PF candidates to reconstruct high-level physics objects, which are used to reconstruct the collision event. [113].

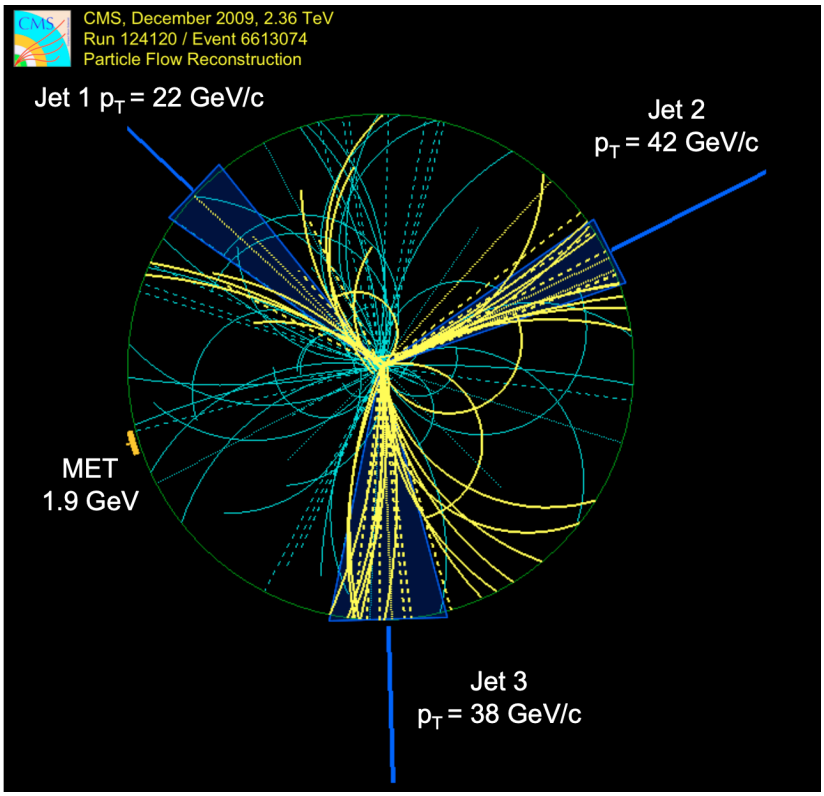

Figure 28 – Display of a particle-flow reconstructed event, recorded at 2.36 TeV, in the view transverse to the beam axis. The particles clustered into jets are shown as thick lines and other particles as thin grey lines. The charged hadrons are shown as solid, bending lines, photons, and long-dashed lines, and neutral hadrons as dotted lines. [114].

The output of the PF algorithm is a collection of PF candidates, classified as muons, electrons, photons, and charged and neutral hadrons, representing the stable particles in the event. These PF candidates are subsequently used to construct higher-level physics objects. The presence of weakly interacting neutral particles can be inferred from the transverse momentum imbalance in the event, obtained through the missing transverse momenta ($\vec{p}_T^{\,\text{miss}}$).

The reconstruction of each physics object is performed with information from different parts of the detector. Photons and electrons are identified by their electromagnetic showers in the ECAL. Muon chambers play a crucial role in muon identification, while jets are primarily reconstructed from calorimeter energy deposits. For the efficient performance of the PF reconstruction, a large volume inner tracker, a calibrated calorimeter for good energy resolution, and a high magnetic field for a good resolution of the transverse momentum are required.

3.4.1 Particle Flow algorithm

In the first stage, the PF algorithm identifies the tracks of the charged particles, and a dedicated clustering PF algorithm is employed for the reconstruction of the calorimeter clusters. A local maximum of the seed is defined for the energy deposition higher than a certain threshold. The PF elements are connected via a link, creating a block of such elements, and by the definition of a geometrical distance between the elements of the block, the quality of the matching employed can be quantified. The match between a track in the tracker and a cluster in the calorimeter is performed by the extrapolation of the last his of the track to the nearest calorimeter cluster. At last, the distance between the extrapolated track and the nearest cluster in the (η, ϕ) plane is defined as the matching distance.

In the PF algorithm, the identification of electrons is done first from the association of a track and ECAL cluster, with its subsequent removal from the PF reconstruction chain. For an energy deposit in the ECAL with no tracks associated, the formed block is classified as a photon, while for a deposit in the HCAL, a neutral hadron is defined. In resume, the PF blocks can be classified as electrons, isolated photons, or muons, while the remaining elements are identified as PF-charged (neutral) hadrons and PF photons.

3.4.1.1 Tracks

The precise reconstruction of charged particle tracks from the tracker measurements is required for the precise measurement of the particle momenta. The reconstruction of tracks of the charged particles in the silicon tracker, often called inner tracks, is performed iteratively with the combinatorial Kalman filter algorithm [115]. The reconstruction procedure starts with the identification of hits in the layers (seeds), allowing a first estimate of the track parameters. Through all the next surrounding layers, the hits found

are then combined with the seeds for the update of the track parameters and the creation of multiple track hypotheses.

Possible ambiguities arise from tracks that share at least half of their fits. For the resolution of such ambiguities, the track with the lower number of hits is discarded. Finally, the track direction and momentum are obtained from a global fit. In the context of track reconstruction, efficiency is defined as the fraction of simulated tracks successfully reconstructed such that at least half of the hits in the reconstructed tracks match with the simulation.

To enhance reconstruction efficiency without significantly increasing the misreconstruction rate, track finding is performed iteratively, potentially up to ten iterations, each employing distinct seeding and quality criteria. The initial iteration aims for the highest-quality tracks with clear signatures. After each iteration, the hits corresponding to reconstructed tracks are masked, gradually reducing the complexity of the combinatorial procedure. Some iterations are designed to tackle specific classes of tracks, such as missing hits in the pixel detector, tracks from displaced vertices, and tracks from high-p_T jets. The final iterations are seeded by tracks from the muon chambers, thereby increasing the reconstruction efficiency of muon tracks within the silicon tracker. The fraction of reconstructed tracks that don't originate from a charged particle (e.g., from detector noise) defines the fake rate.

Considering isolated muons within the pseudorapidity $|\eta| < 2.4$ with $p_T < 100$ GeV, the efficiency is around 99% with no dependence in η or p_T [96], with a negligible fake rate. For isolated charged hadrons and electrons, the efficiency shows some dependence on η, with around 95% efficiency with 2% fake rate for the central region, and around 80% for the forward region of the detector, with a fake rate above 10% in the region between the barrel and the endcaps.

3.4.1.2 Primary vertices

The primary vertex (PV) is defined as the interaction vertex of one particular inelastic proton-proton scattering. Since multiple interactions occur in each bunch crossing, it originates from many PVs, motivating the development of a procedure to correctly identify the PV. The PV reconstruction is a complex problem, and it is solved considering all the vertices together, where the extrapolation of the high-quality inner tracks to the closest point in the beamline and the assignment of uncertainty is performed.

A high-dimensional space is formed by the association of multiple tracks with the unknown PVs. A deterministic annealing algorithm is employed to locate the global minimum within this space [116], by evaluating the probability that each track originated from a particular vertex. This iterative procedure results in the determination of the PV position with a resolution of 20 μm for essentially 100% of PVs with at least three

associated tracks, and 98% for only two tracks associated [96]. Since the reconstruction efficiency is nearly 100%, the number of reconstructed PVs offers a good estimate for the number of pileup events (PU). However, the accurate identification of the PV of the interaction to be used in the physics analyses is becoming increasingly challenging with the increase of the PU level.

The impact parameter (IP), which is defined as the distance of the closest approach of a track to the PV, is calculated considering the longitudinal (d_z), transversal (d_{xy}), and three spatial dimensions. The uncertainty in these measurements is used to obtain the significance of the impact parameter, which can then be employed as a quality criterion for particle selection and further rejection, considering one particular PV.

3.4.1.3 Calorimeter clustering

The electromagnetic showers in the ECAL and hadron showers in the HCAL are typically wider than a single ECAL crystal or HCAL module. For this reason, the energy deposits in these crystals and modules, or calorimeter cells, are clustered to determine the energy of the incident particles that generated the showers. The clustering approach employed is the same for ECAL and HCAL, also considering the barrel and endcap configurations, as well as the two preshower (ES) layers in each endcap.

The clustering process is seeded by cells where the energy deposited is higher than a certain threshold. Then, the neighboring cells (8 in ECAL and ES, and 4 in the HCAL) are associated with the seeds, while the topological clustering is performed, with the addition of nearby cells as long as their energy is at least twice as large as the noise level.

Finally, a maximum-likelihood fit is employed for the reconstruction of the Gaussian energy distributions inside each topological cluster, corresponding to electromagnetic or hadronic showers. It is worth noting that even sharing the same approach, different seeding, clustering, and fitting parameters are applied for each subdetector.

For electron and photon reconstruction, the ECAL energy from the electromagnetic showers is summed in the often called *superclusters*, with a small width in η and a large coverage in ϕ to account for bremsstrahlung photons, photon conversion, and the bending of the electron trajectories in the magnetic field. The superclusters are constructed from a seed crystal, with a subsequent finding of 5×1 arrays around the seeds in the barrel, with their further combination in the superclusters. For the endcaps, the array selected is 5 $times$5. For the final supercluster, different energy thresholds for the seeds and arrays can be employed. The further extrapolation to the ECAL preshower adds the corresponding energy to the superclusters.

The response of the calorimeters is carefully calibrated, using test beams and cosmic rays before the start of the LHC operation. During detector operation, the transparency

of the ECAL crystals is monitored with a dedicated system for the derivation of time-dependent corrections. The ECAL superclusters are corrected and calibrated using an MVA regression algorithm trained with simulated events. Small residual differences between data and simulation are corrected with $Z \to e^+e^-$ events, with the parametrization of the ECAL/HCAL response as a function of the hadrons' simulated energy.

The HCAL is initially calibrated with a test beam setup, with further calibration needed to account for the energy deposited by the hadrons in the ECAL, before reaching the HCAL. Then, the calibrated energy of the hadrons can be obtained from the calibrated ECAL and HCAL energies. Such calibrations are derived separately for different calorimeter regions and also for showers starting in ECAL and those contained only in the HCAL.

3.4.1.4 Link algorithm

After the reconstruction of the tracks, a link algorithm is employed for the match with the calibrated calorimeter clusters and deposits in the muon chambers. The links between the different PF elements are established by the extrapolation of the reconstructed trajectories in the tracker, considering the effect of the magnetic field. The elements are matched geometrically in the (η, ϕ) plane. For multiple combinations of tracks and clusters, the one with minimal ΔR distance is chosen.

Due to bremsstrahlung, the electron tracks linked with ECAL superclusters are calculated taking into account the energy losses in the tracker. For a photon conversion, a dedicated algorithm is used to find tracks from the e^+e^- pairs. The (super)clusters in ECAL, HCAL, and Preshower (ES) detectors are also linked with each other by geometrical matching. The tracks originating from the same secondary vertex are linked together, and finally, the tracks found in the inner tracks and signals in the muon detectors are linked for muon identification. The output of the link algorithm can be characterized by a set of PF blocks, containing a collection of linked elements, typically originating from one or only a few particles.

3.4.1.5 Reconstruction of the PF candidates

The identification and reconstruction of the PF candidates are carried out for each PF block separately. The muons are reconstructed first, with the link between the tracker and muon chamber tracks, followed by electrons, with tracks and ECAL clusters linked and isolated photons, with isolated ECAL clusters with no matched tracks. After the reconstruction of a PF candidate, the corresponding elements (tracks and clusters) are removed from the PF block. The hadrons and non-isolated photons are reconstructed last. The remaining ECAL and HCAL clusters with a linked track are identified as charged hadrons, while for clusters without a linked track, a neutral hadron is reconstructed. For ECAL clusters only without a track, the non-isolated photons are reconstructed.

Muons:

The muons can be reconstructed with high purity based on signals in the muon chambers, where they can be reconstructed as hits with well-defined positions. While the RPC chambers contain only a single layer, the CSC and DT chambers have multiple layers, so hits in their subsequent layers are connected forming straight-line segments. Three types of muons can be reconstructed: *standalone muons*, *global muons*, and *track muons*. The collection of these different types is referred to as PF muons, with a reconstruction efficiency higher than 99% according to simulation.

The *standalone muons* are built based only on the muon chamber signals, by choosing the DT and CSC segments as seeds and using pattern recognition to find the associated hits in all muon detectors. The *global muons* contains a standalone muon track matched to one reconstructed in the tracker system. The matching is performed by the extrapolation of both tracks to a common surface. After matching, a global track fit is performed.

The *tracker muons* are built from the extrapolation of the reconstructed tracks from the tracker to the muon chambers in the transverse plane, and requiring that at least one DT or CSC segment is matched to the extrapolated track. The tracker muons complement the other approaches, especially for the low p_T range, where a proper tracker cannot be reconstructed, and typically only one matching segment in the innermost muon station is found. The isolated global muons are identified first, where the isolation is defined by the requirement of the sum of tracks p_T and E_T of the calorimeter energy deposits corresponds to less than 10% of the muon p_T. For non-isolated muons which are typically found inside jets, tight selection criteria are required.

The momenta of muons are obtained from the curvatures of the corresponding tracks, where the tracker system provides the best momentum resolution for tracks with $p_T \approx 200$ GeV. For higher p_T muons the inclusion of muon chamber track curvature is used to improve the estimate. For the optimized momentum resolution, for each muon candidate above 200 GeV, the p_T is obtained from several track and muon information, where the most precise results are selected.

To suppress punch-through hadrons that might be misidentified as muons, the absence of significant calorimeter deposits and the presence of three track segments in the muon chambers are required. While tight selection criteria typically demand muon track reconstruction in both the muon chambers and the tracker, "tracker muons"(reconstructed primarily in the tracker with minimal muon chamber hits) and "standalone muons"(reconstructed only in the muon chambers) are also accepted.

The efficiencies of each step of the muon reconstruction and identification are measured with the *tag-and-probe* method, where events with two muons are selected

whose invariant mass is compatible with the Z boson mass. One muon is then required to pass tight selection criteria to be considered the *tag* muon. The resolution of a specific reconstruction or selection criteria is then determined by the fraction of the *probes* muons that satisfy the respective reconstruction criteria.

Furthermore, incident cosmic muons in coincidence with a bunch crossing can be reconstructed as standalone muons. However, such muons can be easily identified due to their large impact parameter values.

Electrons and isolated photons:

The electrons and isolated photons are reconstructed employing a similar procedure. This approach is selected due to the bremsstrahlung and photon conversion processes, which happen during the interaction of electrons and photons with the matter of the detector. The electrons, as their passage through the tracker emits bremsstrahlung photons, which account on average for 33% (86%) of the electron energy $|\eta| \approx 0$ ($|\eta| \approx 1.4$). The provided eta ranges correspond to the smallest and largest amounts of tracker material traversed by the particles before reaching the ECAL, respectively. On the other hand, both bremsstrahlung and prompt photons are likely to create e^+e^- pairs, which then radiate photons.

The PF electron candidates are seeded either by an energy deposit in the ECAL, where $E_T > 4$ GeV for the ECAL supercluster, or by reconstructed tracks with $p_T > 2$ GeV, linked with an ECAL supercluster. Such an approach ensures the correct treatment for isolated electrons with large momenta and non-isolated electrons inside jets, and small-p_T electrons.

Under the electron hypothesis, the track parameters are determined using a Gaussian-Sum Filter (GSF) fit [117], which exploits the correlation between the tracker momentum and the associated energy cluster in the electromagnetic calorimeter. A multivariate analysis with the usage of Boosted Decision Trees (BDT) is employed for the combination of the characteristics of the ECAL cluster and the properties of the GSF track. This process generates a discriminating variable used to distinguish electrons from neutral hadrons or photons. With the tuning of the working point of the multivariate analysis applied, different quality criteria can be produced for the electron candidates. For the determination of the reconstruction and identification efficiencies of the electrons, the *Tag-and-Probe* method is employed.

Hadrons and non-isolated photons:

Following the reconstruction of muons, electrons, and isolated photons, these are removed from the ParticleFlow (PF) blocks. Subsequently, hadrons produced from fragmentation and hadronization can be reconstructed. All the remaining ECAL clusters,

independent of a link with an HCAL cluster, without associated tracks, are interpreted as nonisolated photons within the tracker acceptance of $|\eta| < 2.5$. Similarly, the neutral hadrons are built from all the HCAL clusters without associated tracks. Outside the tracker's acceptance, charged and neutral hadrons cannot be distinguished, so their classification relies solely on calorimeter information. In this region, all HCAL clusters are initially classified as hadrons, while ECAL clusters not linked with an HCAL cluster are interpreted as photons.

Missing Transverse momentum:

For a collision, while the longitudinal momentum of the initial state of the partonic interaction is unknown, the momentum in the transverse plane (x,y) is zero. Due to the momentum conservation, the sum of momenta of all reconstructed particles in the event is expected to be zero, except for events where unobserved particles were created. The missing transverse momentum is defined as the negative vector sum of the transverse momentum of all PF candidates, including the ones not identified as a physical object (electrons, muons, photons, or hadrons), which are defined as unclustered energy. In the computation of the MET, the overlap between reconstructed jets and leptons is removed.

The reconstructed events can contain genuine p_T^{miss} from neutrinos, or other weakly interacting particles that escape the detector undetected, but also anomalous p_T^{miss}, which originate from misidentification of particles.

A large p_T^{miss} is an important signature for specific SM processes as well as many BSM signals, considering that they are composed only of genuine contributions. Studies in the correlation of the p_T and p_T^{miss} for high-p_T particles are performed, since an artificial p_T^{miss} contribution can arises in such scenarios. For a large correlation, the PF reconstruction is re-evaluated, with an alternative interpretation for such events.

To reduce sources of anomalous missing transverse momentum, several strategies are employed. First, cosmic-ray muons with trajectories deviating more than 1 cm from the beam axis are removed if they significantly affect p_T^{miss}, thereby preserving genuine displaced muons that might arise from processes like b hadron decays. Second, for muons with $p_T > 20$ GeV, multiple momentum reconstruction methods are evaluated, and the one that minimizes p_T^{miss} is chosen to mitigate misreconstruction effects. Third, for p_T muons (> 100 GeV) or charged hadrons that are nearly collinear with p_T^{miss}, hypotheses such as hadron punch-through or misidentification are tested. If adopting an alternative hypothesis reduces p_T^{miss} by at least 50%, the PF candidate list is updated.

Since the p_T^{miss} can be calculated only after the reconstruction of all PF candidates, the corrections are performed only at the end of the sequence, while the genuine p_T^{miss} contributions is not significantly modified by such corrections.

3.4.2 Reconstruction of physics objects

3.4.2.1 Isolated muons

As discussed in Section 3.4.1.5, ParticleFlow (PF) muons are reconstructed, and their momentum is measured by combining signals from both the tracker and muon chambers. Any PF candidate classified as muon is defined to satisfy the loose muon identification if it passes the selection criteria for either tracker or global muons.

For the tight muon identification, a loose muon is required to be reconstructed both as a tracker and a global muon. It should have a track with associated hits in at least six layers of the tracker and with at least one in the pixel detector. It also required a segment traversing at least two muon stations, with a high-quality global track with $\chi^2/N_{\text{dof}} < 10$ compatible with the primary vertex, and with impact parameters smaller than 0.2 cm and 0.5 cm, for transverse and longitudinal, respectively. The objective of such criteria for tight muons is to provide a pure sample of prompt muons, with the efficient suppression of secondary muons, and misidentified muons from punch-through and cosmic muons.

To distinguish prompt, isolated muons from secondary muons originating from processes like b-hadron decays within jets, isolation criteria are frequently applied. These criteria are typically based on the reconstructed tracks or ParticleFlow (PF) candidates found in the vicinity of the muon candidate.

3.4.2.2 Isolated electrons

The electron reconstruction can be seeded in two complementary ways. Most electrons can be reconstructed from seeds based on ECAL superclusters. The electron candidate is built by the association of the GSF tracks with the supercluster. Only superclusters with $E_T > 4$ GeV and no significant matching energy deposits in HCAL are considered. Alternatively, electron reconstruction can be seeded by a reconstructed track with pT > 2 GeV, and linked with an ECAL cluster, with the inclusion of the additional deposits from bremsstrahlung. The track seeding approach can be employed to improve the reconstruction efficiency of low-p_T electrons.

The energies of the ECAL clusters are corrected as a function of the cluster energy and η to account for the energy lost in the tracker, where the electron candidates are required to have similar magnitude cluster energy and GSF track momentum. Then, the electron identification is performed by a BDT that combines information from the tracks and associated calorimeter clusters. The BDT considers several properties of the candidate, such as the GSF track fits, the compatibility between the candidate direction and momentum, supercluster substructure, and the fraction of the energy lost in bremsstrahlung. The BDT is trained in different intervals of p_T and η of the electron candidates, considering barrel and endcap regions separately, and also the hypothesis of

isolated and non-isolated electrons.

To distinguish prompt electrons from both jets misidentified as electrons and from electrons produced within a jet, an isolation requirement based on hadronic activity is typically applied. Their energies are summed within an isolation cone around the electron candidate to quantify this isolation.

3.4.2.3 Jets

The jets can be reconstructed from the combination of particles, using the anti-kt algorithm [118], which is chosen due to its fast computation and collinear properties. For such combination, a distance parameter $d_{\mathrm{i,j}}$, between two particles i and j is defined as

$$d_{ij} = \min\left(p_{T,i}^{-2},\ p_{T,j}^{-2}\right)\frac{\Delta_{ij}^2}{R^2} \tag{3.4}$$

where $\Delta_{ij}^2 = (v_i - v_j)^2 + (\phi_i - \phi_j)^2$ is the distance between the seed particle (PF candidate) i to each surrounding particle j, and the radius parameter R controls the size of the jet, being R = 0.4 the standard choice in the CMS.

Then a variable d_{ij} reflects the distance and the transverse momentum of the particles. First, the particle j that minimizes d_{ij} is selected, and it is clustered in the same jet as particle i for $d_{\mathrm{ij}} < p_{T_i}^{-2}$. The clustering continues considering all particles j that minimizes d_{ij}, and only finishes when all j particles that satisfy $d_{\mathrm{ij}} < p_{T_i}^{-2}$ are clustered to the jet containing the seed particle i. The result of this clustering process in the plane $v - \phi$ can be observed in Figure 29.

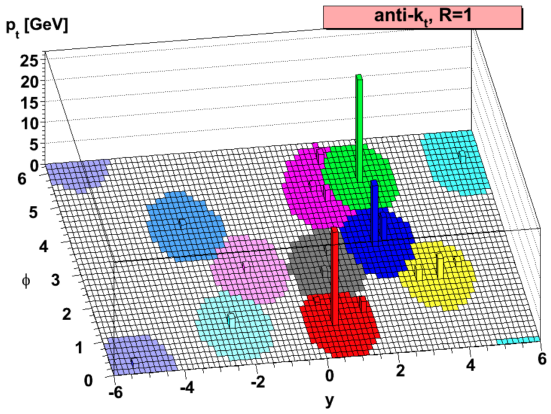

Figure 29 – The application of the anti-kt algorithm for clustering particles into a jet with parameter radius of R = 1.0 [118].

The chosen d_{ij} distance ensures the clustering of the soft particles into jets with high-momentum particles, rather than among themselves, allowing the anti-kt to produce a collection of hard jets. The anti-kt algorithm is characterized by infrared safety, where

the addition of very soft particles doesn't modify the clustering, and also collinear safety, where a set of collinear particles with some total momentum is processed in the same way as a single particle with the same momentum.

After clustering, the momentum of a jet is then obtained from the vectorial sum of momenta of all the PF candidates clustered, with charged PF hadron candidates from PU vertices removed before the clustering process.

The very forward region of the detector ($|\eta| > 2.5$) is characterized by the absence of coverage by the tracker, where jets coming from PU can be associated with the PV of the interaction with a higher probability. An MVA based on a BDT classification algorithm is employed for the identification of jets from PU, combining information on the jet shape and particle multiplicity.

Jet calibration:

Despite the calibration of calorimeter clusters and the precise measurement of the particle momenta by the tracker, additional calibrations are needed to make the momenta of the clustered jets match with the corresponding particle-level jets. Such jets are defined based on the generator-level information from simulated events, where all stable particles, except the neutrinos, are clustered into jets with the anti-kt algorithm. Differences between the reconstructed and particle-level jets can originate from energy deposits of pileup interaction, initial and final state radiation, electronics noise, and other effects.

The jet energy calibration is factorized into several levels, containing pileup offset corrections, simulated response corrections, and residual corrections. The corrections are applied as a multiplicative factor for the jet momentum, where the first two levels are applied to both data and simulated events, while the residual corrections are only applied for data, to increase the data and simulation agreement.

The pileup offset calibration is designed to correct the jet energy by subtraction of the energy corresponding to pileup contributions inside the jet. For this purpose, the correction factors are derived from simulated QCD multijet events with and without pileup contributions. The corrections factors are applied as a function of the uncorrected jet p_T, η, and the jet area in the (η,ϕ) plane.

In a second stage, the jet simulated response correction is applied, where the momentum response is defined from the ratio between the momenta of the reconstructed jet and the generator-level jets. The match between the reconstructed and generator-level jets is performed with the requirement $\Delta R < 0.2$. Such corrections are dependent on the regions of the detector.

The residual corrections take advantage of momentum conservation in the trans-

verse plane to estimate the energy scale of the recoiling jet, using an object with a precisely measured energy scale. The information of measurements in the barrel regions is extrapolated to the endcaps, where events such as $Z \to e^+e^-/\mu^+\mu^-$+jet and γ+jet are employed for momentum correction in the p_T range up to 700 GeV. The p_T of the Z boson or photon is measured at high precision and provides an estimate of the miscalibration for the recoiling jet, where a correction is derived. The calibrations can be extrapolated to the TeV range, employing QCD multijet events with high-p_T. After the application of all corrections, the jet energy resolution amounts to typically 15% at 10 GeV, 8% at 100 GeV, and 4% at 1 TeV [119].

3.4.2.4 Heavy-flavor jets

The hadronization of b and c quarks leads to the formation of short-lived heavy-flavor hadrons, with flight distances ranging from mm to 1 cm, depending on the hadron p_T. The decay of these short-lived hadrons is observed with the presence of secondary vertices reconstructed from the tracks of the decay products. The significant mass difference between b and c quarks compared to light quarks (u, d, s) and massless gluons leads to distinct kinematic distributions, notably in their transverse momentum p_T distribution. Consequently, the identification of jets originating from b and c quarks is crucial for analyses involving these objects in the final state. This is achieved via *b/c-tagging* algorithms, where the presence of soft leptons can be used for the identification. In simulated events, the jets containing at least one b hadron are classified as b jets, while jets with at least one c hadron and no b hadrons are labeled as c jets.

Several algorithms are employed in CMS for the tagging of heavy-flavor jets. Such algorithms use the properties of tracks, secondary vertices, and soft leptons as inputs. A collection of high-quality tracks with $p_T > 1$ GeV is used as input, with additional criteria designed to suppress tracks from pileup, from long-lived particles, and misreconstruction. The secondary vertices (SV) are reconstructed using the inclusive vertex finding algorithm, providing reconstruction efficiencies of 75%, 37%, and 12% for b,c, and light quark jets, respectively. The SV finding allows the reconstruction of the invariant mass of the hadron and the determination of the flight distance from the primary vertex.

3.4.2.5 Missing transverse momentum

As discussed in the Section 3.4.1.5, the missing transverse momentum ($\vec{p}_T^{\,\text{miss}}$) is reconstructed from the negative vector sum of the transverse momentum of all reconstructed PF candidates. This includes muons, electrons, photons, jets, and other physics objects built from PF candidates, as well as the unclustered energy, which is defined as the energy of all PF candidates not clustered into any specific physics object. Therefore, the estimation ($\vec{p}_T^{\,\text{miss}}$) is affected by spatial and energy resolutions of all PF candidates, in

addition to genuine momentum imbalance; it can be altered by mismeasurement and detector artifacts.

The ($\vec{p}_T^{\text{miss}}$) is calibrated by the propagation of the jet energy corrections described in the Section . The *Type-I corrected* $\vec{p}_T^{\text{miss}}$ is defined as:

$$\vec{p}_T^{\text{miss}} = \vec{p}_T^{\text{miss,uncorrected}} - \sum_{\text{jets}} \left(\vec{p}_T^{\text{corrected}} - \vec{p}_T^{\text{uncorrected}} \right), \tag{3.5}$$

where $\vec{p}_T^{\text{corrected}}$ ($\vec{p}_T^{\text{uncorrected}}$) is the jet momentum before (after) the jet energy corrections.

To suppress the pileup jets, only the jets with the corrected p_T above 15 GeV are included in the sum. As the correction is designed for quark and gluon jets, the jets corresponding to electromagnetic showers from electrons and photons are removed. This is achieved by excluding jets that have more than 90% of the jet energy deposited in the ECAL. For the same reason, jets, including global or standalone muons, are excluded from the sum.

3.5 Luminosity of collider experiments

3.5.1 Overview and Van der Meer scans

For the observation of a collision process $\alpha\beta \to X$, the event rate R(t) = dN/dt is obtained from the cross-section σ of the process and the instantaneous luminosity $\mathcal{L}$, as can be seen in the Equation 3.6, which highlights the crucial role the luminosity plays in a particle collider.

$$\frac{dN}{dt}(\alpha\beta \to X) = \mathcal{L} \cdot \sigma \tag{3.6}$$

The cross-section σ can be evaluated from the underlying interaction theory, the center-of-mass energy ($\sqrt{s}$), and the mass of the final-state particles, among other parameters. Experimentally, from a collision experiment, the σ can be obtained by the Equation 3.7. This approach is based on the counting of the number of events N_{events} of a given process collected during a data-taking period, considering the appropriate corrections for efficiency, background contributions, and detector acceptance.

$$\sigma = \frac{N_{\text{events}}}{L} \tag{3.7}$$

where the event yield is proportional to the cross section σ, and the integrated luminosity $L = \int dt\mathcal{L}$ serves as the proportionality constant.

Since the cross-section is both calculable and measurable, the comparison between the two values can be used to extract theoretical parameters from the experimental measurements. The precision of the measurements depends on the precision of the measurement of the three components: the measurement of the process itself quantified by N_{events}, the luminosity measurement (L), and the precision of the theoretical calculation. A key objective of luminosity measurements is to achieve a precision comparable to that of the other two measurements [120].

In general, the luminosity of a collider experiment can be obtained from the machine parameters. Considering two beams with N_1 and N_2 particles, described the normalized particle distributions $f_1(x, y)$, and $f_2(x, y)$, distributed in the plane transverse to the beam direction, and circulating a revolution frequency ν, the instantaneous luminosity $\mathcal{L}$ can be obtained by:

$$\mathcal{L} = \nu N_1 N_2 \int dx \int dy f_1(x, y) \cdot f_2(x, y) = \frac{\nu N_1 N_2}{A_{overlap}} \tag{3.8}$$

The double integral corresponds to the inverse of the effective area in which the collisions take place (A_{overlap}). The revolution frequency ν is well-defined for a particle

collider, and the number of particles can be precisely measured with beam currents. The limited knowledge of this effective area at the collision points is the main limitation for the precise estimation of the luminosity [121].

On the other hand, particle collider experiments are able to obtain measurements of some processes with very good precision. For these processes, with well-known cross sections, the inverse of the Equation 3.7 can be employed to obtain measurements of the luminosity. The Section 3.5.4 is dedicated to this topic.

At the world's first proton-proton collider, the CERN Intersecting Storage Rings (ISR), a procedure employing beam separation scans was proposed by Simon van der Meer to estimate the beam overlap area [122]. From the formulation of Carlo Rubbia [123] and the consideration of a luminosity detector that measures a rate R proportional to the instantaneous luminosity, the beam overlap area could be obtained from

$$A_{\text{overlap}} = 2\pi\Sigma_x\Sigma_y \tag{3.9}$$

where the parameters Σ_x and Σ_y describe the effective widths of the beam overlap area along two orthogonal directions.

The value of the effective widths can be obtained from the so-called Van der Meer (VdM) scan, and the R(t) can also be measured. For such a scan, the two beams are separated in the respective direction and then moved in steps across each other, where a sketch can be observed in Figure 30.

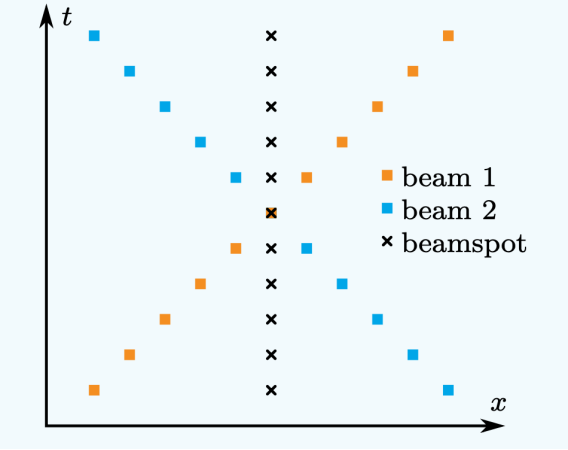

Figure 30 – Sketch of the beam position during a vdM scan. [124]

The use of the VdM method allows for the estimation of the luminosity for head-on collisions under the specific conditions of a VdM scan. The measured luminosity can then be used to calibrate the often-called *visible cross section* σ_{vis}, which corresponds to the absolute scale of the rate measurement of the luminosity detector, independent of beam conditions. In other words, the *visible cross section* σ_{vis} can be understood as the

calibration factor that links the number of collisions counted by a dedicated detector to the true luminosity delivered by the accelerator. Typically, the process used to measure the luminosity via Equation 3.6 is the elastic particle scattering, and the *visible cross section* (σ_{vis}) incorporates acceptance and efficiency of the specific detector [125].

For a van der Meer (vdM) scan, the beams start with an initial separation of about 6 σb, which corresponds to the transverse size of the bunches. They are then moved across each other in 25 steps, each lasting 30 seconds, with a step size on the order of 0.5 σb. The vdM scans are always performed in pairs of two scans along the horizontal and vertical directions, respectively. For consistency and reproducibility checks, as well as for ongoing monitoring throughout a fill, multiple vdM scans are performed, known as a vdM campaign.

The systematic uncertainties on the luminosity measurement can be divided into two groups: the normalization uncertainties, mainly related to the calibration, and integration uncertainties, which are related to the *luminometers* used in the data taking. Since the integration uncertainties have a strong dependency on the pileup and the linearity of the corresponding detector, it is expected to become the most likely dominant part of the uncertainty. Such behavior is due to the delivery of higher instantaneous luminosity by the LHC, where $\langle N_{\mathrm{PU}} \rangle \approx 50$ for the Run 3, and it is expected to increase to $\langle N_{\mathrm{PU}} \rangle \approx 200$ in the HL-LHC. This increase in the pileup levels will demand the development of new *luminometers* and methods to account for the new conditions of the HL-LHC for the achievement of the target precision of 1 %.

3.5.2 Luminosity Measurement at the CMS Experiment

At the CMS Experiment, the luminosity measurement is performed in two steps. First, the VdM method is employed for the calibration of the absolute luminosity scale of one or more luminosity detectors. During a data-taking period, one or more LHC fills are provided with special beam optics specifically designed to allow for VdM scans. From the VdM scans from these fills, the σ_{vis} of the *luminometers* is obtained from the rate measurements, via:

$$\sigma_{\mathrm{vis}} = \frac{2\pi \Sigma_x \Sigma_y R(0,0)}{\nu N_1 N_2} \tag{3.10}$$

The revolution frequency of the LHC corresponds to $\nu = 11245$Hz. The uncertainties in the σ_{vis} determination arise from the measurement of the beam currents N_1 and N_2, from the uncertainties in the VdM scan evaluation, among other sources.

In the second step, the integrated luminosity of a given data set is then obtained by integrating the rate measured by the luminosity detectors over the entire data-taking period, normalized by the calibrated visible cross-section σ_{vis}.

For an ideal integration, the dedicated detectors for the luminosity measurement are required to have a linear response to the instantaneous luminosity and also be independent of pileup or the bunch structure of the LHC filling scheme. However, most of the detectors show some nonlinearity in their response, making it one of the most relevant sources of systematic uncertainty. This motivates the development and application of various corrections. Typical nonlinear effects that can be mentioned are the afterglow, or out-of-time pileup, which is the spill-over of hits from one bunch crossing into the time window of the next crossing.

The performance of linearity corrections for each luminosity detector can be monitored with the emittance scans, short variations of the VdM scans employing a reduced number of steps. Such scans are typically performed in the CMS Experiment at the start of all fills. From the analyses of the emittance scans, the obtained σ_{vis} values can be used to monitor changes in the detector response as a function of time. After the application of all the linearity corrections, the overall linearity response could be evaluated by cross-detector comparisons, where the ratio between two given luminosity detectors can be determined as a function of the instantaneous luminosity during a fill.

In Table 1, the list of systematic uncertainties contributing to the total uncertainty for the luminosity measurement for the 2023 proton-proton collisions data.

3.5.3 Luminosity detectors at the CMS Experiment

The CMS luminosity detectors illustrated in Figure 31, and often referred to as *luminometers*, are responsible for providing measurements for the rate $R(t)$ of the hits, the tracks, and the clusters. To measure the absolute scale of the luminosity, the visible cross-section (σ_{vis}) must be estimated during the calibration procedure, as it is generally not well-known from first principles. The combination of the measurements of such detectors allows for the reduction of systematic uncertainties. For the *luminometers*, a high rate is required to allow their precise calibration and the measurement of the luminosity in short time intervals. The fulfillment of such requirements aims to minimize statistical uncertainty.

It is expected that the proportionality between the rate $R(t)$ and the luminosity $\mathcal{L}(t)$ will hold for the high pileup scenario, achieving the linearity property desired. Additionally, it could be expected that the rate $R(t)$ can be high enough to allow the measurement of the luminosity for single bunch crossings. However, nonlinearities can originate, for instance, from particles produced in the preceding bunches, which can affect the rate measurements of the later bunches. The second important property of a *luminometer* is the long-term stability. The stability property can be achieved with the maintenance, by the *luminometer*, of the visible cross-section (σ_{vis}) during the data-taking period, which corresponds to around 1 year. The effects of the radiation damage of failing parts

Source	Uncertainty (%)
Calibration	
Beam current	0.20
Ghosts & satellites	0.10
Orbit drift	0.02
Residual beam positions	0.16
Beam-beam effects	0.34
Length scale	0.20
Factorization bias	0.67
Scan-to-scan variation	0.28
Bunch-to-bunch variation	0.06
Cross-detector consistency	0.16
Integration	
Cross-detector stability	0.71
Cross-detector linearity	0.59
Calibration	0.89
Integration	0.92
Total	1.28

Table 1 – The prreliminary measurement of the offline luminosity in the 2023 proton-proton collision data at CMS has been performed using the BCM1F, DT, HF (ET and OC), PCC and PLT. The luminosity detectors have been calibrated from the VdM program performed at LHC fill 8999. The sources of the uncertainties for the total integrated luminosity arise from the calibration method and possible nonlinearities of the detector [126].

of the *luminometer* can introduce instability in the measurements. As a last step of characterization, the *luminometers* can be classified as online devices, which provide the luminosity measurements instantaneously, and offline devices, where the luminosity measurement is provided at a later time.

The *Pixel Cluster Counting* (PCC) is an offline *luminometer*, which is based on the pixel detectors of the inner silicon tracker [127]. It is expected that the number of pixel clusters hits is proportional to the luminosity, and this serves as the rate $R(t)$. The PCC method exploits the very large number of pixels in the inner part of the CMS detector, around 7×10^7. Because of this fine granularity, the probability that two charged particles hit the same pixel cluster is very small and can be neglected. The average number of clusters per interaction is approximately 200, with an average of about 5 pixels per cluster. This behavior is maintained in the high pile-up scenario, with $\mu = 100$, with the fraction of occupied pixels at the permille level. As a result, it is expected that there will be a linear relationship between the number of hit pixel clusters per bunch crossing and the number of interactions per crossing. This linear relationship allows the PCC to provide a very good measurement of the luminosity. To further ensure good stability for the luminosity measurement, problematic pixel clusters during the data taking are removed from the

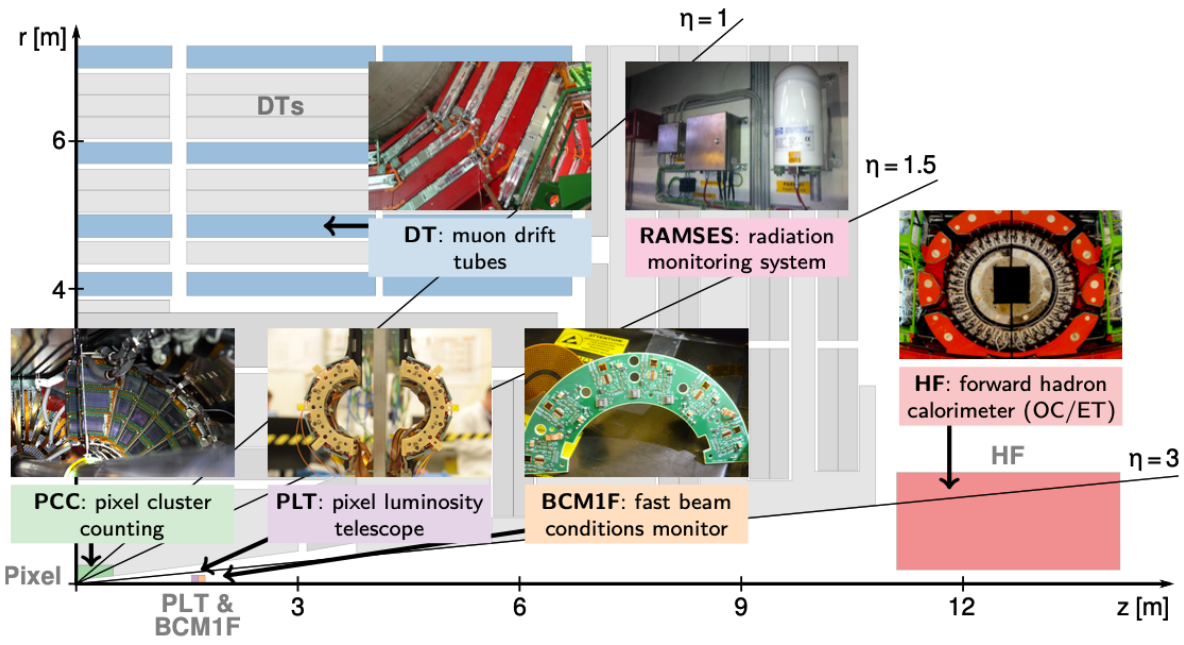

Figure 31 – The luminosity detectors employed in the CMS Experiment with its placement in the r-z plane. The muon drift tubes (DT), radiation monitoring system (RAMSES), forward hadron calorimeter (HFET/HFOC), fast beam conditions monitor (BCM1F), pixel cluster counting (PCC) and pixel luminosity telescope (PLT) are presented.

luminosity determination.

The HF luminosity measurement [128] provides the primary online luminosity measurement for the CMS, utilizing a dedicated readout system installed in the Hadronic Forward (HF) calorimeter. Two distinct algorithms are available. The occupancy method (HFOC) relies on the fraction of occupied towers where the signal measurement exceeds a certain energy threshold. The HFOC was the main *luminometer* for the 2017 data-taking. The second algorithm is the HFET, based on the sum of the transverse energy in the HF, and was chosen as the main method for luminosity determination in 2018.

The *Pixel Luminosity Telescope* [129] consists of a stand-alone detector, designed for the measurement of the online luminosity. The PLT is located at the end of the CMS pixel endcaps and it consists of 48 silicon pixel sensors in 16 "telescopes". The PLT measures the rate of "triple coincidences", where a hit is observed in all three planes. This behavior typically corresponds to a track from a particle originating in the interaction point. The overall mean rate for the PLT is estimated assuming that the number of triple coincidences follows a Poisson distribution with a mean $\mu = -ln f_0$, where f_0 corresponds to the fraction of events where the triple coincidences are observed. For such a procedure, the PLT places a contrast to the rate measuring *luminometers*, since it measures the fraction of events where no track signature can be observed. This method resolves the

problem of the overlapping tracks and the problem of occupancy, leading to good stability in the luminosity measurement.

The *Fast Beam Condition Monitor* (BCM1F) [130] is a detector designed for the measurement of the online luminosity and the machine-induced background (MIB). It consists of a total of 24 sensors assembled on the same carriage as the PLT. The BCM1F readout provides a fast readout with a time resolution of 6.25 ns. The combination of the precise time measurement and the position of the BCM1F, 1.8m from the center of the CMS, allows the separation between the hits from the collision products and the hits originating from the MIB, because the incoming background and the outgoing collision products are separated in time. This signal-background separation capability allows the study of systematic effects related to the background in different and promising ways.

The luminosity measurement based on the DT muon detector [131] is based on the muons produced in the CMS barrel, which is an efficient trigger on a low-background physics object. The muon track segments from the muon barrel DT stations are sent every bunch crossing for the generation of the first-level triggers. The number of tracks in time windows of approximately 23 seconds is read out and stored, where it can be used to estimate the luminosity. The rate of muons in the DT is significantly lower than the rate for most other observables from other detectors. However, during the VdM scans, due to the low pileup conditions, there are no muon tracks to provide a precise measurement of σ_{vis}, and so the system is calibrated by the PCC luminosity measurement. On the other hand, the muon candidate rate has been observed to be linear with luminosity and rather stable over time. The luminosity data of this system are integrated over all bunches.

3.5.4 Luminosity determination with physics processes

The approach of measuring luminosity using a physics process has been employed in previous experiments. This method exploits a process with a very clean signature, where its events can be easily identified and understood.

For electron-positron colliders, the Bhabha scattering $e^+e^- \to e^+e^-$ is a process with a very well-known cross-section from perturbative QED calculations. Exploiting the large event rate and the simple detection of its signature, a measurement of the luminosity with this physics process can be performed with high precision.

The Bhabha scattering was employed at the CERN *Large Electron-Positron* (LEP) collider for the measurement of the integrated luminosity, with an overall uncertainty better than 0.1% [132, 133]. The current luminosity measurement uncertainty on B factories like SuperKEKB [134] and BEPCII [135, 136] is around 0.7%. Considering the experiment Belle II at SuperKEKB the dominant source of uncertainty originated from a machine parameter, which affects the precision measurement of $\sqrt{s}$, required for the

Bhabha cross-section calculation.

However, in the context of hadron colliders, the luminosity measurements increase in complexity due to the composite nature of protons and the non-perturbative regime of QCD at small energies.

For the DESY *Hadron-Electron Ring Accelerator* (HERA), the process $ep \to ep\gamma$ (bremsstrahlung), which is predictable from QED, is used to provide a luminosity measurement with an uncertainty around 1.7%, while the precise luminosity measurement in proton-proton or proton-antiproton collisions poses a bigger challenge.

At the CERN *Intersecting Storage Rings* (ISR) experiment, the VdM method was employed for luminosity measurements, allowing precisions better than 1% [137]. However, for the $Sp\bar{p}S$ and Tevatron, respectively, at CERN and Fermilab, such a method could not be employed due to insufficient achievable transverse beam separation. Thus, the luminosity measurements were performed based on measurements of scattering processes or from machine parameters.

At the moment, there are two hadron colliders in operation with proton-proton collisions and heavy-ion collisions: the *Relativistic Heavy Ion Collider* (RHIC) at Brookhaven National Laboratory and the *Large Hadron Collider* (LHC) at CERN. For both experiments, the VdM method is employed for the calibration of the luminosity measurement for different collision configurations [125]. For the Run 1 data-taking of the LHC at $\sqrt{s} = 8$ TeV, the precision of the luminosity measurements along the different experiments ranges between 1.2% and 2.6% [138, 139, 140, 141], with the best precision achieved by the LHCb experiment. Preliminary results for Run 2 luminosity measurements in proton-proton collisions at $\sqrt{s} = 13$ TeV yield uncertainties between 1.2% and 2.5% [142, 143], including results from the CMS experiment [144, 145, 146].

For the future operation of the LHC and the upcoming High-Luminosity LHC, with a higher instantaneous luminosity, luminosity measurements are challenged by the expected higher collision rates. To perform accurate luminosity measurements under these conditions, a proposal combining the Van der Meer (VdM) method with the measurement of a well-defined physical state, termed ZCounting, has been considered. This proposal exploits the independence of theoretical prediction accuracy and the proton Parton Distribution Function (PDF) knowledge from the VdM method, while the ZCounting method allows for the determination of the reconstruction efficiencies from data. In this scheme, the fiducial cross-section of the Drell-Yan process $pp \to Z \to \mu\mu$ is measured in a dedicated low pileup run with a precise luminosity determination from the VdM scan. In the second step, the cross-section is then used in the regular data taking for the measurement of the luminosity, employing an in-situ determination of the muon reconstruction efficiency. [147, 148].

For the development of this thesis, the determination of the luminosity from the

measurement of the production rate of $Z \to \mu\mu$ is presented and will be documented in the next chapter.

4 Luminosity determination using Z boson production

The objective of this chapter is to describe the high-precision determination of the luminosity in the pp collision data taken at $\sqrt{s} = 13.6$ TeV during the years between 2022 and 2024. The luminosity can be determined using Z boson events in the final state with two muons by the following equation:

$$\mathcal{L} = \frac{N^{\mathrm{Z}}_{\mathrm{reco}}}{\sigma^{\mathrm{Z}}_{\mathrm{fid}} \epsilon^{\mathrm{Z}}_{\mathrm{ID}}} \tag{4.1}$$

where $N^{\mathrm{Z}}_{\mathrm{reco}}$ is the background subtracted number of the reconstructed Z boson, and $\epsilon^{\mathrm{Z}}_{\mathrm{ID}}$ is the reconstruction efficiency of the Z boson candidates. The fiducial cross-section $\sigma^{\mathrm{Z}}_{\mathrm{fid}}$ can be written as

$$\sigma^{\mathrm{Z}}_{\mathrm{fid}} = A\sigma^{\mathrm{Z}}\mathcal{B}(Z \to \mu\mu) \tag{4.2}$$

where the σ^{Z} is the inclusive Z boson production cross section, $\mathcal{B}(Z \to \mu\mu)$ is the branching fraction of the Z decay channel into two muons, and A is the acceptance factor for the two muons in the detector.

The Z boson decays with two muons in the final state has a remarkably clean signature, where the $Z \to \mu\mu$ events can be identified and reconstructed with a high efficiency by the CMS detector. The reconstructed invariant mass spectrum of both muons has a peak in the value of the Z boson mass of about 91 GeV. On the other hand, the background processes with two muons, or two particles wrongly identified as muons, usually have a flat nonresonant spectrum, which allows the efficient subtraction of the background events. Since this decay channel has a large effective cross-section, the number of Z bosons in a data taking of 20 minutes can be calculated with a statistical accuracy smaller than 1%, reducing the overall uncertainties in the measurement.

For the reconstruction efficiency of a Z boson, the trigger, identification, and reconstruction efficiencies of its constituent muons are utilized. These muon efficiencies can be measured *in situ*, using the identical event sample as the Z boson rate measurement. From that approach, no biases or uncertainties arise from the assumption of the calibration transfer between two distinct event samples. Only the correlation between the two muons of the Z boson decay and the correlation between the track components of each muon might require residual corrections.

In the following section of this chapter, the Z boson production for the relative and absolute luminosity measurements is presented. In Section 4.1, an overview of the analysis strategy employed in this work is given. The description of the samples used for the measurement can be found in Section 4.2. The binned maximum likelihood fit of signal and background shapes used to extract the signal contribution is described in Section 4.3. In the Section 4.4, the selection criteria of muon and Z candidates, along with the simultaneous extraction of the number of reconstructed Z bosons and the single muon trigger efficiency is described. The correlation between the trigger efficiencies of the two muons and their dependency on pileup is briefly discussed. In Section 4.5, the measurement of the identification and reconstruction efficiencies of the muon track components is explained, and the performance of fits on the muons' pair invariant mass spectrum for the subtraction of the background contribution is mentioned. Results on the relative and absolute luminosity determination using the Z bosons and its stability are given in Sections 4.6, 4.7, and 4.8, respectively. Finally, a brief overview of the possible sources of systematic uncertainties is provided in Section 4.9.

4.1 Introduction

The production of Z bosons is known as a *standard candle* due to its well-known properties, which are used in a variety of fundamental measurements. Among these, one can mention the calibration of the energy scale and momentum of muons [131] and electrons [149] based on the Z boson's mass and width, as well as the precise measurement of LHC luminosity using Z boson production [150].

The total inclusive cross-section times the branching fraction of a Z boson decaying into two muons for a pp collision at 13 TeV can be written as [151].

$$\sigma^{\mathrm{Z}}\mathcal{L}(Z \to \mu\mu)[\mathrm{nb}] = 1.977 \pm 0.009(\mathrm{stat}) \pm 0.041(\mathrm{syst}) \pm 0.042(\mathrm{lumi}) \tag{4.3}$$

Typically, about one-third of the total number of produced Z boson events are reconstructed in the fiducial volume of the detector [152]. On the other hand, the limited knowledge of the proton PDF and higher-order corrections, in the order of 3%, consists in the current uncertainty in the prediction of the fiducial cross section. [153]. Within this uncertainty, the Z boson rate can be used to directly determine the integrated luminosity. However, the Z boson rate can also be used to measure the relative and absolute luminosity without the input of the theory cross-section.

4.1.1 Relative luminosity determination using Z boson production

In Section 3.5.4, the uncertainties that affect the luminosity measurement by the conventional methods are discussed. However, the luminosity measurement from Z boson production is affected by completely different systematic uncertainties. Furthermore, the relative luminosity determination with the Z boson rate method consists of a valuable tool for cross-checks and a useful complementary method for the monitoring of the relative instantaneous luminosity and stability delivered to both ATLAS and CMS experiments. Since the summer of 2017, the ratio of efficiency-corrected number of Z bosons (N^Z), from ATLAS and CMS experiments, has been regularly monitored, allowing for its usage in the determination of the luminosity. The ratio of N^Z can be directly compared with the luminosity measurements from both experiments using the Equation 4.4. For the same fiducial phase space between ATLAS and CMS, the fiducial cross-section σ^Z_{fid} cancels out for the luminosity ratio, as evident from Equation 4.1. As shown in Figure 32, the N^Z ratio is in good agreement with unity, which indicates that the same luminosity has been recorded by both experiments.

$$\frac{\mathcal{L}(\text{ATLAS})}{\mathcal{L}(\text{CMS})} = \frac{N^Z(\text{ATLAS})}{N^Z(\text{CMS})} \tag{4.4}$$

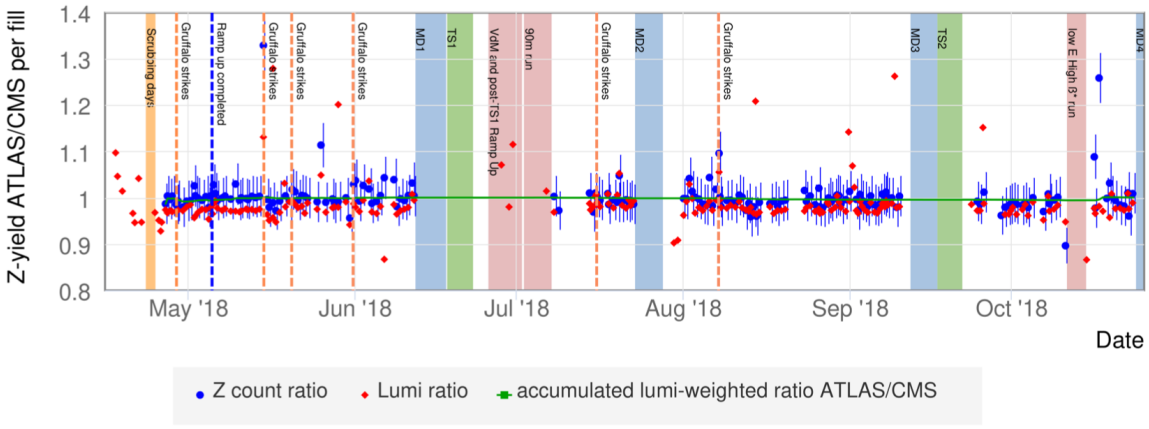

Figure 32 – Distribution of the Z-yield ratio between ATLAS and CMS per fill for the 2018 data taking, where the dates of the data taking can be observed in the x-axis. In the distribution, the blue points represent the ratio between ATLAS and CMS Experiments for the number of Z bosons measured. For the red points, the ratio of the recorded luminosity of the two experiments is presented. The accumulated ratio of the Z yields weighted by the collected luminosity over time is represented by the green line. Additionally, changes in the beam settings are indicated by the blue dashed lines while the presence of the Gruffalo strikes are indicated in the orange dashed lines. The colored areas indicate other phases like technical stops (TS) in green, machine developments (MD) in blue and special beam optics in red.

The measurement of the relative luminosity using Z bosons has also been employed by the ATLAS Experiment, for Z boson decays in muons and electrons [154]. The measurements for the luminosity with both lepton decay flavors present consistent results with a spread around unity of 0.8% over the entire Run 2 period. The results show good long-term stability in the reference luminosity for the full Run 2 data-taking period from 2015 to 2018.

4.1.2 Absolute luminosity determination using Z boson production

The Z boson counting method exploits the fact that the cross-section (σ^Z_{fid}) remains constant throughout all the pp collisions during a data-taking period at a given center-of-mass energy, 13 TeV for the Run 2 and 13.6 TeV for the Run 3. From this characteristic, the ratio of the efficiency-corrected number of Z bosons (N^Z) between data sets can be used to transfer the luminosity calibration from one data set to another. Furthermore, the precision knowledge of the (σ^Z_{fid}) from the theory isn't necessary, and also, if it is of interest to the approach, can be estimated using the Z boson counting method.

For good precision in the luminosity calibration, a data set under specific conditions, such as a low pileup level, is used. For the Run 2 data-taking, such a special run occurred in the era H of 2017 (2017H). The calibration obtained can then be employed to derive the luminosity of the data sets with a higher level of pileup, where the interesting collisions for physics take place. The equation for such derivation follows below:

$$\mathcal{L}_{\text{highPU}} = \frac{N^Z_{\text{highPU}}}{N^Z_{\text{lowPU}}} \mathcal{L}^{\text{Ref.}}_{\text{lowPU}} \tag{4.5}$$

The Equation 4.5 provides a method to determine the integrated luminosity of data collected under high-pileup conditions by comparing it to a well-calibrated low-pileup dataset. The great advantage of the data sets with low pileup levels is to exploit the highly precise measurement of the reference luminosity under such conditions, due to the reduced number of overlapping proton–proton interactions.

The method exploits the fact that the production cross section of the Z boson, particularly in the $Z \to \mu\mu$ decay channel, is both theoretically well known and experimentally stable when beam conditions are similar. This stability allows it to serve as a reliable "standard candle"for transferring luminosity information between datasets.

In this approach, the quantities N^Z_{highPU} and N^Z_{lowPU} represent the number of reconstructed Z boson events in high- and low-pileup data, respectively. Importantly, these yields are corrected for detector acceptance and reconstruction efficiency. This ensures that the comparison reflects the true number of Z bosons produced in each dataset, rather than differences in detector performance. By comparing these efficiency-corrected yields, the luminosity measured in the low-pileup regime ($\mathcal{L}^{\text{Ref.}}_{\text{lowPU}}$) can be transferred to high-pileup

data, where direct calibration is more challenging due to the large number of simultaneous proton–proton interactions.

An important strength of this method is that many systematic uncertainties cancel out in the ratio used in Equation 4.5, especially those that are common between the two datasets. This cancellation reduces the overall uncertainty of the extrapolated luminosity measurement. Moreover, trigger and selection efficiencies are measured *in situ*, using the same dataset and decay channel, which makes the method more robust against variations in detector performance and changing beam conditions.

4.2 Datasets and simulated samples

4.2.1 Datasets

The data for this study were collected during LHC Run 3 in 2022, 2023, and 2024. The measurements are organized in terms of luminosity blocks, which divide each data-taking run into intervals of about 23 seconds, recorded during the full operation of the CMS detector. For the Run 3 data collection, the muon trigger was updated to `HLT_IsoMu24`, which has a requirement of $p_T > 24$ GeV and uses isolation criteria. For the 2022 data-taking period, only eras 2022E, 2022F, and 2022G were deemed suitable for physics analyses, primarily due to changes in muon prefiring behavior and alignment conditions earlier in the year.

In terms of luminosity, the total delivered and recorded values for each year are as follows: in 2022, 32.73 fb^{-1} was delivered and 30.10 fb^{-1}recorded; in 2023, 41.47 fb^{-1} was delivered and 38.01 fb^{-1} recorded; and in 2024, 122.15 fb^{-1} was delivered, with 112.70 fb^{-1} successfully recorded.

4.2.1.1 The low pileup data-taking period in 2017

For the measurement of the absolute luminosity of the Run 2 data-taking, the Equation 4.5 was used in the low pileup data-taking period from 2017. For such a period, on average, three interactions per bunch crossing occurred, where the corresponding pileup distribution can be observed in Figure 33.

For the given data period in 2017, the single muon trigger employed in the high pileup data was not active. This motivated the emulation of such a trigger to remove the differences between these triggers, which introduced additional systematic uncertainties. The recorded integrated luminosity is obtained by requiring the single muon trigger to be active during the data-taking. The recorded luminosity amounts to $\mathcal{L}^{\text{Ref.}}_{\text{lowPU}} = 199.3\ \text{pb}^{-1}$ utilizing the latest luminosity calibrations and considering only the luminosity blocks in which the CMS detector was fully operational.

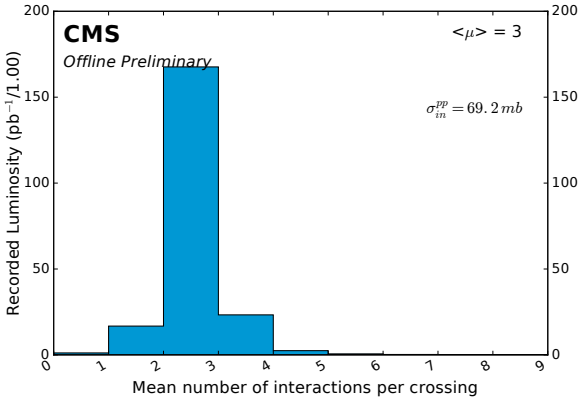

Figure 33 – Mean number of interactions per bunch crossing for the 2017 proton-proton run with low pileup conditions (Run2017H) at 13 TeV. The plot assumes a total inelastic proton-proton cross-section of 69.2 mb, which is determined by finding the best agreement with data, as recommended for CMS analyses.

For Run 3, a dedicated low-pileup run is planned for 2025 or 2026. As the representative of the ZCounting working group, I presented our requirements for this special run at CMS Physics Days in November 2024. The ZCounting team specifically requested that the same trigger used in the high-pileup run be maintained, that the beam optics conditions remain identical, that the pileup level be kept as low as possible, and that a Van der Meer (VdM) scan be performed immediately beforehand. These requirements aim to reduce systematic uncertainties in the measurement, particularly those arising from transferring the visible cross-section σ_{vis}^{Z} to the physics conditions and from potential trigger emulation. Discussions are currently ongoing regarding the amount of data to be collected. For the ZCounting method, a larger sample size is preferable, as statistical uncertainty dominates the measurement's precision.

A dedicated low-pileup run is essential for ZCounting because it allows for the precise determination of σ_{vis}, the one-time calibration constant for the method. Unlike conventional luminosity measurements that rely on frequent VdM scans, ZCounting depends on establishing this constant with high accuracy only once. The key reason to perform the calibration at low pileup is to minimize integration uncertainty, which increases with pileup. At low pileup, these effects are significantly reduced, making the resulting σ_{vis} more reliable. Once determined, this constant can be applied across the full data-taking period, assuming a stable center-of-mass energy, enabling consistent and precise luminosity monitoring without additional calibrations.

4.2.2 Simulated samples

The measurement provided by the ZCounting method is almost entirely independent of simulated events. The simulated Drell-Yan samples are employed solely for the signal

extraction, by generating the expected Z boson signal shape as it would be measured in the CMS detector, and for the determination of residual pileup-dependent corrections to efficiency measurements.

The simulated events are produced at LO in perturbative QCD and EW with `MadGraph 5` [155] event generator (PDF). Higher-order corrections are modeled with the parton shower using `Pythia` [156] with the CP5 tune. The effects of pileup are simulated with `Pythia` to study the dependency of these events. The detector simulation has been performed using the `GEANT4` [111] toolkit.

Simulated events with a generated Z boson decaying into a pair of muons are selected. To identify the signal signature, a matching condition between the reconstructed and generated muons from the Z boson decay is applied, defined by $\Delta R = \sqrt{\Delta\eta^2 + \Delta\phi^2} < 0.05$. For muons reconstructed only in the muon chamber without a corresponding signature in the inner silicon tracker, the spatial resolution is reduced. Consequently, a looser matching condition of $\Delta R < 0.6$ is applied for these cases.

4.3 Statistical model

The number of reconstructed Z bosons, along with the muon trigger, identification, and reconstruction efficiencies, is determined using maximum likelihood fits to account for background contributions. In each case, the data are binned according to the invariant mass of the dimuon candidates.

4.3.1 Signal Modeling

The signal component is modeled using a convolution of a Monte Carlo–derived invariant mass template with a Gaussian function (`MCxGauss`). This histogram template is derived from simulated Drell-Yan samples, following the same selection criteria as the $Z \to \mu\mu$ events in the data. To account for the residual discrepancies in the detector resolution between data and simulation, the MC and Gaussian convolution introduce an additional adjustable smearing. The width of this Gaussian is treated as a free parameter in the fit, allowing the overall resolution of the model to match the data precisely. Since no significant dependence on the number of primary vertices (N_{PV}) was observed, the same template can be applied throughout each data-taking period. To isolate signal-only contributions, muons are further required to be matched to generator-level muons. The signal model for various free parameters is shown in Figure 34.

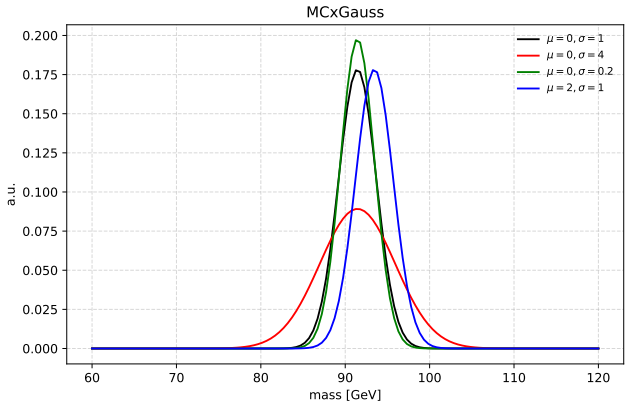

Figure 34 – The signal model (`MCxGauss`) for different free parameters as a function of the dimuon invariant mass, normalized to a unit area.

4.3.2 Background Modeling

The background contribution is modeled using the `CMSShape` function described by the Equation 4.6

$$\mathbf{CMS}_{\text{Shape}}(x; \alpha, \beta, \gamma) = (1 - \text{erf}(\alpha - x)\beta)\, e^{-(x - m_Z)\gamma} \tag{4.6}$$

where $m_Z = 91.188$ GeV is the mass of the Z boson [157].

The `CMSShape` is an empirical probability density function widely used in high-energy physics analyses to model invariant mass distributions near resonances such as the Z boson. The function combines an error function term, which introduces a smooth turn-on or asymmetry in the low-mass region, with an exponential term that governs the high-mass tail. The parameters α and β control the position and steepness of the error-function transition, respectively, while γ determines the exponential decay rate of the tail. By adjusting these parameters, the CMSShape can accurately reproduce the effects from detector resolution effects and final-state radiation, providing a flexible model for resonance fitting in CMS data analyses.

4.4 Extraction of the reconstructed Z bosons and the muon selection

4.4.1 Muon identification

The muon candidates are required to have $p_T > 27$ GeV and selected within the pseudorapidity range of $|\eta| < 2.4$. The selection of these parameters ensures the full coverage by the inner tracks and muon systems, guarantees that the muons are well-reconstructed and identified, and ensures they have a plateau-level trigger efficiency. For the maintenance of the T&P efficiency measurement, the application of symmetric cuts on

both muons is employed. Both muons are required to be reconstructed in the muon system with the presence of an outer track, denoted as a *standalone* muon, and with an inner track reconstructed in the silicon detector. For the outer track, it is required to have signals in at least two muon stations. The inner track must have at least one valid hit in the silicon pixel detector and hits in more than five strip tracker layers. With the additional quality criteria on the global muon track, a global muon candidate can be defined. At last, the muon candidate has to be successfully reconstructed with the PF algorithm [112].

4.4.2 Reconstructed Z boson and trigger efficiency extraction

For the reconstruction of the Z boson candidates, two muons of opposite electric charge with an invariant mass in the range $66 < m_{\mu\mu} < 116$ GeV are selected. It is required that at least one muon candidate is matched with a reconstructed muon at the trigger level, within $\Delta R < 0.1$, and that this muon was triggered by the single muon trigger. Moreover, an angular distance between the muons of $\Delta R > 0.8$ is required. Such requirements are to account for the possibility of the association of both muons with the same trigger-level object or the overlap between the two muon signals.

For the extraction of the reconstructed Z boson candidates (N^{Z}_{reco}) and the single muon HLT efficiency ($\epsilon^{\mu}_{\text{HLT}}$), both quantities are measured simultaneously with the consideration of events where only one or both muons, denoted by (N_1) and (N_2) respectively, fired the single muon trigger. The number of events in each one of the scenarios can be described by the following equations.

$$N_1 = 2 \cdot \epsilon^{\mu}_{\text{HLT}} \left(1 - C_{\text{HLT}} \cdot \epsilon^{\mu}_{\text{HLT}}\right) N^{Z}_{\text{reco}} + N^{\text{bkg}}_{1}, \tag{4.7}$$

$$N_2 = C_{\text{HLT}} \cdot \left(\epsilon^{\mu}_{\text{HLT}}\right)^2 \cdot N^{Z}_{\text{reco}} + N^{\text{bkg}}_{2} \tag{4.8}$$

where C_{HLT} corresponds to the correlation factor for the probability of the second muon passing the High-Level Trigger (HLT) if the first one has already passed it. The number of background events in both scenarios can be denoted by (N^{bkg}_{1}) and (N^{bkg}_{2}), respectively.

The simultaneous measurement of the reconstructed number of Z bosons (N^{Z}_{reco}) and the single muon HLT efficiency ($\epsilon^{\mu}_{\text{HLT}}$) is achieved by the simultaneous fit of the invariant masses of the muons' pair. The fits application can be divided into two scenarios. For the first scenario, only the Z boson candidates where only one of the muons passes the HLT selection are considered for the fit, with the number of Z boson candidates obtained by the Equation 4.7. For the second scenario, the fit is applied in the invariant mass of the Z boson candidates where both muons passed the HLT selection, and the Equation 4.8 provides the number of reconstructed Z bosons for this scenario. From the fits, the parameter C_{HLT} is a constant taken from the simulation, while the (N^{Z}_{reco}) and the ($\epsilon^{\mu}_{\text{HLT}}$)

are considered free parameters in the fit. In Figure 35, it is possible to observe the fit application in the invariant mass of the Z boson candidate, for the two mentioned scenarios. Such plots were the result of the efforts to publish a CMS Detector Performance Summary [158] for the establishment of the method for the early 2022 data.

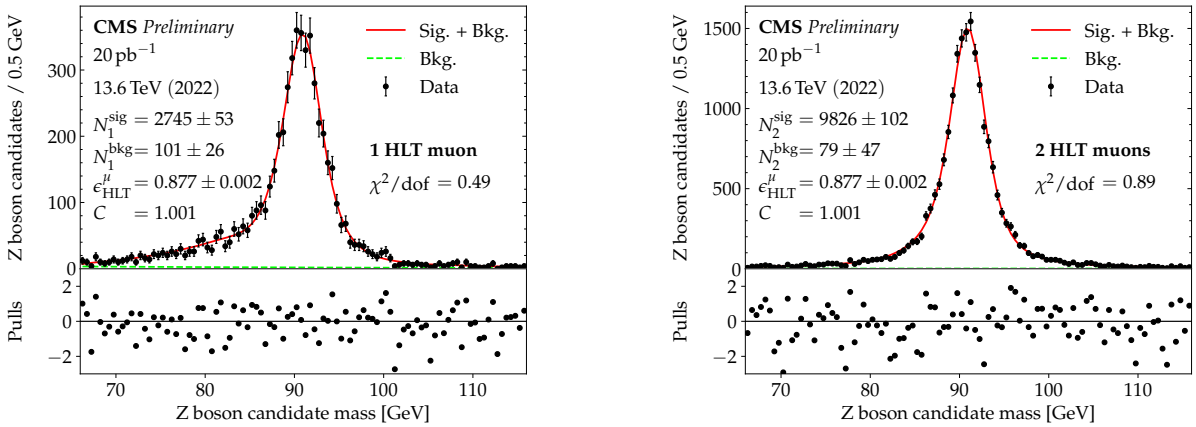

Figure 35 – The reconstructed invariant mass distributions of Z boson candidates for 20 pb^{-1} of data where one (left) or two (right) muons pass the single muon trigger selection. In the upper panel, the background distribution is shown by the green curve, while the full model distribution, represented by the red curve, corresponds to the fit that combines both the signal and background contributions. In the lower panel, the differences between the data and the fit model in each bin, divided by the statistical uncertainty are shown.

4.4.3 Muon correlation and the trigger selection

The correlation between the two HLT muons is described by the correlation factor C_{HLT}, as introduced in equations 4.7 and 4.8. This factor can also be obtained by the combination of the same equations, typically from an MC simulation of $Z \to \mu\mu$ events. The dependence of C_{HLT} on the pileup is relevant for this analysis, as it constitutes an important source of systematic uncertainty. Furthermore, for the upcoming HL-LHC where the pileup levels could reach $< \mu > \approx 200$, this correlation factor is expected to play a significant role in the Z boson counting method. This correlation has been investigated in simulation and could be understood to originate from the online isolation criteria, which are part of the trigger selection.

$$C_{\mathrm{HLT}} = \frac{4 \cdot N_Z^{\mathrm{reco}} \cdot N_2^{\mathrm{sig}}}{(N_1^{\mathrm{sig}} + 2 \cdot N_2^{\mathrm{sig}})^2} \tag{4.9}$$

where (N_1^{sig}) and (N_2^{sig}) are signal only events from N_1 and N_2. The pileup dependence of C_{HLT} can be observed in Figure 36.

The validation of the C_{HLT} correlation factor can be performed using data from events triggered independently of the muon trigger. Specifically, a $p_T^{\mathrm{miss}} > 120$ GeV trigger

is used, which excludes the muon contribution [159]. This method allows the selection of candidates where two muons pass the identification criteria, but neither fires the single muon trigger. Currently, this validation has been conducted for Run 2 data. A similar procedure for the ongoing Run 3 data has yet to be performed.

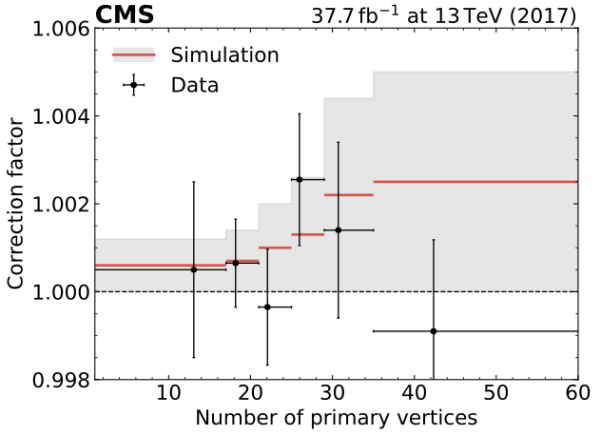

Figure 36 – Correlation factor C_{HLT} for the correlation between the two HLT muons as a function of the reconstructed number of primary vertices (N_{PV}). The red lines correspond to the simulation while the black points to the data. The data points were drawn at the mean value of N_{PV} in each bin of measurement. The gray band indicates an uncertainty of 100% in the correlation factor while the horizontal error bars correspond to the statistical uncertainties. [159]

4.5 The Z boson reconstruction efficiency measurement

The number of reconstructed Z bosons (N^{Z}_{reco}) is extracted from the fit and subsequently corrected by the Z reconstruction efficiency, denoted by ($\epsilon^{\mathrm{Z}}_{\mathrm{ID}}$). This $\epsilon^{\mathrm{Z}}_{\mathrm{ID}}$ is composed of the reconstruction and identification efficiencies of the individual muons ($\epsilon^{\mu}_{\mathrm{ID}}$), and their correlation. The muon identification criteria are specifically chosen to ensure that the two muons are completely uncorrelated. Simulated data, as observed in Figure 37, can be used to verify that there is no significant correlation between the two muons.

In that scenario, the reconstruction efficiency of the Z bosons is given by the reconstruction and identification efficiencies of the two muons. Then, the efficiency-corrected number of Z bosons is given by the following equation:

$$N_Z = \frac{N^{Z}_{\mathrm{reco}}}{\epsilon^{Z}_{\mathrm{ID}}} = \frac{N^{Z}_{\mathrm{reco}}}{(\epsilon^{\mu}_{\mathrm{ID}})^2} \tag{4.10}$$

The muon identification efficiency is then factorized in the following components

$$\epsilon^{\mu}_{\mathrm{ID}} = \epsilon^{\mu}_{\mathrm{ID|Glo}} \cdot \epsilon^{\mu}_{\mathrm{Glo|Sta}} \cdot \epsilon^{\mu}_{\mathrm{Sta|Trk}} \cdot c^{-1}_{\mathrm{I/O}} \tag{4.11}$$

The $\epsilon^{\mu}_{\mathrm{ID|Glo}}$ is the identification efficiency under the assumption that the muon is a global muon, including several quality criteria described in Section 4.5. The quantity $\epsilon^{\mu}_{\mathrm{Glo|Sta}}$ is the efficiency of a standalone muon to be reconstructed as a global muon, which incorporates the inner track reconstruction efficiency and its link to an outer track to compose a valid global track. The quantity $\epsilon^{\mu}_{\mathrm{Sta|Trk}}$ can be understood as the outer track efficiency, as it corresponds to the efficiency of reconstructing a standalone muon from all the muons that possess a valid inner track. A summary of the requirements for the different components of the muon efficiency is provided in Table 2.

When only the product of the individual muon efficiency components from Equation 4.11 is considered, the correlation between the inner and outer track efficiencies results in an overestimation of the overall muon reconstruction efficiency ($\epsilon^{\mu}_{\mathrm{ID}}$). To account for this effect, a correlation factor between the inner and outer tracks is applied as a correction ($c_{\mathrm{I/O}}$). The determination of this correlation factor is described in Section 4.5.2.

Requirement	**Trk**	**Sta**	**Glo**	**ID**	**HLT**
$p_T > 27\,\mathrm{GeV}$	✓	✓	✓	✓	✓
$\lvert\eta\rvert < 2.4$	✓	✓	✓	✓	✓
Has inner track	✓	—	✓	✓	✓
Muon seed veto	✓	—	—	—	–
Number of tracker layer hits > 5	✓	—	—	✓	✓
Number of pixel hits > 0	✓	—	—	✓	✓
Has outer track	—	✓	✓	✓	✓
Has global track	—	—	✓	✓	✓
Is PF muon	—	—	—	✓	✓
Global track $\chi^2/ndf < 10$	—	—	—	✓	✓
Global track hits > 0	—	—	—	✓	✓
Number of matched stations > 1	—	—	—	✓	✓
HLT object (`HLT_IsoMu27`)	—	—	—	—	✓

Table 2 – Requirements on the inner track (Trk), outer track (Sta), global muon (Glo), identified muon (ID), and trigger muon (HLT).

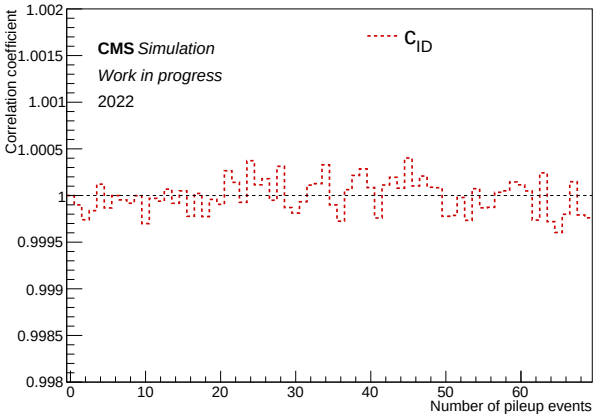

Figure 37 – The correlation factor C_{ID} between the two muons as a function of the N_{PU} for the 2022 data-taking period, with the usage of $Z \to \mu\mu$ simulated events.

4.5.1 The Tag and Probe method and measurements

The measurement of the reconstruction and identification efficiencies is performed using the *tag-and-probe* (T&P) method [131, 149]. For each event, the muons that satisfy the *tag* requirement, meaning they are identified muons that have passed the single muon trigger, are selected. After the selection of each *tag* muon, the muons that pass the *probe* requirements are chosen, and then a T&P pair is built. To be considered a valid pair, the muons should have opposite electric charges and an invariant mass of $66 < m_{\mu\mu} < 116$ GeV with a spatial separation of $\Delta R > 0.8$. The probe muons are further divided into two classes, where they can be considered as passing or failing probes. The muon efficiency is then given by the following equation:

$$\epsilon^{\mu} = \frac{n_p^{\mathrm{sig}}}{n_p^{\mathrm{sig}} + n_f^{\mathrm{sig}}} \tag{4.12}$$

where the correspondent background subtracted numbers for the passing and failing probes are defined by n_p^{sig} and n_f^{sig}, respectively.

For each event, multiple tag muons are allowed, while they can form multiple T&P pairs with the probe muons. This ensures that the T&P from the Z boson decay is among the selected pairs, given that the necessary track component is reconstructed. The track quality of the best available track is, on average, better for the passing probes compared to the failing ones. In most cases, the best track parameters are determined from the inner track. The failing probes often do not have an inner track, relying solely on the outer track, which has a worse resolution. For an unbiased measurement, the track parameters are taken from the outer track from both passing and failing probes.

In a similar procedure of the extraction of N_{reco}^{Z} and ϵ_{HLT}^{μ}, a maximum likelihood fit is performed in the $m_{\mu\mu}$ distribution simultaneously in the histograms for the passing

and failing probes, with the same shapes from signal and background, mentioned in the sections 4.3.1 and 4.3.2.

In Figure 38, examples fit for the measurement of the three components of the muon identification and reconstruction efficiency defined in the Equation 4.11 are presented. The poorer resolution of the outer track used in the determination of the component $\epsilon^{\mu}_{Glo|Sta}$ leads to a broader spectrum for the T&P pair mass, as can be observed in the upper plots. The employment of the inner track in the T&P measurement of $\epsilon^{\mu}_{Sta|Trk}$ leads to a more accurate determination of the muon momentum, as can be noticed in the middle and lower plots and their correspondingly narrow peak of the Z boson mass.

The extraction of the number of reconstructed Z bosons in each interval is performed using a binned maximum-likelihood fit to the invariant mass distributions of the Tag-and-Probe pairs. The fits are implemented with the `RooFit` framework, using the `MINUIT` minimization library to find the best-fit parameters by minimizing the negative log-likelihood.

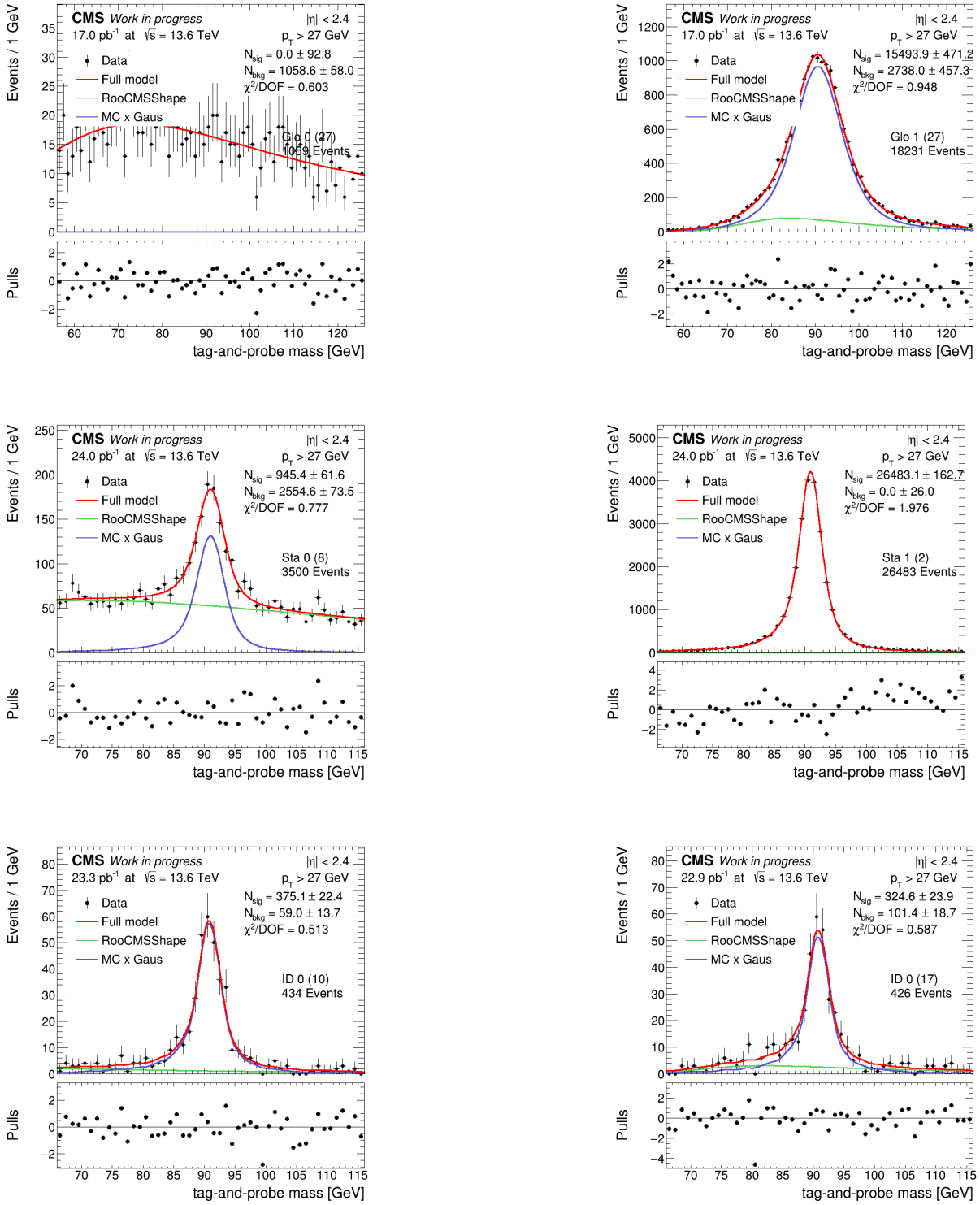

Figure 38 – Results of the fits to the invariant mass distributions used for the determination of $\epsilon^{\mu}_{\text{Glo|Sta}}$ (upper), $\epsilon^{\mu}_{\text{Sta|Trk}}$ (middle), and $\epsilon^{\mu}_{\text{ID|Glo}}$ (lower). The upper panels show the reconstructed invariant mass distributions of the Tag-and-Probe pairs for different data-taking intervals. The blue curve represents the signal component, modeled by a Monte Carlo–based template convolved with a Gaussian function (MC × Gauss), while the green curve shows the background contribution, modeled using the `CMSShape` function. The red curve corresponds to the total fit, combining signal and background components. The quantities N_{sig} and N_{bkg} correspond to the number of signal and background candidates for this given interval, respectively, where the error bars correspond to the statistical uncertainty. The lower panels display the pull distributions for each fit.

4.5.2 Correlation between the inner and outer tracks

The values for the correlation factor $C_{\mathrm{I/O}}$ can be observed in Figure 39. Such values are extracted from the ratio of the measured muon efficiencies relative to the true efficiency $\epsilon_{\mathrm{Glo}}^{\mu(\mathrm{true})}$ obtained in simulated $Z \to \mu\mu$ events.

$$C_{\mathrm{I/O}} = \frac{\epsilon_{\mathrm{Glo|Sta}}^{\mu} \cdot \epsilon_{\mathrm{Sta|Trk}}^{\mu}}{\epsilon_{\mathrm{Glo}}^{\mu(\mathrm{true})}} \tag{4.13}$$

The origin of this correlation has not yet been fully understood, but is expected to originate from the current treatment of the *muon-seeded* tracks. In the track reconstruction chain, the outer track is used as a seed for the fitting of the inner tracks, which serves to improve the quality of existing inner tracks or even to create new tracks that would not have been found without the muon seed. Ideally, the procedure would be to use the track collection before the update using the outer track information. However, such collections weren't available for the Run 2 dataset, and this limitation is propagated to Run 3, to avoid the computing resources required for this purpose.

The validation of data would be desirable to establish the correct description of the correlation by the simulation. Such validation could exploit the possibility of using $Z \to \mu\mu$ events where one muon is identified and selected by the single muon trigger while the second muon has neither a reconstructed outer nor an inner track for the determination of the correlation coefficient $C_{\mathrm{I/O}}$. Such a proposal should rely only on the information of the first muon and on the E_T^{miss} of the event, where the challenge arises from the background subtraction from the W boson production.

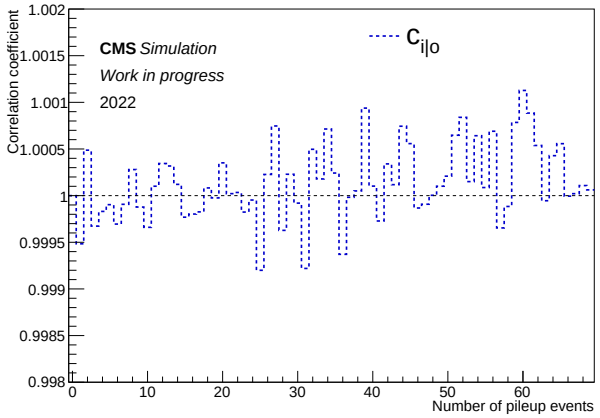

Figure 39 – The correlation factor $C_{\mathrm{I|O}}$ between the inner- and outer-track as a function of the N_{PU} for the 2022 data-taking period, with the usage of $Z \to \mu\mu$ simulated events.

4.6 Relative luminosity from Z boson rates

In sections 4.4 and 4.5, the strategy for extracting the Z boson rate and calibrating it through the muon efficiencies was presented. The measurement is performed almost completely independently from the simulation, relying only on small simulation-based corrections to achieve good closure in the validation tests. To account for potential variations in detector conditions, the number of reconstructed Z bosons is determined for each run within an LHC fill. Only runs containing at least 20 luminosity blocks are considered to ensure reliable fit results. For each run, the measurement is further performed in intervals of approximately 20 minutes, as defined by the reference luminosity detector. The size of intervals was chosen to obtain a statistical precision of 1% per interval, with the collection of about 10.000 reconstructed Z bosons. The luminosity blocks without reconstructed Z candidates are considered invalid and removed for a recorded luminosity greater than 0.02 pb^{-1}.

It is expected that the Z boson rate scales linearly with the instantaneous luminosity. To check for this linearity, the Z boson rate measured in short time intervals is compared to the instantaneous luminosity obtained by a dedicated or a combination of dedicated luminosity detectors, with the latest calibrations and corrections. The integral of the Z boson rates are normalized to the integral of the reference luminosity.

4.6.1 Online x Offline

The luminosity mask, or lumimask, serves as a filtering tool to define luminosity sections that meet specific criteria for a particular analysis. The *Golden* lumimask is the most widely adopted for physics analyses. It includes luminosity sections where the CMS detector was fully operational, with all detector systems functioning properly and meeting data quality standards. This ensures the integrity of the data for precision measurements and discovery analyses.

In the context of the CMS Experiment, the data is recorded in units of *luminosity sections* (LS), which are short time intervals (typically 23 seconds) during which beam conditions and detector status are considered stable. Each LS is identified by a Run Number and Luminosity Section Number.

The Detector Control System Only (`DCSOnly`) lumimask includes luminosity sections where the CMS detector was powered and operating with stable conditions. While it offers broader data coverage than the Golden lumimask, it is produced with reduced data quality since it does not require the same strict quality criteria. The `DCSOnly` lumimask is well-suited for integrated luminosity calculations as it maximizes data availability. Additionally, the `DCSOnly` can be updated daily, while the Golden lumimask typically experiences some delay before being finalized.

In Figure 40, the shapes of the two independent measurements — the luminosity derived from Z boson rates and that from conventional luminosity detectors — show very good agreement. However, some minor discrepancies are observed at the beginning of the fill, which are most noticeable when compared to the *Golden* counterpart.

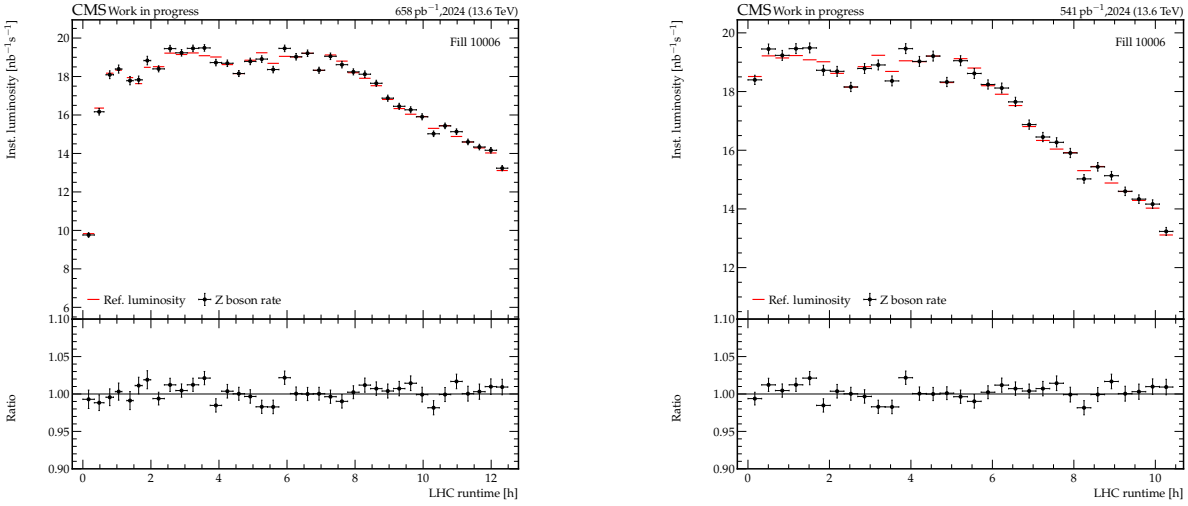

Figure 40 – In the upper plots, the efficiency-corrected Z boson rate, compared to the reference luminosity as a function of the LHC fill time for the fill 10006 of the 2024 Run 3 data taking. The total luminosity of this fill depends on the luminosity sections considered by the lumi masks employed. For the *Golden* (left), which have the best data quality, the luminosity is 658 pb^{-1}, while for the `DCSOnly` (right) is 541 pb^{-1}. The total luminosity of the fill is divided in of about 20 minutes of data. For allow the shape comparison, the Z boson rate is normalized to the reference integrated luminosity. The lower panels show the ratio of the two measurements.

4.6.2 Offline comparison, different luminosity detectors

In the Figure 41, the instantaneous luminosities are shown as a function of the LHC fill time for the fill 10006 of the LHC 2024 Run 3 data-taking, for different luminosity detectors. Meanwhile, for the Figure 42, the instantaneous luminosity is presented as a function of the pileup.

The instantaneous luminosity in the Fill 10006 decreased from the initial 18 $nb^{-1}s^{-1}$, corresponding to a pileup level of about 60, to about 14 $nb^{-1}s^{-1}$, corresponding to a pileup level of approximately 40. However, for the integrated luminosity, it is important to notice that the values could be different due to the usage of different luminosity detectors.

In the CMS Experiment, different luminosity detectors can report slightly varying integrated luminosity values, even when observing data from the same LHC fill. These discrepancies arise from a combination of factors related to detector design, calibration, and operational conditions. Each luminosity detector employs distinct measurement techniques, such as the Pixel Drift Tubes (DT), the Fast Beam Conditions Monitor (BCM1F), and the Forward Hadronic Calorimeter (HF), each of which has unique sensitivities, acceptance ranges, and systematic uncertainties.

It is observed that the shapes of the two independent measurements, the luminosity from the Z boson rates and from the conventional luminosity detectors, shows a very good agreement. The instantaneous reference luminosities for the combination of the best measurements, as well as for the HFET, DT, and BCM1FμTCA, were provided using their respective normtags.

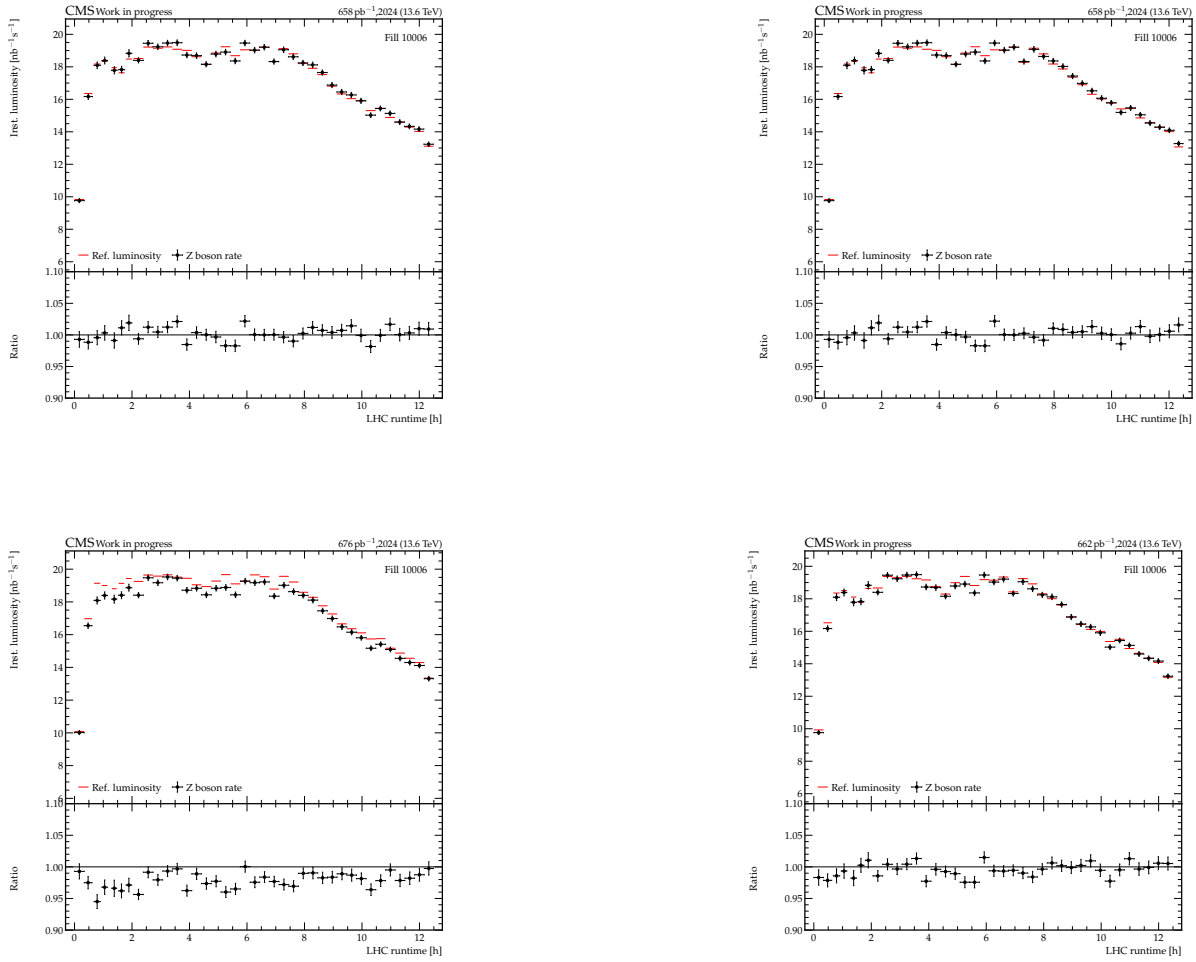

Figure 41 – In the upper plots, the efficiency-corrected Z boson rate, compared to the reference luminosity as a function of the LHC fill time for the fill 10006 of the 2024 Run 3 data taking. The total luminosity of this fill depends on the luminosity detector employed. For BRIL (upper left), which is the combination of the best measurements, the luminosity is 658 pb^{-1}, while for the HFET (upper right) is also 658 pb^{-1}, DT (lower left) is 676 pb^{-1} and for BCM1FμTCA (lower right) is 662 pb^{-1}. The total luminosity of the fill is divided in of about 20 minutes of data. For allow the shape comparison, the Z boson rate is normalized to the reference integrated luminosity. The lower panels show the ratio of the two measurements.

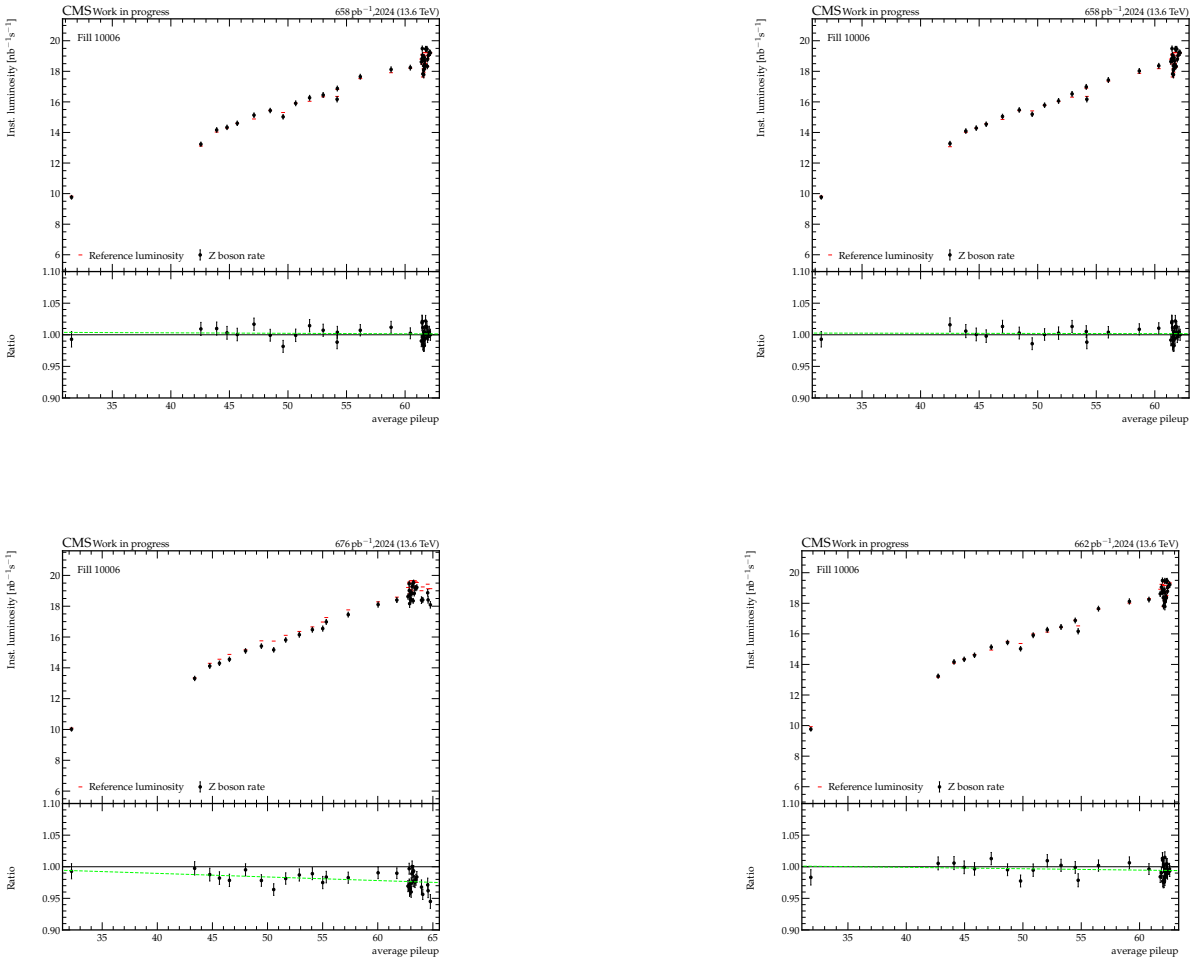

Figure 42 – In the upper plots, the efficiency-corrected Z boson rate, compared to the reference luminosity as a function of the pileup for the fill 10006 of the 2024 Run 3 data taking. The total luminosity of this fill depends on the luminosity detector employed. For BRIL (upper left), which is the combination of the best measurements, the luminosity is 658 pb^{-1}, while for the HFET (upper right) is also 658 pb^{-1}, DT (lower left) is 676 pb^{-1} and for BCM1FμTCA (lower right) is 662 pb^{-1}. The total luminosity of the fill is divided in of about 20 minutes of data. For allow the shape comparison, the Z boson rate is normalized to the reference integrated luminosity. The lower panels show the ratio of the two measurements.

4.6.3 Single Muon trigger efficiencies

The single muon trigger efficiencies employed for the Z boson rate calibration during the same fill are presented in Figure 43. For the HLT muon efficiency, a significant dependence on time, and thus on pileup, can be observed.

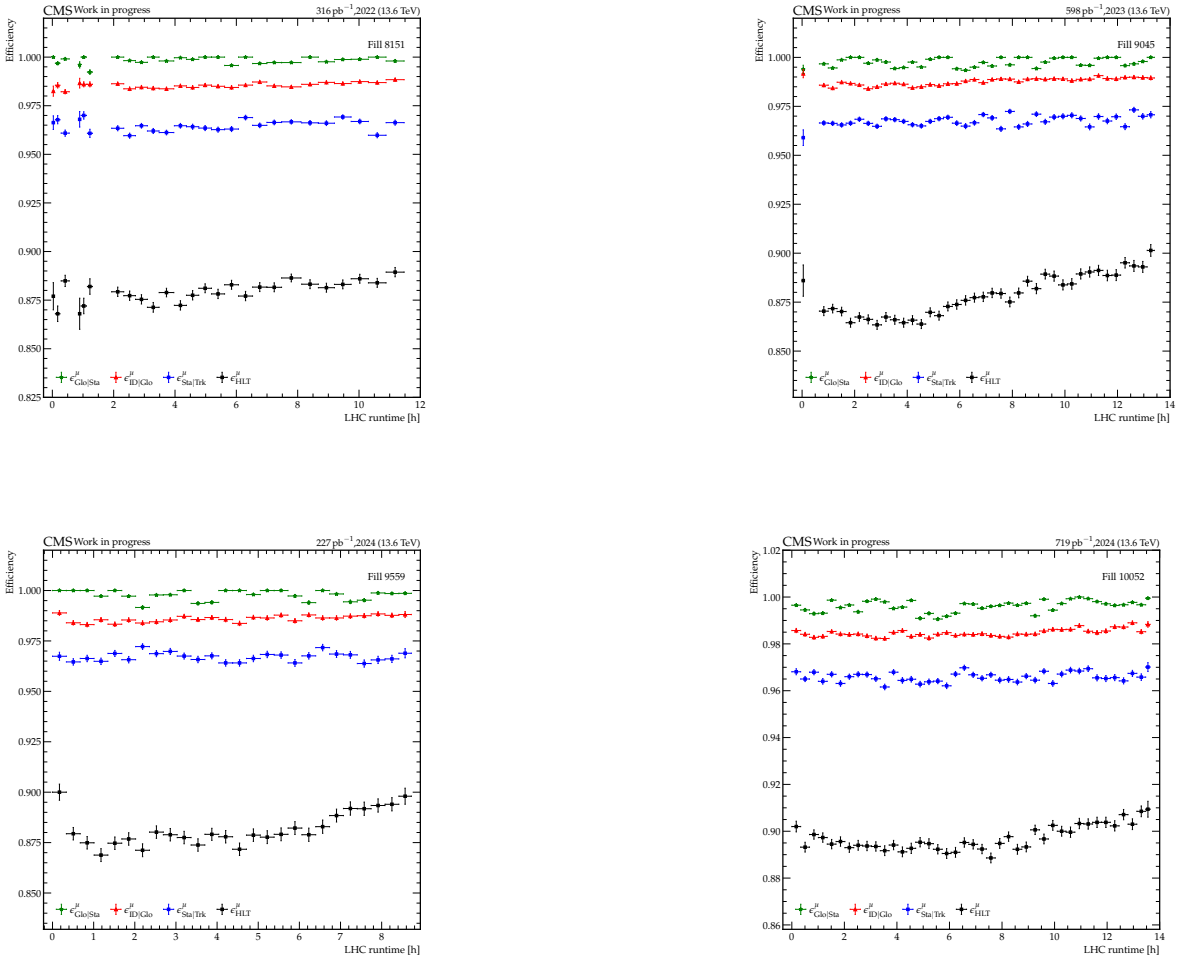

Figure 43 – The single-muon efficiencies obtained from the Z boson rate calibration are shown as a function of the LHC fill time for fills 8151 (upper left), 9045 (upper right), 9559 (lower left), and 10052 (lower right). The efficiencies correspond to $\epsilon^{\mu}_{\mathrm{Glo|Sta}}$ (green), $\epsilon^{\mu}_{\mathrm{ID|Glo}}$ (red), $\epsilon^{\mu}_{\mathrm{Sta|Trk}}$ (blue), and the single muon trigger efficiency $\epsilon^{\mu}_{\mathrm{HLT}}$ (black).

4.6.4 Linearity for the early 2022 data

The combination of all the Z boson measurements across the whole data-taking period allows the production of more statistically significant results. The fiducial cross section, defined as $\sigma^{Z}_{fid} = N^{Z}/\mathcal{L}^{Ref.}$, is calculated in fine bins of the instantaneous luminosity measured by a reference luminosity detector. This procedure is a vital systematic check to test the stability of the Z boson counting method and to confirm the linearity of the luminosity determination under varying pileup conditions. As demonstrated in Figure 44, excellent linearity is observed for the early 2022 data-taking period, validating the robustness of the Z boson selection against the high-pileup environment.

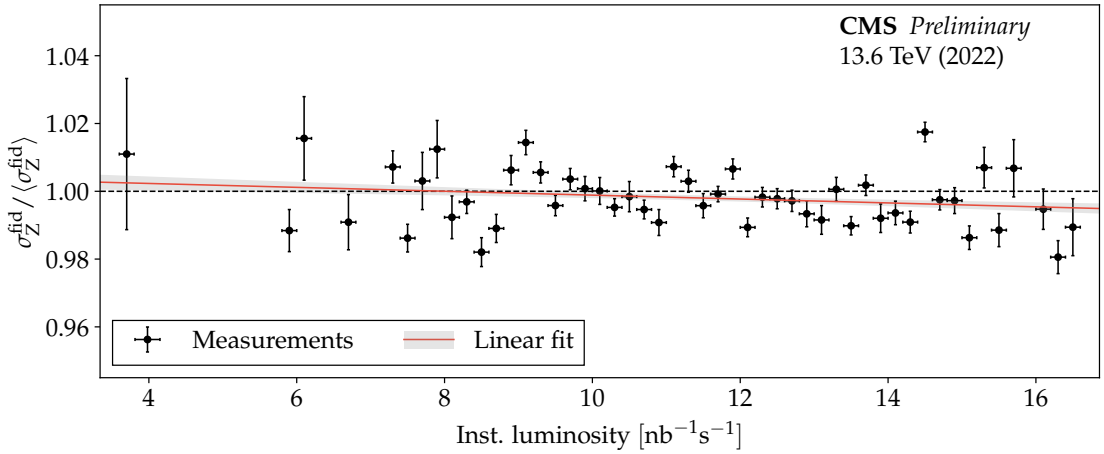

Figure 44 – The fiducial Z boson cross section, defined as the efficiency-corrected number of reconstructed Z bosons divided by the luminosity, as a function of the instantaneous recorded luminosity, normalized to the average measured cross section $\langle \sigma_Z^{fid} \rangle$ over the period. This plot tests the Z boson counting linearity against pileup effects. In each data point (black), there are multiple measurements of the delivered Z rates, which are combined. The error bars correspond to the statistical uncertainties of the Z rates. The inclusion of a linear fit (red) confirms the expected flat behavior, indicating that the Z boson efficiency corrections are robust against variations in the instantaneous luminosity. The results were obtained for the early 2022 data collected at $\sqrt{s} = 13.6$ TeV [158].

4.7 Absolute luminosity from Z boson rates

From Equation 4.5, the integrated luminosity in physics conditions, or high pileup (highPU), which is referred to as *Z luminosity*, is determined from the integrated luminosity of the low pileup (lowPU) data. The ratio between the luminosity obtained from the Z boson counting method and the reference luminosity measured with the conventional method can then be observed.

In the Figure 45, a comparison between the `DCSOnly` and *Golden* lumimasks is presented for the years 2023 and 2024, showing the ratio between the luminosity obtained from the Z boson counting method and the measured reference luminosity. For both years, two main contributions can be observed in the histograms from `DCSOnly`, lowering the mean value and increasing the width of the distribution. This behavior can be further evaluated with the exploration of the stability of the measurements as a function of the integrated luminosity.

Each entry in the histogram corresponds to an interval of typically 20 minutes of data recorded under physics conditions during Run 3. The width of the distributions is mainly caused by statistical fluctuations in the determination of the Z boson rates and muon efficiencies. Since the histogram distribution represents the ratio between the Z boson luminosity and the reference luminosity, a deviation from unity could indicate an inaccurate measurement of the Z boson luminosity or the reference luminosity.

4.7.1 Online x Offline

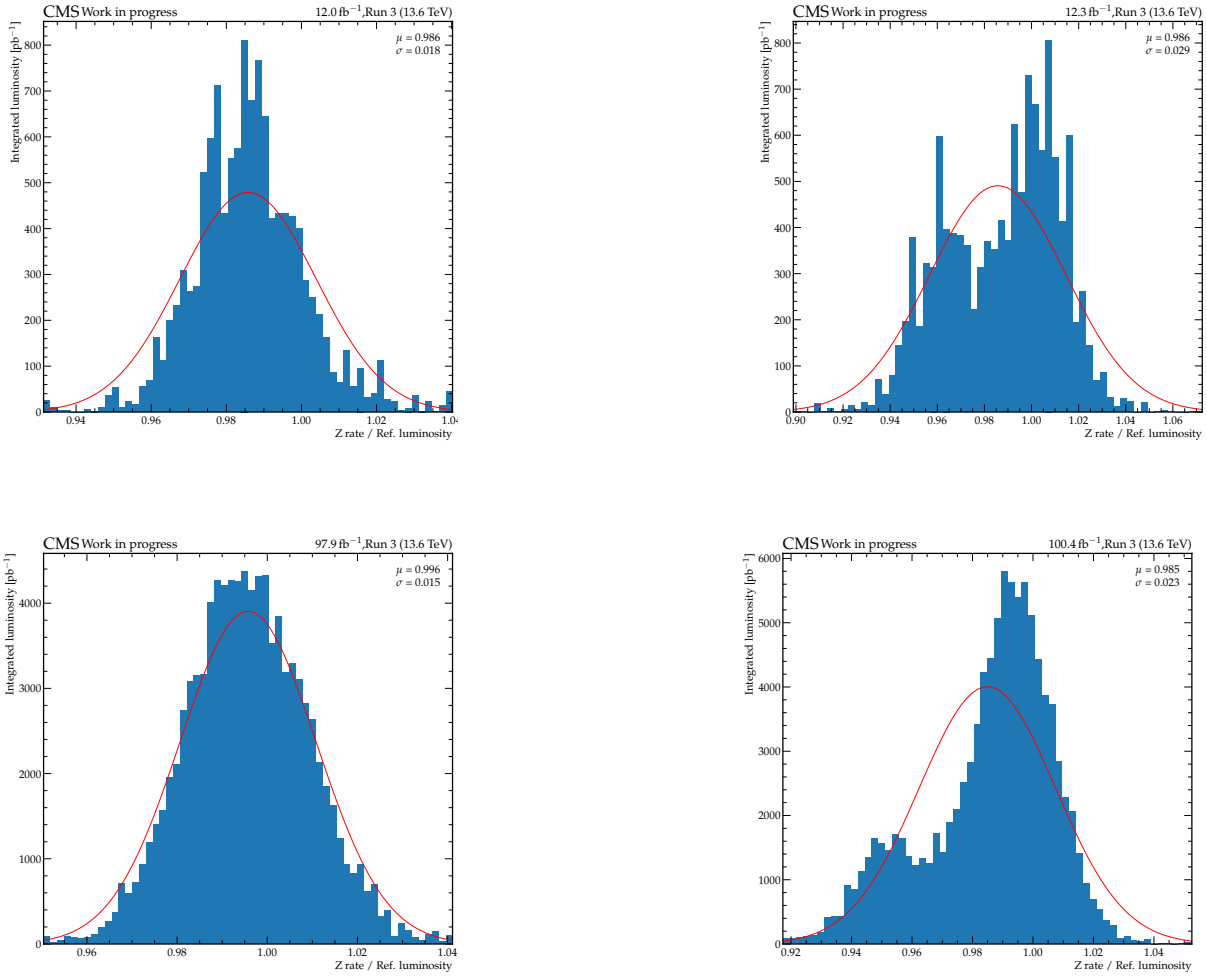

Figure 45 – Histograms for the *Golden* 2023 (upper left), `DCSOnly` 2023 (upper right), *Golden* 2024 (lower left) and `DCSOnly` 2024 (lower right). For the histograms, each entry corresponds the measurement of the luminosity from the Z bosons in intervals of about 20 min of data. The obtained rate is then divided by the integrated reference luminosity from a dedicated luminosity detector for the same interval. The first and last bins include the underflow and overflow contributions.

4.7.2 Offline comparisons, different normtags

In Figure 46, the ratio of the Z luminosity and the reference luminosity for the different luminosity detectors is presented. Since different luminosity detectors can provide different integrated luminosities for the same fill, the ratio is affected, as can be observed in the mentioned plots.

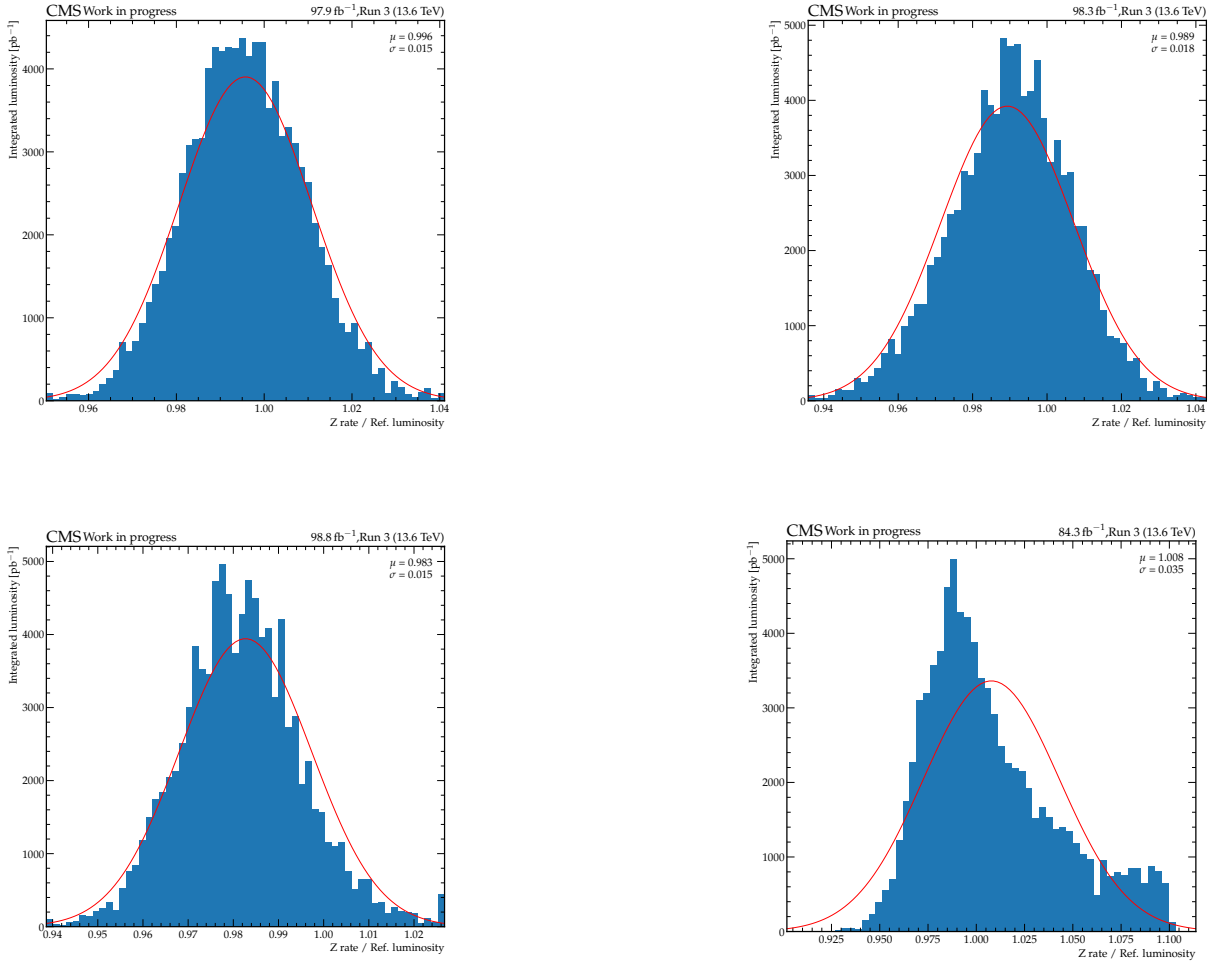

Figure 46 – In the histograms, the ratio of the luminosity measured from Z bosons to the reference luminosity is shown for BRIL (upper left), hfet (upper right), dt (lower left) and BCM1FμTCA (lower right) for the year 2024 of the Run 3 data-taking. The histogram is fitted with a Gaussian distribution, shown in red. For the histograms, each entry corresponds the measurement of the luminosity from the Z bosons in intervals of about 20 min of data. The obtained Z rate is then divided by the integrated reference luminosity from a dedicated luminosity detector for the same interval. The first and last bins include the underflow and overflow contributions.

4.8 Stability of the Z luminosity measurement

For the investigation of the stability of the Z luminosity over time, the ratio between the luminosities obtained by the Z boson counting method and the reference luminosity is presented as a function of the accumulated integrated luminosity in Figure 47 for the year 2023 and Figure 48 for 2024.

The offline data generally offers higher quality and is more commonly used in physics analyses. However, data from the online `DCSOnly` lumimask can provide larger integrated luminosity and serve as a valuable tool for identifying potential differences in detector performance or calibration. These studies can involve searching for significant deviations or steps in stability distributions, as illustrated in Figures 47 and 48. Further refinement of these analyses could be achieved by evaluating the same stability distributions as a function of the LHC fill number or even the run number, enabling a more detailed temporal understanding of detector behavior.

4.8.1 Online x Offline

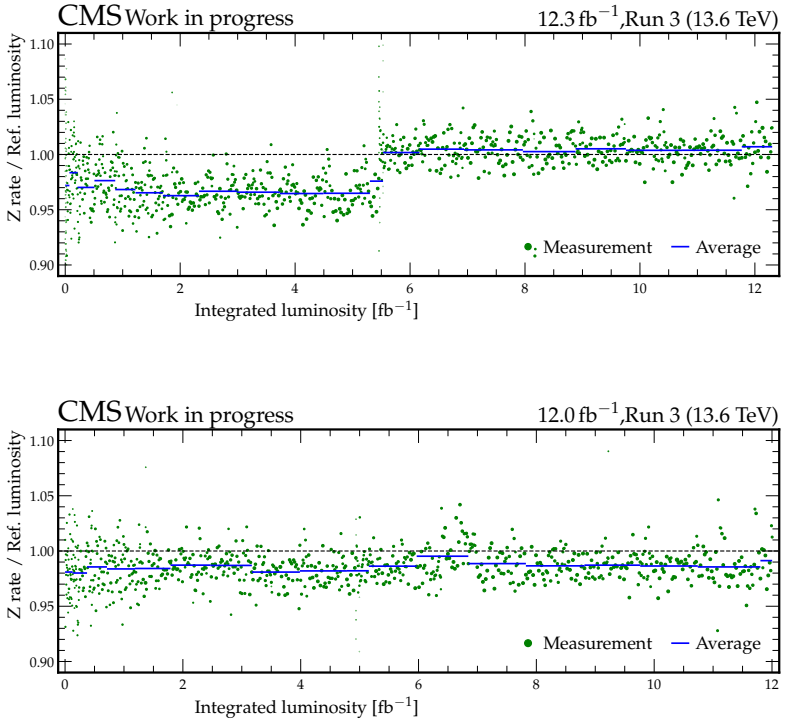

Figure 47 – Ratio of the luminosity measured using Z boson yields to the reference luminosity as a function of the integrated luminosity for the `DCSOnly` (upper plot) and *Golden* (lower plot) data-quality selections (lumimasks) during 2023 data-taking. Each point represent the Z luminosity values measured in an interval of typically 20 minutes of data, while the size of the point reflects the reference luminosity contained in each measurement.

Ratio of the luminosity measured using Z boson yields to the reference luminosity as a function of the integrated luminosity for the `DCSOnly` (upper) and *Golden* (lower) data-quality selections (lumimasks) during 2023 data-taking.

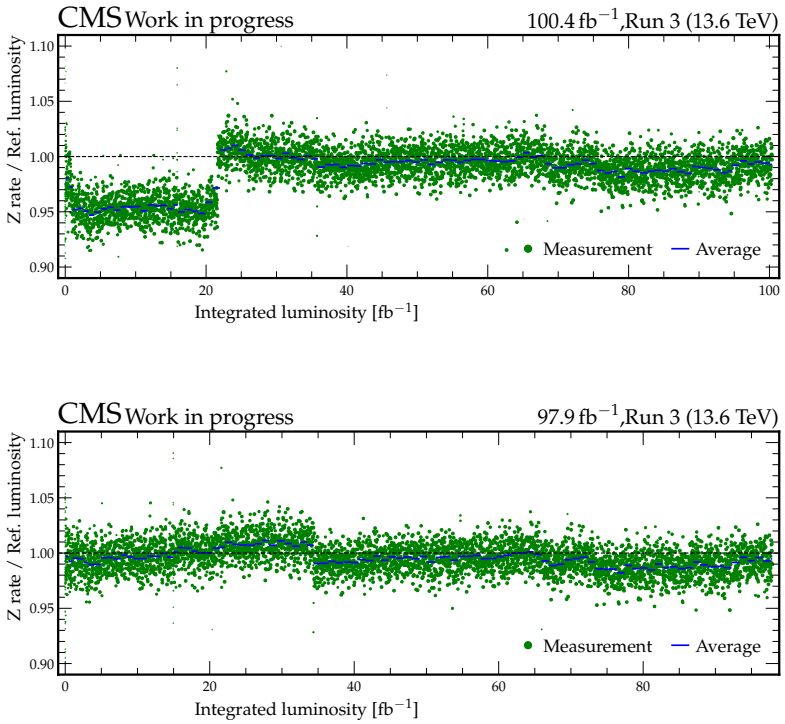

Figure 48 – Ratio of the luminosity measured using Z boson yields to the reference luminosity as a function of the integrated luminosity for the `DCSOnly` (upper plot) and *Golden* (lower plot) data-quality selections (lumimasks) during 2024 data-taking. Each point represent the Z luminosity values measured in an interval of typically 20 minutes of data, while the size of the point reflects the reference luminosity contained in each measurement.

4.8.2 Offline comparison, different luminosity detectors

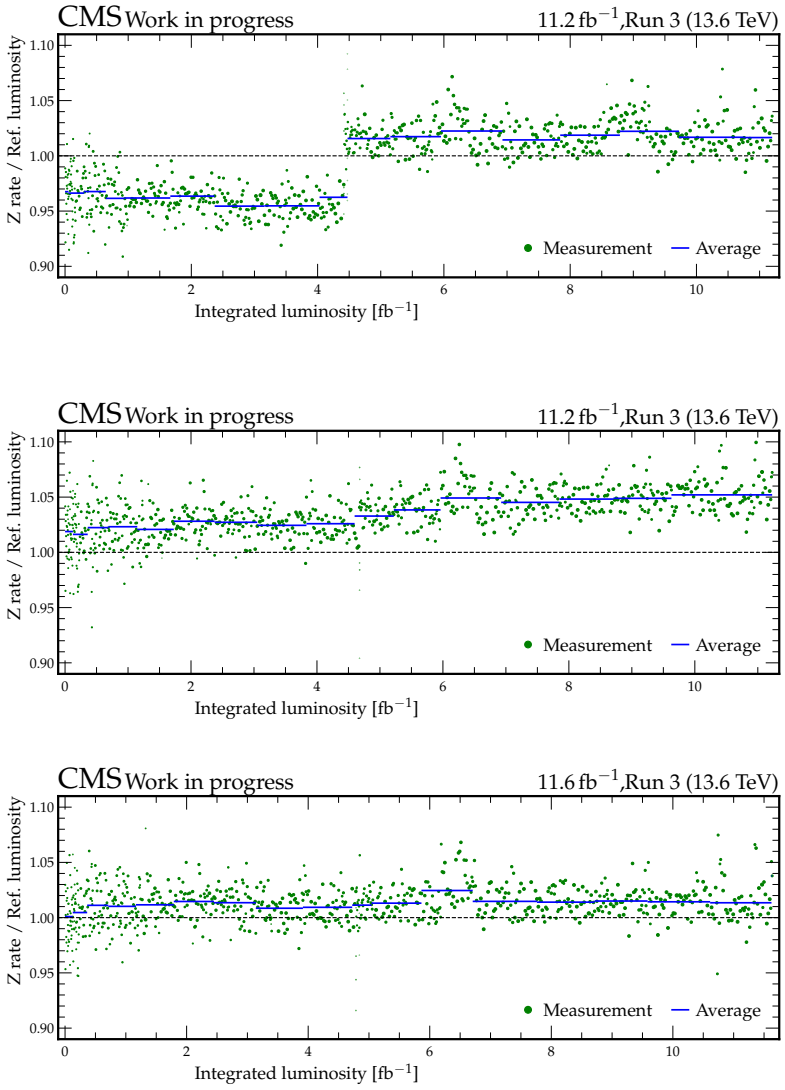

Figure 49 – The ratio between the luminosity measured from the Z bosons and the reference as a function of the integrated luminosity for HFET (upper), BCM1FμTCA (middle) and DT (lower) for the year 2023. Each point represent the Z luminosity values measured in an interval of typically 20 minutes of data, while the size of the point reflects the reference luminosity contained in each measurement.

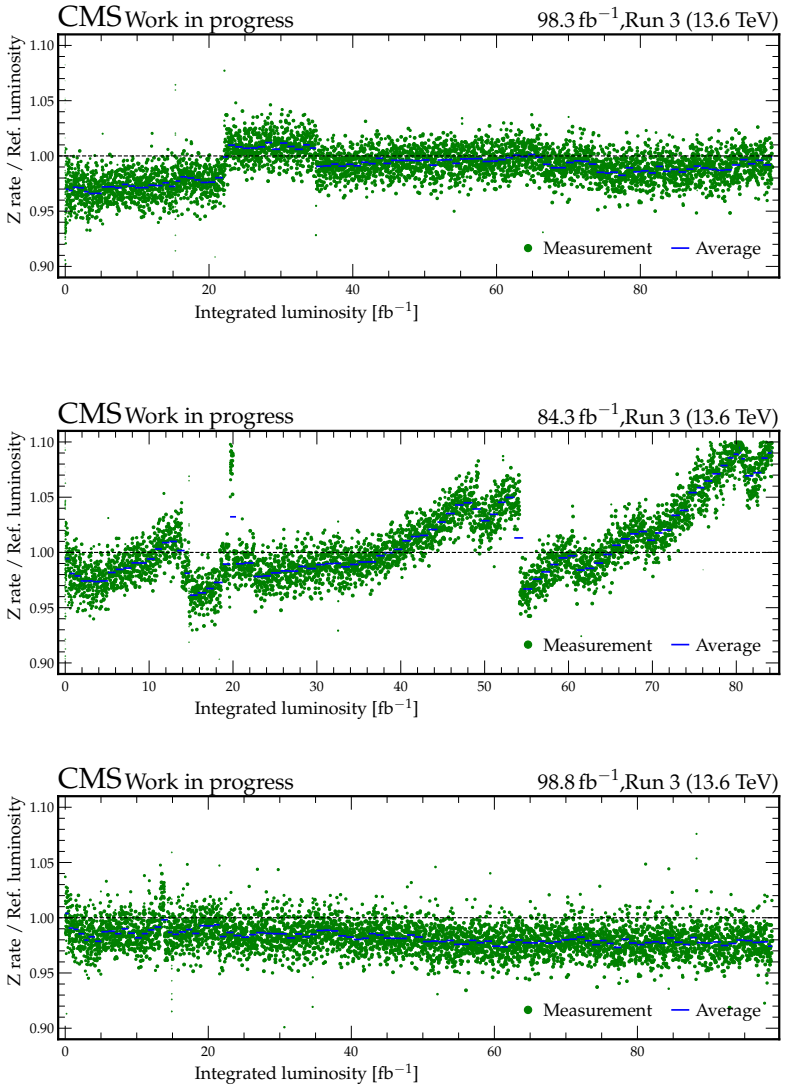

Figure 50 – The ratio between the luminosity measured from the Z bosons and the reference as a function of the integrated luminosity for HFET (upper), BCM1FμTCA (middle) and DT (lower) for the year 2024. Each point represent the Z luminosity values measured in an interval of typically 20 minutes of data, while the size of the point reflects the reference luminosity contained in each measurement.

4.9 Study of systematic Uncertainties

The uncertainties of the Z boson counting method analysis are focused on the called transfer factor r, defined by the Equation 4.14. This transfer factor serves as a proportionality constant between the luminosity at low pileup conditions and that under physics conditions. The list of systematic uncertainties will be obtained for each year of data-taking, with particular consideration for the dedicated low-pileup data, which is currently planned to take place in 2025 or 2026 during the Run 3 data-taking period.

$$r = \frac{N^{Z}_{\text{highPU}}}{N^{Z}_{\text{lowPU}}} \tag{4.14}$$

The statistical uncertainty component is driven by the number of available Z bosons. It should affect the determination of the number of Z bosons, their rates, and the muon efficiencies. The statistical component plays a significant role in the low pileup data set with typically less than 1 fb^{-1}, while for the full high pileup data sets, it can be considered negligible. For comparison, for the Run 2 data set, mentioned in Section 4.2.1.1, held at 2017RunH, the dataset contains about 200 pb^{-1}, which led to a contribution of about 0.35% of systematic uncertainty.

From Run 2 studies, several key sources of systematic uncertainty have been identified. One of the main contributions comes from the uncertainty in the C_{HLT} correlation factor, which accounts for the relationship between the trigger efficiencies of the two muons. This factor is essential for accurately modeling the trigger response in events with multiple muons.

Another significant source of uncertainty arises from the measurements of the inner and outer muon tracks. The limited resolution of the reconstructed tracks can introduce biases in the measurement. For the inner track, the bias is expected to be small but dependent on pileup conditions. In contrast, the outer track, which has poorer resolution, can introduce a larger bias that is not pileup-dependent.

Additionally, the modeling of the signal plays a role in the overall systematic uncertainty. An improved description of the signal is currently under study and could allow the method to reach its full precision potential. Previous analyses, such as the measurements of the Z boson differential cross-section [152] and the Drell-Yan process [160], have shown that this uncertainty can be reduced to a sub-dominant level with better modeling, suggesting that further refinement in this area could significantly benefit the analysis.

5 Magnetic monopoles simulation

In this chapter, a detailed description of the simulation of monopole production and monopole interaction with the CMS detector is provided. The discussion will begin with an examination of the theoretical framework for monopole production, including the various proposed models and their associated properties. The chapter will then explore the different production mechanisms relevant to high-energy colliders, such as Drell-Yan and photon-fusion, presenting their respective kinematic distributions of monopoles across various mass points.

Finally, the chapter will elaborate on the distinct signature of magnetic monopoles within the CMS detector, as predicted by simulation. This encompasses their unique interaction characteristics with the detector's sub-systems, including the tracker and calorimeters, taking into consideration the strong magnetic field of CMS and the exceptionally high ionization expected from monopoles.

5.1 Monopole Production

At the LHC, the CMS detector is employed to investigate new physics models. Among the particles predicted by these models, *Long-lived particles* (LLP), are of particular interest, given their diverse possible origins. The lifetimes of LLPs are hypothesized to be long enough to pass through the detector before their decay. In this context, the monopoles are interpreted as LLPs and considered to be stopped in the ECAL.

Given the large coupling derived from Dirac quantization, there is no field theory prediction for the monopole pair production. This absence necessitates the selection of benchmark processes, such as the Drell-Yan (DY) and photon fusion (PF), as the primary production mechanisms. The typical DY process involves a quark-antiquark annihilation into a virtual photon as the propagator, resulting in the production of a lepton and anti-lepton pair in the final state. In contrast, the photon fusion (PF) mechanism involves the interaction of two initial-state photons, typically radiated from the electromagnetic fields of the incoming protons, which fuse to form a highly energetic intermediate state capable of producing a monopole-antimonopole pair. Unlike the Drell–Yan process, which proceeds via a quark-antiquark annihilation into a virtual photon, the photon fusion process is mediated by real or quasi-real photons, which are sensitive to the magnetic charge and spin of the monopoles due to their strong coupling to photons. These benchmark processes were chosen because they have been used in previous searches and align with the new duality transformation from Dirac monopoles.

It is therefore reasonable to assume that a proper field theory treatment for monopole pair production, with the duality transformation applied, would reproduce the electron production in the Drell-Yan and Photon Fusion processes. The Feynman diagrams for the monopole production processes with generic spin are presented in Figure 51.

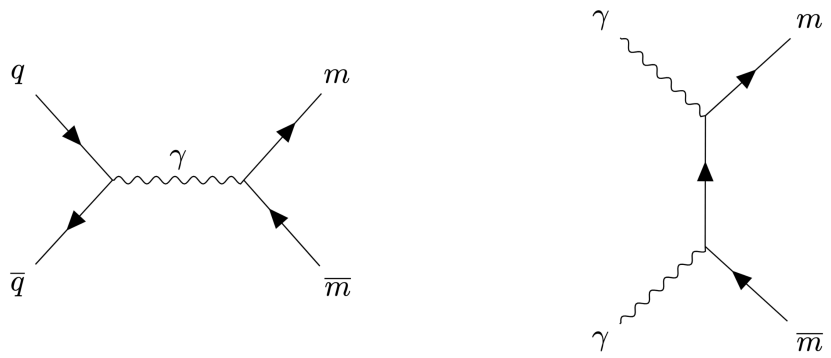

Figure 51 – Feynman diagrams for Drell-Yan (left) and Photon Fusion (right) pair-produced monopoles denoted with m.

The magnetic monopoles were simulated across a mass range of 1000 to 4500 GeV, in 500 GeV intervals, with an electric charge of 68.5e. This selection populates a wide range of the phase space while minimizing model-dependent assumptions. For each mass point, 100,000 Monte Carlo (MC) events were simulated for all specified processes during the 2017 and 2018 MC campaigns, with 50,000 events generated for the 2016 and 2016APV MC campaigns. It is worth noting that the model is β-independent, which means the production cross-section of the monopoles does not depend on the velocity β. In Table 5.1, all the parameters and the PDF model employed in the simulation can be found.

Magnetic monopole production models were generated, and their corresponding production cross-sections were obtained using `MadGraph5_aMC@NLO2.9.6`. Subsequently, `PYTHIA` was employed for the parton showering and hadronization processes. For the parton distribution functions, the `NNPDF2.3LO` [161] was used for Drell-Yan production, while LUXQED [162] was utilized for Photon Fusion production.

The interaction of the generated particles within the CMS detector is simulated with `GEANT4` [111]. The software for simulating Magnetic Monopoles in `GEANT4` was initially developed as additional code [163], but it is now fully integrated in `GEANT4` software [164, 165]. The Monopole energy loss in matter is treated according to the full model developed by S.P. Ahlen, including higher-order corrections such as density and Bloch corrections [166, 167]. The δ-ray particles are explicitly generated above a configurable energy threshold, which is varied as a systematic uncertainty. Furthermore, the acceleration of the monopoles in a magnetic field is implemented by providing a new equation of motion, which depends on the local magnetic field and electric field, to the `GEANT4` numerical integration algorithm.

Property	Parameter
Process	Drell-Yan and Photon Fusion
Spin	0, 1/2
Charge	1 g_D (Dirac monopole)
$\sqrt{s}$	13 TeV
Mass points (TeV)	1, 1.5, 2, 2.5, 3, 3.5, 4, 4.5
particle ID (PID)	$\pm$ 4110000
PDF model	NNLOPDF

Table 3 – Summary of key parameters used in the magnetic monopole signal MC simulations. The table lists the production mechanisms (Drell–Yan and Photon Fusion), spin hypotheses (0 and 1/2), monopole charge (Dirac charge, 1 g_D), center-of-mass energy ($\sqrt{s} = 13$ TeV), simulated mass points, the ID defined by the *Particle Data Group*, and the parton distribution function (PDF) model used (NNLOPDF).

In Figure 52, the kinematic distributions for spin 1/2 monopoles produced through the Drell-Yan production mechanism are shown. The distribution in pseudorapidity (η) indicates that most of the monopoles are produced within the coverage of the ECAL, for $|\eta| < 3$, with most occurring in the ECAL barrel, for $|\eta| < 1.48$. For the figures on the top, the distribution of the transverse momentum of the monopoles increases as a function of the mass, since the momentum in the z-component is sufficiently great. It is expected that heavier monopoles travel slowly, even at non-relativistic speed, which can lead to possible bias in the cluster reconstruction that will be discussed in a dedicated session.

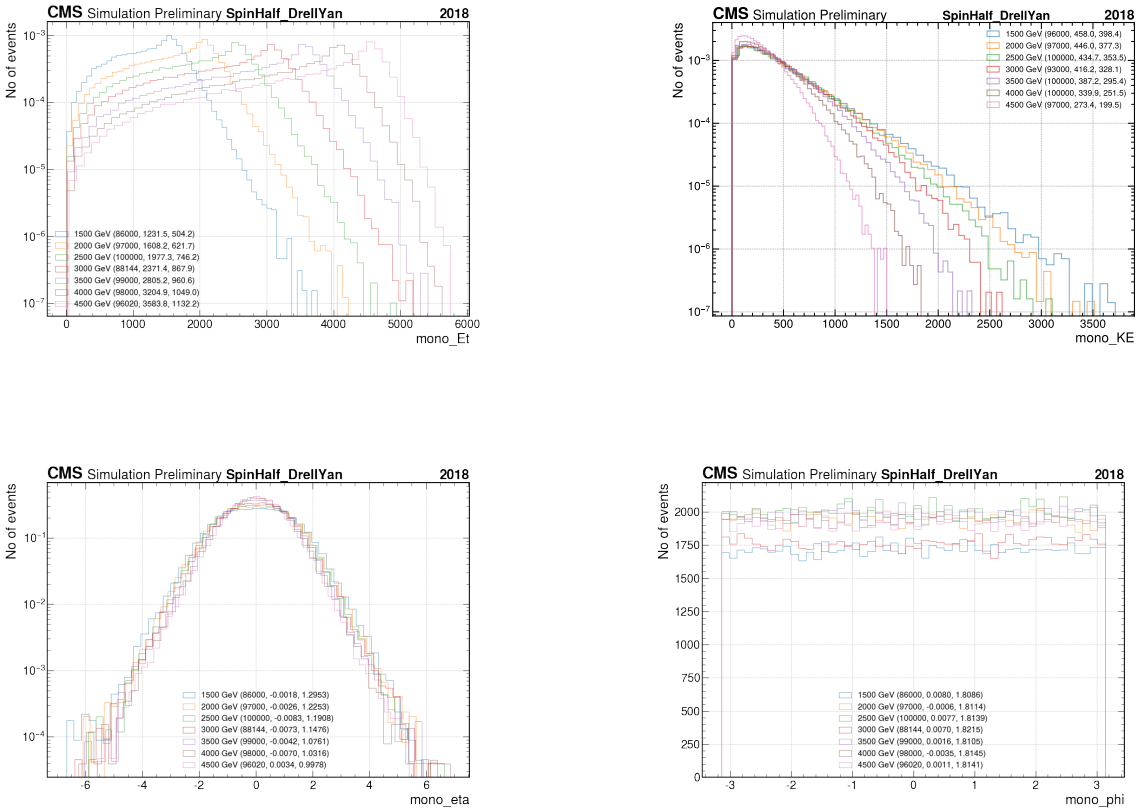

Figure 52 – Transverse Energy (E_T) (upper left), transverse momentum (p_T) (upper right), pseudorapidity (η) (lower left) and ϕ (lower right) for generated Spin-1/2 monopoles from the Drell-Yan production process.

The samples generated for photon fusion and Drell-Yan processes, across both spin states, can be found in the following tables: Table 4 corresponds to the 2018 MC campaign, Table 5 to the 2017 MC campaign, while tables 6 and 7 corresponds to the 2016APV and 2016 MC campaigns, respectively.

Spin	**Process**	**Dataset**
1/2	Photon Fusion	/Monopole_SpinHalf_PhotonFusion_M-MASS_TuneCP5_13TeV_madgraph-pythia8/RunIISummer20UL18RECO/.../GEN-SIM-RECO
0	Photon Fusion	/Monopole_SpinZero_PhotonFusion_M-MASS_TuneCP5_13TeV_madgraph-pythia8/RunIISummer20UL18RECO/.../GEN-SIM-RECO
1/2	Drell-Yan	/Monopole_SpinHalf_DrellYan_M-MASS_TuneCP5_13TeV_madgraph-pythia8/RunIISummer20UL18RECO/.../GEN-SIM-RECO
0	Drell-Yan	/Monopole_SpinZero_DrellYan_M-MASS_TuneCP5_13TeV_madgraph-pythia8/RunIISummer20UL18RECO/.../GEN-SIM-RECO

Table 4 – Simulated signal datasets used in this analysis for magnetic monopole production in proton-proton collisions at $\sqrt{s} = 13$ TeV. Each entry corresponds to a single sample per production mechanism (Photon Fusion or Drell-Yan) and spin hypothesis (spin-1/2 or spin-0), for the 2018 MC campaign year. The mass value has been replaced by a placeholder "MASS" to denote generic monopole mass hypotheses between 1000 and 4500 GeV.

Spin	**Process**	**Dataset**
1/2	Photon Fusion	/Monopole_SpinHalf_PhotonFusion_M-MASS_TuneCP5_13TeV_madgraph-pythia8/RunIISummer20UL17RECO/.../GEN-SIM-RECO
0	Photon Fusion	/Monopole_SpinZero_PhotonFusion_M-MASS_TuneCP5_13TeV_madgraph-pythia8/RunIISummer20UL17RECO/.../GEN-SIM-RECO
1/2	Drell-Yan	/Monopole_SpinHalf_DrellYan_M-MASS_TuneCP5_13TeV_madgraph-pythia8/RunIISummer20UL17RECO/.../GEN-SIM-RECO
0	Drell-Yan	/Monopole_SpinZero_DrellYan_M-MASS_TuneCP5_13TeV_madgraph-pythia8/RunIISummer20UL17RECO/.../GEN-SIM-RECO

Table 5 – Simulated signal datasets used in this analysis for magnetic monopole production in proton-proton collisions at $\sqrt{s} = 13$ TeV. Each entry corresponds to a single sample per production mechanism (Photon Fusion or Drell-Yan) and spin hypothesis (spin-1/2 or spin-0), for the 2017 MC campaign year. The mass value has been replaced by a placeholder "MASS" to denote generic monopole mass hypotheses between 1000 and 4500 GeV.

Spin	Process	Dataset
1/2	Photon Fusion	/Monopole_SpinHalf_PhotonFusion_M-MASS_TuneCP5_13TeV_madgraph-pythia8/RunIISummer20UL16RECOAPV/.../GEN-SIM-RECO
0	Photon Fusion	/Monopole_SpinZero_PhotonFusion_M-MASS_TuneCP5_13TeV_madgraph-pythia8/RunIISummer20UL16RECOAPV/.../GEN-SIM-RECO
1/2	Drell-Yan	/Monopole_SpinHalf_DrellYan_M-MASS_TuneCP5_13TeV_madgraph-pythia8/RunIISummer20UL16RECOAPV/.../GEN-SIM-RECO
0	Drell-Yan	/Monopole_SpinZero_DrellYan_M-MASS_TuneCP5_13TeV_madgraph-pythia8/RunIISummer20UL16RECOAPV/.../GEN-SIM-RECO

Table 6 – Simulated signal datasets used in this analysis for magnetic monopole production in proton-proton collisions at $\sqrt{s} = 13$ TeV. Each entry corresponds to a single sample per production mechanism (Photon Fusion or Drell-Yan) and spin hypothesis (spin-1/2 or spin-0), for the 2016APV MC campaign year. The mass value has been replaced by a placeholder "MASS" to denote generic monopole mass hypotheses between 1000 and 4500 GeV.

Spin	Process	Dataset
1/2	Photon Fusion	/Monopole_SpinHalf_PhotonFusion_M-MASS_TuneCP5_13TeV_madgraph-pythia8/RunIISummer20UL16RECO/.../GEN-SIM-RECO
0	Photon Fusion	/Monopole_SpinZero_PhotonFusion_M-MASS_TuneCP5_13TeV_madgraph-pythia8/RunIISummer20UL16RECO/.../GEN-SIM-RECO
1/2	Drell-Yan	/Monopole_SpinHalf_DrellYan_M-MASS_TuneCP5_13TeV_madgraph-pythia8/RunIISummer20UL16RECO/.../GEN-SIM-RECO
0	Drell-Yan	/Monopole_SpinZero_DrellYan_M-MASS_TuneCP5_13TeV_madgraph-pythia8/RunIISummer20UL16RECO/.../GEN-SIM-RECO

Table 7 – Simulated signal datasets used in this analysis for magnetic monopole production in proton-proton collisions at $\sqrt{s} = 13$ TeV. Each entry corresponds to a single sample per production mechanism (Photon Fusion or Drell-Yan) and spin hypothesis (spin-1/2 or spin-0), for the 2016 MC campaign year. The mass value has been replaced by a placeholder "MASS" to denote generic monopole mass hypotheses between 1000 and 4500 GeV.

5.2 Implementation of monopole model at MadGraph

For relativistic, fast-moving monopoles, passage through material results in the production of a large number of electron-positron pairs, which can serve as a distinctive signature for their detection and subsequent identification. The monopole velocity, often parameterized in theoretical models, is expressed in terms of the monopole mass M and the partonic center-of-mass energy s, since the kinematics of the produced particles depend on the energy available to the interacting partons. This relationship can be described by the following equation:

$$\beta = \sqrt{1 - \frac{4M^2}{s}} \tag{5.1}$$

Since no reliable calculation of the monopole production cross-section is available, theoretical models are limited to *Leading Order* (LO) approximations based on tree-level Feynman diagrams. While Next-to-Leading Order (NLO) calculations could, in principle, improve accuracy, they rely on perturbative methods that are not currently applicable to monopole production due to the lack of a well-defined coupling. As a result, only tree-level diagrams are considered, as higher-order contributions are expected to be subdominant and require theoretical inputs that are not yet available.

In Table 8, the cross-sections used for Spin Zero and Spin Half processes as a function of mass for both production modes are presented. These same cross-section values are also visualized in Figure 53, which clearly illustrates a one order of magnitude difference between the cross-section values for Photon Fusion and Drell-Yan production processes.

Mass (GeV)	σ(s=0, PF) (fb)	σ(s=0, DY) (fb)	$\sigma(s = 1/2$, PF) (fb)	$\sigma(s = 1/2$, DY) (fb)
1000	1.090×10^{4}	1.450×10^{1}	5.100×10^{4}	2.400×10^{2}
1500	8.620×10^{2}	8.120×10^{-1}	3.650×10^{3}	1.630×10^{1}
2000	9.130×10^{1}	6.040×10^{-2}	3.530×10^{2}	1.470×10^{0}
2500	1.050×10^{1}	4.990×10^{-3}	3.710×10^{1}	1.430×10^{-1}
3000	1.150×10^{0}	4.420×10^{-4}	3.730×10^{0}	1.440×10^{-2}
3500	1.070×10^{-1}	4.170×10^{-5}	3.220×10^{-1}	1.540×10^{-3}
4000	7.620×10^{-3}	3.690×10^{-6}	2.120×10^{-2}	1.650×10^{-4}
4500	3.500×10^{-4}	2.370×10^{-7}	9.050×10^{-3}	1.380×10^{-5}

Table 8 – Theoretical production cross sections for magnetic monopoles with spin 0 and 1/2, generated via Photon Fusion (PF) and Drell–Yan (DY) processes at $\sqrt{s} = 13$ TeV. Values are shown as a function of monopole mass, ranging from 1000 to 4500 GeV. The cross-sections are given in fb^{-1} and demonstrate the rapid decrease with increasing mass, especially in the DY channel.

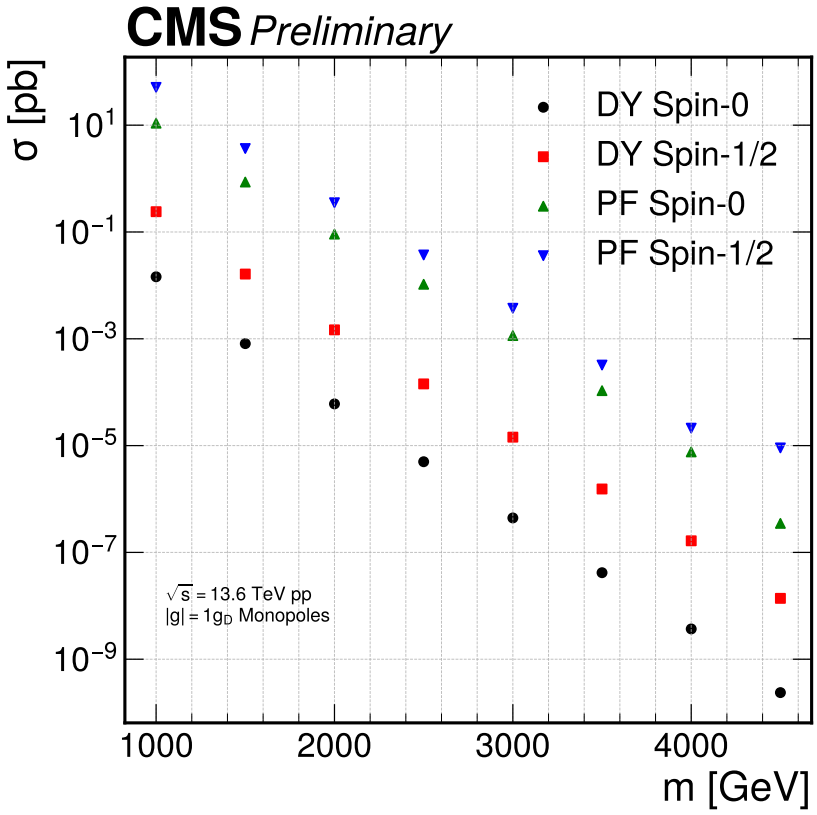

Figure 53 – The cross sections for spin-0 and spin-1/2 monopoles by Drell-Yan (DY) and photon fusion (PF) in proton-proton collisions.

5.3 Signatures in the CMS subdetectors

For magnetic monopole searches, two discriminant variables are combined to identify these particles. These variables are related to both the inner tracking system and the electromagnetic calorimeter. Within the inner tracking system, tracks with high dE/dx values can identify the magnetic monopole track. Due to the action of the magnetic field, it is expected that such tracks will show a parabolic trajectory in the $r - z$ plane, aligned with the direction of the magnetic field. It is also important to note that the dominant energy loss mechanism for monopoles occurs via the ionization process.

Such behavior is unique in comparison with any other electrically charged particles, where a bend in the $x - y$ plane is expected, perpendicular to the magnetic field. In Figure 54, the trajectory of a monopole with 1000 GeV of mass in the z plane for a uniform solenoid magnetic field in the ALICE, ATLAS, and CMS experiments from the LHC is shown.

The magnetic monopoles must traverse the beryllium beam pipe surrounding the interaction point, where monopoles with low kinetic energy would be trapped in the CMS

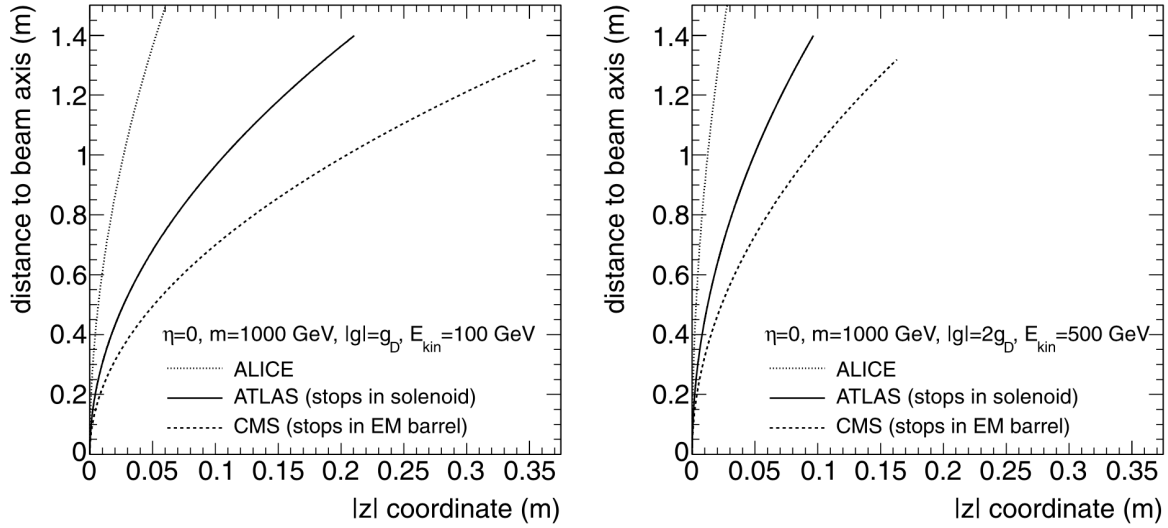

Figure 54 – The approximate trajectory of a 1000 GeV mass monopole for a uniform solenoid magnetic field in the ALICE (B = 0.5 T), ATLAS (B = 2 T), and CMS (B = 3.8 T) detectors at $\eta = 0$. The left plot corresponds to a monopole with $|g| = g_D$ and the right plot to $|g| = 2g_D$.

beam pipe. It is expected that only a magnetic monopole with high kinetic energy will pass through the beam pipe, reaching the inner track, allowing its identification.

Within the inner track, it is expected that the monopole tracks should be easily distinguishable from other ordinary particles. The high ionization capacity of the monopoles yields a very peculiar signature, in the order of 4 orders of magnitude higher ionization capacity in comparison with an ordinary particle. This behavior leads to saturated energy loss dE/dx measurements. It is also expected that the monopole track to be curved in the z-plane due to the magnetic field.

However, since the standard tracking algorithm was designed to provide measurements for particles with only electric charge, it results in very low efficiency for identifying monopole tracks. To overcome this limitation, a new and customized tracking algorithm was developed to deal with the peculiar characteristics of the monopole track.

Finally, the monopoles are stopped in the ECAL, depositing most of their energy in the $PbWO_4$. Given the monopole's equivalent of 68.5e electric charge, it radiates all its kinetic energy within the ECAL, with almost negligible or no leakage in the HCAL. However, due to this abrupt deposition in the ECAL crystals, the deposition pattern of a monopole is similar to an ECAL spike, since it can be contained in just one crystal of the ECAL. Unlike electrons and photons, the monopole does not deposit its energy dispersively across multiple crystals, forming the so-called electromagnetic (EM) shower. This peculiar and highly concentrated energy deposit from the monopole significantly impacts the trigger system, often leading to a failure to retain these signal events.

5.3.1 δ-ray production model

During the interaction of the monopoles with the material of the inner layers of the CMS Experiment, electrons with energies on the order of a few keV are liberated. These electrons are known as *δ-rays*, with typically posses higher kinetic energy than electrons resulting from the ionization process. In the Figure 55, the *δ-rays* clustered around the monopole trajectory can be observed.

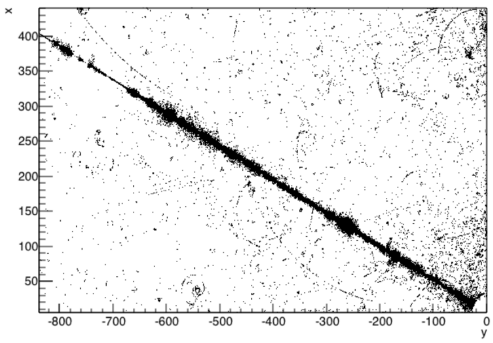

Figure 55 – The produced δ-rays clustered around the monopole trajectory in the x-y plane.

The models for the monopole energy loss via the production of the δ-rays are implemented via the `GEANT4` with an associated uncertainty of 3% [168]. The production of δ-rays affects the topological cluster variable f_{51}, which is employed as one of the discriminant variables for the monopole search at CMS.

6 Search for magnetic monopoles at CMS Detector

6.1 Introduction

The objective of this chapter is to describe the search for magnetic monopoles in the CMS experiment using proton-proton collision data collected at $\sqrt{s} = 13$ TeV during the Run 2 data-taking period, spanning from 2016 to 2018.

As discussed in greater detail in Chapter 2, magnetic monopoles are predicted by various theoretical models aiming to symmetrize Maxwell's equations and address the quantization of electric charge. In this analysis, a Dirac magnetic monopole with magnetic charge of $1g_D$ produced via the benchmark production modes was considered.

Sections 6.2, 6.3, 6.4, and 6.5 discuss the unique properties of monopole tracks. These characteristics necessitate the development of a custom tracking algorithm, given the inefficiency of the standard CMS tracking approach. Further details are provided on the ionization and curvature characteristics of monopole trajectories.

Section 6.6 focuses on the clustering procedure employed by the CMS ECAL. It describes the algorithm used for cluster formation and introduces the discriminant variable f_{51}. The section also discusses the use of the "unclean" clusters collection to recover clusters that are otherwise lost by the `sFGVB` algorithm. Additionally, the impact of the non-zero arrival time of monopoles in the ECAL crystals is examined, including an evaluation of the arrival time at various mass points based on the ECAL reconstructed hits. Further validation of the f_{51} topological variable is presented in Section 6.6.4. Finally, the behavior of the monopoles in the HCAL is evaluated by the calculation of the hadronic isolation variable described in Section 6.7.

Section 6.9 presents the two analysis strategies employed, while Section 6.8 describes the datasets used. These approaches consider the similarities between highly energetic photons and magnetic monopoles, and the hypothesis that monopoles might be rejected by the `sFGVB` algorithm—leading to large missing transverse energy (MET) recovered through the `Particle Flow` (PF) algorithm. The overall cutflows for both strategies are defined by the use of dedicated High-Level Trigger (HLT) paths, with associated discriminant cuts derived from the Tracking and ECAL systems. The trigger paths used are further discussed in Section 6.10.

Sections 6.11 and 6.12 present the signal and relative efficiencies for both analysis strategies. The low overall efficiency is noted, with a particular focus on the impact of the

trigger requirements. The relative efficiency analysis highlights that the main source of inefficiency arises from low trigger acceptance, while the discriminant cuts themselves are relatively efficient.

Given the absence of Standard Model background processes, a data-driven ABCD method is employed for background estimation, as described in Section 6.13. Additional considerations are given to the contribution of spike-like events and their impact on the final background estimate. Finally, Section 6.14 discusses the systematic uncertainties associated with the analysis. The dominant sources include the potential creation of secondary electrons and possible cross-talk between adjacent channels in the Tracking system. Other sources of uncertainty include those from background estimation methods, luminosity measurements, and MET corrections.

6.2 The Monopole tracking reconstruction

Since the magnetic monopoles gain energy while passing through the solenoidal magnetic field of the CMS, their track are expected to exhibit some curvature along the beam axis. This behavior is characteristic of particles with a magnetic charge associated. In contrast, electrically charged particles, where the *Standard Model* (SM) particles can be mentioned, circulate on the $x - y$ plane in the magnetic field.

However, given the particular behavior of the monopoles, characterized by their track curvature along the beam axis, the track reconstruction standard algorithm of the central framework of the CMS is highly inefficient for identifying these signatures. Therefore, the development of a new tracking algorithm is necessary. This new algorithm has the capacity to reconstruct tracks originating from monopole candidates by the combination of multiple straight track segments, measured in the $x - y$ plane, into a single curved track in the *Tracking* system.

Therefore, a new tracking algorithm is required to reconstruct monopole candidate tracks. The algorithm combines multiple straight track segments—measured in the x-y plane—into a single curved trajectory within the tracking system.

Apart from the different behavior concerning the tracks and trajectories, monopoles induce an energy loss in the tracker that is several orders of magnitude higher than that of an ordinary particle. The interaction of the monopole with the tracker system often leads to the production of saturated silicon strips, resulting in significant energy loss in the tracker. This affects the measurement of the energy loss function, specifically the dE/dX variable, derived from the Bethe-Bloch equation.

Considering these particular properties, a track left by a monopole candidate would be easily distinguishable from an ordinary track, even with the strong limitations of the

standard track algorithm of the CMS. The *Tracking* algorithm of the CMS is used to reconstruct the trajectory of the charged particles produced in the collisions, using the local track parameters to define any helical trajectory (p_T, η, ϕ, z_0 and d_0).

6.3 Track Combiner Algorithm

The `Track Combiner` algorithm in the CMS experiment was specifically developed to reconstruct the trajectory of Magnetic Monopoles (MMs). The algorithm is designed to combine multiple high-dE/dX track segments, consisting of saturated hit clusters that the standard reconstruction algorithm is not designed to handle, into a single curved track. The process starts by selecting an initial segment and then iteratively scans through all unassigned segments in the event. A segment is successfully combined with the existing hit set if the resulting trajectory satisfies two distinct, specialized fits that account for the monopole's motion in the CMS magnetic field.

The first of the two fits consists of a circular trajectory in the xy plane, a standard projection for a helical track. This circular fit can be expressed by Equation 6.1.

$$\mathrm{y} = \mathrm{a} + \mathrm{Sign(c)} \times \sqrt{\mathrm{c}^2 - (\mathrm{x} - \mathrm{b})^2} - \mathrm{c} \tag{6.1}$$

where x and y represent the system coordinates, which rotate with the polar angle of the first hit in the detector frame ϕ_0. The fit parameters a,b, and c correspond to the impact parameter, the radius of the circle, and the azimuthal angle (ϕ_0), respectively.

The application of the circle fit ensures that no monopole candidates are missed, even if they are electrically charged, which is not the case for the MC samples used in this analysis. However, for high momentum monopole candidates, the fit parameter b will be large, which means that the curvature radius is such that the track of the particle can be considered as a straight line.

The second fit consists of a parabola in the $\rho - z$ plane, which can be expressed by Equation 6.2.

$$\mathrm{z} = \mathrm{d} + \mathrm{f}\rho + \mathrm{g}\rho^2 \tag{6.2}$$

where ρ is the transverse distance from the beam line, which could also be understood as a radial distance r. The fit parameter d corresponds to the distance of the monopole candidate moves along the z direction, which is aligned with the strong magnetic field. The parameter f is the gradient in the $\rho - z$ plane, while g represents the plane curvature.

It is worth noting that a particle with no magnetic charge would also satisfy these fits. In such a case, the parabola degenerates into a straight line, a similar behavior that

can be observed for the first fit, where the circular pattern degenerates into a straight line. From the two fits, six parameters (a,b,c,d,f and g) can be extracted. These are saved as the track properties for the extrapolation of the track to the ECAL. A pre-selection on these parameters is performed, and it can be found in Table 9. Additionally, the distribution for the fit parameters can be observed in Figure 56.

Pre-selections	Parameters	Cuts
Circular fit parameters	$\lvert\text{XYPar0}\rvert \rightarrow d_0 = \sqrt{(a-c)^2 + b^2 - \lvert c\rvert}$	< 0.6 cm
	$\lvert\text{XYPar2}\rvert \rightarrow$ radius of the circle	> 1000 cm
Parabola fit parameters	$\lvert\text{RZPar0}\rvert \rightarrow Z_0 = \lvert d\rvert$	< 10 cm
	$\lvert\text{RZPar1}\rvert \rightarrow \eta_0 = \lvert f\rvert$	< 999
	$\lvert\text{RZPar2}\rvert \rightarrow \rho - Z$ curvature $= \lvert g\rvert$	< 0.005 cm^{-1}
Matching parameters	$\Delta R = \sqrt{\eta^2 + \phi^2}$	< 0.5
	HCAL Isolation	< 10 GeV

Table 9 – Summary of preselection criteria applied to fitted parameters from circular and parabolic trajectory models, as well as the matching variable ΔR. These conditions are used to filter the monopole candidates' reconstructed tracks. The thresholds on parameters such as the radius of the circular fit, vertex position z, and curvature-related terms ensure consistency with expected detector geometry and kinematics.

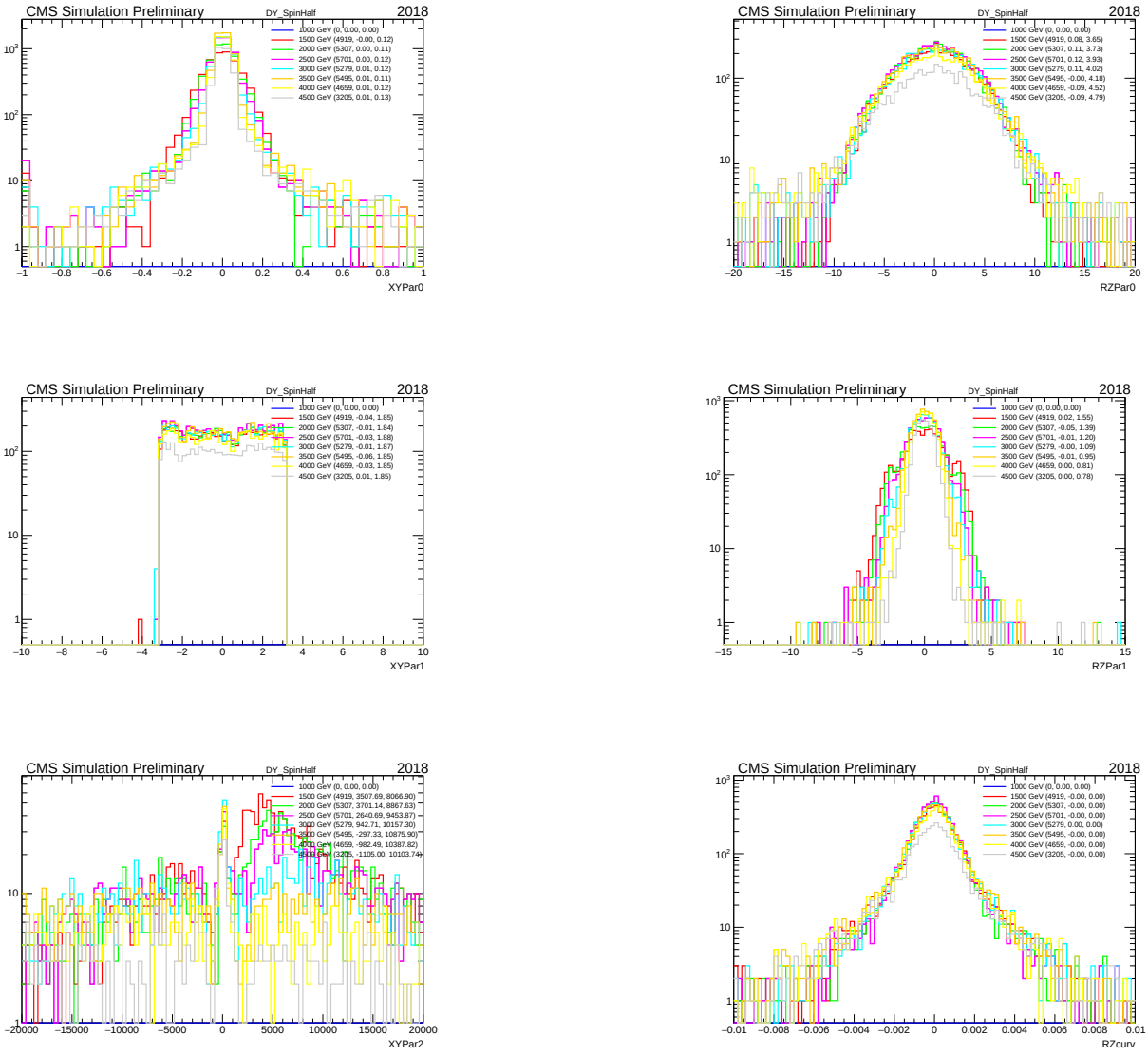

Figure 56 – Normalized distributions of the fit parameters for spin-1/2 magnetic monopoles generated via Drell–Yan production at $\sqrt{s} = 13$ TeV. Each subplot shows a different variable, `XYPar0` (upper left), `RZPar0` (upper right), `XYPar1` (middle left), `RZPar1` (middle right), `XYPar2` (lower left) and `RZcurv` (lower right). The colored lines correspond to the different mass points from 1000 GeV to 4500 GeV for the 2018 MC campaign

6.4 Track Ionization

When a high-energy particle traverses the silicon strips in the tracker, the energy loss from the particles excites charge currents within the silicon. The energy loss is proportional to the charge collection, so the general measurement of energy loss involves counting the *Analog-to-Digital Converter* (ADC) number of collection charges present in the cluster [169]. The saturated strips are defined as those with an ADC count that exceeds the a specific threshold.

With the establishment of the track sets, the ionization for each set associated with a monopole candidate can be measured. Because monopoles produce saturated hits on the silicon strips, the energy loss measurement is highly sensitive to fluctuations, particularly from hits near boundaries or lower-energy hits. These can be mistakenly included in the reconstructed track, affecting the accuracy of the ionization measurement.

The dE/dX measurements are determined by the harmonic average of the energy loss function for the tracks, with the attribution of a higher weight to the low-energy hits in comparison with the high-energy hits. In Figure 57, a display of the fraction of saturated strips versus the total number of strips for the monopole candidates with a mass of 1000 GeV of a 2018 MC sample can be observed.

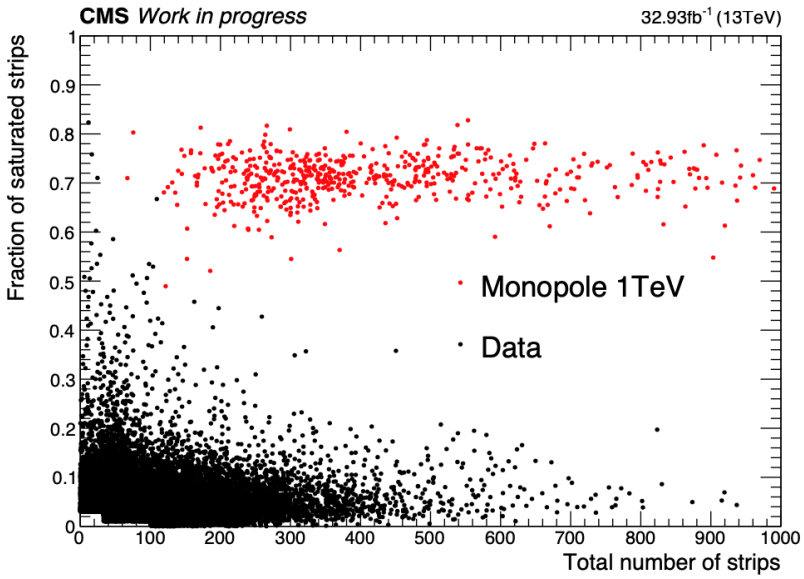

Figure 57 – Distribution of the fraction of saturated strips as a function of the total number of strips in the CMS detector. The red points represent simulated magnetic monopole signals with mass 1 TeV, while the black points correspond to CMS blinded data. Monopole candidates exhibit a significantly higher fraction of saturated strips compared to standard data, highlighting this variable's discriminating power for identifying highly ionizing particles.

For monopole candidates, the number of saturated strips is approximately equal to the number of strips, resulting in a fraction of saturated strips close to 1, as can be observed by the red dots in Figure 57. The average fraction of saturation for a monopole candidate is around 0.7, while the saturation probability for the background is approximately 0.07, as determined from the saturated fraction distribution.

The discriminant variable ($dE/dX_{\texttt{significance}}$), defined by Equation 6.3, exploits the saturation probability of the monopole tracks. This variable corresponds to the combination of the total number of strips with the fraction of saturated strips, offering better discrimination between highly ionizing monopole candidates and minimum ionizing background events.

In the derivation of the $dE/dX_{\texttt{significance}}$ variable, it is assumed that each strip, due to noise or a high-energy particle, has a small probability of being saturated. While this probability has a minor effect, it's not independent, as angular parameters can influence its value.

$$\mathrm{dE/dX_{significance}} = \sqrt{-\log(\mathrm{BinomialI}(0.07, \mathrm{TotalStrips}, \mathrm{SaturatedStrips}))} \tag{6.3}$$

where the `BinomialI(p,n,k)`, implemented from the `ROOT::TMath::BinomialI` class object, represents the binomial probability function for at least k trials out of n independent trials has a probability p to be successful.

In Figure 58, the distributions for the $dE/dX_{\texttt{significance}}$ variable can be found for different mass points from 1000 GeV to 4500 GeV for the 2018 MC campaign. The results were obtained for the four production modes considered: Drell-Yan and Photon Fusion for spin 0 and spin 1/2 states. The distributions have a significant difference between the signal and the possible minimum ionizing background. Hence, $dE/dX_{\texttt{significance}}$ will be employed as a discriminant variable for monopole identification, built from the custom tracking algorithm.

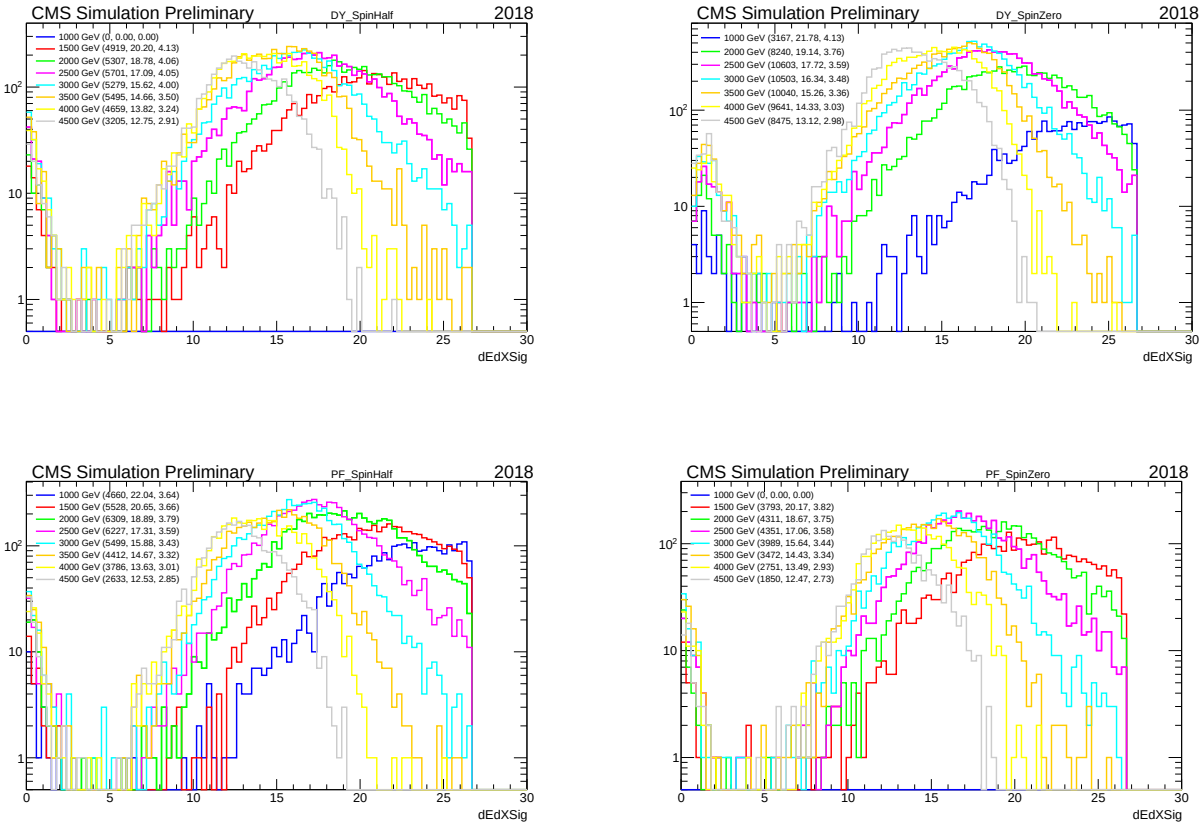

Figure 58 – The normalized distribution of $dE/dx_{\texttt{Significance}}$ for Run II signal MC for the generated mass points for Spin Half Drell-Yan (upper left), Spin Zero Drell-Yan (upper right), Spin Half Photon Fusion (lower left) and Spin Zero Photon Fusion (lower right) production modes.

6.5 Track Curvature

The curvature of the monopole candidate track in the $\rho - z$ plane lacks the discriminant capacity of the ionization. Since a high-momentum monopole candidate will produce a small curvature in the tracking chambers, it will exhibit a behavior similar to that of a non-charged, ordinary particle.

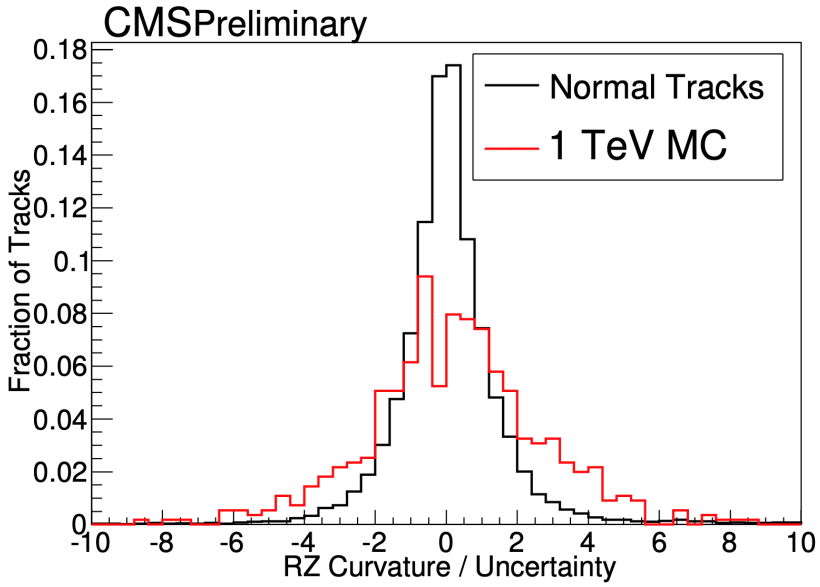

Figure 59 – Curvature in the ρ–z plane, represented by the `RZCurv` parameter in Figure 56, is shown for the MC derived in LHC Run 1. The red distribution corresponds to a 1 TeV magnetic monopole, while the black distribution represents a set of standard particle tracks.

6.6 The clusters in the Electromagnetic Calorimeter

Due to its high equivalent electric charge, a magnetic monopole candidate radiates all its kinetic energy over a small distance when interacting with the dense crystals of the CMS ECAL. Consequently, a monopole candidate is expected to deposit most of its energy in a single crystal, in contrast to the dispersed pattern across several crystals, observed for standard EM showers, from photons and electrons. These energy deposits are then grouped into *clusters* using two different types of clustering algorithms: the *Hybrid* and the *Island* algorithms. In a second moment, the clusters from both methods are combined to form a *SuperCluster*, which will lead to the definition of the E_{55} variable, which will be mentioned in the further sections.

In a second moment, the clusters from both methods are combined to form a *SuperCluster*, which will lead to the definition of the E_{55} variable, which will be mentioned in the further sections.

While the *Hybrid* and *Island* clustering algorithms have a similar approach for the start of the clustering process, their methods for building clusters diverge, resulting in two distinct cluster types. For the *Hybrid* algorithm, the final cluster has a fixed size and shape, whereas for the *Island*, a cluster with no fixed size or shape is built.

The *Hybrid* clustering Algorithm is based on the energy present in a given $\eta - \phi$ geometry ECAL barrel. The clustering strategy starts with a seed crystal *dominoes* with the dimension 1×3 in the $\eta - \phi$ plane, with $E_T > 0.1$ GeV, which is aligned with the

center of the *dominoes* seed crystal. If one of the selected seed crystals has an energy higher than a certain threshold, the *dominoes* are spread to 1×5 crystals, in $\eta - \phi$. After this selection, the algorithm performs a scan for a given number of steps in the ϕ direction to find a cluster with $E_T > 1$ GeV to construct the final clusters centered in the selected seed crystal.

The *Island* clustering algorithm has an opposite approach for cluster building in comparison to the *Hybrid* algorithm, where, for the second, the clusters have a fixed shape and size. The *Island* algorithm starts with a list of seeds, from which high-energy adjacent seeds are removed. For each remaining seed of the list, the algorithm performs a scan in the ϕ direction, collecting the energy of the crystals until a discontinuity, which can be either a rise or a hole, is detected. Subsequently, another scan in ϕ is performed, for one crystal over in η. The *Island* algorithm continues to increase the steps in the η direction. The steps in η are incremented until a discontinuity is detected. The algorithm also ensures that no crystal is attributed to two different clusters since all collected crystals can't be used in another cluster. In that sense, the final product of the *Island* algorithm is a cluster with no fixed size or shape, a direct contrast to the fixed-size clusters of the *Hybrid* algorithm.

A relevant technical background for this analysis is the presence of anomalous signals in the ECAL crystals [103], particularly within the barrel region of the ECAL. There were some variables developed to mitigate the effect of these anomalous signals, which can also be referred to as *spike* events. Given the unique interaction pattern between the monopole candidate and the ECAL crystals, a high rate of monopole clusters is associated with these *spike* events. Furthermore, there is a filter designed for the rejection of such anomalous signals, which are employed in the L1 Trigger, the HLT, and in the offline reconstruction, which was discussed in Section 3.2.7.2.

The L1 *spike* filter assigns a single bit to each 1×5 strip in $\eta - \phi$ within a 5×5 trigger tower. If two or more cells in a given strip exceed a 350 MeV threshold, their associated bit is set to 1. These five bits, one for each strip, are then combined with a logical operation OR, resulting in two different scenarios: an output value of 1 indicates the tower is accepted as a *spike*-like event, and for the value 0, the trigger tower is rejected under the same criteria. For the HLT, the cuts are applied on the event timing and in the ratio of energy in four neighboring cells to the seed cell, involving the application of the *Swiss-cross* variable, as illustrated in Figure 60.

For the offline reconstruction algorithms, similar selection criteria used by the HLT are employed, which results in two distinct cluster collections. The clean clusters collection comprises those that pass the offline *spike* rejection filter, while the unclean collection includes clusters that do not.

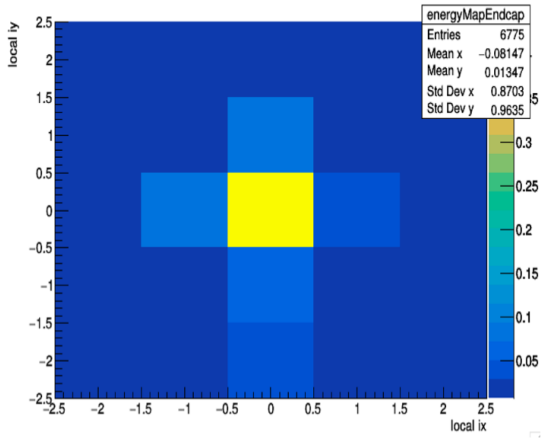

Figure 60 – The average $E_{\text{crystal}}/E_{5\times5}$ for monopoles candidates with a mass of 1 TeV, in the barrel region of the CMS ECAL.

6.6.1 The Superclustering Algorithm in the ECAL

In the ECAL barrel region, the clustering algorithm starts with a set of seed crystals, each possessing a transverse energy above a certain threshold, based on the $\eta - \phi$ geometry. Depending on the values of that energy, the seed crystals are combined into a *domino*, containing 3 or 5 crystals aligned in η with the seed crystal. This procedure to build crystals *dominoes* is repeated for all available crystals, with the seed crystal aligned in η in each direction along the ϕ direction, limited to a maximum number of crystals.

Subsequently, the crystal *dominoes* are clustered in ϕ and it is required for each formed structure to have a seed *domino* with an energy larger than a given threshold. The resultant cluster from the *Hybrid* clustering algorithm is combined to form the *SuperCluster*. The total energy of this cluster is obtained from the sum of the energies of the individual crystals.

In Figure 61, the distributions for $E_{5\times5}$ cluster variable, a square of 5 × 5 crystals, can be found for different mass points from 1000 GeV to 4500 GeV for the 2018 MC campaign. The results were obtained for the four production modes considered: Drell-Yan and Photon Fusion for spin 0 and spin 1/2 states.

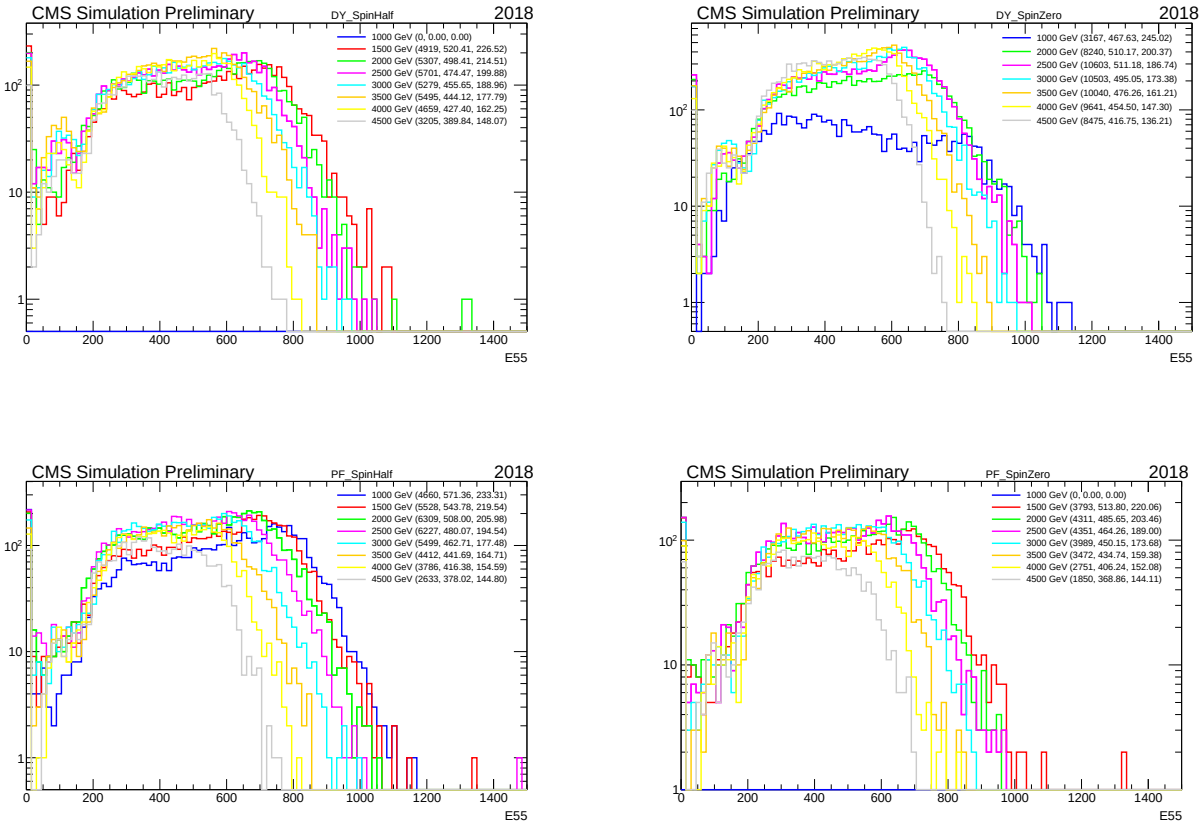

Figure 61 – The normalized distribution of $E_{5\times5}$ cluster energy for Run II signal MC for the generated mass points for Spin Half Drell-Yan (upper left), Spin Zero Drell-Yan (upper right), Spin Half Photon Fusion (lower left) and Spin Zero Photon Fusion (lower right) production modes.

For the monopole analysis, due to its particular signature, it is expected that the monopole deposits all of its energy into a single crystal, the seed crystal. The ratio of the seed crystal and the square of 5 × 5 crystals is expected to be approximately 1, or slightly below 1. This particular behavior is exploited to build a discriminant variable, called the f_{51}.

The topological cluster variable f_{51} is defined as the ratio of the energy within a 5 × 1 strip of cells in the η–ϕ plane to the total energy ($E_{5\times5}$) in the surrounding 5 × 5 cell region. A schematic representation of this configuration is shown in Figure 62, and the formal definition is provided in Equation 6.4. Figure 63 presents the f_{51} distributions for various monopole mass points, ranging from 1000 GeV to 4500 GeV, based on the 2018 Monte Carlo campaign. Results are shown for four production modes: Drell–Yan and photon fusion, each for spin-0 and spin-1/2 states. A clear separation is observed between signal and the minimum ionizing background.

$$f_{51} = \frac{E_{5\times1}}{E_{5\times5}} \tag{6.4}$$

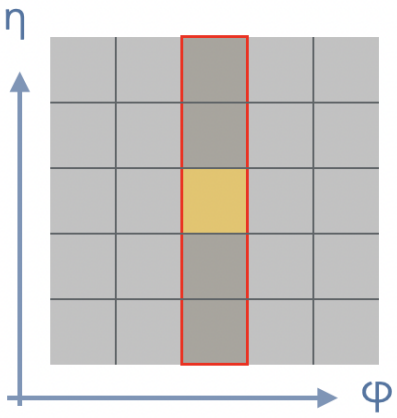

Figure 62 – Illustration of the topological cluster variable f_{51}. The yellow square marks the seed crystal with the highest energy deposition. The red frame shows the 5 × 1 strip arrangement in the η–ϕ plane. The full cluster is composed of a 5 × 5 grid of cells.

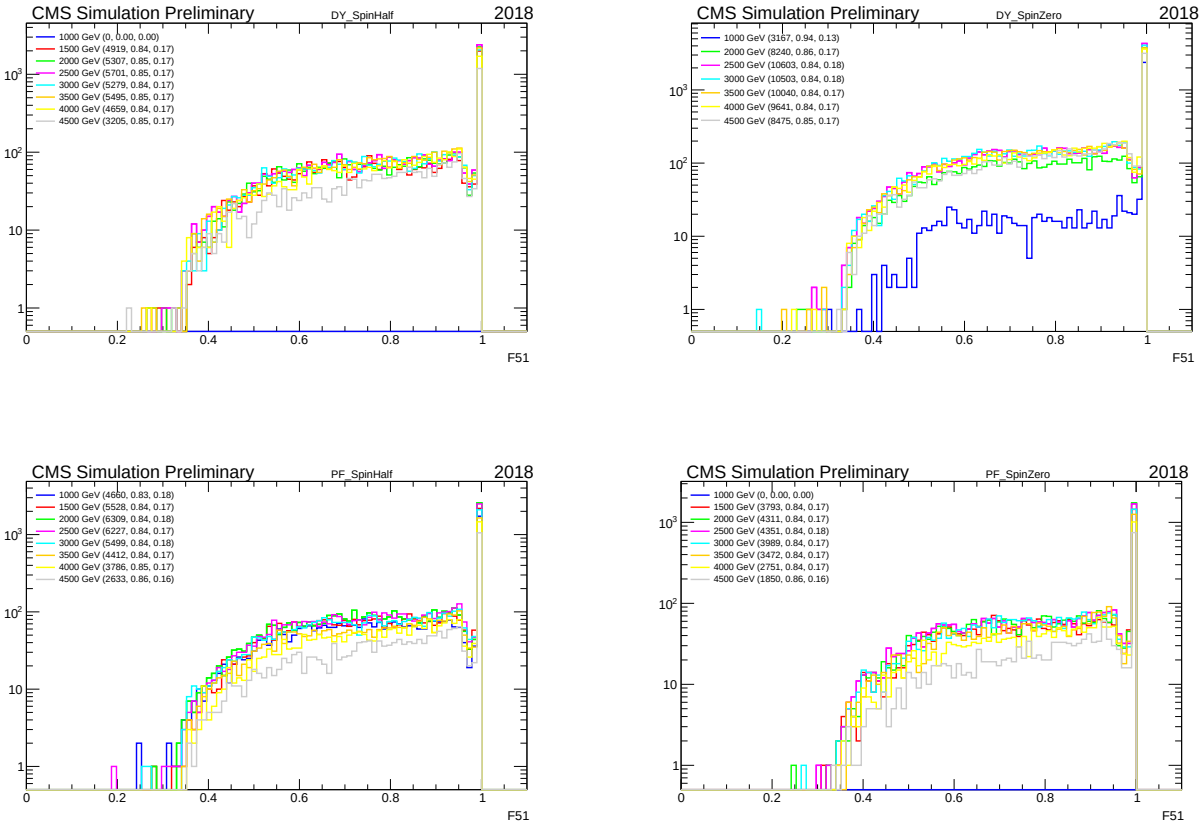

Figure 63 – The normalized distribution of topological cluster variable f_{51} for Run II signal MC for the generated mass points for Spin Half Drell-Yan (upper left), Spin Zero Drell-Yan (upper right), Spin Half Photon Fusion (lower left) and Spin Zero Photon Fusion (lower right) production modes.

6.6.2 Unclean clusters

When the signal is confined to a single channel within a trigger tower, it is highly likely to be rejected by the L1 spike killer, which prevents the event from firing the relevant L1 seeds, as described in Section 3.2.7.2. A similar restriction is placed in the HLT, where the Swiss-cross pattern is also applied. The influence of the L1 spike killer directly impacts the signal efficiency when the `Single Photon` or `MET` paths are employed, which rely on these L1 calorimeter seeds.

However, if the event is triggered for another reason, such as a second monopole spreading across multiple crystals or the presence of another distinct calorimeter signature, all the ECAL `RecHits` will be read out, regardless of whether they are classified as spikes. In this scenario, these "spike-like" hits will be saved in the reconstruction, and they can be found in the datasets produced by the monopole `SKIM`. The Skimming of a dataset consists of the application of a script to keep only specific collections, to improve the efficiency of any analysis.

On the other hand, an uncleaned cluster refers to a reconstructed energy cluster where standard spike-rejection criteria, built into the L1 trigger, are deliberately bypassed. Specifically, the ECAL `RecHits`, which are flagged as "spike-like", based on topological features, are included without applying the usual cleaning cuts. This approach includes the ECAL `RecHits` that (1) fail the Swiss-cross cut (indicative of isolated energy deposits from instrumental noise), (2) fail the extended Swiss-cross cut used to identify double spikes, and (3) fail the timing cut that filters out-of-time energy deposits.

Allowing uncleaned clusters in the reconstruction process enables the detection of monopole events even when they are not the primary trigger source. By bypassing standard spike-rejection criteria, this approach enhances the offline reconstruction efficiency for monopole signals, increasing sensitivity to events that might otherwise be excluded.

In summary, the uncleaned cluster is a collection of clusters that do not pass the offline spike rejection filter, while the collection of clean clusters is composed of the clusters that pass the offline spike rejection filter. For the track-cluster matching performed to build the monopole candidate for this analysis, a combination of both collections of clusters is employed to improve the signal efficiency.

6.6.3 Monopole Timing studies

As discussed in Section 3.2.4, the electromagnetic calorimeter of the CMS Experiment is a homogeneous calorimeter composed of 74848 $PbWO_4$ scintillating crystals. These crystals have an effective time decay compatible with 25 ns of the bunch crossing interval of the LHC. The stability of the time resolution, for a high energy resolution, is in the order of 1 ns [170]. This time resolution, combined with the electronic pulse shaping and the sampling rate of the ECAL, provides an excellent opportunity for triggering possible LLP signals, allowing background rejection from a precise time measurement performance. For each ECAL crystal, a timing offset is calibrated to ensure that a particle traveling at the speed of light yields a zero arrival time [171].

Due to its high mass, the magnetic monopoles are expected to arrive at the ECAL with a delay of a few nanoseconds, which increases for the higher mass scenarios. Such time evaluation was performed considering $\beta = v/c$, with the monopoles traveling with $\beta < 1$. An estimate of the arrival time can be performed considering the distance from the impact parameter (IP) and the inner radius of the ECAL, with d = 1.5m. For instance, a monopole with 3000 GeV is expected to cover this distance in $\approx$ 11.7 ns, given by $t = 1.5/(0.3 * 0.43) \approx 11.627$ ns, where 0.3 m/ns is the speed of light and average $\beta = 0.43$ extracted from Figure 64. This study was proposed in [172], where further details can be found, especially considering the calibration of the detector and the true arrival time. The propositions regarding reconstructed ECAL hits, in particular, are further explored in this thesis.

In Figure 65, the estimated arrival time of the monopoles with different masses is presented. It is worth noting the increase in the average delay for the higher masses. As proposed in [172], it was expected that the arrival delay of the monopoles could be employed as a discriminating parameter in the analysis. On the other hand, this nonprompt arrival of the particle in the ECAL crystal might introduce biases or inefficiencies in the energy reconstruction. This should be taken into consideration, motivating either corrections or associated systematic uncertainties.

The amplitude of a given pulse from energy deposits in the ECAL crystals is sensitive to a shift in the position of the maximum time (T_{max}) of the signal pulse. This timing shift can be caused by variations of the pulse shapes over time, both independently from crystal to crystal and coherently [173]. For the estimation of the sensitivity of the reconstructed amplitudes to changes in the template timing ΔT_{max}, the amplitude of a given pulse is reconstructed several times, with different values of ΔT_{max}. The observed changes in the ratio of the reconstructed amplitude($\langle A \rangle$) to the true amplitude (A_{true}), as a function of ΔT_{max} can be observed in Figure 66, where single-crystal pulses of 50 GeV in the electromagnetic barrel (EB) and endcap (EE), respectively, were considered. Small differences between EB and EE arise mostly from the slightly different rise times of the

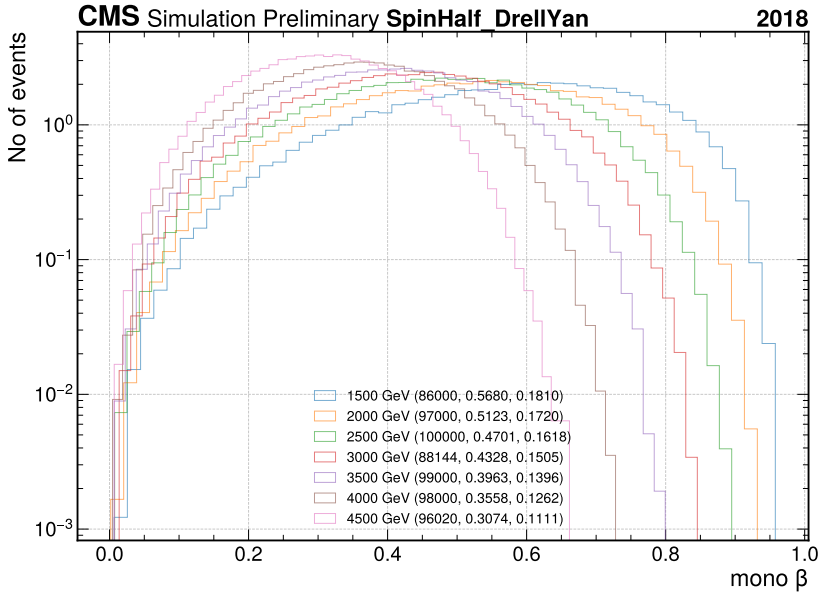

Figure 64 – Normalized velocity β of the generated (GEN) monopoles. The distribution is produced for the different mass hypothesis ranging from 1500 GeV to 4500 GeV, for the Spin 1/2 Drell-Yan production mode. The timing is measured in ns, where a clear shift toward later times is observed with increasing monopole mass, consistent with the slower velocities of heavier monopoles.

barrel and endcap pulses and the difference in energy distributions from PU interactions in a single crystal in the two regions.

The differences between the actual pulse shapes and the assumed templates are absorbed by the crystal-to-crystal energy intercalibrations. However, any changes with time in the relative position of the template will affect the reconstructed amplitudes, affecting the energy resolution, leading to the necessity of monitoring $T_{\max}$, with periodic correction for the templates.

From the expected arrival delay of the monopole candidates in the ECAL, as can be observed in 65, a non-zero $\Delta T_{\max}$ is observed concerning the pulses produced from the interaction with the ECAL crystals. For such delay, a 1% overestimation is expected for each 1 nanosecond delay, impacting the clustering techniques applied to reconstruct the energy of the monopole.

For the verification of such delays, it is necessary to evaluate the reconstructed hits (ECAL `RecHits`) of the monopole candidate signal. It is expected that a non-zero time would be found in the `RecHits` related to the monopole candidate interaction with the ECAL.

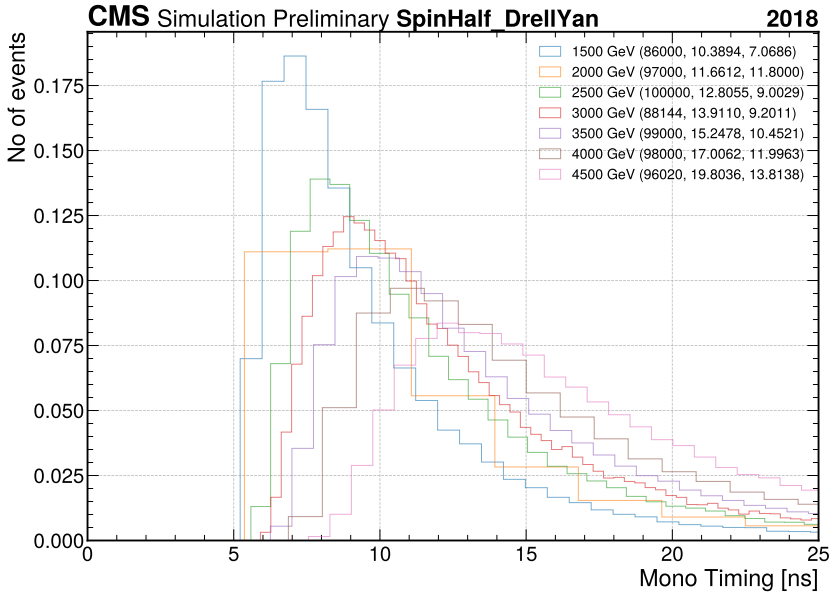

Figure 65 – Normalized estimative for the arrival time of the generated (GEN) monopoles, obtained via $t = d/(v * c)$, where c is the speed of light and m/ns and β is the velocity of the monopoles. The distribution is produced for the different mass hypothesis ranging from 1500 GeV to 4500 GeV, for the Spin 1/2 Drell-Yan production mode. The timing is measured in ns, where a clear shift toward later times is observed with increasing monopole mass, consistent with the slower velocities of heavier monopoles.

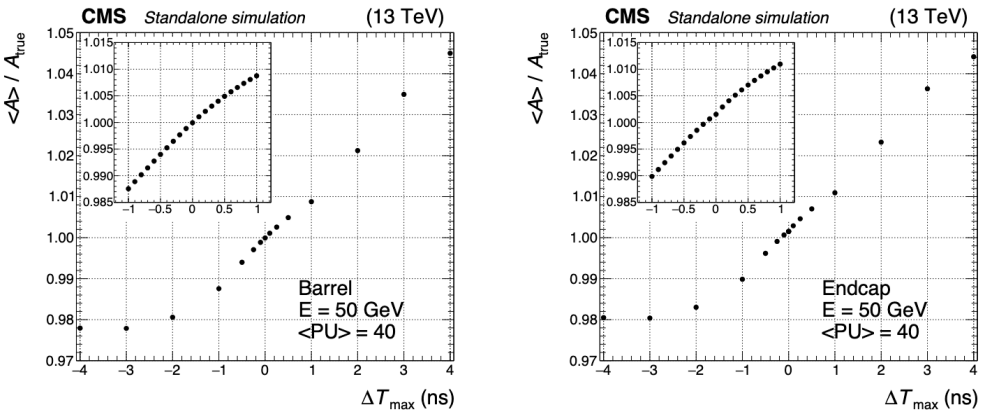

Figure 66 – Reconstructed amplitude over true amplitude ($\langle A \rangle / A_{\text{true}}$) as a function of the timing shift of the pulse template (ΔT_{max}) for a single-crystal pulse of E = 50 GeV in the electromagnetic barrel (EB), in the left, and for the electromagnetic end-caps (EE), in the right. The insets show an enlargement in the ± 1 ns range with finer ΔT_{max} granularity.

6.6.3.1 ECAL Reconstructed Hits

In the Compact Muon Solenoid (CMS) experiment at the LHC, the electromagnetic calorimeter (ECAL) reconstructed hits, or `RecHits` [98], consists in the fundamental units of energy measurement used for physics object reconstruction. When a high-energy electromagnetic particle traverses the ECAL, it initiates an electromagnetic shower, depositing energy across multiple ($PbWO_4$) crystals. These energy deposits are first digitized and then processed through a series of reconstruction steps to form `RecHits`.

A reconstructed hit (`RecHit`) corresponds to a calibrated energy deposit in a single ECAL crystal. The reconstruction process involves the deconvolution of digitized signals using known pulse shapes, correction for pedestal noise, timing, and inter-calibration constants, as well as an energy scale calibration derived from test beams and in situ physics processes (electrons from $Z \to e^+e^-$ decays). Each `RecHit` includes not only the energy and timing information but also quality flags that could be used to indicate potential anomalies.

These `RecHits` are the primary inputs to higher-level reconstruction algorithms, including clustering and particle identification, where an unexpected behavior or pattern in the `RecHits` could impact the clustering techniques employed in general analysis, but with special attention in the analysis, due to the non-zero arrival time of the monopole signal.

6.6.3.2 ECAL RecHits Timing Maps

In searches for non-relativistic particles such as magnetic monopoles, the timing characteristics of ECAL `RecHits` could play a crucial role. Due to their large mass and delayed arrival at the detector, the monopole candidates are expected to produce energy deposits in the electromagnetic calorimeter (ECAL) that are both spatially and temporally distinct from those of SM particles. In particular, the timing of high-energy ECAL `RecHits` associated with monopole candidates may be significantly shifted, which can be observed in Figure 67.

To investigate this effect, a study was conducted using simulated Drell-Yan-like production of spin 1/2 monopoles for different mass hypotheses. Only the ECAL `RecHits` with energy deposits greater than 200 GeV were considered, to isolate those likely to originate from monopole candidate showers, since it is expected that the higher energy deposition in comparison with minimum ionizing particles.

In Figure 67, the distribution of `RecHits` timing as a function of its energy was evaluated for each mass point considered in this analysis. The density of `RecHits` is displayed on a logarithmic color scale, highlighting the concentration of high-energy hits around a few nanoseconds. As anticipated, a non-negligible tail is observed at late

times, suggesting the presence of delayed energy deposits. This behavior may impact clustering algorithms such as $E_{5\times5}$ clustering, and motivates timing-dependent corrections or systematic uncertainties in the monopole analysis, to mitigate the impact on the reconstructed energy.

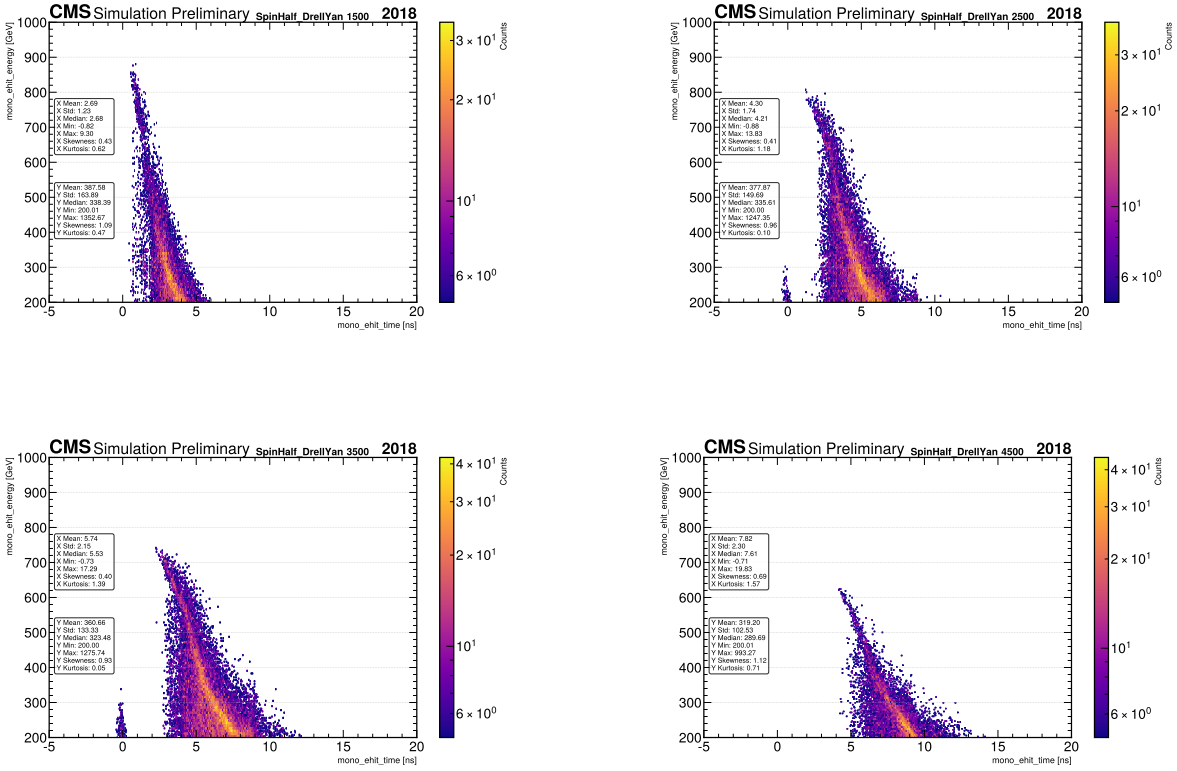

Figure 67 – Two-dimensional distribution of ECAL `RecHit` energy versus `RecHit` time for simulated monopoles for the mass points considered between 1 TeV and 4.5 TeV, produced via a spin 1/2 Drell-Yan-like mechanism. Only `RecHits` with energy greater than 200 GeV are considered to isolate contributions likely associated with delayed monopole candidates. The color scale represents the logarithmic density of `RecHits` per bin. A significant tail at late times is visible, consistent with delayed energy deposits expected from slow-moving monopoles.

6.6.4 F51 modeling validation

In the search for magnetic monopoles at the CMS experiment, the f_{51} variable plays a crucial role in the event selection strategy, exploiting the expected narrow and highly localized energy deposition characteristic of monopole interactions. The f_{51} variable defined by the Equation 6.4 is particularly sensitive to the topology of such exotic signals. To ensure the accurate modeling of this variable in MC simulations and to assess potential discrepancies between data and simulation, a detailed validation study was carried out using ECAL crystal-level information derived from the ECAL `RecHits` stored in the *Analysis Object Data* AOD format. This allowed for a precise reconstruction of the f_{51}variable, as well as associated quantities such as $E_{5\times1}$(the energy in a 5×1 cluster window) and $E_{5\times5}$ (the total energy in a 5×5 cluster window).

The validation was conducted using a high-purity $Z \to e^+e^-$ control region, defined by requiring both electrons to have transverse momentum $p_T < 25$ GeV, pseudorapidity $|\eta| < 2.5$, and an invariant mass of the electrons' pair between 80 and 100 GeV. This selection ensures a clean sample of electromagnetic objects with well-understood detector signatures. The Drell-Yan (`DYJetsToLL`) MC sample was used as the simulated reference, and the `Run2018B EGamma` dataset was employed to represent real collision data, both corresponding to the UL2018 (`Ultra-Legacy` 2018) reconstruction.

In the Figure 68, the distributions for MC and data of f_{51}, $E_{5\times1}$, and $E_{5\times5}$, as well the reconstructed Z boson mass are presented. Similarly, the same set of plots is presented in Figure 69 for the end-caps. As can be observed in the mentioned figures, especially for the EB, the distribution between data and MC simulation exhibits very good agreement, indicating a consistent modeling of the electromagnetic shower shape.

The overall shape of the distribution is well reproduced across the full range, especially in the mid and high f_{51} regions that are particularly relevant for monopole identification. Minor deviations at the low and high extremes are within expected systematic variations. The ratio of data to MC remains close to unity throughout the distribution, affirming the reliability of the simulation and validating the use of f_{51} as a discriminant in the monopole analysis.

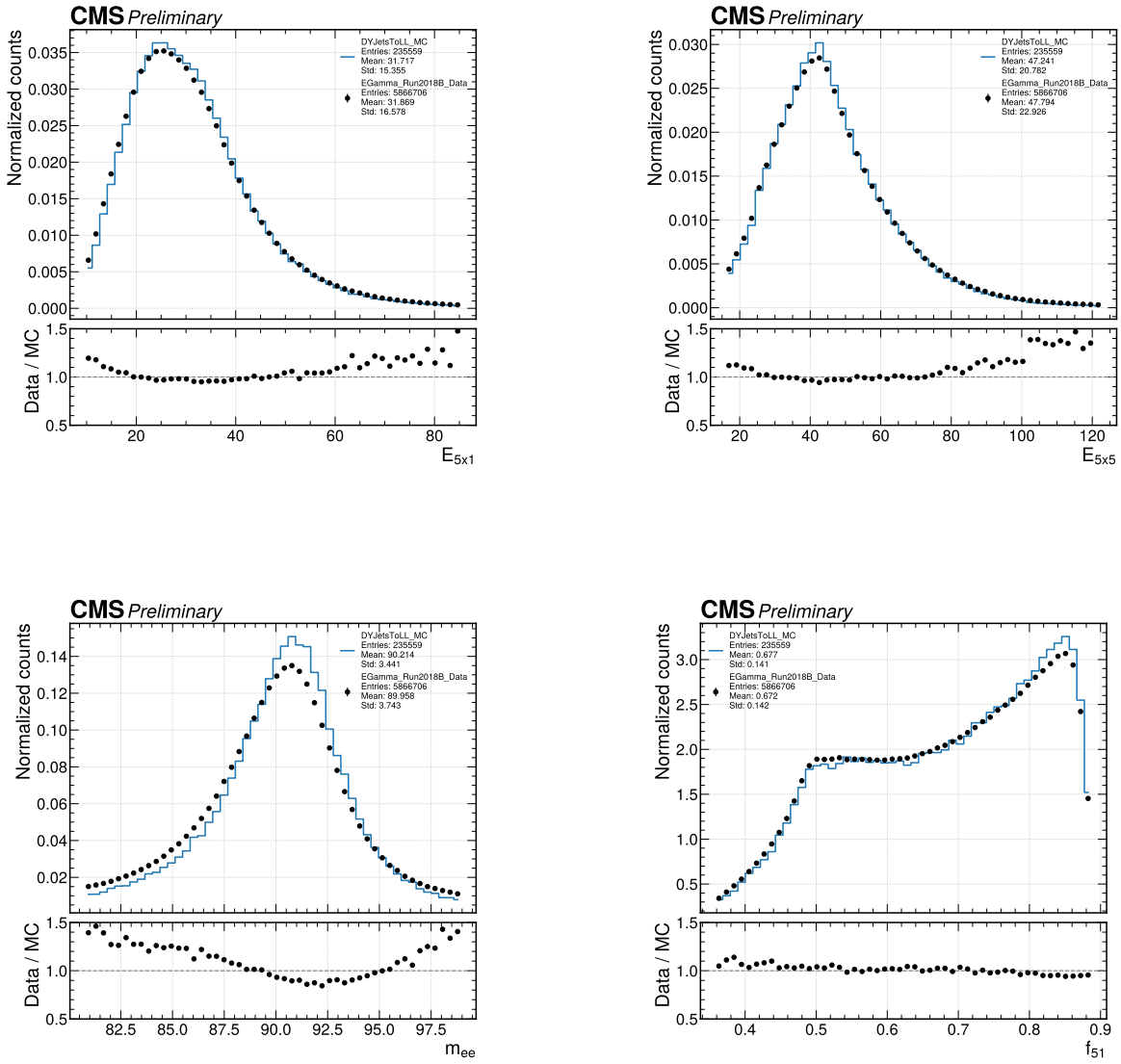

Figure 68 – Distribution of the variable $E_{5\times1}$ (upper left), $E_{5\times5}$ (upper right), invariant mass of the electrons' pair (lower right), and f_{51} (lower right) in the $Z \to e^+e^-$ control region for data and simulation, considering only the `RecHits` located in the electromagnetic barrel (EB). The solid blue histogram corresponds to the DYJetsToLL Monte Carlo simulation, while the black points represent data from the Run2018B EGamma dataset. Both distributions are normalized to the unit area to allow shape comparison. The lower panel shows the data/MC ratio as a function of f51, with a dashed line at unity to guide the eye. The control region is defined by requiring both electrons to have $p_T > 25$ GeV, $|\eta| < 2.5$, and an invariant mass between 80 and 100 GeV.

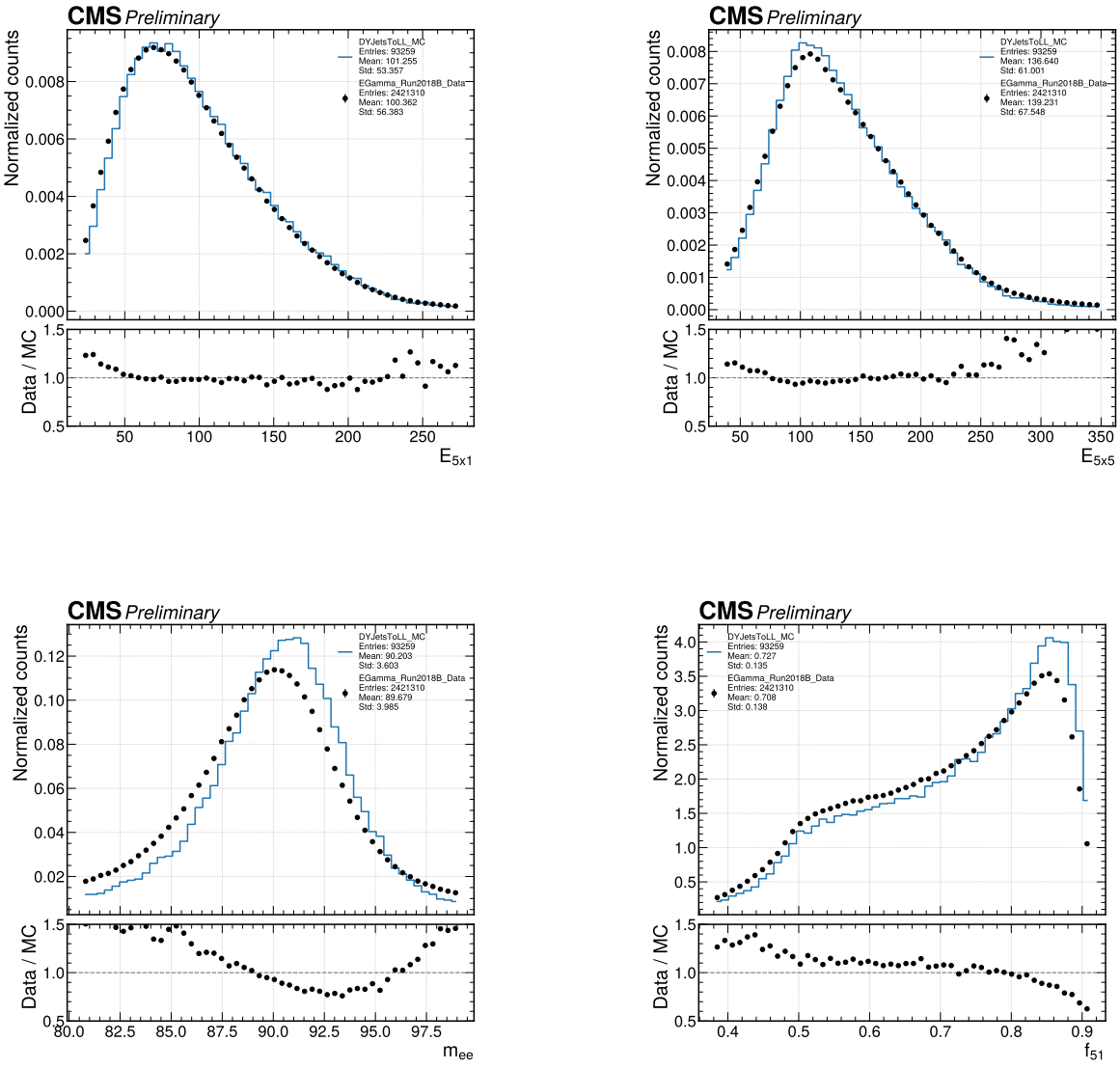

Figure 69 – Distribution of the variable $E_{5\times1}$ (upper left), $E_{5\times5}$ (upper right), invariant mass of the electrons' pair (lower right), and f_{51} (lower right) in the $Z \to e^+e^-$ control region for data and simulation, considering only the `RecHits` located in the electromagnetic end-cap (EE). The solid blue histogram corresponds to the DYJetsToLL Monte Carlo simulation, while the black points represent data from the Run2018B EGamma dataset. Both distributions are normalized to the unit area to allow shape comparison. The lower panel shows the data/MC ratio as a function of f51, with a dashed line at unity to guide the eye. The control region is defined by requiring both electrons to have $p_T > 25$ GeV, $|\eta| < 2.5$, and an invariant mass between 80 and 100 GeV.

6.7 The isolation in the Hadronic Calorimeter

The energy deposits in the hadronic calorimeter (HCAL) near electromagnetic clusters can be calculated as the sum of the energies deposited in a ring with a radius of $0.1 < \Delta R < 0.4$, centered on the electromagnetic crystal. Since the monopole candidates lose their energy in the ECAL faster than an ordinary particle, significant HCAL energy deposits aren't expected. In other words, it is possible to expect an electromagnetic cluster with little or no associated hadronic activity at all. The HCAL isolation variable is defined as the total hadronic energy of all *CaloTowers* in the first segmentation of the HCAL. For the monopole identification, a pre-selection cut is employed in the HCAL isolation, requiring it to be less than 10 GeV.

In Figure 70, the distributions for the Hadronic Isolation variable can be found for different mass points ranging from 1000 GeV to 4500 GeV, for the 2018 MC campaign. The results were obtained for the four production modes considered: Drell-Yan and Photon Fusion for spin 0 and spin 1/2 states.

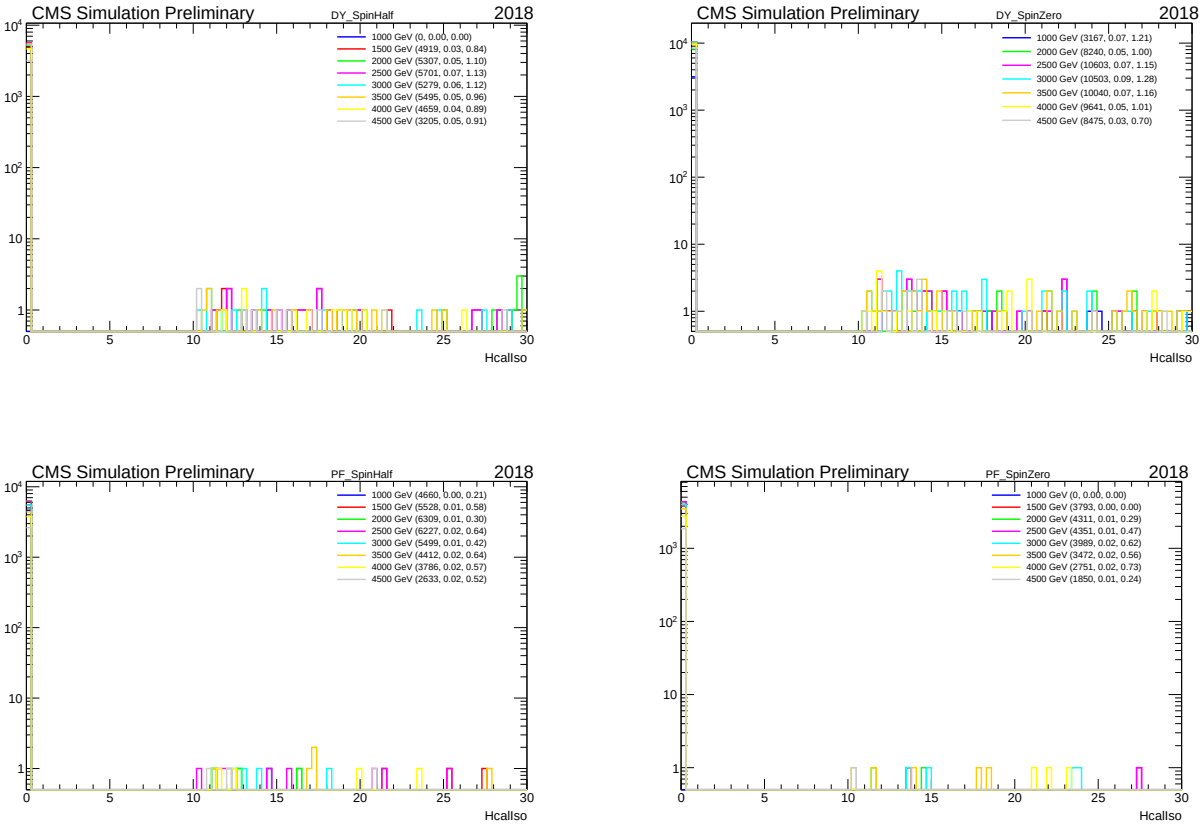

Figure 70 – The normalized distribution of Hadronic Isolation (*HCalIso*) for Run II signal MC for the generated mass points for Spin Half Drell-Yan (upper left), Spin Zero Drell-Yan (upper right), Spin Half Photon Fusion (lower left) and Spin Zero Photon Fusion (lower right) production modes.

6.8 Monopole Datasets

In this thesis, the reprocessed `Ultra Legacy` (UL) data taken during Run 2 (2016, 2017, and 2018), composed of the `SinglePhoton` or `EGamma` and the `MET` datasets, was used. In the Table 10, the `EGamma` datasets can be found, while the `MET` datasets are presented in the Table 11.

For the `EGamma` datasets, for the year 2016, the total integrated luminosity is 36.33 fb^{-1}, while for 2017 and 2018, 41.48 fb^{-1} and 59.39 fb^{-1}, respectively, totaling 137.2 fb^{-1}. Regarding the `MET` datasets, the same integrated luminosity was used for 2016 and 2018 as for EGamma. However, since the MET trigger path employed in the analysis was not available for the entire 2017 data-taking period, only 36.7 fb^{-1} of integrated luminosity for that year. In Table 12, the total delivered and recorded integrated luminosity can be found for the `SinglePhoton/EGamma` and `MET` datasets.

Year	Run	Datasets
2016 - APV	2016B	/SinglePhoton/Run2016B-EXOMONOPOLE-21Feb2020.ver1_UL2016_HIPM-v1/USER
	2016C	/SinglePhoton/Run2016C-EXOMONOPOLE-21Feb2020_UL2016_HIPM-v1/USER
	2016D	/SinglePhoton/Run2016D-EXOMONOPOLE-21Feb2020_UL2016_HIPM-v1/USER
	2016E	/SinglePhoton/Run2016E-EXOMONOPOLE-21Feb2020_UL2016_HIPM-v1/USER
	2016F	/SinglePhoton/Run2016F-EXOMONOPOLE-21Feb2020_UL2016_HIPM-v1/USER
2016	2016F	/SinglePhoton/Run2016F-EXOMONOPOLE-21Feb2020_UL2016-v1/USER
	2016G	/SinglePhoton/Run2016G-EXOMONOPOLE-21Feb2020_UL2016-v1/USER
	2016H	/SinglePhoton/Run2016H-EXOMONOPOLE-21Feb2020_UL2016-v1/USER
2017	2017B	/SinglePhoton/Run2017B-EXOMONOPOLE-09Aug2019_UL2017-v1/USER
	2017C	/SinglePhoton/Run2017C-EXOMONOPOLE-09Aug2019_UL2017-v1/USER
	2017D	/SinglePhoton/Run2017D-EXOMONOPOLE-09Aug2019_UL2017-v1/USER
	2017E	/SinglePhoton/Run2017E-EXOMONOPOLE-09Aug2019_UL2017-v1/USER
	2017F	/SinglePhoton/Run2017F-EXOMONOPOLE-09Aug2019_UL2017-v1/USER
2018	2018A	/EGamma/Run2018A-EXOMONOPOLE-12Nov2019_UL2018-v2/USER
	2018B	/EGamma/Run2018B-EXOMONOPOLE-12Nov2019_UL2018-v2/USER
	2018C	/EGamma/Run2018C-EXOMONOPOLE-12Nov2019_UL2018-v2/USER
	2018D	/EGamma/Run2018D-EXOMONOPOLE-12Nov2019_UL2018-v4/USER

Table 10 – The SinglePhoton/EGamma datasets of the 2016, 2016APV, 2017 and 2018 years used in this analysis.

Year	Run	Datasets
2016 - APV	2016B	/MET/Run2016B-EXOMONOPOLE-21Feb2020_ver2_UL2016_HIPM-v1/USER
	2016C	/MET/Run2016C-EXOMONOPOLE-21Feb2020_UL2016_HIPM-v1/USER
	2016D	/MET/Run2016D-EXOMONOPOLE-21Feb2020_UL2016_HIPM-v1/USER
	2016E	/MET/Run2016E-EXOMONOPOLE-21Feb2020_UL2016_HIPM-v1/USER
	2016F	/MET/Run2016F-EXOMONOPOLE-21Feb2020_UL2016_HIPM-v1/USER
2016	2016F	/MET/Run2016F-EXOMONOPOLE-21Feb2020_UL2016-v1/USER
	2016G	/MET/Run2016G-EXOMONOPOLE-21Feb2020_UL2016-v1/USER
	2016H	/MET/Run2016H-EXOMONOPOLE-21Feb2020_UL2016-v2/USER
2017	2017B	/MET/Run2017B-EXOMONOPOLE-09Aug2019_UL2017_rsb-v1/USER
	2017C	/MET/Run2017C-EXOMONOPOLE-09Aug2019_UL2017_rsb-v1/USER
	2017D	/MET/Run2017D-EXOMONOPOLE-09Aug2019_UL2017_rsb-v1/USER
	2017E	/MET/Run2017E-EXOMONOPOLE-09Aug2019_UL2017_rsb-v1/USER
	2017F	/MET/Run2017F-EXOMONOPOLE-09Aug2019_UL2017_rsb-v1/USER
2018	2018A	/MET/Run2018A-EXOMONOPOLE-12Nov2019_UL2018_rsb-v1/USER
	2018B	/MET/Run2018B-EXOMONOPOLE-12Nov2019_UL2018_rsb-v1/USER
	2018C	/MET/Run2018C-EXOMONOPOLE-12Nov2019_UL2018_rsb-v1/USER
	2018D	/MET/Run2018D-EXOMONOPOLE-12Nov2019_UL2018_rsb-v2/USER

Table 11 – The MET datasets of the 2016, 2016APV, 2017 and 2018 years used in this analysis.

Years	`SinglePhoton/EGamma` (fb^{-1})	`MET` (fb^{-1})
2016 + 2016APV	35.9	35.9
2017	41.5	36.7
2018	59.8	59.8
Total	137.2	133.5

Table 12 – The integrated luminosity delivered and recorded by the CMS detector for Run 2 data-taking, in units of fb^{-1}. The total delivered luminosity is 137.2 fb^{-1}, with 132.7 fb^{-1} successfully recorded for the `SinglePhoton/EGamma` datasets, and 133.5 fb^{-1} for the `MET` datasets.

6.9 Monopole Identification and Analysis Strategies

As discussed in the previous sections, the monopole candidate reconstruction relies on three components: the track fit parameters, exploiting the peculiar trajectory of the monopoles, the track ionization, due to its remarkable ionization capacity, and the ECAL cluster. In the second step, these reconstructed monopole tracks are then matched with ECAL clusters to form a monopole candidate.

Monopole candidates are reconstructed by extrapolating their tracks to the ECAL and matching them to the nearest ECAL cluster. A requirement is imposed on the spatial separation between the track and the cluster, defined by $\Delta R = \sqrt{\phi^2 + \eta^2} < 0.5$, to ensure a consistent match.

The combination of these characteristics is used to build the event selection criteria employed in this analysis, as presented in Table 9.

This analysis employs two distinct strategies. The first is the `Photon Analysis Strategy`, which is based on the `SinglePhoton` trigger paths. This strategy exploits the scenario where a monopole candidate could be interpreted as a fake photon, activating the `SinglePhoton` trigger. The second is the `PFMET Analysis Strategy`, which employs `PFMET` trigger paths. This approach investigates the possibility of monopole candidates being reconstructed as `ParticleFlow` objects. Both of these analyses, along with their specific event selection criteria, will be discussed in more detail in dedicated sections.

For both approaches, a set of preselections and tight selections through which events must be satisfied to be considered as monopole candidates. The combination of both sets of trigger paths is considered to improve the signal efficiency of the analysis, which is deeply affected by the `sFGVB`, commonly known as the "spike-killer" algorithm built in L1, described in Section 3.2.7.2.

6.9.1 Photon Analysis Strategy

The `Photon Strategy` is motivated by the possibility that a monopole candidate could be interpreted as a fake photon that can activate the *Single Photon* trigger. However, due to the L1 `sFGVB` "spike-killer" algorithm, this analysis considers only monopole candidates that do not deposit all their energy into a single central ECAL crystal. For an energy deposition pattern that spreads for more than one crystal, the behavior of a monopole candidate and a photon appears similar. On the other hand, the energy deposition of a monopole candidate and a photon is very different, since for the latter a dispersed energy deposition is expected rather than a narrow and concentrated pattern produced by the monopoles.

To retrieve some of the rejected events by the `sFGVB` algorithm, to improve the signal efficiency, we incorporate unclean clusters (as described in Section 6.6.2). These clusters, which were rejected by the sFGVB algorithm, are incorporated into the offline reconstruction chain via the combined cluster collection.

For this analysis, an unprescaled trigger path is used. For the 2017 and 2018 datasets, `HLT_Photon200_v*` is employed, while for the 2016 datasets, the `HLT_Photon175_v*` is used. This change for 2017 and 2018 was necessary because the 2016 trigger path became prescaled in those years. For the `Single Photon` trigger paths, an object is required with a transverse energy (E_T) of 200 GeV and 175 GeV, matching the trigger path thresholds.

The trigger efficiency of the `Photon Strategy` for the monopoles is highest when the hits are located in the detector end-caps, where the spike-rejection criteria are less stringent. In contrast, the ECAL barrel applies stricter spike suppression, allowing triggers primarily from monopoles that hit near cell boundaries. Although the Drell–Yan production mechanism favors central monopole production, a significant fraction of the trigger efficiency still originates from end-cap hits. Since heavier monopoles are produced more centrally, it is expected that there will be a decrease in the trigger and signal efficiency for the higher mass points. The identification selection criteria applied to the monopole candidate identification for the `Photon Strategy` are described in the Table 13.

Identification selection	variable	value
Trigger selection	HLT_Photon200_v* (2017,2018) HLT_Photon175_v* (2016)	
Energy variable	E_{5x5} (2017,2018) E_{5x5} (2016) HCAL isolation	> 200 GeV > 175 GeV < 10 GeV
Significant variable	$dE/dx_{significance}$ f_{51}	> 9 > 0.85

Table 13 – Identification selection criteria applied to the monopole candidates under the `Photon Strategy`. The trigger requirements vary by data-taking year, to ensure the employment of unprescaled trigger paths. The energy variable ensures high transverse energy candidates and the significance of energy loss per unit length $dE/dX_{\texttt{Significance}}$ and the topological cluster variable f_{51} are used to enhance signal purity.

6.9.2 PFMET Analysis Strategy

In the CMS Experiment, the missing transverse momentum ($\vec{p}_T^{\,\text{miss}}$) often referred to as the *Missing Transverse Energy* (MET), is defined as the negative vector sum of the transverse momenta of all reconstructed particles, as given by the Equation 6.5. The negative sign ensures that the vector points in the direction opposite to the total visible momentum in the transverse plane, thereby reflecting the momentum carried away by undetected particles. In CMS, this quantity is computed using all Particle-Flow (PF) candidates, and its magnitude, $\vec{p}_T^{\,\text{miss}} = |\vec{p}_T^{\,\text{miss}}|$, is typically used in analyses and event selection.

$$\vec{E}_T^{\text{miss}} = -\sum \vec{p}_T \tag{6.5}$$

From the conservation of momentum, the total transverse momentum from a pp collision in the CMS detector is expected to be zero. However, contributions from undetected particles such as neutrinos or dark matter candidates, among others, lead to a violation of momentum conservation. The MET can be categorized into `CaloMET` and `PFMET` contributions. The first is defined as the sum of transverse momentum from the energies contained in calorimeter towers, while the second corresponds to the reconstruction with the `Particle Flow` (PF) [112] algorithm to obtain the sum of transverse momentum of the PF.

The application of the `PFMET` trigger paths is motivated by the conjecture that a large MET contribution arises from the failure of the monopole reconstruction. The conjecture is that one of the monopoles is rejected by the "spike-killer" while the second monopole is not rejected and then reconstructed, which fires the `PFMET` trigger.

The definition of PFMET means that for monopoles to contribute to the PFMET

calculation, they must be identified as ParticleFlow (PF) candidates. If a monopole isn't recognized by the PF algorithm, it won't contribute to the PFMET, leading to an apparent MET. In this scenario, there should be a larger MET due to the violation of momentum conservation. This situation is suitable for `CaloMET`, which takes into consideration all the transverse momentum in the ECAL, rather than considering the PF momentum. However, the efficiency of the unprescaled `CaloMET` trigger is significantly lower than the `PFMET` trigger paths, leading to the preference of the latter. In Figure 71, the signal efficiency of the `PFMET` and `CaloMET` trigger paths considered is presented.

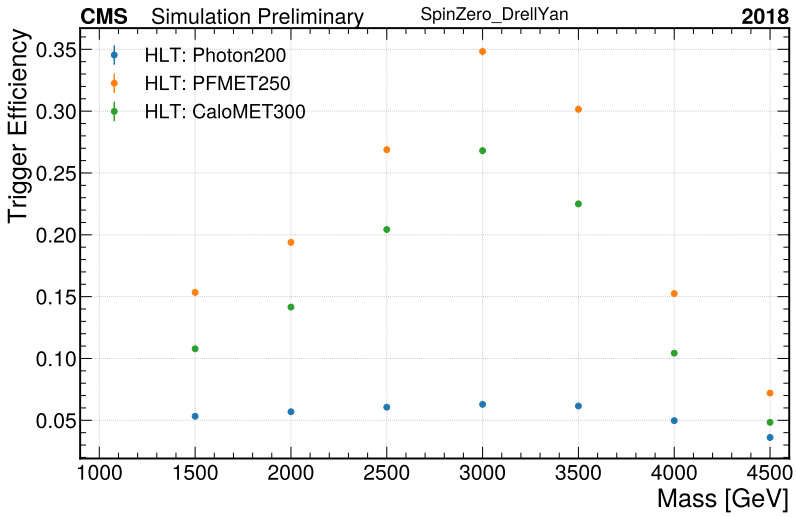

Figure 71 – Signal Efficiency for all the mass points considered for Drell-Yan Spin Zero production mode considering the 2018 MC campaign. The blue dots correspond to the efficiency of the `HLT_Photon200` trigger path, the green dots to the `HLT_PFMET250_HBHECleaned` trigger path, and the orange dots correspond to the `HLT_CaloMET300_HBHECleaned` trigger path. It is worth noting the significantly higher efficiencies for both MET-related triggers, with the `PFMET`-related the trigger path with the higher efficiency.

6.9.2.1 Monopole as PF candidates - Categories

In this study, a reconstructed monopole can be defined as a particle candidate that satisfies the selection criteria listed in Table 9, along with an additional requirement that the cluster energy exceeds $E_{5\times5} > 50$ GeV.

To study the efficiency of the identification of a monopole as a PF candidate, a two-step matching process is used. First, the reconstructed monopole is matched to a generated monopole to ensure it is the real monopole. Second, the reconstructed monopole is matched to the PF candidates to evaluate its correspondence with any PF candidate, employing a distance between two particles $\Delta R < 0.15$.

A reconstructed monopole, which has been confirmed as a real monopole, will be called a PF-like monopole if it is identified as any PF candidate. While a reconstructed monopole will be defined in the absence of a PF matching.

In a given event, one or two monopoles can be reconstructed, considering a monopole and the anti-monopole. These can, in turn, be identified as either one or two PF-like monopoles. To explore these scenarios, a clear categorization of the possibilities has been developed, as illustrated in Table 14.

Combinations
1 PF-like + 1 Reco Mono
1 PF-like
2 PF-like
2 Reco Mono
1 Reco Mono
0 monopole

Table 14 – Classification of events based on the combination of PF-like monopoles (identified as PF candidates) and reconstructed monopoles (real monopoles not matched to any PF candidate). The table summarizes the expected PFMET for each category. Large PFMET is expected when one or more real monopoles are not identified by the PF algorithm; small PFMET occurs when all monopoles are either fully identified or absent.

Based on the combination and expected magnitude of MET, we can determine which type of particle the PF-like monopoles correspond to for each categorization. The average MET value for these categorizations is calculated using the PFMET algorithm. In Figure 72, the average MET as a function of the particle ID (PID) is presented.

A monopole has a higher probability of being identified as an electron or a photon compared to other particles. This is expected due to its similar behavior to an electromagnetic particle, given that both electrons and photons are stopped in the ECAL. On the other hand, a monopole could be identified as any kind of PF candidate and counted in the total PF momentum. The numerical scheme for the particle ID (PID) is available in

PID	Type
0	dummy, unknown
1	charged hadron
2	electron
3	muon
4	photon
5	neutral hadron

Table 15 – Table with Particle ID (PID) definitions for PF candidates. Each PID corresponds to a specific particle type used in PF classification, including charged and neutral hadrons, electrons, muons, photons, and unknown types.

Table 15.

The evaluation of the average value of the PFMET for each category considered in this study is illustrated in Figure 16, where the higher expected values are observed for the categories including the monopole candidate as PF candidate.

Combinations	Expected PFMET	Efficiency
1 PF-like + 1 Reco Mono	467.48 ± 193.30	0.02891
1 PF-like	450.63 ± 196.74	0.01584
2 PF-like	500.26 ± 254.27	0.003565
2 Reco Mono	341.87 ± 198.71	0.01842
1 Reco Mono	445.92 ± 200.14	0.03984
0 monopole	97.90 ± 109.80	0.8934

Table 16 – The table summarizes the average value of the PFMET for each category defined, for a combination of MC samples of Spin Half Drell-Yan considering the masses 1000, 1500, and 2000 GeV. Large PFMET is expected when one or more real monopoles are not identified by the PF algorithm. A large PFMET is expected considering that the monopole candidate is reconstructed as the monopole and matched to a PF candidate. Monopole candidates fleeing from the PF algorithm also leads to a large MET. These scenarios are expected to be triggered by the PFMET trigger paths.

This study, based on the 2018 MC sample at the 1000 GeV mass point, confirms that a reconstructed monopole identified as a PF candidate can contribute to a large PFMET. Moreover, scenarios where only one monopole is reconstructed and not matched to any PF candidate also result in large MET. Even when a single monopole is both reconstructed and matched to a PF candidate, significant MET can still be observed. These categories, all leading to elevated PFMET, indicate that the PFMET trigger is effective for capturing monopole events. This makes it a valuable tool for monopole analyses, especially in cases where monopole candidates are likely to be rejected by the CMS Level-1 trigger.

For the development of the analysis strategy (`PFMET Strategy`) applied in this thesis, a combination of unprescaled trigger paths is used. For 2017 and 2018, the events

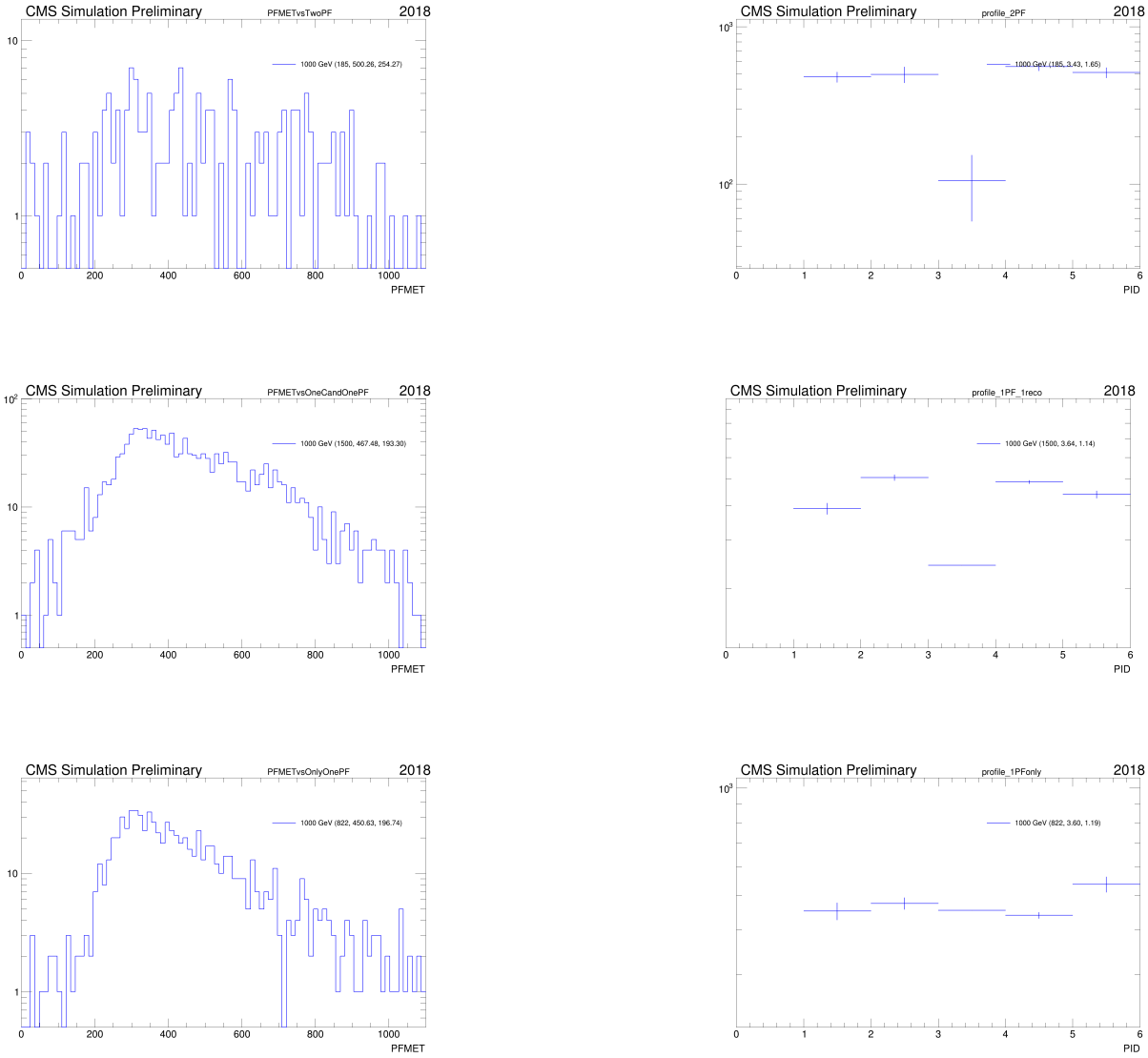

Figure 72 – On the left, the profile diagrams of PFMET versus the type of the PF candidate to which the monopole was matched, from Table 15 where in the right the PFMET for each categorization is illustrated. On the right, the corresponding PFMET distributions for each category are shown. The top row corresponds to the "2 PF-like" categorization, the middle row to "1 PF-like + 1 Reco Mono", and the bottom row to "1 PF-like".

considered were the ones that pass the `HLT_PFMET250_HBHECleaned_v*` but don't fire the `HLT_Photon200_v*`. A similar procedure is considered for 2016 datasets, but with the `HLT_PFMET300` and `HLT_Photon175_v*` trigger paths. Additionally, a requirement on the `PFMET` is required with thresholds of 400 GeV and 500 GeV for 2017(2018) and 2016(2016APV), respectively. The identification selection criteria applied to the monopole candidate identification for the `PFMET Strategy` are described in the Table 17.

Identification selection	variable	value
Trigger selection	HLT_PFMET250_HBHECleaned_v* `AND NOT` HLT_Photon200_v* (2017,2018) HLT_PFMET300_v* `AND NOT` HLT_Photon175_v* (2016)	
PFMET variable	PFMET_{pt} (2017,2018) PFMET_{pt} (2016) HCAL isolation	> 400 GeV > 500 GeV < 10 GeV
Significant variable	$dE/dx_{significance}$ f_{51}	> 9 > 0.85

Table 17 – Identification selection criteria applied to the monopole candidates under the `PFMET Strategy`. The trigger requirements vary by data-taking year, to ensure the employment of unprescaled trigger paths. The `PFMET` requirement ensures high transverse energy candidates and the significance of energy loss per unit length $dE/dX_{\texttt{Significance}}$ and the topological cluster variable f_{51} are used to enhance signal purity.

6.9.3 Words on the analysis strategies

The search for magnetic monopoles in CMS requires innovative approaches due to the particle's extreme energy deposition and anomalous interaction with detector subsystems. In this analysis, two orthogonal strategies, `Photon` and `PFMET`, have been developed to maximize sensitivity. Their design is rooted in complementary assumptions about how monopoles interact with the detector and how they appear (or fail to appear) in the trigger and reconstruction chains. These strategies are not only based on different trigger objects but also probe distinct physical signatures. The `Photon Strategy` benefits from precise EM-like detection, while the `PFMET Strategy` is sensitive to reconstruction failures.

While the two strategies are mostly orthogonal, a subset of events can, in principle, pass both `Photon` and `PFMET` triggers. To prevent double counting, the `PFMET Strategy` is defined to include only events that pass the `PFMET` trigger but fail the corresponding `Photon` trigger. In the overlap region, events are assigned to the `Photon Strategy`, which offers higher efficiency compared to the `PFMET Strategy`. This ensures the statistical inde-

pendence of the two event samples, simplifying the further combination and interpretation of the results. By enforcing this veto condition on the `PFMET Strategy`, each strategy owns a disjoint set of triggered events, allowing for a clean and conservative combination of limits later in the analysis.

A simultaneous statistical combination of the `Photon` and `PFMET` strategies is implemented later in the analysis for the evaluation of the production cross-section upper limits. Given the disjoint nature of the event sets, the combination proceeds under the assumption of independent likelihoods, allowing for straightforward aggregation of signal efficiencies. This separation extends to their dominant background sources and systematic uncertainties, further supporting statistical independence. As a result, the combined limit is built from the product of two independent likelihoods, enabling a robust, unbiased search that leverages the strengths of both approaches while mitigating the dependence on a single trigger or reconstruction method.

6.10 Trigger Efficiencies

The thresholds for both analysis strategies were chosen to correspond to the plateau region of the respective trigger efficiency curves. In this region, the trigger exhibits its highest and most constant efficiency. For the MET triggers, the efficiency at the plateau is close to 1, since the quantities are well measured, meaning that the events with a high MET value will very unlikely be lost by the trigger.

For the `Photon Strategy` the `HLT_Photon200` (`HLT_Photon175`) requires a transverse momentum (p_T) greater than 200 GeV (175 GeV), with an L1 trigger requirement of an electromagnetic object with $p_T > 40$ GeV. The efficiency of such a trigger path is obtained using a *Tag-&-Probe* method with $Z \to e^+e^-$ with the requirement of an isolated electron with $p_T > 35$ GeV. From the trigger efficiency plateau value, a threshold of 200 GeV can be found for 2017 and 2018. [174].

For the `PFMET Strategy`, a combination with the `HLT_PFMET250_HBHECleaned` (2017, 2018) and `HLT_PFMET300` (2016) was applied, where the PFMET trigger efficiency was obtained with the orthogonal method. The orthogonal method is used to evaluate the efficiency of a given trigger in a data-driven way, independent of the trigger itself. In this approach, events are first selected using a trigger that is uncorrelated with PFMET, such as a single-electron or single-muon trigger, ensuring that the sample is unbiased concerning MET. The offline PFMET is then calculated for these events, and the fraction of events that also pass the PFMET trigger is measured as a function of offline PFMET. This method provides a robust estimate of trigger efficiency, minimizing systematic errors in the efficiency estimation. For the `PFMET Strategy`, the thresholds selected were 400 GeV for 2017 and 2018, and 500 GeV for the 2016 [175]. The trigger efficiency turn-on

curves for the MC samples obtained through the cut-and-count method are presented in the Appendix C.

6.11 Signal Efficiency

The signal *Monte Carlo* (MC) magnetic monopole samples were generated for the entire Run 2 period, considering the years of 2016, 2016APV, 2017, and 2018 to study the MC selection efficiency. These samples cover a range of mass points from 1 TeV to 4.5 TeV, as described in Chapter 5

The signal efficiency (ϵ_{sig}) is defined by the Equation 6.6:

$$\epsilon_{sig} = \frac{\text{number of events after the selections applied}}{\text{number of generated events}} \tag{6.6}$$

Although two different analysis strategies are employed on the monopole analysis, the method for the calculation of the signal efficiency holds for both strategies. For the `Photon Strategy`, the HLT trigger, the loose preselection, and the candidate energy cut are applied. On the other hand, for the `PFMET Strategy`, the candidate energy cut is replaced by a cut on the MET reconstructed by the `Particle Flow` (PF) algorithm. After the application of the previous cuts, the monopole candidates are sorted to retrieve the candidate with the highest $dE/dx_{\texttt{Significance}}$. As the last step, a tighter selection of $dE/dx_{\texttt{Significance}}$ and f_{51} was applied for the monopole identification.

The signal efficiency from the cutflow, defined as a series of step-by-step cuts, for the `PFMET Strategy` of the Drell-Yan Spin Half production mode for the year 2018 is presented at Table 18, for 2017 in Table 19, while for 2016 and 2016APV are presented in tables 20 and 21, respectively. In a similar approach, concerning the cutflow of the `Photon Strategy`, the years of 2018, 2017, 2016 an 2016APV are presented in the tables 22, 23, 24 and 25, respectively.

In Appendix B, the additional tables for the Drell-Yan Spin Zero, Photon Fusion Spin Half, and Photon Fusion Spin Zero production modes for both analysis strategies are presented.

Mass [GeV]	1000	1500	2000	2500	3000	3500	4000	4500
Generated	0	96000	97000	100000	93000	100000	100000	94000
Trigger	0	11215	14892	22408	27899	25527	11707	4457
PFMET_pt > 400	0	6212	8610	13775	17462	14839	5414	1967
Preselections	0	5823	8119	12892	16004	13337	4751	1602
$f51 > 0.85$	0	4097	5737	9208	11115	8884	3010	1064
$dEdXSig > 9.0$	0	3742	5164	7991	9004	6653	2165	759
signal efficiency (%)	nan	3.898%	5.324%	7.991%	9.682%	6.653%	2.165%	0.807%

Table 18 – The analysis Cutflow for the `PFMET strategy` for SpinHalf-Drell-Yan samples for the 2018 MC campaign. The table shows the number of signal events surviving each selection step across the generated monopole mass points, from 1000 to 4500 GeV. The steps include the HLT application, missing transverse momentum requirement, standard preselection, and the discriminant variable cuts on variables $f_{51} > 0.85$ and $dEdX_{\texttt{Significance}} > 9.0$. The final row corresponds to the overall signal efficiency for each mass point.

Mass [GeV]	1000	1500	2000	2500	3000	3500	4000	4500
Generated	0	91000	95000	100000	93000	100000	99000	96000
Trigger	0	10840	14960	22868	28450	26302	12078	4602
PFMET_pt > 400	0	6032	8768	14014	17652	14934	5466	1935
Preselections	0	5730	8245	13084	16203	13345	4729	1624
$f51 > 0.85$	0	4133	5881	9286	11301	8896	2970	1085
$dEdXSig > 9.0$	0	3769	5253	7976	9044	6705	2130	775
signal efficiency (%)	nan	4.142%	5.529%	7.976%	9.725%	6.705%	2.152%	0.807%

Table 19 – The analysis Cutflow for the `PFMET strategy` for SpinHalf-Drell-Yan samples for the 2017 MC campaign. The table shows the number of signal events surviving each selection step across the generated monopole mass points, from 1000 to 4500 GeV. The steps include the HLT application, missing transverse momentum requirement, standard preselection, and the discriminant variable cuts on variables $f_{51} > 0.85$ and $dEdX_{\texttt{Significance}} > 9.0$. The final row corresponds to the overall signal efficiency for each mass point.

Mass [GeV]	1000	1500	2000	2500	3000	3500	4000	4500
Generated	49092	50000	50000	49086	45420	48601	49082	49081
Trigger	3692	4704	6215	9194	11309	10138	4434	1710
PFMET_pt > 500	1536	2088	2844	4531	5775	4644	1535	588
Preselections	1424	1947	2617	4072	5058	3873	1233	449
$f51 > 0.85$	1101	1406	1844	2972	3683	2640	796	302
$dEdXSig > 9.0$	1065	1336	1728	2694	3260	2180	652	243
signal efficiency (%)	2.169%	2.672%	3.456%	5.488%	7.177%	4.486%	1.328%	0.495%

Table 20 – The analysis Cutflow for the `PFMET strategy` for SpinHalf-Drell-Yan samples for the 2016 MC campaign. The table shows the number of signal events surviving each selection step across the generated monopole mass points, from 1000 to 4500 GeV. The steps include the HLT application, missing transverse momentum requirement, standard preselection, and the discriminant variable cuts on variables $f_{51} > 0.85$ and $dEdX_{\texttt{Significance}} > 9.0$. The final row corresponds to the overall signal efficiency for each mass point.

Mass [GeV]	1000	1500	2000	2500	3000	3500	4000	4500
Generated	49117	50000	48228	49112	50000	50000	50000	49108
Trigger	3714	4700	6030	8971	12610	10382	4529	1651
PFMET_pt > 500	1414	1929	2654	4377	6361	4657	1540	562
Preselections	1342	1804	2475	4035	5659	4075	1276	444
$f51 > 0.85$	1040	1342	1809	2992	4214	2895	876	325
$dEdXSig > 9.0$	990	1238	1642	2564	3192	2040	569	221
signal efficiency (%)	2.016%	2.476%	3.405%	5.221%	6.384%	4.080%	1.138%	0.450%

Table 21 – The analysis Cutflow for the `PFMET strategy` for SpinHalf-Drell-Yan samples for the 2016APV MC campaign. The table shows the number of signal events surviving each selection step across the generated monopole mass points, from 1000 to 4500 GeV. The steps include the HLT application, missing transverse momentum requirement, standard preselection, and the discriminant variable cuts on variables $f_{51} > 0.85$ and $dEdX_{\texttt{Significance}} > 9.0$. The final row corresponds to the overall signal efficiency for each mass point.

Mass [GeV]	1000	1500	2000	2500	3000	3500	4000	4500
Generated	0	96000	97000	100000	93000	100000	100000	94000
Trigger	0	5112	5521	6061	5848	6156	4973	3395
Quality	0	5044	5428	5950	5701	5991	4779	3235
$e55 > 200$	0	4637	4969	5335	4883	5103	4287	2880
$f51 > 0.85$	0	2565	2868	2974	2595	2766	2366	1690
$dEdXSig > 9.0$	0	2546	2836	2940	2555	2704	2277	1582
signal efficiency (%)	0	2.652%	2.924%	2.940%	2.747%	2.704%	2.277%	1.683%

Table 22 – The analysis Cutflow for the `Photon strategy` for SpinHalf Drell-Yan samples for the 2018 MC campaign. The table shows the number of signal events surviving each selection step across the generated monopole mass points, from 1000 to 4500 GeV. The steps include the HLT application, candidate energy requirement, standard preselection, and the discriminant variable cuts on variables $f_{51} > 0.85$ and $dEdX_{\texttt{Significance}} > 9.0$. The final row corresponds to the overall signal efficiency for each mass point.

Mass [GeV]	1000	1500	2000	2500	3000	3500	4000	4500
Generated	0	91000	95000	100000	93000	100000	99000	96000
Trigger	0	5124	5573	6248	6234	6108	4944	3468
Quality	0	5019	5456	6116	6082	5927	4741	3321
$e55 > 200$	0	4576	4982	5402	5168	5075	4130	2965
$f51 > 0.85$	0	2544	2857	3009	2760	2752	2275	1726
$dEdXSig > 9.0$	0	2527	2829	2973	2696	2658	2172	1629
signal efficiency (%)	0	2.777%	2.978%	2.973%	2.899%	2.658%	2.194%	1.697%

Table 23 – The analysis Cutflow for the `Photon strategy` for SpinHalf Drell-Yan samples for the 2017 MC campaign. The table shows the number of signal events surviving each selection step across the generated monopole mass points, from 1000 to 4500 GeV. The steps include the HLT application, candidate energy requirement, standard preselection, and the discriminant variable cuts on variables $f_{51} > 0.85$ and $dEdX_{\texttt{Significance}} > 9.0$. The final row corresponds to the overall signal efficiency for each mass point.

Mass [GeV]	1000	1500	2000	2500	3000	3500	4000	4500
Generated	49092	50000	50000	49086	45420	48601	49082	49081
Trigger	2706	3191	3311	3359	3157	3050	2507	1639
Quality	2581	3070	3184	3260	3047	2900	2380	1534
$e55 > 175$	2281	2826	2936	2947	2650	2525	2155	1441
$f51 > 0.85$	1250	1557	1676	1664	1406	1385	1234	847
$dEdXSig > 9.0$	1242	1550	1663	1647	1387	1351	1180	803
signal efficiency (%)	2.530%	3.100%	3.326%	3.355%	3.054%	2.780%	2.404%	1.636%

Table 24 – The analysis Cutflow for the `Photon strategy` for SpinHalf Drell-Yan samples for the 2016 MC campaign. The table shows the number of signal events surviving each selection step across the generated monopole mass points, from 1000 to 4500 GeV. The steps include the HLT application, candidate energy requirement, standard preselection, and the discriminant variable cuts on variables $f_{51} > 0.85$ and $dEdX_{\texttt{Significance}} > 9.0$. The final row corresponds to the overall signal efficiency for each mass point.

Mass [GeV]	1000	1500	2000	2500	3000	3500	4000	4500
Generated	49117	50000	48228	49112	50000	50000	50000	49108
Trigger	2702	3242	3143	3327	3318	3220	2583	1782
Quality	2597	3129	3050	3221	3195	3101	2474	1680
$e55 > 175$	2324	2893	2815	2902	2803	2709	2235	1555
$f51 > 0.85$	1274	1672	1616	1606	1531	1442	1242	905
$dEdXSig > 9.0$	1263	1649	1600	1578	1474	1357	1152	829
signal efficiency (%)	2.571%	3.298%	3.318%	3.213%	2.948%	2.714%	2.304%	1.688%

Table 25 – The analysis Cutflow for the `Photon strategy` for SpinHalf Drell-Yan samples for the 2016APV MC campaign. The table shows the number of signal events surviving each selection step across the generated monopole mass points, from 1000 to 4500 GeV. The steps include the HLT application, candidate energy requirement, standard preselection, and the discriminant variable cuts on variables $f_{51} > 0.85$ and $dEdX_{\texttt{Significance}} > 9.0$. The final row corresponds to the overall signal efficiency for each mass point.

Figure 73 presents the signal efficiency for the `PFMET strategy` for all considered mass points, covering the 2017 and 2018 datasets and four production modes (Drell-Yan Spin Half, Drell-Yan Spin Zero, Photon Fusion Spin Half, and Photon Fusion Spin Zero). Notably, the Drell-Yan production modes exhibit higher efficiency values. Corresponding results for 2016 and 2016APV are shown in Figure 74. Similarly, Figures 75 and 76 present the signal efficiencies for the `Photon strategy` for the 2017/2018 and 2016/2016APV periods, respectively.

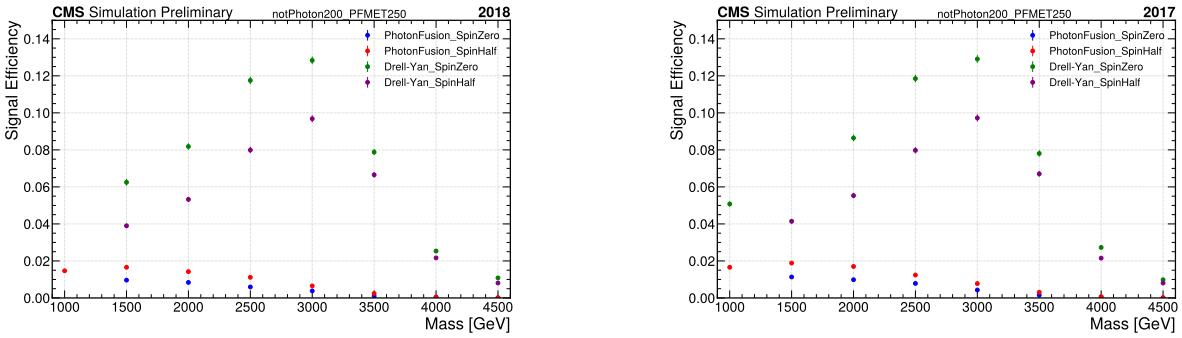

Figure 73 – Signal Efficiency for all the mass points considered, 2018 (left) and 2017 (right) for the `PFMET Strategy`. Drell-Yan Spin Half (blue), Drell-Yan Spin Zero (blue), Photon Fusion Spin Half (blue) Photon Fusion Spin Zero (blue).

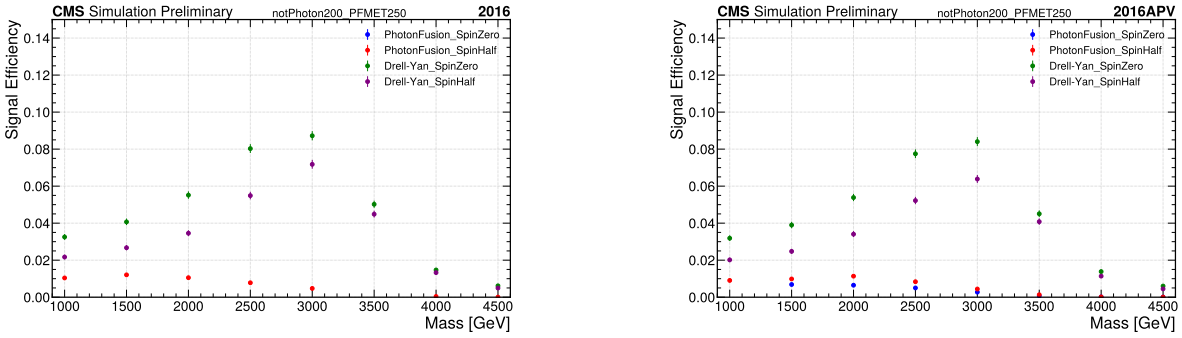

Figure 74 – Signal Efficiency for all the mass points considered, 2016 (left) and 2016APV (right) for the `PFMET Strategy`. Drell-Yan Spin Half (blue), Drell-Yan Spin Zero (blue), Photon Fusion Spin Half (blue) Photon Fusion Spin Zero (blue).

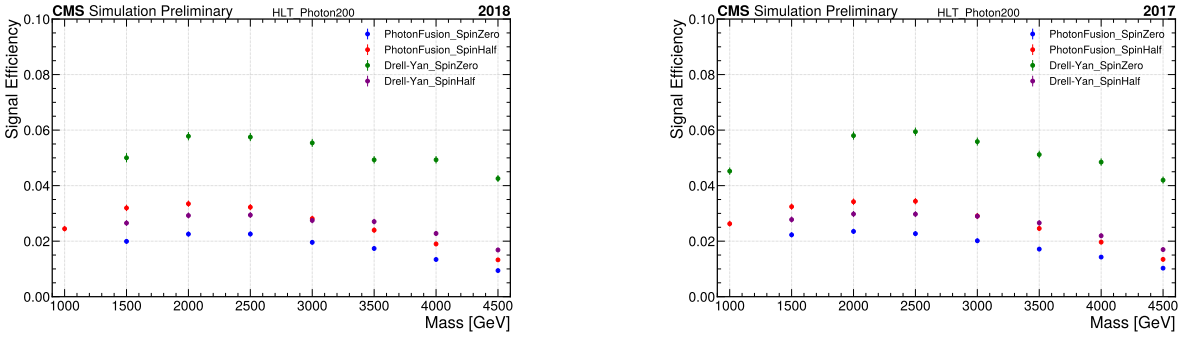

Figure 75 – Signal Efficiency for all the mass points considered, 2018 (left) and 2017 (right) for the `Photon Strategy`. Drell-Yan Spin Half (blue), Drell-Yan Spin Zero (blue), Photon Fusion Spin Half (blue) Photon Fusion Spin Zero (blue).

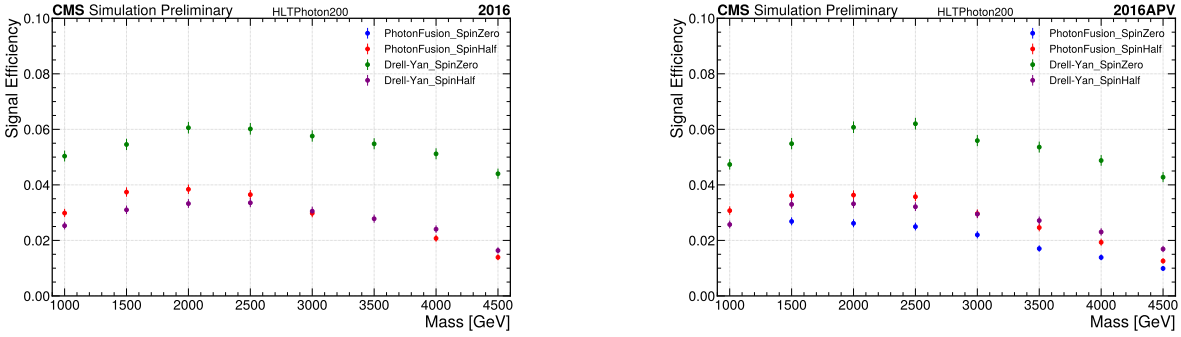

Figure 76 – Signal Efficiency for all the mass points considered, 2016 (left) and 2016APV (right) for the `Photon Strategy`. Drell-Yan Spin Half (blue), Drell-Yan Spin Zero (blue), Photon Fusion Spin Half (blue) Photon Fusion Spin Zero (blue).

The overall signal efficiency is dependent on the production mode and strategy considered. The signal efficiency for the Drell-Yan processes is about 2% to 10% for the `PFMET Strategy` and 3% to 6% for the `Photon Strategy`, while for the Photon Fusion process, the signal efficiency is less than 2% for the `PFMET Strategy` and 1% to 3% for the `Photon Strategy`.

It is worth noting the very low signal efficiency from the `Photon Strategy`, primarily due to the presence of the `sFGVB` "spike-killer", as described in Section 3.2.7.2. To recover some of these lost events, the `PFMET Strategy` was proposed and applied. This approach shows an increase in signal efficiency, particularly for the Drell-Yan production mode.

The joint distribution of the $dE/dX_{\texttt{Significance}}$ and f_{51} for the monopole candidates that pass the trigger selection, preselection, and energy requirement, and the matching with the GEN (Truth) is presented in figures 77 and 78. From the distributions, it is possible to observe that most of the monopoles have a high value of $dE/dX_{\texttt{Significance}}$. Furthermore, the spectrum of f_{51} is wider, but with a high concentration of candidates with values higher than 0.85.

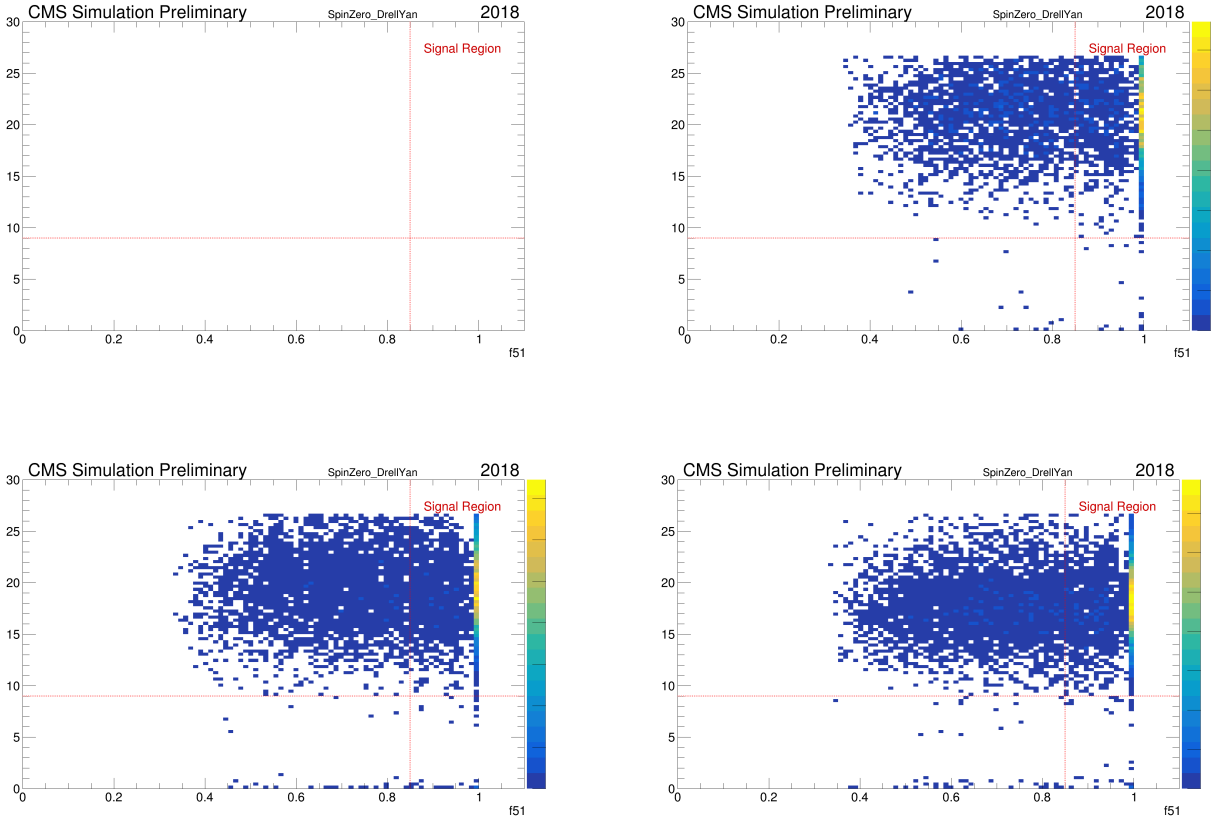

Figure 77 – The joint distribution of $dE/dX_{\texttt{Significance}}$ and f_{51} for the 1000 GeV (upper left), 1500 GeV (upper right), 2000 GeV (lower left) and 2500 GeV (lower right) mass points. The distribution is considering the HLT, preselection, and energy requirements for the 2018 Spin Half Drell Yan MC campaign. The events are filled only once, with the keep of the candidate with the highest $dE/dX_{\texttt{Significance}}$. The Signal Region, defined by $dE/dX_{\texttt{Significance}} > 9.0$ and $f_{51} > 0.85$, is represented by the red dotted lines.

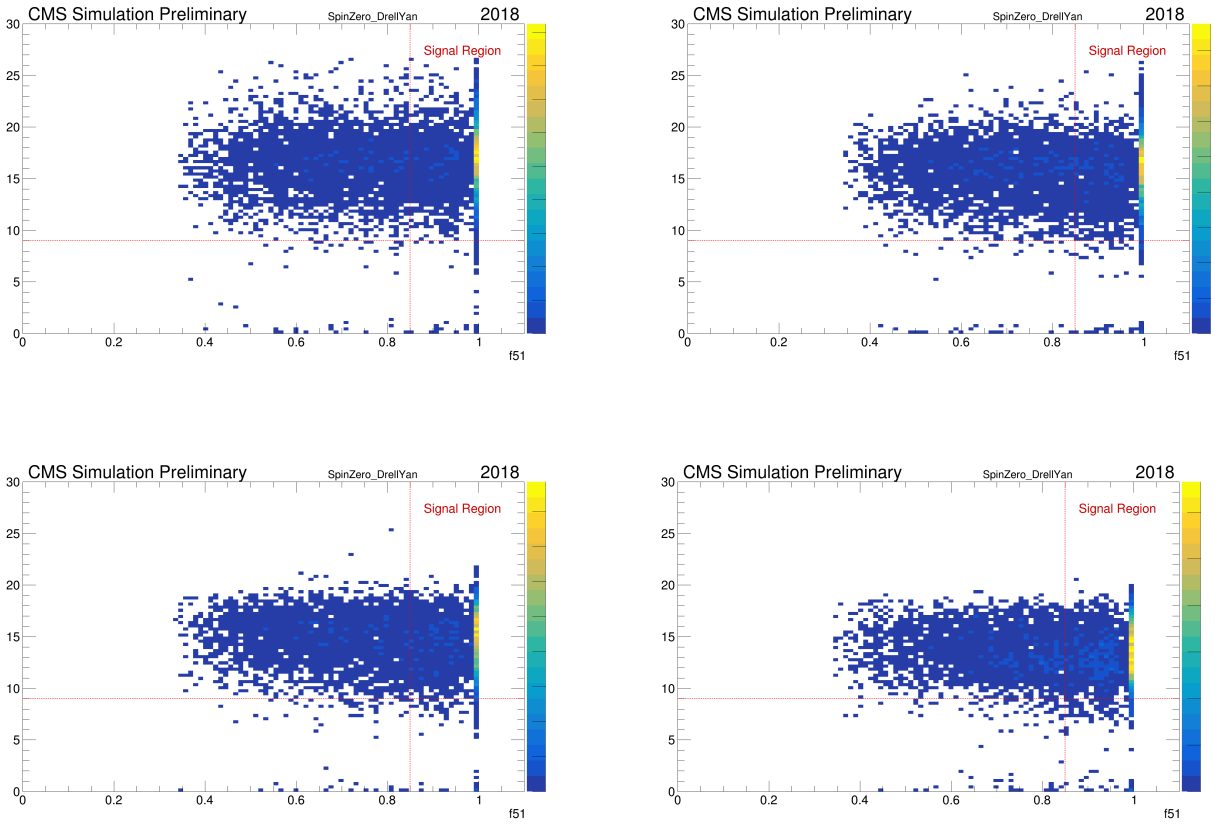

Figure 78 – The joint distribution of $dE/dX_{\texttt{Significance}}$ and f_{51} for the 3000 GeV (upper left), 3000 GeV (upper right), 4000 GeV (lower left) and 4500 GeV (lower right) mass points. The distribution is considering the HLT, preselection, and energy requirements for the 2018 Spin Half Drell Yan MC campaign. The events are filled only once, with the keep of the candidate with the highest $dE/dX_{\texttt{Significance}}$. The Signal Region, defined by $dE/dX_{\texttt{Significance}} > 9.0$ and $f_{51} > 0.85$, is represented by the red dotted lines.

6.11.1 Impact of the sFGVB Spike-Rejection Algorithm on Monopole Signal Efficiency

A critical challenge in the search for magnetic monopoles at the CMS experiment is the impact of the `sFGVB` (Spike Filter Global Veto Bit) spike-filtering algorithm, which operates in both the Level-1 (L1) and High-Level Trigger (HLT) systems. While effective at suppressing instrumental ECAL spikes, this algorithm introduces a significant inefficiency in the detection of the monopole signals. This is because the monopole's unique signature is similar to the noise-like spike patterns that the algorithm is designed to eliminate.

To evaluate the magnitude of this inefficiency, we replicated the full monopole analysis workflow under two conditions: one using the standard `SinglePhoton` trigger with the `Photon Strategy`, and another where the HLT is not applied. For both conditions, all the subsequent reconstruction and analysis cuts were kept identical across both datasets to ensure a consistent comparison.

The central metric for quantifying the signal loss is the spike rejection percentage, computed as:

$$\text{Spikes } (\%) = \left(\frac{N_{\text{noTRG}} - N_{\text{TRG}}}{N_{\text{noTRG}}} \right) \times 100 \tag{6.7}$$

where N_{noTRG} is the number of signal events surviving all analysis selections **without** applying the HLT trigger and N_{TRG} is the number of signal events surviving the same selections **with** the HLT trigger applied.

This evaluation estimates the fraction of monopole events that are rejected by the trigger, particularly by the sFGVB algorithm, because they are incorrectly interpreted as ECAL spikes.

The results for the `Photon Strategy` without the HLT trigger are presented for Drell-Yan Spin Zero, in Table 26, Drell-Yan Spin Half, in Table 27, Photon Fusion Spin Zero, in Table 28, and Photon Fusion Spin Half, Table 29 are presented. It is worth noting how the signal efficiency, on average, is improved by a factor of 10, from the average 2% found for the standard `Photon Strategy`, presented in Section 6.11. The spike percentage is defined by Equation 6.7.

Mass [GeV]	1000	1500	2000	2500	3000	3500	4000	4500
Generated	43000	88000	80000	98000	97000	98000	98010	100000
Trigger	38348	81830	75431	92894	92349	93021	91345	89909
Quality	34271	73150	67156	82979	82632	83312	80956	78108
$e55 > 200$	25186	58261	54760	68424	68374	67095	61871	52546
$f51 > 0.85$	22419	50140	45799	56030	55331	54277	50665	44239
$dEdXSig > 9.0$	22238	49639	45269	55058	53942	52154	47805	40482
signal efficiency (%)	51.716%	56.408%	56.586%	56.182%	55.610%	53.218%	48.776%	40.482%
spikes percentage (%)	90.14%	90.03%	90.04%	90.15%	90.27%	90.57%	89.74%	89.36%

Table 26 – The analysis Cutflow for the `Photon strategy` for SpinZero-DrellYan samples for the 2018 MC campaign. The table shows the number of signal events surviving each selection step across the generated monopole mass points, from 1000 to 4500 GeV. The cutflow is developed without the consideration of the HLT trigger path (`HLT_Photon200/175`), where the steps include candidate energy requirement, standard preselection, and the discriminant variable cuts on variables $f_{51} > 0.85$ and $dEdX_{\texttt{Significance}} > 9.0$. The final two row correspond to the overall signal efficiency and the spikes percentage for each mass point, respectively.

Mass [GeV]	1000	1500	2000	2500	3000	3500	4000	4500
Generated	67000	86000	97000	100000	88144	99000	98000	96020
Trigger	42513	59791	69236	71996	64363	71646	66766	58140
Quality	33906	47350	54793	56965	50943	57647	53629	46553
$e55 > 200$	19396	30020	35195	37428	33114	36485	31812	23270
$f51 > 0.85$	17582	26240	30073	31578	27714	30455	27015	20224
$dEdXSig > 9.0$	17418	25878	29507	30724	26618	28659	24708	17880
signal efficiency (%)	25.997%	30.091%	30.420%	30.724%	30.198%	28.948%	25.212%	18.621%
spikes percentage (%)	91.24%	91.2%	91.01%	91.08%	91.1%	90.7%	90.88%	90.96%

Table 27 – The analysis Cutflow for the `Photon strategy` for SpinHalf-DrellYan samples for the 2018 MC campaign. The table shows the number of signal events surviving each selection step across the generated monopole mass points, from 1000 to 4500 GeV. The cutflow is developed without the consideration of the HLT trigger path (`HLT_Photon200/175`), where the steps include candidate energy requirement, standard preselection, and the discriminant variable cuts on variables $f_{51} > 0.85$ and $dEdX_{\texttt{Significance}} > 9.0$. The final two row correspond to the overall signal efficiency and the spikes percentage for each mass point, respectively.

Additionally, Figure 79 presents the results for both signal efficiency (left plot) and spike percentage (right plot) across all production modes. In such results, the signal efficiency is around 60% for the Drell-Yan Spin Zero production mode, while the spike occurrence is around 90% for all the production modes. A weaker dependence of the signal efficiency on the monopole mass could be observed, which is not as visible in the spike percentage.

This study highlights the need for a dedicated HLT trigger path or an alternative reconstruction approach. Such a solution would preserve monopole sensitivity without compromising the essential ECAL spike suppression required for standard physics analyses.

Mass [GeV]	1000	1500	2000	2500	3000	3500	4000	4500
Generated	0	93000	97000	99000	100000	98000	100000	99000
Trigger	0	59766	64354	65866	64529	60575	56638	49339
Quality	0	45745	49354	50795	49689	46769	43676	37743
$e55 > 200$	0	27778	30494	30880	28376	24683	20183	14580
$f51 > 0.85$	0	24186	26074	26121	23991	21100	17507	12968
$dEdXSig > 9.0$	0	23897	25675	25479	23067	19713	15928	11435
signal efficiency (%)	-	25.696%	26.469%	25.736%	23.067%	20.115%	15.928%	11.551%
spikes percentage (%)	-	92.04%	92.23%	91.74%	91.62%	91.23%	91.44%	91.63%

Table 28 – The analysis Cutflow for the `Photon strategy` for SpinZero-Photon Fusion samples for the 2018 MC campaign. The table shows the number of signal events surviving each selection step across the generated monopole mass points, from 1000 to 4500 GeV. The cutflow is developed without the consideration of the HLT trigger path (`HLT_Photon200/175`), where the steps include candidate energy requirement, standard preselection, and the discriminant variable cuts on variables $f_{51} > 0.85$ and $dEdX_{\texttt{Significance}} > 9.0$. The final two row correspond to the overall signal efficiency and the spikes percentage for each mass point, respectively.

Mass [GeV]	1000	1500	2000	2500	3000	3500	4000	4500
Generated	93000	93000	98000	98000	99000	99000	100000	99000
Trigger	64610	69181	74016	73296	71950	68373	63632	54903
Quality	52465	56097	60208	59430	58031	54608	50139	42977
$e55 > 200$	32187	38798	42427	41098	38195	32924	26764	18920
$f51 > 0.85$	29053	33783	35855	34350	31977	27810	23005	16565
$dEdXSig > 9.0$	28821	33418	35375	33675	30896	26369	21079	14799
signal efficiency (%)	30.990%	35.933%	36.097%	34.362%	31.208%	26.635%	21.079%	14.948%
spikes percentage (%)	90.81%	90.65%	91.2%	91.13%	91.16%	90.88%	90.84%	90.92%

Table 29 – The analysis Cutflow for the `Photon strategy` for SpinHalf-Photon Fusion samples for the 2018 MC campaign. The table shows the number of signal events surviving each selection step across the generated monopole mass points, from 1000 to 4500 GeV. The cutflow is developed without the consideration of the HLT trigger path (`HLT_Photon200/175`), where the steps include candidate energy requirement, standard preselection, and the discriminant variable cuts on variables $f_{51} > 0.85$ and $dEdX_{\texttt{Significance}} > 9.0$. The final two row correspond to the overall signal efficiency and the spikes percentage for each mass point, respectively.

Similar to the results in Section 6.11, the joint distribution of the discriminant variables $dE/dX_{\texttt{Significance}}$ and f_{51} is presented in figures 80 and 81. These figures show monopole candidates that passed the pre-selection, energy requirements, and the matching with the GEN (Truth), but without the application of the SinglePhoton HLT path.

From these distributions, it is possible to observe that most of the monopoles have a high value of $dE/dX_{\texttt{Significance}}$. Furthermore, the f_{51} spectrum is wider, but with a high concentration of candidates with values higher than 0.85.

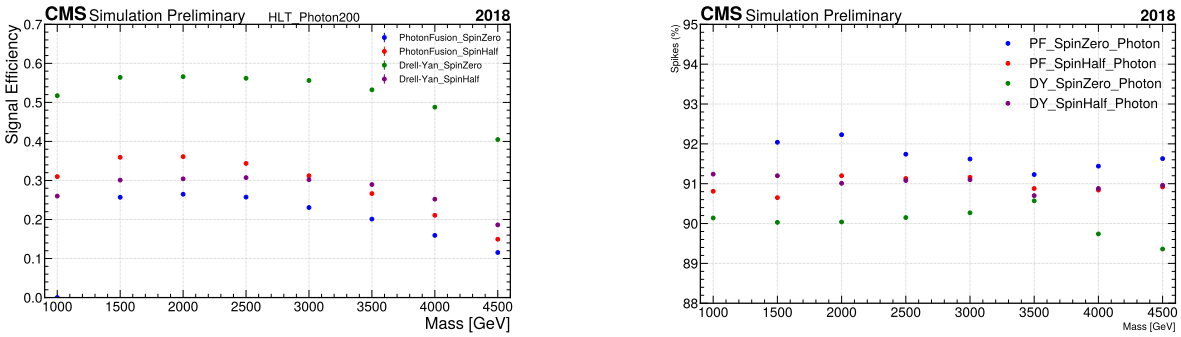

Figure 79 – The left plot corresponds to the Signal Efficiency for the `Photon Strategy` concerning all the mass points considered for the 2018 MC campaign. The production modes are represented by Drell-Yan Spin Half (blue), Drell-Yan Spin Zero (blue), Photon Fusion Spin Half (blue) Photon Fusion Spin Zero (blue). Following the same color logic, the right plot corresponds to the spike percentage values for each considered mass point, following the Eq. 6.7.

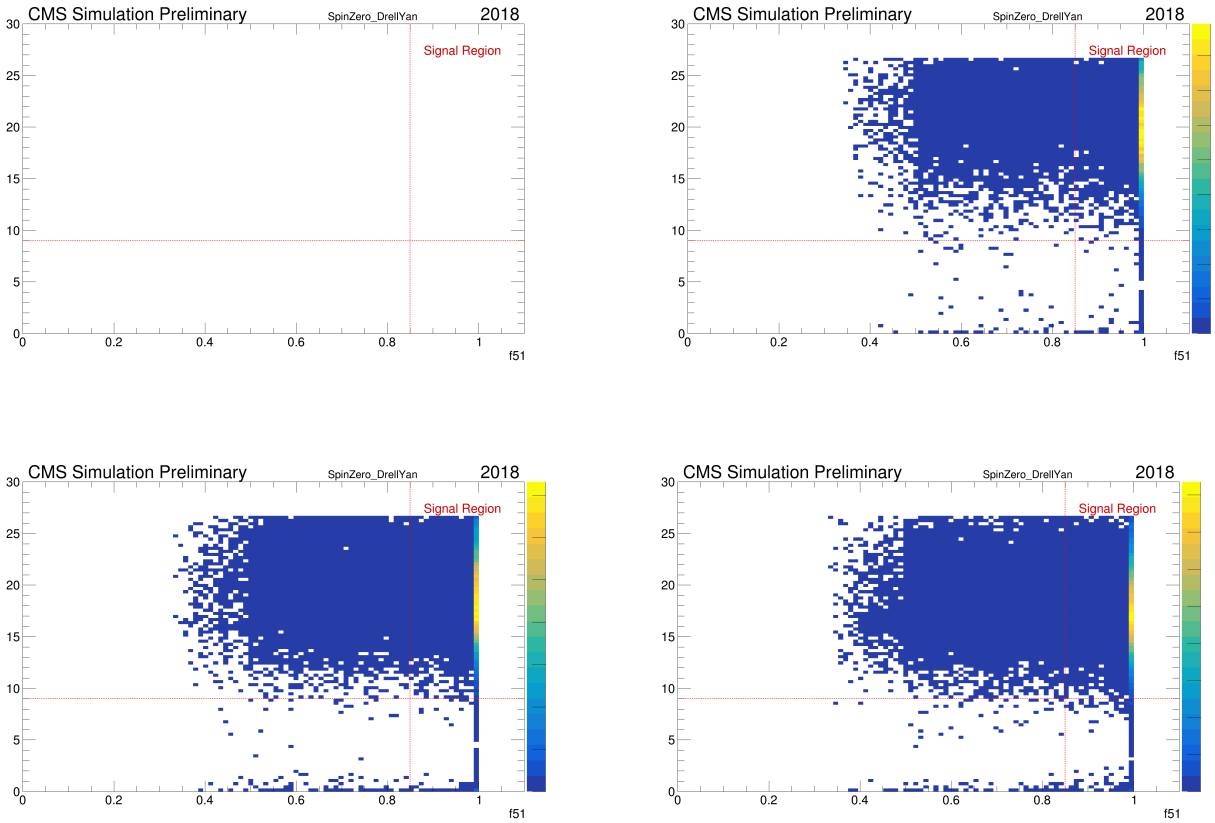

Figure 80 – The joint distribution of $dE/dX_{\texttt{Significance}}$ and f_{51} for the 1000 GeV (upper left), 1500 GeV (upper right), 2000 GeV (lower left) and 2500 GeV (lower right) mass points. The distribution is considering the preselection and energy requirements, without the application of the HLT, for the 2018 Spin Half Drell Yan MC campaign. The events are filled only once, with the keep of the candidate with the highest $dE/dX_{\texttt{Significance}}$. The Signal Region, defined by $dE/dX_{\texttt{Significance}} > 9.0$ and $f_{51} > 0.85$, is represented by the red dotted lines.

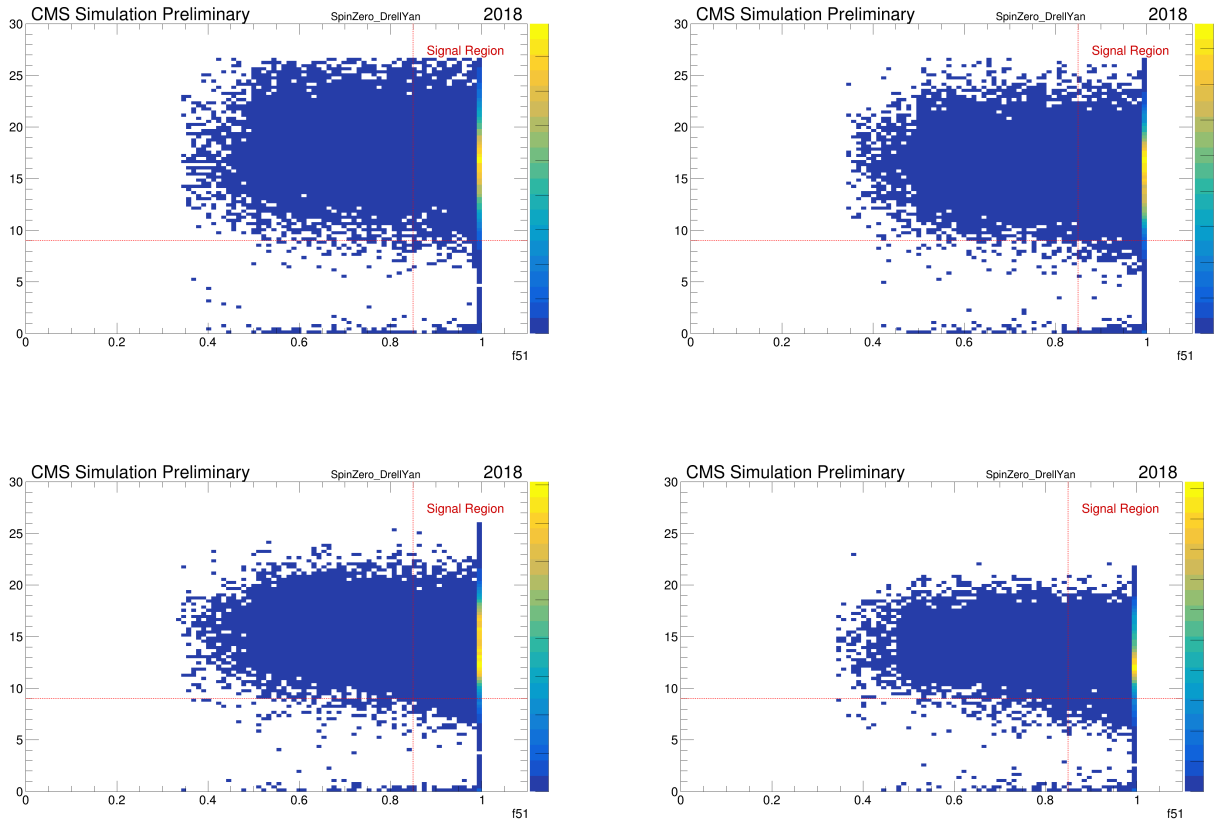

Figure 81 – The joint distribution of $dE/dX_{\texttt{Significance}}$ and f_{51} for the 3000 GeV (upper left), 3500 GeV (upper right), 4000 GeV (lower left) and 4500 GeV (lower right) mass points. The distribution is considering the preselection and energy requirements, without the application of the HLT, for the 2018 Spin Half Drell Yan MC campaign. The events are filled only once, with the keep of the candidate with the highest $dE/dX_{\texttt{Significance}}$. The Signal Region, defined by $dE/dX_{\texttt{Significance}} > 9.0$ and $f_{51} > 0.85$, is represented by the red dotted lines.

6.12 Relative Efficiency

The efficiency of each applied cut can be evaluated using the relative efficiency, a metric defined by Equation 6.8. This definition is consistent and holds for both analysis strategies explored in this work.

$$\epsilon_{rel} = \frac{\text{number of events after the selections}}{\text{number of events of the previous selection}} \tag{6.8}$$

For the `PFMET Strategy`, the tables 30, 31, 32 and 33 corresponds to relative efficiency for the years 2018, 2017, 2016 and 2016APV, respectively.

Mass [GeV]	1000	1500	2000	2500	3000	3500	4000	4500
Trigger	0	0.117	0.154	0.224	0.300	0.255	0.117	0.047
PFMET_pt > 400	0	0.554	0.578	0.615	0.626	0.581	0.462	0.441
Quality	0	0.937	0.943	0.936	0.917	0.899	0.878	0.814
f51 > 0.85	0	0.704	0.707	0.714	0.695	0.666	0.634	0.664
dEdXSig > 9.0	0	0.913	0.900	0.868	0.810	0.749	0.719	0.713

Table 30 – The relative efficiency for `PFMET strategy` for Spin Half Drell-Yan samples for the 2018 MC campaign. Efficiencies are shown for each mass point from 1000 to 4500 GeV and are computed relative to the number of events entering each selection stage and by the Equation 6.8. The steps include the HLT application, missing transverse momentum requirement, standard preselection, and the discriminant variable cuts on variables $f_{51} > 0.85$ and $dEdX_{\texttt{Significance}} > 9.0$.

Mass [GeV]	1000	1500	2000	2500	3000	3500	4000	4500
Trigger	0	0.119	0.157	0.229	0.306	0.263	0.122	0.048
PFMET_pt > 400	0	0.556	0.586	0.613	0.620	0.568	0.453	0.420
Quality	0	0.950	0.940	0.934	0.918	0.894	0.865	0.839
f51 > 0.85	0	0.721	0.713	0.710	0.697	0.667	0.628	0.668
dEdXSig > 9.0	0	0.912	0.893	0.859	0.800	0.754	0.717	0.714

Table 31 – The relative efficiency for `PFMET strategy` for Spin Half Drell-Yan samples for the 2017 MC campaign. Efficiencies are shown for each mass point from 1000 to 4500 GeV and are computed relative to the number of events entering each selection stage and by the Equation 6.8. The steps include the HLT application, missing transverse momentum requirement, standard preselection, and the discriminant variable cuts on variables $f_{51} > 0.85$ and $dEdX_{\texttt{Significance}} > 9.0$.

Mass [GeV]	1000	1500	2000	2500	3000	3500	4000	4500
Trigger	0.075	0.094	0.124	0.187	0.249	0.209	0.090	0.035
PFMET_pt > 500	0.416	0.444	0.458	0.493	0.511	0.458	0.346	0.344
Quality	0.927	0.932	0.920	0.899	0.876	0.834	0.803	0.764
f51 > 0.85	0.773	0.722	0.705	0.730	0.728	0.682	0.646	0.673
dEdXSig > 9.0	0.967	0.950	0.937	0.906	0.885	0.826	0.819	0.805

Table 32 – The relative efficiency for `PFMET strategy` for Spin Half Drell- Yan samples for the 2016 MC campaign. Efficiencies are shown for each mass point from 1000 to 4500 GeV and are computed relative to the number of events entering each selection stage and by the Equation 6.8. The steps include the HLT application, missing transverse momentum requirement, standard preselection, and the discriminant variable cuts on variables $f_{51} > 0.85$ and $dEdX_{\texttt{Significance}} > 9.0$.

Mass [GeV]	1000	1500	2000	2500	3000	3500	4000	4500
Trigger	0.076	0.094	0.125	0.183	0.252	0.208	0.091	0.034
PFMET_pt > 500	0.381	0.410	0.440	0.488	0.504	0.449	0.340	0.340
Quality	0.949	0.935	0.933	0.922	0.890	0.875	0.829	0.790
f51 > 0.85	0.775	0.744	0.731	0.742	0.745	0.710	0.687	0.732
dEdXSig > 9.0	0.952	0.923	0.908	0.857	0.757	0.705	0.650	0.680

Table 33 – The relative efficiency for `PFMET strategy` for Spin Half Drell-Yan samples for the 2016APV MC campaign. Efficiencies are shown for each mass point from 1000 to 4500 GeV and are computed relative to the number of events entering each selection stage and by the Equation 6.8. The steps include the HLT application, missing transverse momentum requirement, standard preselection, and the discriminant variable cuts on variables $f_{51} > 0.85$ and $dEdX_{\texttt{Significance}} > 9.0$.

For the `Photon Strategy`, the tables 34, 35, 36, and 37 correspond to relative efficiency for the years 2018, 2017, 2016, and 2016APV, respectively. For the given strategy, it is worth noting the trigger (`SinglePhoton`) as the main source of inefficiency for this strategy, and therefore the analysis, due to the sFGVB filtering algorithm as mentioned in Section 3.2.7.2.

Mass [GeV]	1000	1500	2000	2500	3000	3500	4000	4500
Trigger	0	0.053	0.057	0.061	0.063	0.062	0.050	0.036
Quality	0	0.987	0.983	0.982	0.975	0.973	0.961	0.953
e55 > 200	0	0.919	0.915	0.897	0.857	0.852	0.897	0.890
f51 > 0.85	0	0.553	0.577	0.557	0.531	0.542	0.552	0.587
dEdXSig > 9.0	0	0.993	0.989	0.989	0.985	0.978	0.962	0.936

Table 34 – The relative efficiency for `Photon strategy` for Spin Half Drell-Yan samples for the 2018 MC campaign. Efficiencies are shown for each mass point from 1000 to 4500 GeV and are computed relative to the number of events entering each selection stage and by the Equation 6.8. The steps include the HLT application, candidate energy requirement, standard preselection, and the discriminant variable cuts on variables $f_{51} > 0.85$ and $dEdX_{\texttt{Significance}} > 9.0$.

Mass [GeV]	1000	1500	2000	2500	3000	3500	4000	4500
Trigger	0	0.056	0.059	0.062	0.067	0.061	0.050	0.036
Quality	0	0.980	0.979	0.979	0.976	0.970	0.959	0.958
$e55 > 200$	0	0.912	0.913	0.883	0.850	0.856	0.871	0.893
$f51 > 0.85$	0	0.556	0.573	0.557	0.534	0.542	0.551	0.582
$dEdXSig > 9.0$	0	0.993	0.990	0.988	0.977	0.966	0.955	0.944

Table 35 – The relative efficiency for `Photon strategy` for Spin Half Drell-Yan samples for the 2017 MC campaign. Efficiencies are shown for each mass point from 1000 to 4500 GeV and are computed relative to the number of events entering each selection stage and by the Equation 6.8. The steps include the HLT application, candidate energy requirement, standard preselection, and the discriminant variable cuts on variables $f_{51} > 0.85$ and $dEdX_{\texttt{Significance}} > 9.0$.

Mass [GeV]	1000	1500	2000	2500	3000	3500	4000	4500
Trigger	0.055	0.064	0.066	0.068	0.070	0.063	0.051	0.033
Quality	0.954	0.962	0.962	0.971	0.965	0.951	0.949	0.936
$e55 > 175$	0.884	0.921	0.922	0.904	0.870	0.871	0.905	0.939
$f51 > 0.85$	0.548	0.551	0.571	0.565	0.531	0.549	0.573	0.588
$dEdXSig > 9.0$	0.994	0.996	0.992	0.990	0.986	0.975	0.956	0.948

Table 36 – The relative efficiency for `Photon strategy` for Spin Half Drell-Yan samples for the 2016 MC campaign. Efficiencies are shown for each mass point from 1000 to 4500 GeV and are computed relative to the number of events entering each selection stage and by the Equation 6.8. The steps include the HLT application, candidate energy requirement, standard preselection, and the discriminant variable cuts on variables $f_{51} > 0.85$ and $dEdX_{\texttt{Significance}} > 9.0$.

Mass [GeV]	1000	1500	2000	2500	3000	3500	4000	4500
Trigger	0.055	0.065	0.065	0.068	0.066	0.064	0.052	0.036
Quality	0.961	0.965	0.970	0.968	0.963	0.963	0.958	0.943
$e55 > 175$	0.895	0.925	0.923	0.901	0.877	0.874	0.903	0.926
$f51 > 0.85$	0.548	0.578	0.574	0.553	0.546	0.532	0.556	0.582
$dEdXSig > 9.0$	0.991	0.986	0.990	0.983	0.963	0.941	0.928	0.916

Table 37 – The relative efficiency for `Photon strategy` for Spin Half Drell-Yan samples for the 2016APV MC campaign. Efficiencies are shown for each mass point from 1000 to 4500 GeV and are computed relative to the number of events entering each selection stage and by the Equation 6.8. The steps include the HLT application, candidate energy requirement, standard preselection, and the discriminant variable cuts on variables $f_{51} > 0.85$ and $dEdX_{\texttt{Significance}} > 9.0$.

For the Photon Strategy, the very low trigger efficiency is the main source of inefficiency for both the strategy and the overall analysis. The pre-selection and energy requirements have a high overall efficiency of more than 85%. The discriminant cuts, however, have efficiencies of around 50–60% for f_{51} and at least 90% for $dE/dX_{\texttt{Significance}}$.

From these results, one can conclude that the overall analysis strategy is quite efficient, apart from the trigger, which remains a significant bottleneck. This highlights a clear opportunity for a substantial gain in efficiency through the development of a dedicated High-Level Trigger (HLT) path for magnetic monopoles or other highly ionizing particles.

For the `PFMET Strategy`, it is worth noting that the trigger efficiency is significantly higher, reaching almost 30% for some mass points. On the other hand, the *PFMET* requirement has an efficiency of about 35-60% depending on the mass points, removing a significant fraction of events "retrieved"by the higher trigger efficiency. The requirement is especially stringent for the higher mass points, where it reaches 35-40%. The preselection presents a relative efficiency of around 80-90%. For the discriminant cuts, they have efficiencies around 60-75% and 70-95% for f_{51} and $dE/dX_{\texttt{Significance}}$, respectively, which is a little less efficient than the `Photon Strategy`.

6.13 Background Estimation

We use a data-driven two-dimensional sideband method (ABCD method) to estimate the background. This method requires two independent variables to define one signal region and three control regions. In Figure 82, the concept of the ABCD method is illustrated. The Region D serves as the *Signal Region* (SR), while Regions A, B, and C are the *Control Regions* (CR), for the estimation of the background contribution within the SR.

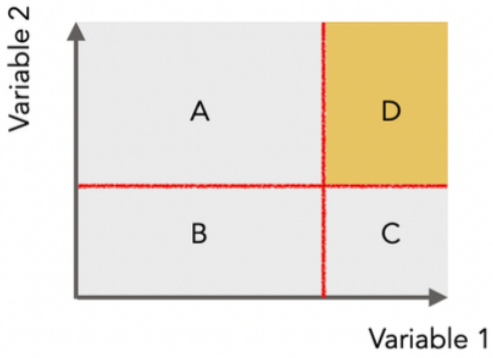

Figure 82 – Schematic representation of the ABCD method used for background estimation. The plane is divided into four regions (A, B, C, D) based on two uncorrelated variables. Region D (shaded) represents the signal-enriched region, while regions A, B, and C are used to predict the background in D.

For the simple ABCD scheme, the number of background events in region D can be estimated from the number of events in regions A, B, and C, by the formula:

$$N_D = \frac{N_A \times N_C}{N_B} \tag{6.9}$$

For this analysis, the two discriminant variables (f_{51} and $dE/dX_{\texttt{Significance}}$) are independent, enabling the use of the ABCD method for background estimation in this analysis.

To increase the confidence of the ABCD estimate, we employ in the magnetic monopoles search at the CMS Experiment the *Double*ABCD method. This method divides the phase space into 9 regions, as illustrated in Figure 83. In this method, regions 5,6, and 8 serve as CRs, defined by the loose values of the discriminant variables f_{51} and $dE/dX_{\texttt{Significance}}$. Region 9 is the SR, defined by the tighter selection on both variables. The remaining regions are background-dominated and used to model the expected background in the SR.

$$N_5 = \frac{N_2 \times N_4}{N_1}, \quad N_6 = \frac{N_3 \times N_4}{N_1}, \quad N_8 = \frac{N_2 \times N_7}{N_1} \tag{6.10}$$

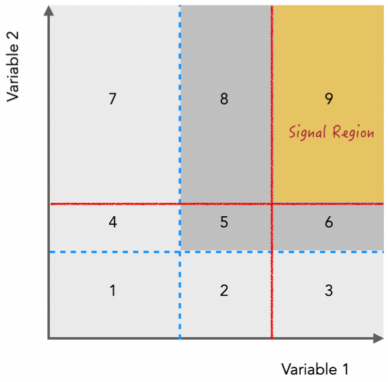

Figure 83 – Double ABCD schematic using a 3 × 3 grid defined by two uncorrelated variables. The plane is divided into nine regions, with Region 9 representing the Signal Region. The regions 5,6 and 8 are the Control Regions. At last, the remaining regions are the background-dominated regions.

$$N_9 = \frac{(N_3 + N_6)(N_7 + N_8)}{(N_1 + N_2 + N_4 + N_5)} \tag{6.11}$$

In the initial stage of the analysis, regions 5, 6, and 8 are blinded. Regions 1, 2, 3, 4, and 7 are used to estimate the expected number of background events in the CRs using the equations in 6.10. Once the expected number of events of the CRs is in good agreement with the actual number from data in these regions, the expected background events can be obtained with the equation 6.11. The loose selection criteria used to define the CRs were optimized separately for 2016, 2017, and 2018, as detailed below:

for 2016 and 2016 APV:

$$0 \leq f_{51} \leq 0.6, \quad 0.6 \leq f_{51} \leq 0.85, \quad 0.85 \leq f_{51} \leq 1$$
$$0 \leq dE/dx_{sig} \leq 6.5, \quad 6.5 \leq dE/dx_{sig} \leq 9, \quad 9 \leq dE/dx_{sig} \leq \infty$$

for 2017 and 2018:

$$0 \leq f_{51} \leq 0.75, \quad 0.75 \leq f_{51} \leq 0.85, \quad 0.85 \leq f_{51} \leq 1$$
$$0 \leq dE/dx_{sig} \leq 7, \quad 7 \leq dE/dx_{sig} \leq 9, \quad 9 \leq dE/dx_{sig} \leq \infty$$

At this stage of the analysis, only blinded LHC data is used to estimate the expected background in the Control Regions (CRs) and the Signal Region (SR). Figures 84 and 85 show the application of the ABCD method to the `SinglePhoton/EGamma` and `MET` datasets, respectively. In this context, "blinded" means that data events falling within the CR and SR are excluded to avoid biasing the analysis. Initially, the CR is unblinded to compare the actual event counts with the ABCD-based background prediction. If the observed and predicted values agree well, the background estimate for the SR is updated

using the unblinded CR data. This validation step supports the final unblinding of the SR, completing the background estimation process.

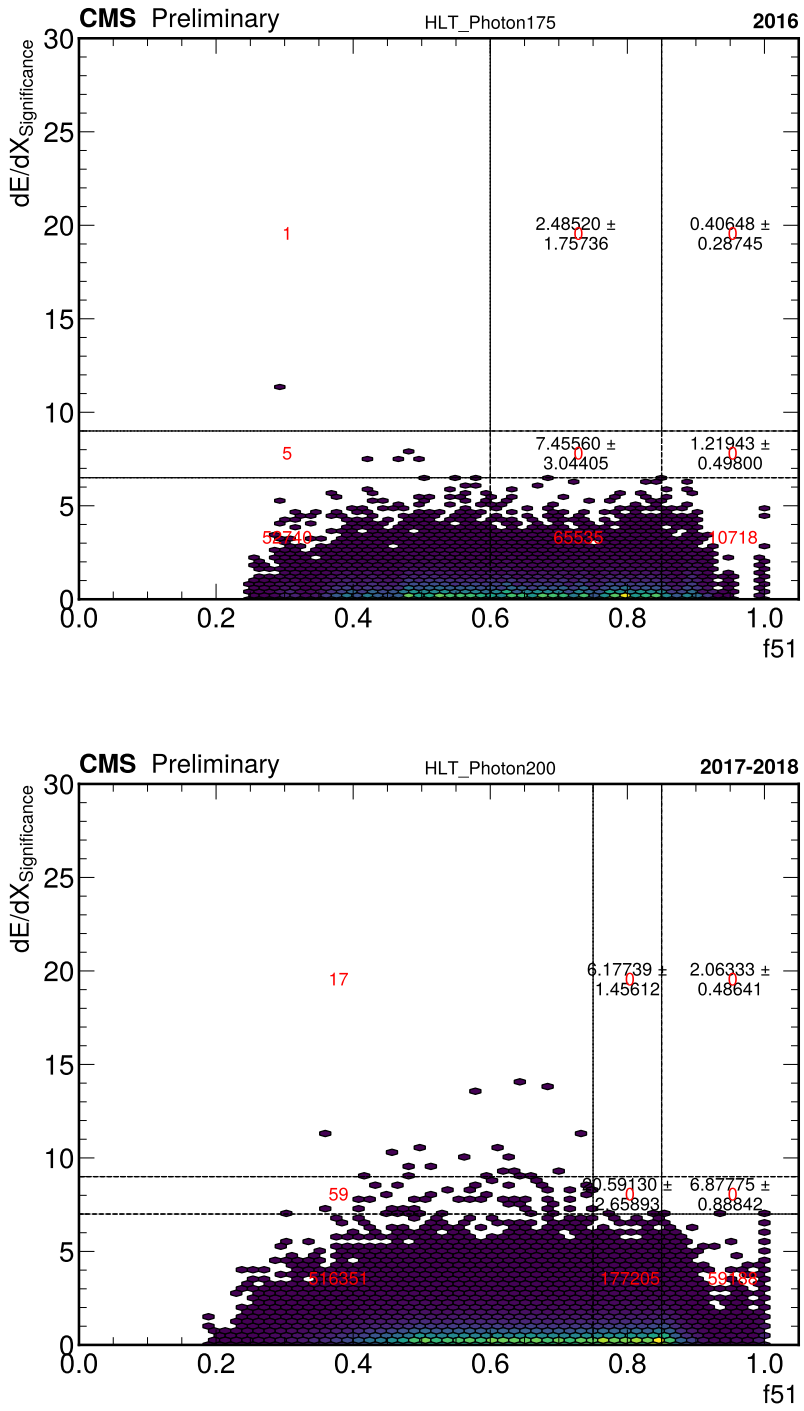

Figure 84 – The data from 2016 (including 2016 APV) are shown in the upper plot, while data from 2017 and 2018 are presented in the lower plot. These datasets are used to estimate the expected background in the signal region for the `SinglePhoton/EGamma` triggers under the `Photon Strategy`. The black numbers indicate the number of expected background events, and the red numbers show the observed event counts in data.

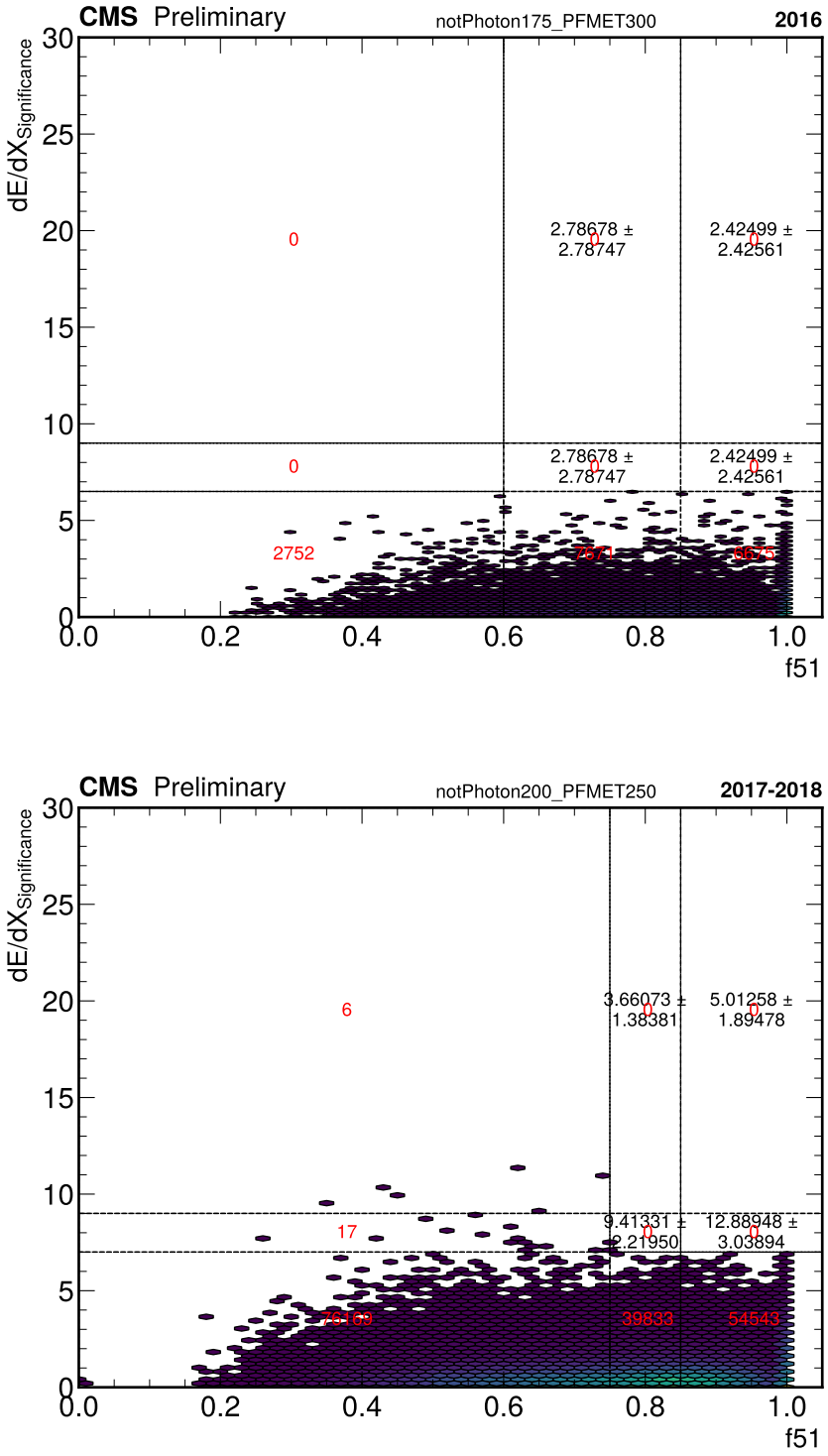

Figure 85 – The data from 2016 (including 2016 APV) are shown in the upper plot, while data from 2017 and 2018 are presented in the lower plot. These datasets are used to estimate the expected background in the signal region for the `PFMET` triggers under the `PFMET strategy`. The black numbers indicate the number of expected background events, and the red numbers show the observed event counts in data.

	region	**actual**	**stat. uncer. (±)**	**expect**	**stat. uncer. (±)**
control region	1	52740	229.6519		
	2	65535	255.9980		
	3	10718	103.5278		
	4	5	2.2360		
	7	1	1		
cross-check	5			7.45560	3.04405
	6			1.21943	0.49800
	8			2.48520	1.75736
signal region	9			0.40648	0.28745

Table 38 – The actual background counting and the statistical uncertainty from the Poisson errors in the background dominated regions (1,2,3,4 and 7) for the 2016(APV) `SinglePhoton/EGamma` datasets. The expected number of events in the CRs (5,6 and 8) are defined by the loose cut ($f_{51} > 0.6$ and $dE/dX_{\texttt{Sig.}} > 6.5$), and the significant cut ($f_{51} < 0.85$ and $dE/dX_{\texttt{Sig.}} > 9.0$). For the agreement between the expected and actual numbers in the CRs, the expected background events in the SR (9) can be estimated, while the actual number was blinded.

	region	**actual**	**stat. uncer. (±)**	**expect**	**stat. uncer. (±)**
control region	1	516351	718.5757		
	2	177205	420.9572		
	3	59188	243.2858		
	4	59	7.6811		
	7	17	4.123		
cross-check	5			20.59130	2.65893
	6			6.87775	0.88842
	8			6.17739	1.45612
signal region	9			2.06333	0.48641

Table 39 – The actual background counting and the statistical uncertainty from the Poisson errors in the background dominated regions (1,2,3,4 and 7) for the 2017 and 2018 *SinglePhoton/EGamma* datasets. The expected number of events in the CRs (5,6 and 8) are defined by the loose cut ($f_{51} > 0.6$ and $dE/dX_{\texttt{Sig.}} > 6.5$), and the significant cut ($f_{51} < 0.85$ and $dE/dX_{\texttt{Sig.}} > 9.0$). For the agreement between the expected and actual numbers in the CRs, the expected background events in the SR (9) can be estimated, while the actual number was blinded.

	region	**actual**	**stat. uncer. (±)**	**expect**	**stat. uncer. (±)**
control region	1	2752	52.459		
	2	7671	87.584		
	3	6675	81.701		
	4	0	0		
	7	0	0		
cross-check	5			2.78678	2.78747
	6			2.42499	2.42561
	8			2.78678	2.78747
signal region	9			2.42499	2.42561

Table 40 – The table the actual background counting and the statistical uncertainty from the Poisson errors in the background dominated regions (1,2,3,4 and 7) for the 2016(APV) *MET* datasets. The expected number of events in the CRs (5,6 and 8) are defined by the loose cut ($f_{51} > 0.6$ and $dE/dX_{\texttt{Sig.}} > 6.5$), and the significant cut ($f_{51} < 0.85$ and $dE/dX_{\texttt{Sig.}} > 9.0$). For the agreement between the expected and actual numbers in the CRs, the expected background events in the SR (9) can be estimated, while the actual number was blinded.

	region	**actual**	**stat. uncer. (±)**	**expect**	**stat. uncer. (±)**
control region	1	76169	275.987		
	2	39833	199.582		
	3	54543	233.545		
	4	17	4.123		
	7	6	2.450		
cross-check	5			9.41331	2.21950
	6			12.88948	3.03894
	8			3.66073	1.38381
signal region	9			5.01258	1.89478

Table 41 – The table the actual background counting and the statistical uncertainty from the Poisson errors in the background dominated regions (1,2,3,4 and 7) for the 2017 and 2018 *MET* datasets. The expected number of events in the CRs (5,6 and 8) are defined by the loose cut ($f_{51} > 0.6$ and $dE/dX_{\texttt{Sig.}} > 6.5$), and the significant cut ($f_{51} < 0.85$ and $dE/dX_{\texttt{Sig.}} > 9.0$). For the agreement between the expected and actual numbers in the CRs, the expected background events in the SR (9) can be estimated, while the actual number was blinded.

6.13.1 Spike Contamination in the Signal Region

In analyses using MET-triggered datasets, it is important to account for non-physics contributions to missing transverse energy, particularly from detector effects such as ECAL spikes. For some studies, these spikes could be indistinguishable from high-energy deposits without associated particle activity, which can lead to artificially large MET values. Unlike object-specific triggers like the `SinglePhoton`, which requires a reconstructed electromagnetic object, the MET trigger is a global event quantity and can be activated by such detector artifacts. As a result, events containing ECAL spikes may pass the MET trigger without any genuine missing energy. This assumption leads to possible challenges for the ABCD background estimation methods since one of the defined regions could be populated by such spike contributions, which can bias the calculations of the expected events in the Control Regions and the Signal Region.

For the implementation of this analysis concerning the `PFMET Strategy`, Region 3, which is defined by a high value of f_{51} and low $dE/dX_{\texttt{Significance}}$, which could be used to define how an ECAL spike would behave in the ABCD. Hence, when evaluating Region 3, a clear accumulation of events as f_{51} approaches 1, which could be interpreted as spike-like contributions, represents a significant source of contamination when estimating the background yield in the Control Regions with special attention to the Signal Region.

To obtain an estimate of the contribution, a dedicated approach was developed. The spike-like candidates are defined by $f_{51} > 0.95$, which will be employed for the derivation of two different evaluations. The first one considers only the candidates with $0.85 < f_{51} < 0.95$, removing the possible spike contributions to obtain the estimate for the Signal Region. For the second evaluation, the consideration of only the events $f_{51} > 0.95$, which are defined as the spike contributions, will lead to an estimate of the SR based solely on the spike-like contributions.

In the first evaluation, the comparison of the estimative in the Signal Region considering this approach and the standard ABCD implementation allows us to isolate the estimative in the SR that is only provenance for the (expected) physics events, completely removing the spike contributions. Similarly, an estimative can also be performed, but now completely removing these physics contributions in Region 3 ($0.85 < f_{51} < 0.95$), considering only the spike-like contributions. This approach allows the evaluation of how much of the events expected in the SR are provenient only from spike-like contributions, which don't carry a physical meaning or a genuine source of MET.

In Figure 86, the results of both evaluations are presented. The left plot corresponds to the ABCD implementation with only the consideration of the spikes, while the right plot corresponds to the implementation considering only the events defined as spikes in Region 3. The statistics for both implementations can be observed in Tables 42 and 43

for the first and second evaluations, respectively. At last, in Table 44, the evaluation concerning the results from both approaches described and their combination is compared with the default approach, to ensure consistency in the retrieval of the value obtained by the default method from the combination.

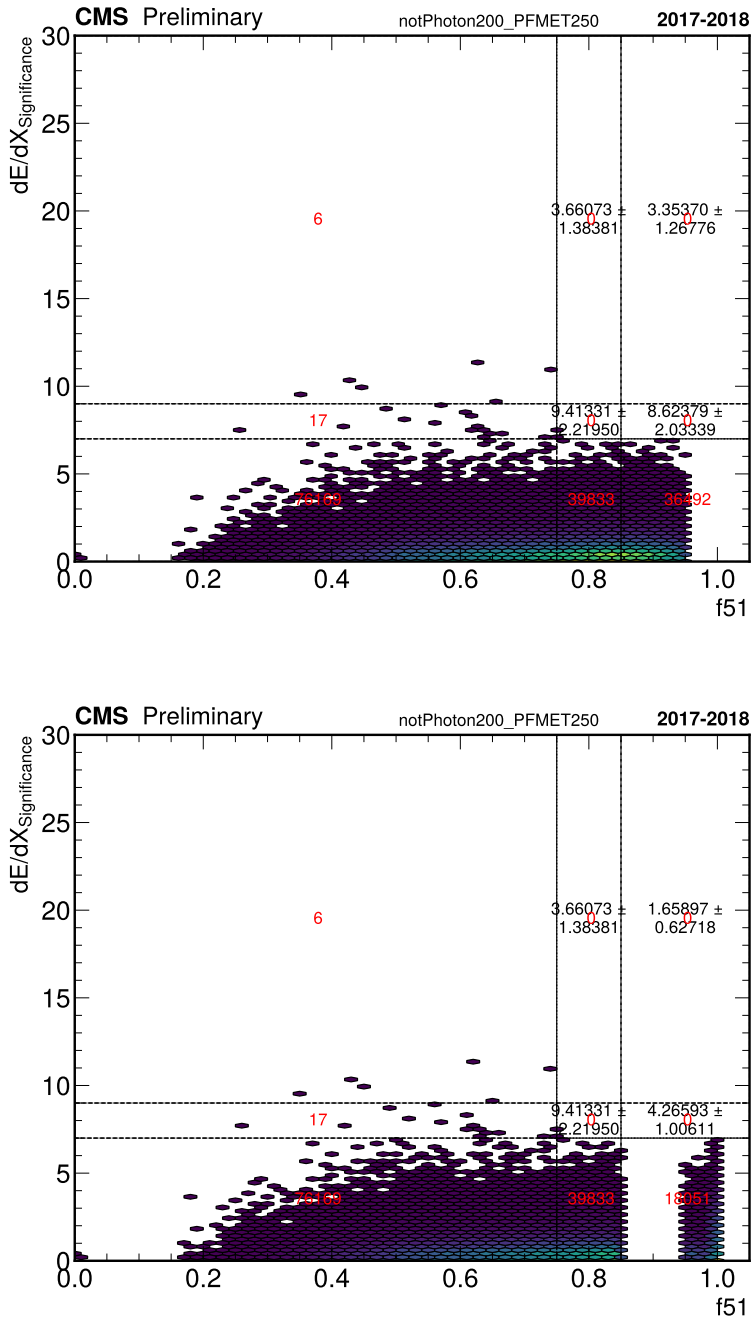

Figure 86 – The data for 2017 and 2018 are used to estimate the expected background in the signal region for the `MET` datasets under the `PFMET strategy`. The black numbers represent the expected values, while red numbers indicate the observed counts from the data. In the upper plot, the results concerning only the assumed physics contributions, and in the lower plot, the results for the consideration of only the spikes are observed.

	region	**actual**	**stat. uncer. (±)**	**expect**	**stat. uncer. (±)**
control region	1	76169	275.987		
	2	39833	199.582		
	3	36492	191.029		
	4	17	4.123		
	7	6	2.450		
cross-check	5			9.41331	2.21950
	6			8.62379	2.03339
	8			3.66073	1.38381
signal region	9			3.35370	1.26776

Table 42 – In the table the actual background counting and the statistical uncertainty from the Poisson errors in the background-dominated regions (1,2,3,4 and 7) for the 2016(APV) *SinglePhoton/EGamma* datasets, without the consideration of the spikes contribution. The expected number of events in the CRs (5,6 and 8) are defined by the loose cut ($f_{51} > 0.6$ and $dE/dX_{\texttt{Sig.}} > 6.5$), and the significant cut ($f_{51} < 0.85$ and $dE/dX_{\texttt{Sig.}} > 9.0$). For the agreement between the expected and actual numbers in the CRs, the expected background events in the SR (9) can be estimated, while the actual number was blinded.

	region	**actual**	**stat. uncer. (±)**	**expect**	**stat. uncer. (±)**
control region	1	76169	275.987		
	2	39833	199.582		
	3	18051	134.354		
	4	17	4.123		
	7	6	2.450		
cross-check	5			9.41331	2.21950
	6			4.26593	1.00611
	8			3.66073	1.38381
signal region	9			1.65897	0.62718

Table 43 – In the table the actual background counting and the statistical uncertainty from the Poisson errors in the background-dominated regions (1,2,3,4 and 7) for the 2016(APV) *SinglePhoton/EGamma* datasets, considering only the spikes contribution. The expected number of events in the CRs (5,6 and 8) are defined by the loose cut ($f_{51} > 0.6$ and $dE/dX_{\texttt{Sig.}} > 6.5$), and the significant cut ($f_{51} < 0.85$ and $dE/dX_{\texttt{Sig.}} > 9.0$). For the agreement between the expected and actual numbers in the CRs, the expected background events in the SR (9) can be estimated, while the actual number was blinded.

ABCD scheme	**Values**
Removing spikes	3.35370 ± 1.26776
Spikes-only	1.65897 ± 0.62718
Combination	5.01267 ± 1.4141
Default	5.01258 ± 1.89478

Table 44 – Estimated background yields and their uncertainties for the different ABCD scheme variations described for the combination of 2017 and 2018 MET datasets. The schemes include: Removing spikes, which excludes spike-like events; Spikes-only, which isolates the spike-like contribution; Combination, which merges spike and standard estimations; and Default, the standard ABCD method. The similarity between Combination and Default supports the stability of the background estimation.

6.14 Systematic Uncertainties

The systematic uncertainties have a key role in the measurement of the physical quantities in any experimental apparatus, starting with a simple pendulum in the early classes of the mechanics classes, and also in the context of a huge particle accelerator in the high-energy physics context.

The source of the systematic uncertainties is associated with the nature of the measurement apparatus, the assumption made by the experimenter, and the model used for the inferences based on the observed data [176]. This set of uncertainties is generally correlated from one measurement to the next. In general, there are no complete theoretical frameworks for the description of these uncertainties in inference or hypothesis testing.

Systematic uncertainties can affect the accuracy of the simulation, leading to discrepancies between simulated events and observed data. In the magnetic monopole analysis in the CMS, several sources of systematic uncertainties are considered. These include the δ-ray production, dE/dX cross-talk in the Tracking system, the data-driven background estimation, and the uncertainties related to the integrated luminosity.

6.14.1 δ-ray Production

When a highly ionizing particle traverses matter, it can transfer enough energy to a secondary electron to eject it from the atom and significantly deviate its path from that of the primary particle.

This process is known as δ-ray production. Given that monopoles deposit energy at rates far exceeding typical particles, the δ-ray production becomes a dominant source of uncertainty in the modeling of their energy loss. This has direct consequences on the calculation of the $dE/dX_{\texttt{significance}}$, which is a key discriminator in the signal selection criteria.

The δ-ray production process can be simulated using the `GEANT4` toolkit with explicit treatment of secondary electron generation. Within the analysis framework, a dedicated flag enables or disables this feature. In the analysis framework, a flag can be altered to reproduce the MC samples with the δ-ray production and without the process. While the δ-ray production is approached via a binary switch in the simulation framework, this simplification does not fully reflect the stochastic and energy-dependent nature of the process. No intermediate models are currently employed in the analysis. More nuanced treatments, such as tuning the energy thresholds for δ-ray tracking or applying reweighting schemes, are theoretically possible but not standard within the general searches pipeline.

Turning δ-ray production off in the simulation allows estimation of its impact by comparing the efficiency of signal selection with and without the effect included. The signal efficiency changes significantly for lower mass monopoles. As shown in Table 45, the 2017 and 2018 campaigns exhibit a drop of up to 20% in signal efficiency for 1000 GeV monopoles when δ-rays are not simulated. This large variation indicates that δ-rays are particularly influential in low-mass regimes, where monopoles traverse more material before stopping and generate more secondary electrons due to their longer path lengths and lower momenta.

To quantify this uncertainty, the signal efficiency is computed in two scenarios: with δ-ray production enabled and with it disabled. The relative difference is defined by:

$$\text{Uncertainty (\%)} = \frac{\text{efficiency} - \text{efficiency without } \delta\text{-ray}}{\text{efficiency with the } \delta\text{-ray}} \tag{6.12}$$

This yields a systematic uncertainty that ranges from about -18% to +20%, depending on the monopole mass and the MC campaign year. This wide variation reflects differences in detector conditions, simulation versions, and physics modeling between campaigns, particularly in how ionization and track reconstruction are affected by secondary electrons.

Mass [GeV]	2018	2017	2016	2016APV
1000	14.71	20.21	1.56	-2.46
1500	14.24	11.43	10.71	6.00
2000	11.16	11.47	10.48	-1.08
2500	6.86	0.18	7.79	-4.20
3000	6.25	4.70	9.03	0.48
3500	5.99	9.81	5.53	1.12
4000	-11.26	0.48	7.12	-12.93
4500	-9.10	-6.07	7.29	-18.13

Table 45 – The systematic uncertainty contribution (%) from the δ-ray production obtained from the Equation 6.12. The results for each mass point concerns the Drell-Yan Spin Half production mode for the MC campaigns of 2016, 2016APV, 2017 and 2018.

6.14.2 dE/dX cross-talk in the Tracking System

In the context of particle detectors, the electronic cross-talk refers to the signal interference between adjacent detector channels or electronics. This occurs when a genuine particle event in one detector element (e.g., a strip, pixel) induces a spurious signal in neighboring channels. Such signals are not related to a particle interaction, but due to coupling through electrical or electronic pathways. The electronic cross-talk could lead to false hits, since detector channels may register hits that do not correspond to actual particle interactions. For tracking detectors, the reconstruction of the particle's trajectory is affected, and for calorimeters, the presence of spurious signals may affect the measurement of deposited energy.

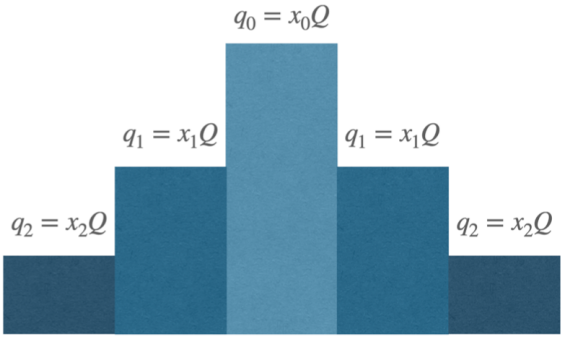

Figure 87 – A schematic distribution of the dE/dx cross-talk clusters, with the parameters x_0, x_1 and x_2 and the induced charge Q.

The Figure 87 illustrates a central strip that a particle travels through, which is coupled to two neighboring strips and two outer strips. The total induced charge in these strips is modeled by the parameter Q. The main strip has a contribution of $Q_0 = x_0Q$, the neighboring strips account for $Q_{\pm1} = x_1Q$, and the outer strips $Q_{\pm2} = x_2Q$. For charge conservation, a constraint on the cross-talk is applied in the form:

$$Q = x_0 + 2x_1 + 2x_2 \tag{6.13}$$

To estimate the systematic uncertainty associated with electronic cross-talk, we varied the parameter x_0 by $\pm$ 10% of its default value, which controls the fraction of charge retained by the main detector strip, while keeping x_2 fixed. When x_0 increases, less charge is shared with neighboring strips (x_1), and when it decreases, more charge spreads out, potentially affecting the saturation count and the dE/dX measurement. This approach provides a practical means of assessing the sensitivity of the analysis to potential mismodeling of cross-talk, which can influence the reconstructed energy deposit and subsequently affect particle identification.

The choice of a ± 10% variation is motivated by several factors. First, the exact modeling of cross-talk is complex due to its dependence on hardware characteristics, signal processing, and calibration procedures, making it difficult to determine precise uncertainties from first principles. Additionally, this method offers a transparent and easily implementable way to propagate uncertainties through the analysis chain, ensuring that the results remain reproducible and systematically controlled.

Finally, this strategy is consistent with standard practices across CMS and other high-energy physics experiments, where this approach is routinely applied to account for uncertainties in detector modeling, energy scales, and calibration parameters. The resulting change in the analysis outcome due to these variations is interpreted as the systematic uncertainty associated with cross-talk, contributing to the overall robustness of the measurement.

These variations were implemented in the digitization step of the simulation by applying a modification on the configuration files, specifically through commands such as `process.SiStripBlock.CouplingConstantDecIB1 = cms.vdouble(`x_0`,`x_1`,`x_2`)`. Inside these configuration files, similar commands are used to define the full set of tracking module typologies: 2 for TIB *Tracker Inner Barrel*, 2 for TOB *Tracker Outer Barrel*, 3 for TID *Tracker Inner Disk*, and 7 for TEC *Tracker Endcap*. After applying the parameter changes, the simulation was reprocessed, and the variation in monopole selection efficiency was analyzed. The observed change is then taken as the systematic uncertainty associated with cross-talk. The systematic uncertainty associated with the dE/dX was found to be about 0.10%, which is a very small contribution.

This method provides a robust estimate of the potential impact of cross-talk, ensuring the stability and reliability of the analysis results.

6.14.3 Data-driven background estimation

The uncertainty in the background estimation is derived from the statistical uncertainty and the expected number of events in the Signal Region. These values are taken from Tables 38 and 39 for the `SinglePhoton/EGamma` dataset, and from Tables 40 and 41 for the `MET` dataset. A summary of these values is shown in Table 46. The final uncertainty is calculated as the ratio of the statistical uncertainty to the expected value, as determined using the *Double*-ABCD method.

Dataset	Luminosity (fb^{-1})	`SinglePhoton`	`MET`
2016(APV)	35.9	0.707	1.000
2017-2018	101.3(97.6)	0.236	0.378

Table 46 – The uncertainty in the background estimation for the Signal Region is provided for the `SinglePhoton/EGamma` and `MET` datasets across the 2016, 2016APV, 2017, and 2018 collision data, along with the corresponding integrated luminosities. For the 2017–2018 period, the value in parentheses indicates the effective luminosity of the `MET` dataset, which accounts for the absence of the MET trigger path during part of the 2017 data-taking period.

The background uncertainty for 2016 is higher due to the lower integrated luminosity compared to the 2017–2018 data. In particular, the uncertainty for the 2016 `MET` dataset is set to 1.0, corresponding to a conservative 100% uncertainty. After unblinding the Control Regions (CRs) and incorporating their values into the Signal Region (SR) estimate, a reduction in the associated uncertainties is expected. This update will refine the background estimate used in setting upper limits on the production cross-section.

6.14.4 Integrated Luminosity

To reflect the uncertainty on the total luminosity recorded by the CMS Experiment, a normalization uncertainty is applied to the total predicted event yields for each year. The uncertainties are, 1.2% [177], 2.3% [178] and 2.5% [179] for 2016, 2017 and 2018, respectively.

6.14.5 MET Correction Uncertainty

Since the employment of the `MET` datasets in this analysis, a systematic uncertainty associated with the jet energy correction (JEC), which may affect the MET reconstruction, should be considered. To estimate this uncertainty, we followed the standard procedure for the 2016, 2017, and 2018 data-taking campaigns. This involves simultaneously varying all jet momenta "Up" and "Down", and consequently the missing transverse momentum, p_T^{miss}, using the official JEC uncertainty files provided by the `JetMET` group. In these files, considering the different years, the percentage uncertainties for jets as functions of pseudorapidity (η) and transverse momentum (p_T) reflect calibration limitations.

At the first step, the uncertainty related to each jet (p_T, η) is extracted for the reconstruction of a new MET object, with two shifted scenarios, based on a multiplicative factor of $(1 \pm \delta_{\text{JEC}})^2$. The same event selection criteria are then applied to each variation to consistently assess the final impact on yield and other observable quantities.

With the comparison of these results with those obtained in the nominal analysis, the impact of this associated systematic uncertainty can be evaluated, where it is found to

be below 1.5% for both variations.

6.14.6 Pileup reweighting

The pileup reweighting was applied to the Monte Carlo (MC) signal samples for magnetic monopoles to account for mismatches between the simulated and observed pileup distributions. To estimate the associated uncertainty, the signal yield was recalculated by varying the total inelastic proton-proton cross-section used in the pileup profile. The nominal value of 69,200 μb was shifted down to 66,000 μb (-4.6%) and up to 72,400 μb (+4.6%). The pileup uncertainty was quantified by computing the relative difference in signal yield between the varied and nominal scenarios, normalized to the nominal yield. The resulting uncertainties were in the order of 0.024% for 2016, 0.10% for 2017, and 0.342% for 2018.

7 The Frequentist CL_S Method for Hypothesis Testing

In searches for new physics, as addressed in this thesis, the primary objective is often to set exclusion limits on potential signals predicted by beyond-the-Standard-Model (BSM) theories. This is typically achieved by comparing two hypotheses: the null hypothesis (H_0), which assumes that the observed data can be entirely explained by Standard Model background processes, and the alternative hypothesis (H_1), which includes contributions from both signal and background.

If the observed data are consistent with the background-only expectation, and no statistically significant excess is found, H_0 is not rejected. In this case, exclusion limits can be placed on the signal model parameters, such as cross section or mass, typically at a 95% confidence level. These limits define the range in which the presence of the hypothetical signal is incompatible with the data under the given statistical framework.

The alternative hypothesis (H_1), which includes both signal and background, is favored when the null hypothesis has been rejected to a certain degree. Since the data remains blinded, the expected limits of the cross-section can be set to investigate the mass range where the magnetic monopole could occur. The cross-section limits are obtained using a frequentist statistical approach.

A common issue in standard frequentist hypothesis testing is that small fluctuations in the observed data can lead to overconfident exclusions of the signal hypothesis. This is particularly problematic when the data appears more background-like than expected. To mitigate such problems, the CL_s method, developed primarily in the context of the Higgs searches performed at LEP [180], introduces a modified frequentist approach that avoids overly aggressive exclusions when the experiment lacks sensitivity.

The method operates within the classical hypothesis testing. Consider a test statistic $q(X)$ based on observed data X, designed such that larger values of q correspond to greater incompatibility with the signal plus background hypothesis. In such a method, the following quantities can be defined. The p_{s+b} corresponds to the probability, under the signal plus background hypothesis, of observing a value of q, and the p_b is defined as the probability, under the background-only hypothesis, of observing the value q.

Then, the modified confidence level can be defined as:

$$\mathrm{CL}_s = \frac{p_{s+b}}{1 - p_b} \tag{7.1}$$

where the signal hypothesis can be excluded at a confidence level $1-\alpha$ if $\mathrm{CL}_s < \alpha$, which ensures that the signal is not excluded in regions where the experiment has little power to discriminate between hypotheses.

A typical choice of test statistic is the **profile likelihood ratio**, defined by:

$$q_\mu = -2\log\left(\frac{L(\mu,\hat{\theta}_\mu)}{L(\hat{\mu},\hat{\theta})}\right) \tag{7.2}$$

where μ is the signal strength parameter, $\hat{\mu}$ and $\hat{\theta}$ are the maximum likelihood estimators (MLE) of the signal and nuisance parameters and $\hat{\theta}_\mu$ is the conditional MLE of the nuisance parameters given fixed μ.

For large samples, the distribution of q_μ under the null hypothesis can be approximated using Wilks' theorem and the Asimov dataset methodology [181]. The calculation of the CL_s starts with the definition of a test statistic q, where a distribution of such a statistic under both H_0 and H_1 hypotheses is generated, either using pseudo-experiments or asymptotic approximations.

At a second step, the probabilities p_{s+b} and p_b, represented by CL_{s+b} and p_b respectively, are computed using the distributions of the test statistic under the signal+background and background-only hypotheses:

$$p_{s+b} = P(q \geq q_{\mathrm{obs}}|H_1) \tag{7.3}$$

$$p_b = P(q \geq q_{\mathrm{obs}}|H_0) \tag{7.4}$$

Then, the CL_s can be then obtained from

$$\mathrm{CL}_s = \frac{\mathrm{CL}_{s+b}}{\mathrm{CL}_b} \tag{7.5}$$

where the signal hypothesis could be excluded at $1-\alpha$ CL if $\mathrm{CL}_s < \alpha$.

In a Poisson counting experiment, the number of observed events, n, is assumed to follow a Poisson distribution. A simple model can be constructed using b as the expected number of background events, s as the expected number of signal events, and n_{obs} as the observed number of events. With these quantities, the Poisson likelihood can be used as the basis for the statistical inference, and it is defined as:

$$L(n|s,b) = \frac{(s+b)^n e^{-(s+b)}}{n!} \tag{7.6}$$

The frequentist CL_s approach incorporates the systematic uncertainties of the measurements via the nuisance parameters θ, which are modeled with prior constraints, from Gaussian or log-normal distributions.

Then the likelihood becomes:

$$L(\mu, \theta) = P(\text{data}|\mu, \theta) \cdot \pi(\theta) \tag{7.7}$$

where the profile likelihood test statistic is then computed by maximizing over nuisance parameters.

The CL$_s$ method offers a more conservative alternative to traditional frequentist or Bayesian exclusion methods, such as the standard p-value method or the Bayesian approach.

7.1 Cross-section upper limits

The experimental sensitivity to magnetic monopole production is determined by incorporating several key inputs: the signal efficiency estimated from MC simulations, the expected number of background events in the Signal Region, the integrated luminosity of the dataset considered, and the associated systematic uncertainties. These factors are used for the calculation of upper limits on the production cross section at 95% confidence level (CL).

To derive these limits, the CMS statistical tool `Combine` [182] is employed. The analysis is based on the full Run 2 dataset, corresponding to an integrated luminosity of either 137 fb^{-1} or 133 fb^{-1}, depending on the dataset, collected at a center-of-mass energy of $\sqrt{s} = 13$ TeV. The `Combine` tool allows for a robust statistical treatment of the signal and background hypotheses, accounting for both statistical and systematic uncertainties.

Figures 88 and 89 present the preliminary expected 95% CL upper limits on the production cross section for magnetic monopoles under two distinct production mechanisms: Drell–Yan and Photon Fusion, respectively. For comparison, the theoretical cross sections computed with `MadGraph` for a range of monopole masses are tabulated in Table 8. The intersection between the theoretical prediction and the expected limit curve determines the mass exclusion limit for each scenario.

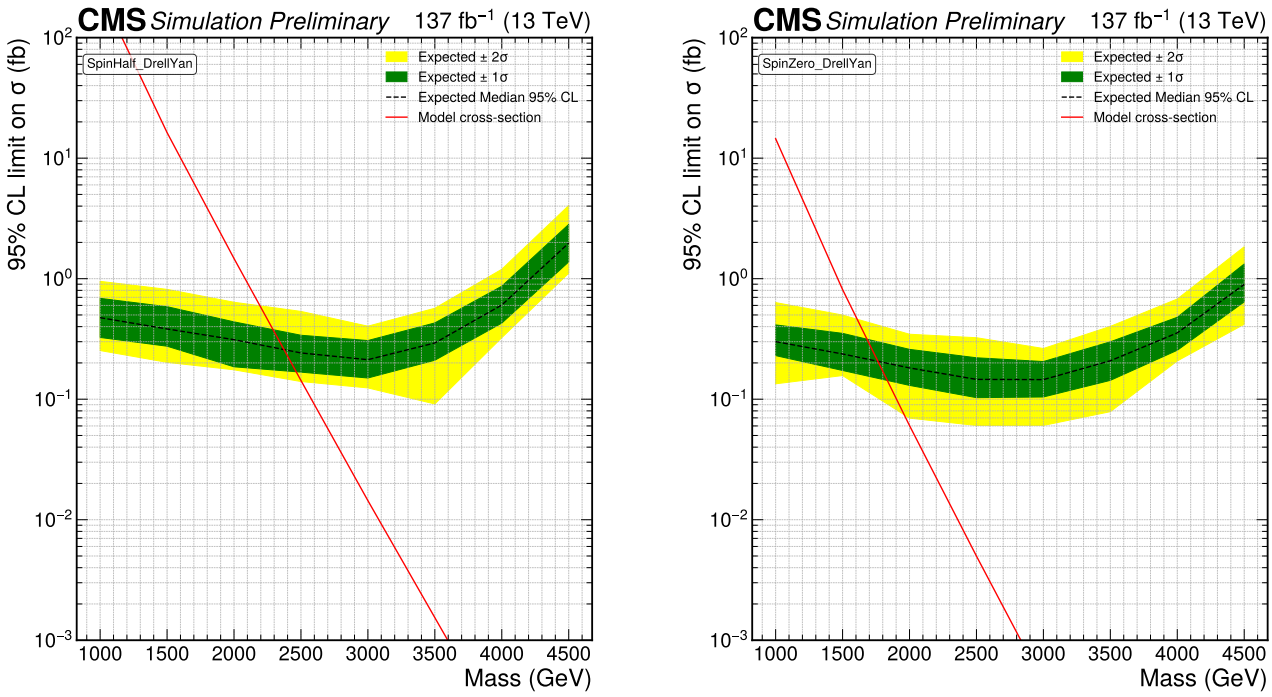

Figure 88 – The preliminary expected 95% confidence level (CL) upper limits magnetic monopoles production cross-section (σ) via Spin Half Drell-Yan (left) and Spin Zero Drell-Yan (right), as a function of resonance mass, for a data corresponding to an integrated luminosity of 137.2 fb^{-1} at a center-of-mass energy of $\sqrt{s} = 13$ TeV in the CMS Experiment. The black dashed line represents the median expected limit, while the green and yellow bands indicate the $\pm\sigma$ and $\pm 2\sigma$ ranges around the expected limit, respectively. The solid red line shows the model-predicted cross-section. The intersection point between the model and the expected limit curve indicates the sensitivity mass threshold beyond which the model is expected to be excluded.

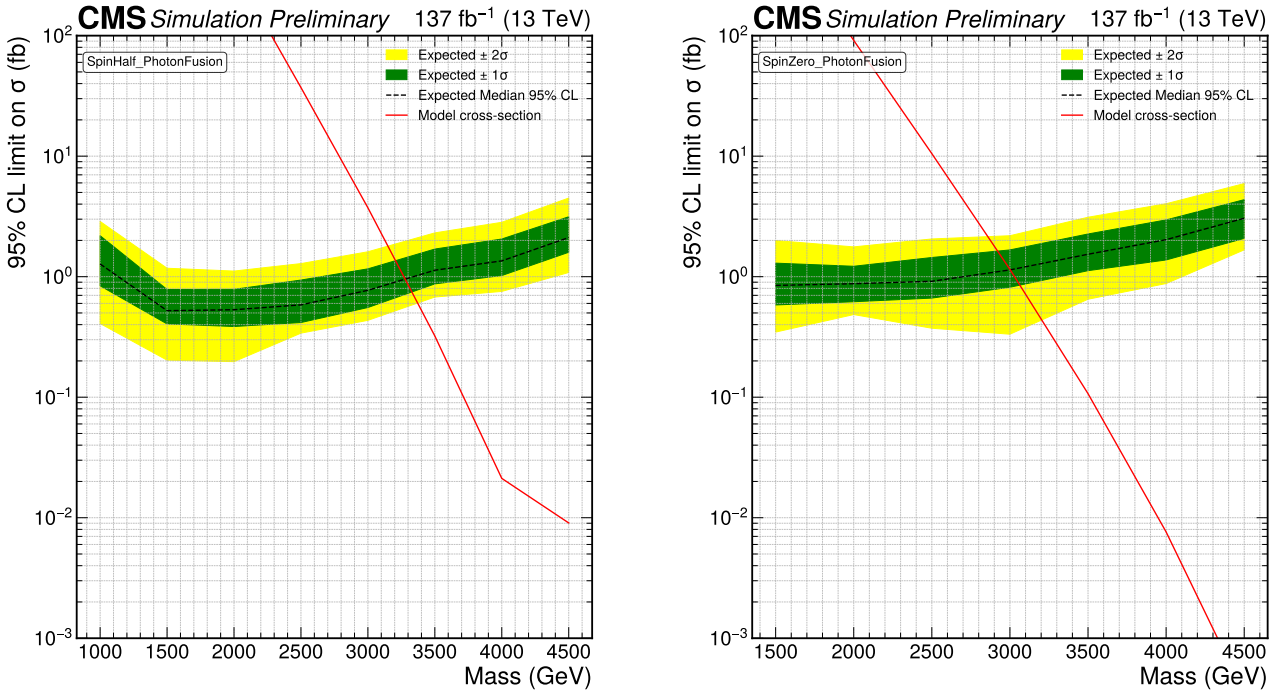

Figure 89 – The preliminary expected 95% confidence level (CL) upper limits magnetic monopoles production cross-section (σ) via Spin Half Photon Fusion (left) and Spin Zero Photon Fusion (right), as a function of resonance mass, for a data corresponding to an integrated luminosity of 137.2 fb^{-1} at a center-of-mass energy of $\sqrt{s} = 13$ TeV in the CMS Experiment. The black dashed line represents the median expected limit, while the green and yellow bands indicate the $\pm\sigma$ and $\pm 2\sigma$ ranges around the expected limit, respectively. The solid red line shows the model-predicted cross-section. The intersection point between the model and the expected limit curve indicates the sensitivity mass threshold beyond which the model is expected to be excluded.

For the results of the cross-section limit analysis, the corresponding mass exclusion limits are extracted by comparing the theoretical predictions with the expected experimental sensitivities. A summary of the resulting 95% confidence level (CL) exclusion limits for different production mechanisms is provided in Table 47.

Production mode	**Mass limit [GeV]**
Drell-Yan spin-½	2370
Drell-Yan spin-0	1760
Photon Fusion spin-½	3280
Photon Fusion spin-0	3000

Table 47 – Expected mass limits for the magnetic monopoles for the four production modes considered in this thesis. The limit values were extracted from the intersection between the theoretical cross-section and the limit obtained by the CL$_s$ method.

7.2 Sensitivity differences between LHC experiments

In a previous study conducted using the 2016 Monte Carlo (MC) campaign, the CMS experiment set an upper limit on the production cross section for magnetic monopoles under the spin-½ Drell–Yan production mode, based on an integrated luminosity of 33 fb^{-1} [183].

The ATLAS experiment performed a similar analysis, setting upper limits at 95% confidence level using the CL$_s$ method. This analysis was based on the full Run 2 dataset, corresponding to 137 fb^{-1} of proton–proton collisions at $\sqrt{s} = 13$ TeV [184]. The resulting limits for the Drell–Yan production mode are shown in Figure 90, where the corresponding lower mass limits are presented in Table 48.

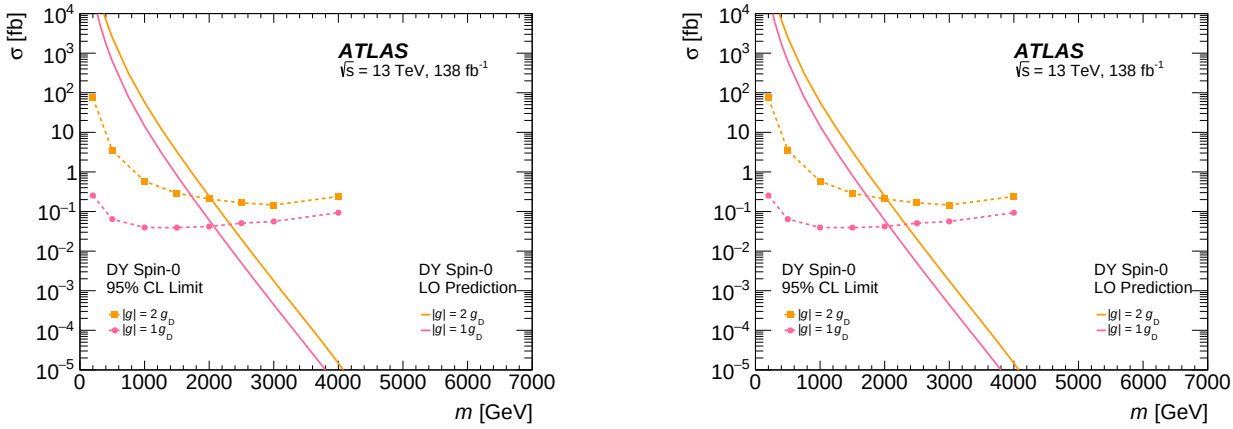

Figure 90 – Observed 95% CL upper limits on the cross section for all masses and charges of Drell-Yan pair-produced monopoles for spin-0 (left) and spin-1/2 (right).

The upper limits on the production cross section of magnetic monopoles were translated into mass exclusion limits by intersecting the predicted theoretical cross sections with the experimental sensitivities at 95% confidence level (CL). Table 47 summarizes the expected mass limits obtained in this thesis using CMS data, while Table 48 presents the corresponding results from the ATLAS experiment. The exclusion limits depend on the assumed production mechanism and the spin of the monopole. For example, CMS sets

Production mode	**Mass limit [GeV]**
Drell-Yan spin-½	2569
Drell-Yan spin-0	2097
Photon Fusion spin-½	3613
Photon Fusion spin-0	3350

Table 48 – Expected mass limits for the magnetic monopoles for the four production modes obtained by the ATLAS Experiment [184].

mass limits of 2370 GeV and 1760 GeV for spin-½ and spin-0 monopoles via Drell–Yan production, respectively, while photon fusion yields more stringent limits of 3280 GeV (spin-½) and 3000 GeV (spin-0). In comparison, ATLAS reports higher exclusion limits across all channels, with mass bounds reaching up to 3613 GeV for photon fusion spin-½ monopoles.

The superior sensitivity achieved by ATLAS is largely attributed to the presence of a dedicated High-Level Trigger (HLT) path specifically tailored for highly ionizing particles and so-called *High-Electric-Charge Compact Objects* (HECOs). This specialized trigger boosts efficiency by up to an order of magnitude compared to the current analysis and the CMS experiment.

Unlike CMS, ATLAS does not have the `sFGVB` filter in its online and offline noise suppression by rejecting concentrated energy deposits, which is precisely the kind of signature expected from monopoles in the ECAL. Because of the absence of this filter, ATLAS maintains much higher signal efficiency, reaching up to 60%, and thus achieves stronger sensitivity and exclusion limits.

8 Summary and Conclusions

The Chapter 4 presented a comprehensive study on the use of Z boson production as a tool for luminosity measurement and monitoring. The strengths of the Z boson rate approach include its long-term stability and self-calibrating nature, which were discussed alongside areas that require further investigation.

One such area is the observed correlation between the two muons from the Z decay and between the inner and outer track efficiencies. Although the origin of this correlation is not fully understood, the Section 4.5.2 offers a possible explanation related to muon-seeded tracks. Adapting the reconstruction chain to reduce dependence on these tracks may help clarify the effect. Further insight could also be gained from detailed studies using simulated samples to explore potential unknown contributions.

The linearity of the method was briefly evaluated for the early 2022 dataset, where good agreement was observed. While pileup dependence is not expected to significantly impact Z Counting under Run 3 conditions, it may become a challenge at the HL-LHC, where the average pileup is projected to reach $< \mu > \approx 200$. Dedicated studies will be needed to assess the method's robustness in such high-pileup environments.

Importantly, the Z boson counting method is inherently self-calibrating. Unlike conventional luminosity detectors, which require annual van der Meer (vdM) scans to recalibrate due to time-dependent efficiency losses, Z Counting allows the measurement of efficiencies directly from the same data used for signal extraction. This approach removes reliance on external corrections or calibrations. Once an absolute normalization (σ_{vis}) is determined using a low-pileup dataset, it can be transferred across the rest of the data-taking period, assuming a constant center-of-mass energy. This makes the method especially attractive for consistent long-term luminosity monitoring. Additionally, this cross-year integration could help to reduce overall systematic uncertainties in the luminosity measurement.

Finally, two dominant sources of uncertainty in current luminosity measurements are the stability and linearity of the integration, both of which could significantly benefit from the Z boson counting approach. By offering an independent, self-consistent, and data-driven method for extrapolating from low to high pileup, Z Counting may play a key role in reducing these systematic uncertainties and improving the overall precision of future luminosity measurements.

The Chapter 6 presented a dedicated search for the hypothetical magnetic monopole particles, originally proposed by Dirac to explain electric charge quantization and restore symmetry to Maxwell's equations. Over the decades, a variety of theoretical models have

predicted monopole-like states, but direct experimental evidence remains elusive. This work focuses on the search for Dirac monopoles with unit magnetic charge ($g_D = 1$) and masses within the TeV scale, within reach of the Large Hadron Collider (LHC).

The signal Monte Carlo samples were generated for both Drell–Yan and photon fusion production mechanisms, covering spin-0 and spin-½ monopole states, as outlined in Chapter 5. Due to their large magnetic charge, monopoles are expected to exhibit extremely high ionization, leading to severe charge saturation in the CMS silicon tracker and highly localized energy deposits in the ECAL. These deposits are typically concentrated in a single $PbWO_4$ crystal, mimicking "spike-like" topologies where the `sFGVB` built in the CMS Level-1 (L1) and High-Level Trigger (HLT) systems is specifically designed to reject. As a result, the monopole trigger efficiency is drastically reduced—posing a major experimental challenge.

To address this, two complementary strategies were developed based on the unique detector signatures of monopoles. The `Photon strategy` exploits the visual and topological similarities between monopoles and high-energy photons by leveraging single-photon triggers. The`PFMET strategy`, on the other hand, is motivated by the hypothesis that trigger rejection of monopole signatures manifests as missing transverse energy (MET), thus utilizing PFMET triggers. Both approaches rely on two robust discriminating variables: the $dE/dx_{\texttt{Significance}}$ from the tracker, and the f_{51} variable from the ECAL, which captures the energy deposition shape. Strategy-specific selections are applied at the event level: an energy threshold for the `Photon strategy` and a MET requirement for the `PFMET strategy`.

A thorough analysis of signal selection criteria, background estimation methods, and systematic uncertainties is detailed in Chapter 6. Special care was taken to account for the unique detector response to monopole-like signatures, including tracking inefficiencies and calorimeter-based anomalies.

Finally, Chapter 7 presents the expected upper limits on monopole production cross sections for all simulated production scenarios. At this stage, the signal region remains blinded, pending a final unblinding and data comparison. The analysis provides the most comprehensive CMS sensitivity to date for monopole masses in the TeV range, under multiple production hypotheses and spin assignments. These results represent a critical step forward in the experimental search for magnetic monopoles at the LHC.

A Monopole Simulation

Samples for Photon Fusion Spin Half

/Monopole_SpinHalf_PhotonFusion_M-1000_TuneCP5_13TeV_madgraph-pythia8/RunIISummer20UL18RECO-106X_upgrade2018_realistic_v11_L1v1-v2/GEN-SIM-RECO
/Monopole_SpinHalf_PhotonFusion_M-1500_TuneCP5_13TeV_madgraph-pythia8/RunIISummer20UL18RECO-106X_upgrade2018_realistic_v11_L1v1-v2/GEN-SIM-RECO
/Monopole_SpinHalf_PhotonFusion_M-2000_TuneCP5_13TeV_madgraph-pythia8/RunIISummer20UL18RECO-106X_upgrade2018_realistic_v11_L1v1-v2/GEN-SIM-RECO
/Monopole_SpinHalf_PhotonFusion_M-2500_TuneCP5_13TeV_madgraph-pythia8/RunIISummer20UL18RECO-106X_upgrade2018_realistic_v11_L1v1-v2/GEN-SIM-RECO
/Monopole_SpinHalf_PhotonFusion_M-3000_TuneCP5_13TeV_madgraph-pythia8/RunIISummer20UL18RECO-106X_upgrade2018_realistic_v11_L1v1-v2/GEN-SIM-RECO
/Monopole_SpinHalf_PhotonFusion_M-3500_TuneCP5_13TeV_madgraph-pythia8/RunIISummer20UL18RECO-106X_upgrade2018_realistic_v11_L1v1-v2/GEN-SIM-RECO
/Monopole_SpinHalf_PhotonFusion_M-4000_TuneCP5_13TeV_madgraph-pythia8/RunIISummer20UL18RECO-106X_upgrade2018_realistic_v11_L1v1-v2/GEN-SIM-RECO
/Monopole_SpinHalf_PhotonFusion_M-4500_TuneCP5_13TeV_madgraph-pythia8/RunIISummer20UL18RECO-106X_upgrade2018_realistic_v11_L1v1-v2/GEN-SIM-RECO

/Monopole_SpinHalf_PhotonFusion_M-1000_TuneCP5_13TeV_madgraph-pythia8/RunIISummer20UL17RECO-106X_mc2017_realistic_v6-v2/GEN-SIM-RECO
/Monopole_SpinHalf_PhotonFusion_M-1500_TuneCP5_13TeV_madgraph-pythia8/RunIISummer20UL17RECO-106X_mc2017_realistic_v6-v2/GEN-SIM-RECO
/Monopole_SpinHalf_PhotonFusion_M-2000_TuneCP5_13TeV_madgraph-pythia8/RunIISummer20UL17RECO-106X_mc2017_realistic_v6-v2/GEN-SIM-RECO
/Monopole_SpinHalf_PhotonFusion_M-2500_TuneCP5_13TeV_madgraph-pythia8/RunIISummer20UL17RECO-106X_mc2017_realistic_v6-v2/GEN-SIM-RECO
/Monopole_SpinHalf_PhotonFusion_M-3000_TuneCP5_13TeV_madgraph-pythia8/RunIISummer20UL17RECO-106X_mc2017_realistic_v6-v2/GEN-SIM-RECO
/Monopole_SpinHalf_PhotonFusion_M-3500_TuneCP5_13TeV_madgraph-pythia8/RunIISummer20UL17RECO-106X_mc2017_realistic_v6-v2/GEN-SIM-RECO
/Monopole_SpinHalf_PhotonFusion_M-4000_TuneCP5_13TeV_madgraph-pythia8/RunIISummer20UL17RECO-106X_mc2017_realistic_v6-v2/GEN-SIM-RECO
/Monopole_SpinHalf_PhotonFusion_M-4500_TuneCP5_13TeV_madgraph-pythia8/RunIISummer20UL17RECO-106X_mc2017_realistic_v6-v2/GEN-SIM-RECO

/Monopole_SpinHalf_PhotonFusion_M-1000_TuneCP5_13TeV_madgraph-pythia8/RunIISummer20UL16RECO-106X_mcRun2_asymptotic_v13-v2/GEN-SIM-RECO
/Monopole_SpinHalf_PhotonFusion_M-1500_TuneCP5_13TeV_madgraph-pythia8/RunIISummer20UL16RECO-106X_mcRun2_asymptotic_v13-v3/GEN-SIM-RECO
/Monopole_SpinHalf_PhotonFusion_M-2000_TuneCP5_13TeV_madgraph-pythia8/RunIISummer20UL16RECO-106X_mcRun2_asymptotic_v13-v3/GEN-SIM-RECO
/Monopole_SpinHalf_PhotonFusion_M-2500_TuneCP5_13TeV_madgraph-pythia8/RunIISummer20UL16RECO-106X_mcRun2_asymptotic_v13-v3/GEN-SIM-RECO
/Monopole_SpinHalf_PhotonFusion_M-3000_TuneCP5_13TeV_madgraph-pythia8/RunIISummer20UL16RECO-106X_mcRun2_asymptotic_v13-v3/GEN-SIM-RECO
/Monopole_SpinHalf_PhotonFusion_M-3500_TuneCP5_13TeV_madgraph-pythia8/RunIISummer20UL16RECO-106X_mcRun2_asymptotic_v13-v3/GEN-SIM-RECO
/Monopole_SpinHalf_PhotonFusion_M-4000_TuneCP5_13TeV_madgraph-pythia8/RunIISummer20UL16RECO-106X_mcRun2_asymptotic_v13-v3/GEN-SIM-RECO
/Monopole_SpinHalf_PhotonFusion_M-4500_TuneCP5_13TeV_madgraph-pythia8/RunIISummer20UL16RECO-106X_mcRun2_asymptotic_v13-v3/GEN-SIM-RECO

/Monopole_SpinHalf_PhotonFusion_M-1000_TuneCP5_13TeV_madgraph-pythia8/RunIISummer20UL16RECOAPV-106X_mcRun2_asymptotic_preVFP_v8-v2/GEN-SIM-RECO
/Monopole_SpinHalf_PhotonFusion_M-1500_TuneCP5_13TeV_madgraph-pythia8/RunIISummer20UL16RECOAPV-106X_mcRun2_asymptotic_preVFP_v8-v2/GEN-SIM-RECO
/Monopole_SpinHalf_PhotonFusion_M-2000_TuneCP5_13TeV_madgraph-pythia8/RunIISummer20UL16RECOAPV-106X_mcRun2_asymptotic_preVFP_v8-v2/GEN-SIM-RECO
/Monopole_SpinHalf_PhotonFusion_M-2500_TuneCP5_13TeV_madgraph-pythia8/RunIISummer20UL16RECOAPV-106X_mcRun2_asymptotic_preVFP_v8-v2/GEN-SIM-RECO
/Monopole_SpinHalf_PhotonFusion_M-3000_TuneCP5_13TeV_madgraph-pythia8/RunIISummer20UL16RECOAPV-106X_mcRun2_asymptotic_preVFP_v8-v2/GEN-SIM-RECO
/Monopole_SpinHalf_PhotonFusion_M-3500_TuneCP5_13TeV_madgraph-pythia8/RunIISummer20UL16RECOAPV-106X_mcRun2_asymptotic_preVFP_v8-v2/GEN-SIM-RECO
/Monopole_SpinHalf_PhotonFusion_M-4000_TuneCP5_13TeV_madgraph-pythia8/RunIISummer20UL16RECOAPV-106X_mcRun2_asymptotic_preVFP_v8-v2/GEN-SIM-RECO
/Monopole_SpinHalf_PhotonFusion_M-4500_TuneCP5_13TeV_madgraph-pythia8/RunIISummer20UL16RECOAPV-106X_mcRun2_asymptotic_preVFP_v8-v2/GEN-SIM-RECO

Samples for Photon Fusion Spin Zero

/Monopole_SpinZero_PhotonFusion_M-1500_TuneCP5_13TeV_madgraph-pythia8/RunIISummer20UL18RECO-106X_upgrade2018_realistic_v11_L1v1-v2/GEN-SIM-RECO
/Monopole_SpinZero_PhotonFusion_M-2000_TuneCP5_13TeV_madgraph-pythia8/RunIISummer20UL18RECO-106X_upgrade2018_realistic_v11_L1v1-v2/GEN-SIM-RECO
/Monopole_SpinZero_PhotonFusion_M-2500_TuneCP5_13TeV_madgraph-pythia8/RunIISummer20UL18RECO-106X_upgrade2018_realistic_v11_L1v1-v2/GEN-SIM-RECO
/Monopole_SpinZero_PhotonFusion_M-3000_TuneCP5_13TeV_madgraph-pythia8/RunIISummer20UL18RECO-106X_upgrade2018_realistic_v11_L1v1-v2/GEN-SIM-RECO
/Monopole_SpinZero_PhotonFusion_M-3500_TuneCP5_13TeV_madgraph-pythia8/RunIISummer20UL18RECO-106X_upgrade2018_realistic_v11_L1v1-v2/GEN-SIM-RECO
/Monopole_SpinZero_PhotonFusion_M-4000_TuneCP5_13TeV_madgraph-pythia8/RunIISummer20UL18RECO-106X_upgrade2018_realistic_v11_L1v1-v2/GEN-SIM-RECO
/Monopole_SpinZero_PhotonFusion_M-4500_TuneCP5_13TeV_madgraph-pythia8/RunIISummer20UL18RECO-106X_upgrade2018_realistic_v11_L1v1-v2/GEN-SIM-RECO

/Monopole_SpinZero_PhotonFusion_M-1500_TuneCP5_13TeV_madgraph-pythia8/RunIISummer20UL17RECO-106X_mc2017_realistic_v6-v2/GEN-SIM-RECO
/Monopole_SpinZero_PhotonFusion_M-2000_TuneCP5_13TeV_madgraph-pythia8/RunIISummer20UL17RECO-106X_mc2017_realistic_v6-v2/GEN-SIM-RECO
/Monopole_SpinZero_PhotonFusion_M-2500_TuneCP5_13TeV_madgraph-pythia8/RunIISummer20UL17RECO-106X_mc2017_realistic_v6-v2/GEN-SIM-RECO
/Monopole_SpinZero_PhotonFusion_M-3000_TuneCP5_13TeV_madgraph-pythia8/RunIISummer20UL17RECO-106X_mc2017_realistic_v6-v2/GEN-SIM-RECO
/Monopole_SpinZero_PhotonFusion_M-3500_TuneCP5_13TeV_madgraph-pythia8/RunIISummer20UL17RECO-106X_mc2017_realistic_v6-v2/GEN-SIM-RECO
/Monopole_SpinZero_PhotonFusion_M-4000_TuneCP5_13TeV_madgraph-pythia8/RunIISummer20UL17RECO-106X_mc2017_realistic_v6-v2/GEN-SIM-RECO
/Monopole_SpinZero_PhotonFusion_M-4500_TuneCP5_13TeV_madgraph-pythia8/RunIISummer20UL17RECO-106X_mc2017_realistic_v6-v2/GEN-SIM-RECO

/Monopole_SpinZero_PhotonFusion_M-1500_TuneCP5_13TeV_madgraph-pythia8/RunIISummer20UL16RECOAPV-106X_mcRun2_asymptotic_preVFP_v8-v2/GEN-SIM-RECO
/Monopole_SpinZero_PhotonFusion_M-2000_TuneCP5_13TeV_madgraph-pythia8/RunIISummer20UL16RECOAPV-106X_mcRun2_asymptotic_preVFP_v8-v2/GEN-SIM-RECO
/Monopole_SpinZero_PhotonFusion_M-2500_TuneCP5_13TeV_madgraph-pythia8/RunIISummer20UL16RECOAPV-106X_mcRun2_asymptotic_preVFP_v8-v2/GEN-SIM-RECO
/Monopole_SpinZero_PhotonFusion_M-3000_TuneCP5_13TeV_madgraph-pythia8/RunIISummer20UL16RECOAPV-106X_mcRun2_asymptotic_preVFP_v8-v2/GEN-SIM-RECO
/Monopole_SpinZero_PhotonFusion_M-3500_TuneCP5_13TeV_madgraph-pythia8/RunIISummer20UL16RECOAPV-106X_mcRun2_asymptotic_preVFP_v8-v2/GEN-SIM-RECO
/Monopole_SpinZero_PhotonFusion_M-4000_TuneCP5_13TeV_madgraph-pythia8/RunIISummer20UL16RECOAPV-106X_mcRun2_asymptotic_preVFP_v8-v2/GEN-SIM-RECO
/Monopole_SpinZero_PhotonFusion_M-4500_TuneCP5_13TeV_madgraph-pythia8/RunIISummer20UL16RECOAPV-106X_mcRun2_asymptotic_preVFP_v8-v2/GEN-SIM-RECO

Samples for Drell-Yan Spin Half

/Monopole_SpinHalf_DrellYan_M-1000_TuneCP5_13TeV_madgraph-pythia8/RunIISummer20UL18RECO-106X_upgrade2018_realistic_v11_L1v1-v3/GEN-SIM-RECO
/Monopole_SpinHalf_DrellYan_M-1500_TuneCP5_13TeV_madgraph-pythia8/RunIISummer20UL18RECO-106X_upgrade2018_realistic_v11_L1v1-v2/GEN-SIM-RECO
/Monopole_SpinHalf_DrellYan_M-2000_TuneCP5_13TeV_madgraph-pythia8/RunIISummer20UL18RECO-106X_upgrade2018_realistic_v11_L1v1-v2/GEN-SIM-RECO
/Monopole_SpinHalf_DrellYan_M-2500_TuneCP5_13TeV_madgraph-pythia8/RunIISummer20UL18RECO-106X_upgrade2018_realistic_v11_L1v1-v2/GEN-SIM-RECO
/Monopole_SpinHalf_DrellYan_M-3000_TuneCP5_13TeV_madgraph-pythia8/RunIISummer20UL18RECO-106X_upgrade2018_realistic_v11_L1v1-v2/GEN-SIM-RECO
/Monopole_SpinHalf_DrellYan_M-3500_TuneCP5_13TeV_madgraph-pythia8/RunIISummer20UL18RECO-106X_upgrade2018_realistic_v11_L1v1-v2/GEN-SIM-RECO
/Monopole_SpinHalf_DrellYan_M-4000_TuneCP5_13TeV_madgraph-pythia8/RunIISummer20UL18RECO-106X_upgrade2018_realistic_v11_L1v1-v2/GEN-SIM-RECO
/Monopole_SpinHalf_DrellYan_M-4500_TuneCP5_13TeV_madgraph-pythia8/RunIISummer20UL18RECO-106X_upgrade2018_realistic_v11_L1v1-v2/GEN-SIM-RECO

/Monopole_SpinHalf_DrellYan_M-1000_TuneCP5_13TeV_madgraph-pythia8/RunIISummer20UL17RECO-106X_mc2017_realistic_v6-v3/GEN-SIM-RECO
/Monopole_SpinHalf_DrellYan_M-1500_TuneCP5_13TeV_madgraph-pythia8/RunIISummer20UL17RECO-106X_mc2017_realistic_v6-v2/GEN-SIM-RECO
/Monopole_SpinHalf_DrellYan_M-2000_TuneCP5_13TeV_madgraph-pythia8/RunIISummer20UL17RECO-106X_mc2017_realistic_v6-v2/GEN-SIM-RECO
/Monopole_SpinHalf_DrellYan_M-2500_TuneCP5_13TeV_madgraph-pythia8/RunIISummer20UL17RECO-106X_mc2017_realistic_v6-v2/GEN-SIM-RECO
/Monopole_SpinHalf_DrellYan_M-3000_TuneCP5_13TeV_madgraph-pythia8/RunIISummer20UL17RECO-106X_mc2017_realistic_v6-v2/GEN-SIM-RECO
/Monopole_SpinHalf_DrellYan_M-3500_TuneCP5_13TeV_madgraph-pythia8/RunIISummer20UL17RECO-106X_mc2017_realistic_v6-v2/GEN-SIM-RECO
/Monopole_SpinHalf_DrellYan_M-4000_TuneCP5_13TeV_madgraph-pythia8/RunIISummer20UL17RECO-106X_mc2017_realistic_v6-v2/GEN-SIM-RECO
/Monopole_SpinHalf_DrellYan_M-4500_TuneCP5_13TeV_madgraph-pythia8/RunIISummer20UL17RECO-106X_mc2017_realistic_v6-v2/GEN-SIM-RECO

/Monopole_SpinHalf_DrellYan_M-1000_TuneCP5_13TeV_madgraph-pythia8/RunIISummer20UL16RECOAPV-106X_mcRun2_asymptotic_preVFP_v8-v2/GEN-SIM-RECO
/Monopole_SpinHalf_DrellYan_M-1500_TuneCP5_13TeV_madgraph-pythia8/RunIISummer20UL16RECOAPV-106X_mcRun2_asymptotic_preVFP_v8-v2/GEN-SIM-RECO
/Monopole_SpinHalf_DrellYan_M-2000_TuneCP5_13TeV_madgraph-pythia8/RunIISummer20UL16RECOAPV-106X_mcRun2_asymptotic_preVFP_v8-v2/GEN-SIM-RECO
/Monopole_SpinHalf_DrellYan_M-2500_TuneCP5_13TeV_madgraph-pythia8/RunIISummer20UL16RECOAPV-106X_mcRun2_asymptotic_preVFP_v8-v2/GEN-SIM-RECO
/Monopole_SpinHalf_DrellYan_M-3000_TuneCP5_13TeV_madgraph-pythia8/RunIISummer20UL16RECOAPV-106X_mcRun2_asymptotic_preVFP_v8-v2/GEN-SIM-RECO
/Monopole_SpinHalf_DrellYan_M-3500_TuneCP5_13TeV_madgraph-pythia8/RunIISummer20UL16RECOAPV-106X_mcRun2_asymptotic_preVFP_v8-v2/GEN-SIM-RECO
/Monopole_SpinHalf_DrellYan_M-4000_TuneCP5_13TeV_madgraph-pythia8/RunIISummer20UL16RECOAPV-106X_mcRun2_asymptotic_preVFP_v8-v2/GEN-SIM-RECO
/Monopole_SpinHalf_DrellYan_M-4500_TuneCP5_13TeV_madgraph-pythia8/RunIISummer20UL16RECOAPV-106X_mcRun2_asymptotic_preVFP_v8-v2/GEN-SIM-RECO

/Monopole_SpinHalf_DrellYan_M-1000_TuneCP5_13TeV_madgraph-pythia8/RunIISummer20UL16RECO-106X_mcRun2_asymptotic_v13-v2/GEN-SIM-RECO
/Monopole_SpinHalf_DrellYan_M-1500_TuneCP5_13TeV_madgraph-pythia8/RunIISummer20UL16RECO-106X_mcRun2_asymptotic_v13-v2/GEN-SIM-RECO
/Monopole_SpinHalf_DrellYan_M-2000_TuneCP5_13TeV_madgraph-pythia8/RunIISummer20UL16RECO-106X_mcRun2_asymptotic_v13-v2/GEN-SIM-RECO
/Monopole_SpinHalf_DrellYan_M-2500_TuneCP5_13TeV_madgraph-pythia8/RunIISummer20UL16RECO-106X_mcRun2_asymptotic_v13-v2/GEN-SIM-RECO
/Monopole_SpinHalf_DrellYan_M-3000_TuneCP5_13TeV_madgraph-pythia8/RunIISummer20UL16RECO-106X_mcRun2_asymptotic_v13-v2/GEN-SIM-RECO
/Monopole_SpinHalf_DrellYan_M-3500_TuneCP5_13TeV_madgraph-pythia8/RunIISummer20UL16RECO-106X_mcRun2_asymptotic_v13-v2/GEN-SIM-RECO
/Monopole_SpinHalf_DrellYan_M-4000_TuneCP5_13TeV_madgraph-pythia8/RunIISummer20UL16RECO-106X_mcRun2_asymptotic_v13-v2/GEN-SIM-RECO
/Monopole_SpinHalf_DrellYan_M-4500_TuneCP5_13TeV_madgraph-pythia8/RunIISummer20UL16RECO-106X_mcRun2_asymptotic_v13-v2/GEN-SIM-RECO

Samples for Drell-Yan Spin Zero

/Monopole_SpinZero_DrellYan_M-1000_TuneCP5_13TeV_madgraph-pythia8/RunIISummer20UL18RECO-106X_upgrade2018_realistic_v11_L1v1-v2/GEN-SIM-RECO
/Monopole_SpinZero_DrellYan_M-1500_TuneCP5_13TeV_madgraph-pythia8/RunIISummer20UL18RECO-106X_upgrade2018_realistic_v11_L1v1-v2/GEN-SIM-RECO
/Monopole_SpinZero_DrellYan_M-2000_TuneCP5_13TeV_madgraph-pythia8/RunIISummer20UL18RECO-106X_upgrade2018_realistic_v11_L1v1-v2/GEN-SIM-RECO
/Monopole_SpinZero_DrellYan_M-2500_TuneCP5_13TeV_madgraph-pythia8/RunIISummer20UL18RECO-106X_upgrade2018_realistic_v11_L1v1-v2/GEN-SIM-RECO
/Monopole_SpinZero_DrellYan_M-3000_TuneCP5_13TeV_madgraph-pythia8/RunIISummer20UL18RECO-106X_upgrade2018_realistic_v11_L1v1-v2/GEN-SIM-RECO
/Monopole_SpinZero_DrellYan_M-3500_TuneCP5_13TeV_madgraph-pythia8/RunIISummer20UL18RECO-106X_upgrade2018_realistic_v11_L1v1-v2/GEN-SIM-RECO
/Monopole_SpinZero_DrellYan_M-4000_TuneCP5_13TeV_madgraph-pythia8/RunIISummer20UL18RECO-106X_upgrade2018_realistic_v11_L1v1-v2/GEN-SIM-RECO
/Monopole_SpinZero_DrellYan_M-4500_TuneCP5_13TeV_madgraph-pythia8/RunIISummer20UL18RECO-106X_upgrade2018_realistic_v11_L1v1-v2/GEN-SIM-RECO

/Monopole_SpinZero_DrellYan_M-1000_TuneCP5_13TeV_madgraph-pythia8/RunIISummer20UL17RECO-106X_mc2017_realistic_v6-v2/GEN-SIM-RECO
/Monopole_SpinZero_DrellYan_M-1500_TuneCP5_13TeV_madgraph-pythia8/RunIISummer20UL17RECO-106X_mc2017_realistic_v6-v3/GEN-SIM-RECO
/Monopole_SpinZero_DrellYan_M-2000_TuneCP5_13TeV_madgraph-pythia8/RunIISummer20UL17RECO-106X_mc2017_realistic_v6-v2/GEN-SIM-RECO
/Monopole_SpinZero_DrellYan_M-2500_TuneCP5_13TeV_madgraph-pythia8/RunIISummer20UL17RECO-106X_mc2017_realistic_v6-v2/GEN-SIM-RECO
/Monopole_SpinZero_DrellYan_M-3000_TuneCP5_13TeV_madgraph-pythia8/RunIISummer20UL17RECO-106X_mc2017_realistic_v6-v2/GEN-SIM-RECO
/Monopole_SpinZero_DrellYan_M-3500_TuneCP5_13TeV_madgraph-pythia8/RunIISummer20UL17RECO-106X_mc2017_realistic_v6-v2/GEN-SIM-RECO
/Monopole_SpinZero_DrellYan_M-4000_TuneCP5_13TeV_madgraph-pythia8/RunIISummer20UL17RECO-106X_mc2017_realistic_v6-v2/GEN-SIM-RECO
/Monopole_SpinZero_DrellYan_M-4500_TuneCP5_13TeV_madgraph-pythia8/RunIISummer20UL17RECO-106X_mc2017_realistic_v6-v2/GEN-SIM-RECO

/Monopole_SpinZero_DrellYan_M-1000_TuneCP5_13TeV_madgraph-pythia8/RunIISummer20UL16RECO-106X_mcRun2_asymptotic_v13-v2/GEN-SIM-RECO
/Monopole_SpinZero_DrellYan_M-1500_TuneCP5_13TeV_madgraph-pythia8/RunIISummer20UL16RECO-106X_mcRun2_asymptotic_v13-v2/GEN-SIM-RECO
/Monopole_SpinZero_DrellYan_M-2000_TuneCP5_13TeV_madgraph-pythia8/RunIISummer20UL16RECO-106X_mcRun2_asymptotic_v13-v2/GEN-SIM-RECO
/Monopole_SpinZero_DrellYan_M-2500_TuneCP5_13TeV_madgraph-pythia8/RunIISummer20UL16RECO-106X_mcRun2_asymptotic_v13-v2/GEN-SIM-RECO
/Monopole_SpinZero_DrellYan_M-3000_TuneCP5_13TeV_madgraph-pythia8/RunIISummer20UL16RECO-106X_mcRun2_asymptotic_v13-v2/GEN-SIM-RECO
/Monopole_SpinZero_DrellYan_M-3500_TuneCP5_13TeV_madgraph-pythia8/RunIISummer20UL16RECO-106X_mcRun2_asymptotic_v13-v2/GEN-SIM-RECO
/Monopole_SpinZero_DrellYan_M-4000_TuneCP5_13TeV_madgraph-pythia8/RunIISummer20UL16RECO-106X_mcRun2_asymptotic_v13-v2/GEN-SIM-RECO
/Monopole_SpinZero_DrellYan_M-4500_TuneCP5_13TeV_madgraph-pythia8/RunIISummer20UL16RECO-106X_mcRun2_asymptotic_v13-v2/GEN-SIM-RECO

/Monopole_SpinZero_DrellYan_M-1000_TuneCP5_13TeV_madgraph-pythia8/RunIISummer20UL16RECOAPV-106X_mcRun2_asymptotic_preVFP_v8-v2/GEN-SIM-RECO
/Monopole_SpinZero_DrellYan_M-1500_TuneCP5_13TeV_madgraph-pythia8/RunIISummer20UL16RECOAPV-106X_mcRun2_asymptotic_preVFP_v8-v2/GEN-SIM-RECO
/Monopole_SpinZero_DrellYan_M-2000_TuneCP5_13TeV_madgraph-pythia8/RunIISummer20UL16RECOAPV-106X_mcRun2_asymptotic_preVFP_v8-v2/GEN-SIM-RECO
/Monopole_SpinZero_DrellYan_M-2500_TuneCP5_13TeV_madgraph-pythia8/RunIISummer20UL16RECOAPV-106X_mcRun2_asymptotic_preVFP_v8-v2/GEN-SIM-RECO
/Monopole_SpinZero_DrellYan_M-3000_TuneCP5_13TeV_madgraph-pythia8/RunIISummer20UL16RECOAPV-106X_mcRun2_asymptotic_preVFP_v8-v2/GEN-SIM-RECO
/Monopole_SpinZero_DrellYan_M-3500_TuneCP5_13TeV_madgraph-pythia8/RunIISummer20UL16RECOAPV-106X_mcRun2_asymptotic_preVFP_v8-v2/GEN-SIM-RECO
/Monopole_SpinZero_DrellYan_M-4000_TuneCP5_13TeV_madgraph-pythia8/RunIISummer20UL16RECOAPV-106X_mcRun2_asymptotic_preVFP_v8-v2/GEN-SIM-RECO
/Monopole_SpinZero_DrellYan_M-4500_TuneCP5_13TeV_madgraph-pythia8/RunIISummer20UL16RECOAPV-106X_mcRun2_asymptotic_preVFP_v8-v2/GEN-SIM-RECO

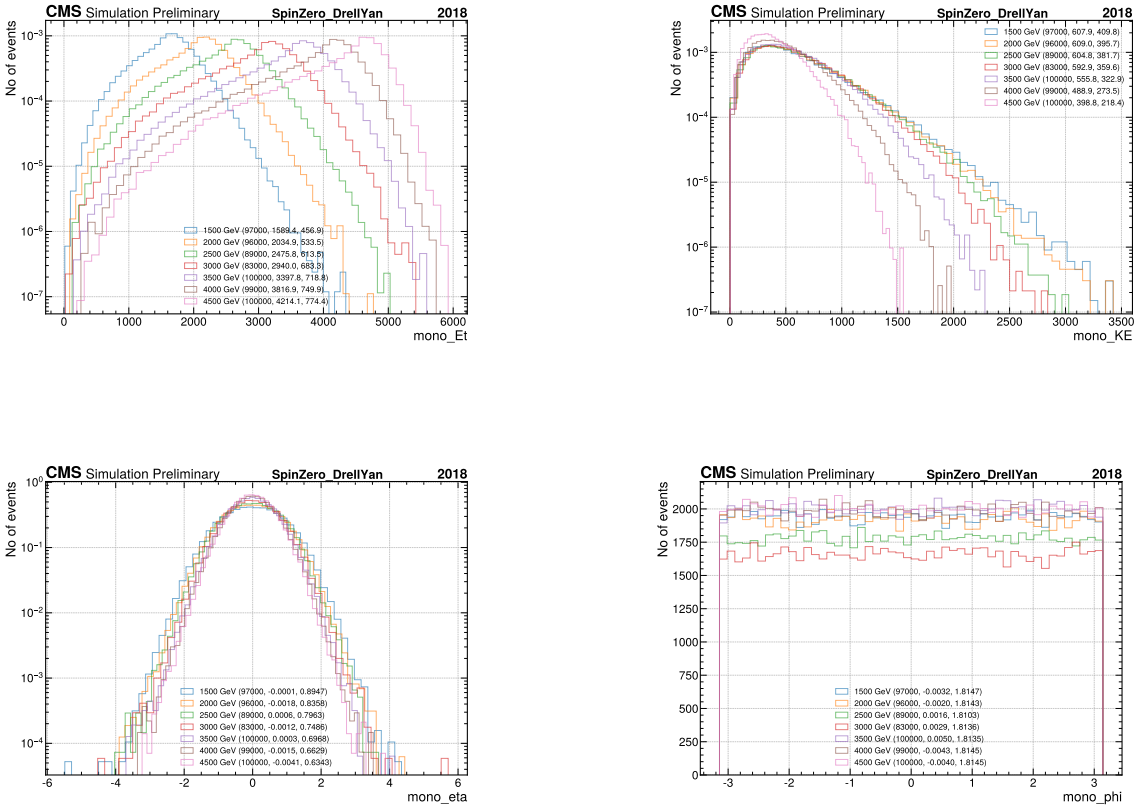

Figure 91 – Transverse Energy (E_T) (upper left), transverse momentum (p_T) (upper right), pseudorapidty (η) (lower left) and ϕ (lower right) for generated Spin-0 monopoles from the Drell-Yan production process.

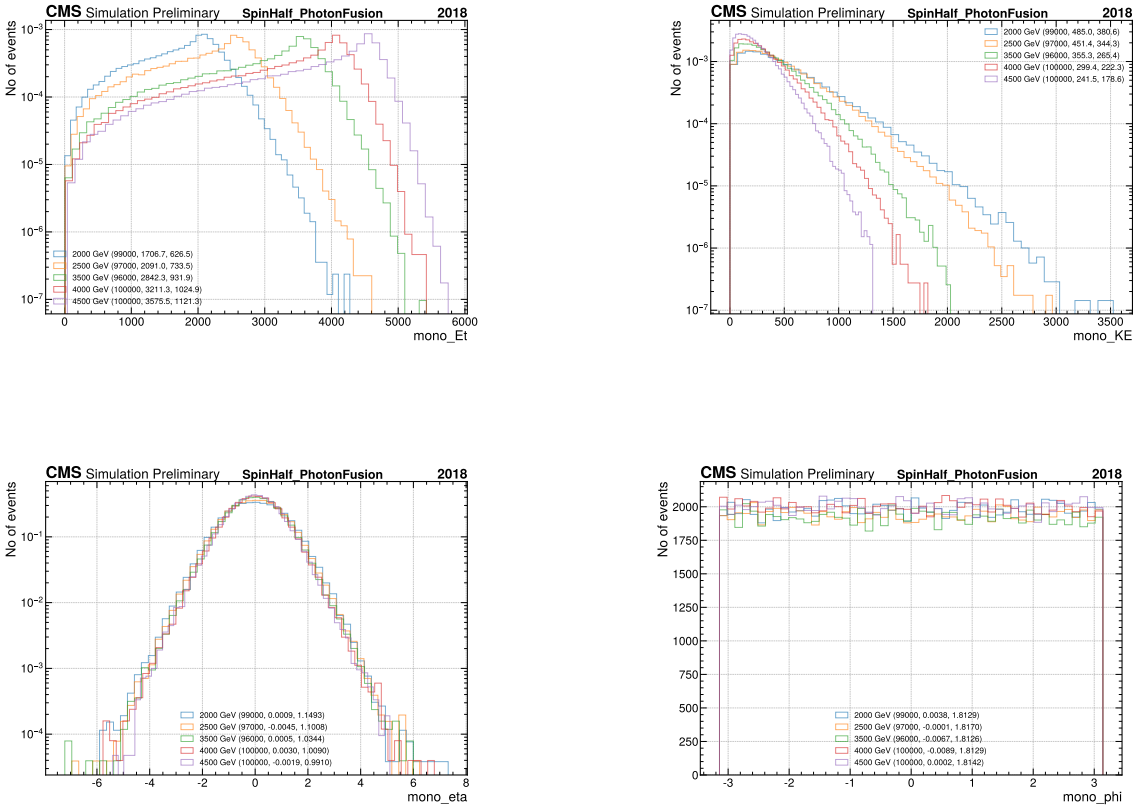

Figure 92 – Transverse Energy (E_T) (upper left), transverse momentum (p_T) (upper right), pseudorapidty (η) (lower left) and ϕ (lower right) for generated Spin-1/2 monopoles from the Photon Fusion production process.

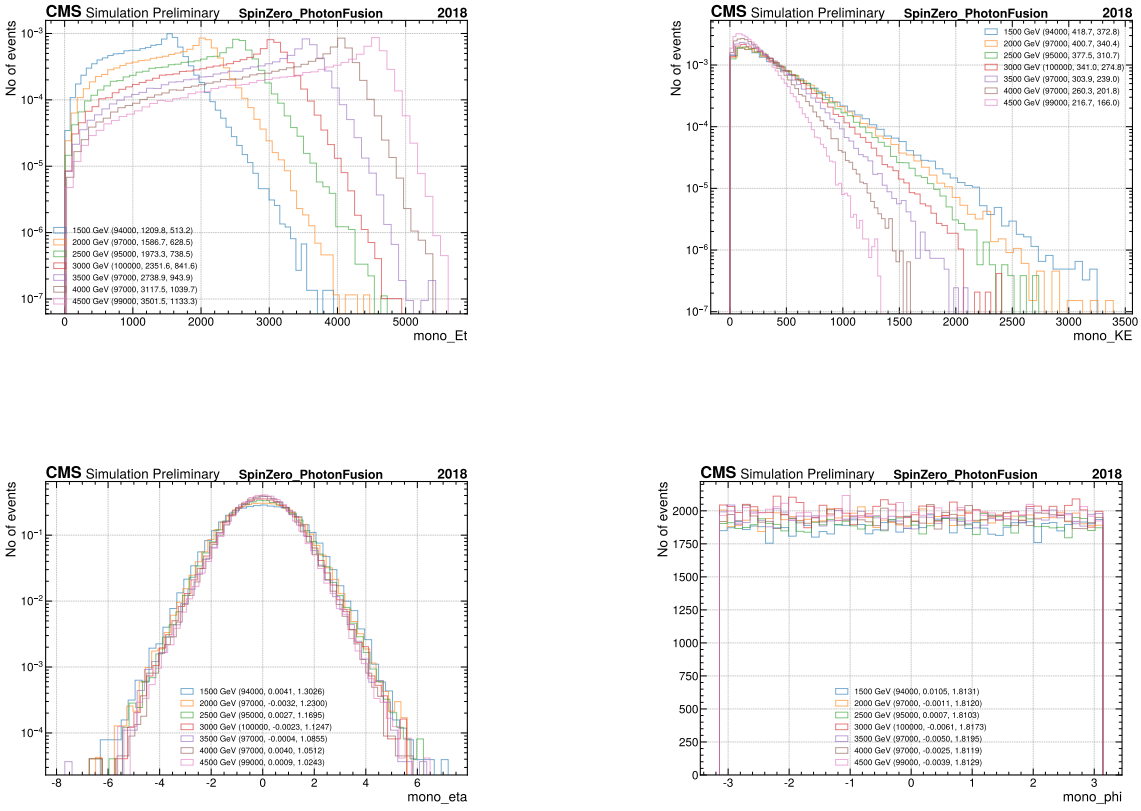

Figure 93 – Transverse Energy (E_T) (upper left), transverse momentum (p_T) (upper right), pseudorapidty (η) (lower left) and ϕ (lower right) for generated Spin-0 monopoles from the Photon Fusion production process.

B Signal and Relative Efficiency Tables

B.1 `Photon Strategy`

Mass [GeV]	1000	1500	2000	2500	3000	3500	4000	4500
Generated	0	67000	95000	98000	98000	100000	100000	100000
Trigger	0	6682	10139	10876	10853	10429	9914	8521
Quality	0	6607	10023	10711	10679	10189	9612	8194
$e55 > 200$	0	6209	9503	10006	9843	9309	8884	7575
$f51 > 0.85$	0	3374	5536	5686	5495	5030	5043	4459
$dEdXSig > 9.0$	0	3352	5490	5634	5428	4929	4930	4255
signal efficiency (%)	nan	5.003%	5.779%	5.749%	5.539%	4.929%	4.930%	4.255%

Table 49 – The analysis Cutflow for the `Photon strategy` for SpinZero-Drell-Yan samples for the 2018 MC campaign. The table shows the number of signal events surviving each selection step across the generated monopole mass points, from 1000 to 4500 GeV. The steps include the HLT application, missing transverse momentum requirement, standard preselection, and the discriminant variable cuts on variables $f_{51} > 0.85$ and $dEdX_{\texttt{Significance}} > 9.0$. The final row corresponds to the overall signal efficiency for each mass point.

Mass [GeV]	1000	1500	2000	2500	3000	3500	4000	4500
Generated	95000	0	97000	98000	98000	99000	100000	97000
Trigger	8869	0	10573	10950	10972	10545	9971	8254
Quality	8749	0	10427	10766	10771	10321	9705	7965
$e55 > 200$	8172	0	9811	10030	9910	9437	8953	7328
$f51 > 0.85$	4332	0	5670	5881	5549	5181	5004	4262
$dEdXSig > 9.0$	4295	0	5627	5824	5474	5068	4848	4072
signal efficiency (%)	4.521%	nan	5.801%	5.943%	5.586%	5.119%	4.848%	4.198%

Table 50 – The analysis Cutflow for the `Photon strategy` for SpinZero-Drell-Yan samples for the 2017 MC campaign. The table shows the number of signal events surviving each selection step across the generated monopole mass points, from 1000 to 4500 GeV. The steps include the HLT application, missing transverse momentum requirement, standard preselection, and the discriminant variable cuts on variables $f_{51} > 0.85$ and $dEdX_{\texttt{Significance}} > 9.0$. The final row corresponds to the overall signal efficiency for each mass point.

Mass [GeV]	1000	1500	2000	2500	3000	3500	4000	4500
Generated	48180	48176	50000	50000	50000	50000	48166	49082
Trigger	4950	5217	5659	5710	5675	5484	4902	4121
Quality	4822	5113	5540	5590	5537	5322	4726	3914
$e55 > 175$	4512	4855	5275	5278	5164	4973	4458	3751
$f51 > 0.85$	2435	2635	3046	3039	2919	2793	2522	2221
$dEdXSig > 9.0$	2426	2628	3029	3008	2879	2739	2465	2160
signal efficiency (%)	5.035%	5.455%	6.058%	6.016%	5.758%	5.478%	5.118%	4.401%

Table 51 – The analysis Cutflow for the `Photon strategy` for SpinZero-Drell-Yan samples for the 2016 MC campaign. The table shows the number of signal events surviving each selection step across the generated monopole mass points, from 1000 to 4500 GeV. The steps include the HLT application, missing transverse momentum requirement, standard preselection, and the discriminant variable cuts on variables $f_{51} > 0.85$ and $dEdX_{\texttt{Significance}} > 9.0$. The final row corresponds to the overall signal efficiency for each mass point.

Mass [GeV]	1000	1500	2000	2500	3000	3500	4000	4500
Generated	50000	47339	50000	50000	50000	50000	48220	48216
Trigger	5028	5203	5771	5931	5614	5595	4799	4117
Quality	4915	5120	5672	5817	5496	5427	4632	3925
$e55 > 175$	4624	4924	5411	5538	5134	5099	4425	3732
$f51 > 0.85$	2389	2618	3064	3138	2872	2791	2463	2219
$dEdXSig > 9.0$	2367	2596	3037	3101	2797	2680	2352	2062
signal efficiency (%)	4.734%	5.484%	6.074%	6.202%	5.594%	5.360%	4.878%	4.277%

Table 52 – The analysis Cutflow for the `Photon strategy` for SpinZero-Drell-Yan samples for the 2016APV MC campaign. The table shows the number of signal events surviving each selection step across the generated monopole mass points, from 1000 to 4500 GeV. The steps include the HLT application, missing transverse momentum requirement, standard preselection, and the discriminant variable cuts on variables $f_{51} > 0.85$ and $dEdX_{\texttt{Significance}} > 9.0$. The final row corresponds to the overall signal efficiency for each mass point.

Mass [GeV]	1000	1500	2000	2500	3000	3500	4000	4500
Generated	0	95000	99000	99000	100000	99000	100000	100000
Trigger	0	3822	4367	4410	4049	3536	2810	1886
Quality	0	3759	4275	4279	3917	3375	2679	1784
$e55 > 200$	0	3557	4029	4032	3660	3138	2471	1625
$f51 > 0.85$	0	1901	2243	2248	1987	1753	1394	997
$dEdXSig > 9.0$	0	1893	2232	2235	1958	1719	1340	941
signal efficiency (%)	nan	1.993%	2.255%	2.258%	1.958%	1.736%	1.340%	0.941%

Table 53 – The analysis Cutflow for the `Photon strategy` for SpinZero Photon Fusion samples for the 2018 MC campaign. The table shows the number of signal events surviving each selection step across the generated monopole mass points, from 1000 to 4500 GeV. The steps include the HLT application, missing transverse momentum requirement, standard preselection, and the discriminant variable cuts on variables $f_{51} > 0.85$ and $dEdX_{\texttt{Significance}} > 9.0$. The final row corresponds to the overall signal efficiency for each mass point.

Mass [GeV]	1000	1500	2000	2500	3000	3500	4000	4500
Generated	0	99000	100000	98000	99000	99000	99000	100000
Trigger	0	4430	4650	4554	4171	3636	2837	2067
Quality	0	4331	4545	4433	4037	3469	2718	1972
$e55 > 200$	0	4057	4279	4168	3771	3194	2469	1798
$f51 > 0.85$	0	2219	2362	2247	2028	1742	1479	1101
$dEdXSig > 9.0$	0	2206	2351	2225	1994	1697	1413	1027
signal efficiency (%)	nan	2.228%	2.351%	2.270%	2.014%	1.714%	1.427%	1.027%

Table 54 – The analysis Cutflow for the `Photon strategy` for SpinZero Photon Fusion samples for the 2017 MC campaign. The table shows the number of signal events surviving each selection step across the generated monopole mass points, from 1000 to 4500 GeV. The steps include the HLT application, missing transverse momentum requirement, standard preselection, and the discriminant variable cuts on variables $f_{51} > 0.85$ and $dEdX_{\texttt{Significance}} > 9.0$. The final row corresponds to the overall signal efficiency for each mass point.

Mass [GeV]	1000	1500	2000	2500	3000	3500	4000	4500
Generated	0	48228	48226	49112	50000	49110	49109	49108
Trigger	0	2531	2420	2352	2152	1802	1333	955
Quality	0	2451	2369	2287	2088	1733	1278	911
$e55 > 175$	0	2337	2298	2209	2022	1671	1236	881
$f51 > 0.85$	0	1303	1277	1250	1120	881	721	547
$dEdXSig > 9.0$	0	1294	1261	1226	1100	837	681	486
signal efficiency (%)	nan	2.683%	2.615%	2.496%	2.200%	1.704%	1.387%	0.990%

Table 55 – The analysis Cutflow for the `Photon strategy` for SpinZero Photon Fusion samples for the 2016APV MC campaign. The table shows the number of signal events surviving each selection step across the generated monopole mass points, from 1000 to 4500 GeV. The steps include the HLT application, missing transverse momentum requirement, standard preselection, and the discriminant variable cuts on variables $f_{51} > 0.85$ and $dEdX_{\texttt{Significance}} > 9.0$. The final row corresponds to the overall signal efficiency for each mass point.

Mass [GeV]	1000	1500	2000	2500	3000	3500	4000	4500
Generated	93000	90000	99000	100000	99000	92000	100000	100000
Trigger	4695	5569	6367	6317	5583	4469	3865	2683
Quality	4629	5484	6254	6135	5386	4277	3674	2555
$e55 > 200$	4341	5222	5953	5827	5066	3982	3374	2331
$f51 > 0.85$	2289	2890	3332	3256	2817	2258	1960	1396
$dEdXSig > 9.0$	2276	2876	3314	3224	2784	2205	1899	1326
signal efficiency (%)	2.447%	3.196%	3.347%	3.224%	2.812%	2.397%	1.899%	1.326%

Table 56 – The analysis Cutflow for the `Photon strategy` for SpinHalf Photon Fusion samples for the 2018 MC campaign. The table shows the number of signal events surviving each selection step across the generated monopole mass points, from 1000 to 4500 GeV. The steps include the HLT application, missing transverse momentum requirement, standard preselection, and the discriminant variable cuts on variables $f_{51} > 0.85$ and $dEdX_{\texttt{Significance}} > 9.0$. The final row corresponds to the overall signal efficiency for each mass point.

Mass [GeV]	1000	1500	2000	2500	3000	3500	4000	4500
Generated	92000	97000	97000	100000	99000	99000	100000	72000
Trigger	5083	6237	6470	6555	5883	4958	3980	1890
Quality	4951	6115	6312	6392	5696	4752	3800	1803
$e55 > 200$	4566	5772	5942	6017	5317	4422	3476	1634
$f51 > 0.85$	2434	3158	3340	3465	2910	2486	2059	1027
$dEdXSig > 9.0$	2417	3145	3318	3438	2878	2433	1966	968
signal efficiency (%)	2.627%	3.242%	3.421%	3.438%	2.907%	2.458%	1.966%	1.344%

Table 57 – The analysis Cutflow for the `Photon strategy` for SpinHalf Photon Fusion samples for the 2017 MC campaign. The table shows the number of signal events surviving each selection step across the generated monopole mass points, from 1000 to 4500 GeV. The steps include the HLT application, missing transverse momentum requirement, standard preselection, and the discriminant variable cuts on variables $f_{51} > 0.85$ and $dEdX_{\texttt{Significance}} > 9.0$. The final row corresponds to the overall signal efficiency for each mass point.

Mass [GeV]	1000	1500	2000	2500	3000	3500	4000	4500
Generated	50000	49090	50000	49085	50000	0	50000	45410
Trigger	3122	3491	3593	3360	2975	0	2020	1183
Quality	3002	3381	3494	3252	2859	0	1915	1118
$e55 > 175$	2775	3211	3374	3162	2766	0	1848	1078
$f51 > 0.85$	1502	1843	1926	1803	1505	0	1072	654
$dEdXSig > 9.0$	1492	1836	1920	1791	1489	0	1037	632
signal efficiency (%)	2.984%	3.740%	3.840%	3.649%	2.978%	nan	2.074%	1.392%

Table 58 – The analysis Cutflow for the `Photon strategy` for SpinHalf Photon Fusion samples for the 2016 MC campaign. The table shows the number of signal events surviving each selection step across the generated monopole mass points, from 1000 to 4500 GeV. The steps include the HLT application, missing transverse momentum requirement, standard preselection, and the discriminant variable cuts on variables $f_{51} > 0.85$ and $dEdX_{\texttt{Significance}} > 9.0$. The final row corresponds to the overall signal efficiency for each mass point.

Mass [GeV]	1000	1500	2000	2500	3000	3500	4000	4500
Generated	50000	50000	49114	49113	49728	50000	46440	50000
Trigger	3167	3584	3409	3352	2945	2506	1819	1296
Quality	3081	3492	3320	3274	2846	2413	1729	1222
$e55 > 175$	2848	3310	3208	3173	2755	2357	1671	1174
$f51 > 0.85$	1548	1821	1801	1780	1514	1295	958	697
$dEdXSig > 9.0$	1536	1806	1784	1755	1473	1231	897	629
signal efficiency (%)	3.072%	3.612%	3.632%	3.573%	2.962%	2.462%	1.932%	1.258%

Table 59 – The analysis Cutflow for the `Photon strategy` for SpinHalf Photon Fusion samples for the 2016APV MC campaign. The table shows the number of signal events surviving each selection step across the generated monopole mass points, from 1000 to 4500 GeV. The steps include the HLT application, missing transverse momentum requirement, standard preselection, and the discriminant variable cuts on variables $f_{51} > 0.85$ and $dEdX_{\texttt{Significance}} > 9.0$. The final row corresponds to the overall signal efficiency for each mass point.

Mass [GeV]	1000	1500	2000	2500	3000	3500	4000	4500
Trigger	nan	0.100	0.107	0.111	0.111	0.104	0.099	0.085
Quality	nan	0.989	0.989	0.985	0.984	0.977	0.970	0.962
$e55 > 200$	nan	0.940	0.948	0.934	0.922	0.914	0.924	0.924
$f51 > 0.85$	nan	0.543	0.583	0.568	0.558	0.540	0.568	0.589
$dEdXSig > 9.0$	nan	0.993	0.992	0.991	0.988	0.980	0.978	0.954

Table 60 – The relative efficiency for `Photon strategy` for Spin Zero Drell-Yan samples for the 2018 MC campaign. Efficiencies are shown for each mass point from 1000 to 4500 GeV and are computed relative to the number of events entering each selection stage and by the Equation 6.8. The steps include the HLT application, missing transverse momentum requirement, standard preselection, and the discriminant variable cuts on variables $f_{51} > 0.85$ and $dEdX_{\texttt{Significance}} > 9.0$.

Mass [GeV]	1000	1500	2000	2500	3000	3500	4000	4500
Trigger	0.093	nan	0.109	0.112	0.112	0.107	0.100	0.085
Quality	0.986	nan	0.986	0.983	0.982	0.979	0.973	0.965
$e55 > 200$	0.934	nan	0.941	0.932	0.920	0.914	0.923	0.920
$f51 > 0.85$	0.530	nan	0.578	0.586	0.560	0.549	0.559	0.582
$dEdXSig > 9.0$	0.991	nan	0.992	0.990	0.986	0.978	0.969	0.955

Table 61 – The relative efficiency for `Photon strategy` for Spin Zero Drell-Yan samples for the 2017 MC campaign. Efficiencies are shown for each mass point from 1000 to 4500 GeV and are computed relative to the number of events entering each selection stage and by the Equation 6.8. The steps include the HLT application, missing transverse momentum requirement, standard preselection, and the discriminant variable cuts on variables $f_{51} > 0.85$ and $dEdX_{\texttt{Significance}} > 9.0$.

Mass [GeV]	1000	1500	2000	2500	3000	3500	4000	4500
Trigger	0.103	0.108	0.113	0.114	0.114	0.110	0.102	0.084
Quality	0.974	0.980	0.979	0.979	0.976	0.970	0.964	0.950
$e55 > 175$	0.936	0.950	0.952	0.944	0.933	0.934	0.943	0.958
$f51 > 0.85$	0.540	0.543	0.577	0.576	0.565	0.562	0.566	0.592
$dEdXSig > 9.0$	0.996	0.997	0.994	0.990	0.986	0.981	0.977	0.973

Table 62 – The relative efficiency for `Photon strategy` for Spin Zero Drell-Yan samples for the 2016 MC campaign. Efficiencies are shown for each mass point from 1000 to 4500 GeV and are computed relative to the number of events entering each selection stage and by the Equation 6.8. The steps include the HLT application, missing transverse momentum requirement, standard preselection, and the discriminant variable cuts on variables $f_{51} > 0.85$ and $dEdX_{\texttt{Significance}} > 9.0$.

Mass [GeV]	1000	1500	2000	2500	3000	3500	4000	4500
Trigger	0.101	0.110	0.115	0.119	0.112	0.112	0.100	0.085
Quality	0.978	0.984	0.983	0.981	0.979	0.970	0.965	0.953
$e55 > 175$	0.941	0.962	0.954	0.952	0.934	0.940	0.955	0.951
$f51 > 0.85$	0.517	0.532	0.566	0.567	0.559	0.547	0.557	0.595
$dEdXSig > 9.0$	0.991	0.992	0.991	0.988	0.974	0.960	0.955	0.929

Table 63 – The relative efficiency for `Photon strategy` for Spin Zero Drell-Yan samples for the 2016APV MC campaign. Efficiencies are shown for each mass point from 1000 to 4500 GeV and are computed relative to the number of events entering each selection stage and by the Equation 6.8. The steps include the HLT application, missing transverse momentum requirement, standard preselection, and the discriminant variable cuts on variables $f_{51} > 0.85$ and $dEdX_{\texttt{Significance}} > 9.0$.

Mass [GeV]	1000	1500	2000	2500	3000	3500	4000	4500
Trigger	nan	0.040	0.044	0.045	0.040	0.036	0.028	0.019
Quality	nan	0.984	0.979	0.970	0.967	0.954	0.953	0.946
$e55 > 200$	nan	0.946	0.942	0.942	0.934	0.930	0.922	0.911
$f51 > 0.85$	nan	0.534	0.557	0.558	0.543	0.559	0.564	0.614
$dEdXSig > 9.0$	nan	0.996	0.995	0.994	0.985	0.981	0.961	0.944

Table 64 – The relative efficiency for `Photon strategy` for Spin Zero Photon Fusion samples for the 2018 MC campaign. Efficiencies are shown for each mass point from 1000 to 4500 GeV and are computed relative to the number of events entering each selection stage and by the Equation 6.8. The steps include the HLT application, missing transverse momentum requirement, standard preselection, and the discriminant variable cuts on variables $f_{51} > 0.85$ and $dEdX_{\texttt{Significance}} > 9.0$.

Mass [GeV]	1000	1500	2000	2500	3000	3500	4000	4500
Trigger	nan	0.045	0.046	0.046	0.042	0.037	0.029	0.021
Quality	nan	0.978	0.977	0.973	0.968	0.954	0.958	0.954
$e55 > 200$	nan	0.937	0.941	0.940	0.934	0.921	0.908	0.912
$f51 > 0.85$	nan	0.547	0.552	0.539	0.538	0.545	0.599	0.612
$dEdXSig > 9.0$	nan	0.994	0.995	0.990	0.983	0.974	0.955	0.933

Table 65 – The relative efficiency for `Photon strategy` for Spin Zero Photon Fusion samples for the 2017 MC campaign. Efficiencies are shown for each mass point from 1000 to 4500 GeV and are computed relative to the number of events entering each selection stage and by the Equation 6.8. The steps include the HLT application, missing transverse momentum requirement, standard preselection, and the discriminant variable cuts on variables $f_{51} > 0.85$ and $dEdX_{\texttt{Significance}} > 9.0$.

B.2 `PFMET Strategy`

Mass [GeV]	1000	1500	2000	2500	3000	3500	4000	4500
Trigger	nan	0.052	0.050	0.048	0.043	0.037	0.027	0.019
Quality	nan	0.968	0.979	0.972	0.970	0.962	0.959	0.954
$e55 > 175$	nan	0.953	0.970	0.966	0.968	0.964	0.967	0.967
$f51 > 0.85$	nan	0.558	0.556	0.566	0.554	0.527	0.583	0.621
$dEdXSig > 9.0$	nan	0.993	0.987	0.981	0.982	0.950	0.945	0.888

Table 66 – The relative efficiency for `Photon strategy` for Spin Zero Photon Fusion samples for the 2016APV MC campaign. Efficiencies are shown for each mass point from 1000 to 4500 GeV and are computed relative to the number of events entering each selection stage and by the Equation 6.8. The steps include the HLT application, missing transverse momentum requirement, standard preselection, and the discriminant variable cuts on variables $f_{51} > 0.85$ and $dEdX_{\texttt{Significance}} > 9.0$.

Mass [GeV]	1000	1500	2000	2500	3000	3500	4000	4500
Trigger	0.050	0.062	0.064	0.063	0.056	0.049	0.039	0.027
Quality	0.986	0.985	0.982	0.971	0.965	0.957	0.951	0.952
$e55 > 200$	0.938	0.952	0.952	0.950	0.941	0.931	0.918	0.912
$f51 > 0.85$	0.527	0.553	0.560	0.559	0.556	0.567	0.581	0.599
$dEdXSig > 9.0$	0.994	0.995	0.995	0.990	0.988	0.977	0.969	0.950

Table 67 – The relative efficiency for `Photon strategy` for Spin Half Photon Fusion samples for the 2018 MC campaign. Efficiencies are shown for each mass point from 1000 to 4500 GeV and are computed relative to the number of events entering each selection stage and by the Equation 6.8. The steps include the HLT application, missing transverse momentum requirement, standard preselection, and the discriminant variable cuts on variables $f_{51} > 0.85$ and $dEdX_{\texttt{Significance}} > 9.0$.

Mass [GeV]	1000	1500	2000	2500	3000	3500	4000	4500
Trigger	0.055	0.064	0.067	0.066	0.059	0.050	0.040	0.026
Quality	0.974	0.980	0.976	0.975	0.968	0.958	0.955	0.954
$e55 > 200$	0.922	0.944	0.941	0.941	0.933	0.931	0.915	0.906
$f51 > 0.85$	0.533	0.547	0.562	0.576	0.547	0.562	0.592	0.629
$dEdXSig > 9.0$	0.993	0.996	0.993	0.992	0.989	0.979	0.955	0.943

Table 68 – The relative efficiency for `Photon strategy` for Spin Half Photon Fusion samples for the 2017 MC campaign. Efficiencies are shown for each mass point from 1000 to 4500 GeV and are computed relative to the number of events entering each selection stage and by the Equation 6.8. The steps include the HLT application, missing transverse momentum requirement, standard preselection, and the discriminant variable cuts on variables $f_{51} > 0.85$ and $dEdX_{\texttt{Significance}} > 9.0$.

Mass [GeV]	1000	1500	2000	2500	3000	3500	4000	4500
Trigger	0.062	0.071	0.072	0.068	0.059	nan	0.040	0.026
Quality	0.962	0.968	0.972	0.968	0.961	nan	0.948	0.945
$e55 > 175$	0.924	0.950	0.966	0.972	0.967	nan	0.965	0.964
$f51 > 0.85$	0.541	0.574	0.571	0.570	0.544	nan	0.580	0.607
$dEdXSig > 9.0$	0.993	0.996	0.997	0.993	0.989	nan	0.967	0.966

Table 69 – The relative efficiency for `Photon strategy` for Spin Half Photon Fusion samples for the 2016 MC campaign. Efficiencies are shown for each mass point from 1000 to 4500 GeV and are computed relative to the number of events entering each selection stage and by the Equation 6.8. The steps include the HLT application, missing transverse momentum requirement, standard preselection, and the discriminant variable cuts on variables $f_{51} > 0.85$ and $dEdX_{\texttt{Significance}} > 9.0$.

Mass [GeV]	1000	1500	2000	2500	3000	3500	4000	4500
Trigger	0.063	0.072	0.069	0.068	0.059	0.050	0.039	0.026
Quality	0.973	0.974	0.974	0.977	0.966	0.963	0.951	0.943
$e55 > 175$	0.924	0.948	0.966	0.969	0.968	0.977	0.966	0.961
$f51 > 0.85$	0.544	0.550	0.561	0.561	0.550	0.549	0.573	0.594
$dEdXSig > 9.0$	0.992	0.992	0.991	0.986	0.973	0.951	0.936	0.902

Table 70 – The relative efficiency for `Photon strategy` for Spin Half Photon Fusion samples for the 2016APV MC campaign. Efficiencies are shown for each mass point from 1000 to 4500 GeV and are computed relative to the number of events entering each selection stage and by the Equation 6.8. The steps include the HLT application, missing transverse momentum requirement, standard preselection, and the discriminant variable cuts on variables $f_{51} > 0.85$ and $dEdX_{\texttt{Significance}} > 9.0$.

Mass [GeV]	1000	1500	2000	2500	3000	3500	4000	4500
Generated	0	67000	95000	98000	98000	100000	100000	100000
Trigger	0	10131	18780	26355	30756	23475	11151	5098
PFMET_pt > 400	0	5901	11116	16377	18618	12263	4157	1735
Preselections	0	5770	10875	15974	18035	11736	3911	1608
$f51 > 0.85$	0	4330	8071	12081	13687	8879	2942	1262
$dEdXSig > 9.0$	0	4186	7773	11517	12578	7880	2535	1083
signal efficiency (%)	nan	6.248%	8.182%	11.752%	12.835%	7.880%	2.535%	1.083%

Table 71 – The analysis Cutflow for the `PFMET strategy` for SpinZero Drell-Yan samples for the 2018 MC campaign. The table shows the number of signal events surviving each selection step across the generated monopole mass points, from 1000 to 4500 GeV. The steps include the HLT application, missing transverse momentum requirement, standard preselection, and the discriminant variable cuts on variables $f_{51} > 0.85$ and $dEdX_{\texttt{Significance}} > 9.0$. The final row corresponds to the overall signal efficiency for each mass point.

Mass [GeV]	1000	1500	2000	2500	3000	3500	4000	4500
Generated	95000	0	97000	98000	98000	99000	100000	97000
Trigger	11653	0	19928	26822	31412	23815	11633	5214
PFMET_pt > 400	6723	0	11906	16440	18737	12169	4366	1579
Preselections	6550	0	11605	16032	18172	11622	4107	1468
$f51 > 0.85$	4965	0	8706	12224	13853	8824	3136	1140
$dEdXSig > 9.0$	4823	0	8383	11615	12649	7727	2729	953
signal efficiency (%)	5.077%	nan	8.642%	11.852%	12.907%	7.805%	2.729%	0.982%

Table 72 – The analysis Cutflow for the `PFMET strategy` for SpinZero Drell-Yan samples for the 2017 MC campaign. The table shows the number of signal events surviving each selection step across the generated monopole mass points, from 1000 to 4500 GeV. The steps include the HLT application, missing transverse momentum requirement, standard preselection, and the discriminant variable cuts on variables $f_{51} > 0.85$ and $dEdX_{\texttt{Significance}} > 9.0$. The final row corresponds to the overall signal efficiency for each mass point.

Mass [GeV]	1000	1500	2000	2500	3000	3500	4000	4500
Generated	48180	48176	50000	50000	50000	50000	48166	49082
Trigger	4927	6060	8197	11298	13056	9512	4257	2009
PFMET_pt > 500	2195	2845	4028	5748	6451	3846	1116	484
Preselections	2120	2775	3911	5536	6110	3584	1027	421
$f51 > 0.85$	1591	1998	2818	4172	4639	2732	789	341
$dEdXSig > 9.0$	1567	1960	2757	4014	4361	2510	708	302
signal efficiency (%)	3.252%	4.068%	5.514%	8.028%	8.722%	5.020%	1.470%	0.615%

Table 73 – The analysis Cutflow for the `PFMET strategy` for SpinZero Drell-Yan samples for the 2016 MC campaign. The table shows the number of signal events surviving each selection step across the generated monopole mass points, from 1000 to 4500 GeV. The steps include the HLT application, missing transverse momentum requirement, standard preselection, and the discriminant variable cuts on variables $f_{51} > 0.85$ and $dEdX_{\texttt{Significance}} > 9.0$. The final row corresponds to the overall signal efficiency for each mass point.

Mass [GeV]	1000	1500	2000	2500	3000	3500	4000	4500
Generated	50000	47339	50000	50000	50000	50000	48220	48216
Trigger	5316	5949	8191	11268	12784	9303	4139	1977
PFMET_pt > 500	2196	2657	3947	5683	6280	3705	1102	475
Preselections	2143	2597	3852	5496	6070	3528	1024	434
f51 > 0.85	1622	1897	2797	4136	4723	2696	810	368
dEdXSig > 9.0	1593	1845	2692	3874	4202	2253	667	290
signal efficiency (%)	3.186%	3.897%	5.384%	7.748%	8.404%	4.506%	1.383%	0.601%

Table 74 – The analysis Cutflow for the `PFMET strategy` for SpinZero Drell-Yan samples for the 2016APV MC campaign. The table shows the number of signal events surviving each selection step across the generated monopole mass points, from 1000 to 4500 GeV. The steps include the HLT application, missing transverse momentum requirement, standard preselection, and the discriminant variable cuts on variables $f_{51} > 0.85$ and $dEdX_{\texttt{Significance}} > 9.0$. The final row corresponds to the overall signal efficiency for each mass point.

Mass [GeV]	1000	1500	2000	2500	3000	3500	4000	4500
Generated	0	95000	99000	99000	100000	99000	100000	100000
Trigger	0	2616	2518	1987	1442	780	403	164
PFMET_pt > 400	0	1490	1410	1035	593	164	41	8
Preselections	0	1439	1352	1001	579	160	39	8
f51 > 0.85	0	960	859	609	388	99	35	8
dEdXSig > 9.0	0	914	830	588	382	98	35	8
signal efficiency (%)	nan	0.962%	0.838%	0.594%	0.382%	0.099%	0.035%	0.008%

Table 75 – The analysis Cutflow for the `PFMET strategy` for SpinZero Photon Fusion samples for the 2018 MC campaign. The table shows the number of signal events surviving each selection step across the generated monopole mass points, from 1000 to 4500 GeV. The steps include the HLT application, missing transverse momentum requirement, standard preselection, and the discriminant variable cuts on variables $f_{51} > 0.85$ and $dEdX_{\texttt{Significance}} > 9.0$. The final row corresponds to the overall signal efficiency for each mass point.

Mass [GeV]	1000	1500	2000	2500	3000	3500	4000	4500
Generated	0	99000	100000	98000	99000	99000	99000	100000
Trigger	0	2769	2590	2147	1478	894	432	174
PFMET_pt > 400	0	1750	1643	1292	707	264	62	7
Preselections	0	1671	1563	1243	682	254	61	6
f51 > 0.85	0	1154	1019	805	442	154	45	6
dEdXSig > 9.0	0	1122	986	769	426	150	43	5
signal efficiency (%)	nan	1.133%	0.986%	0.785%	0.430%	0.152%	0.043%	0.005%

Table 76 – The analysis Cutflow for the `PFMET strategy` for SpinZero Photon Fusion samples for the 2017 MC campaign. The table shows the number of signal events surviving each selection step across the generated monopole mass points, from 1000 to 4500 GeV. The steps include the HLT application, missing transverse momentum requirement, standard preselection, and the discriminant variable cuts on variables $f_{51} > 0.85$ and $dEdX_{\texttt{Significance}} > 9.0$. The final row corresponds to the overall signal efficiency for each mass point.

Mass [GeV]	1000	1500	2000	2500	3000	3500	4000	4500
Generated	0	48228	48226	49112	50000	49110	49109	49108
Trigger	0	1174	1062	788	535	308	159	65
PFMET_pt > 500	0	521	532	418	229	69	13	2
Preselections	0	502	514	407	221	64	13	2
f51 > 0.85	0	335	318	252	138	36	9	2
dEdXSig > 9.0	0	331	312	246	137	35	8	2
signal efficiency (%)	nan	0.686%	0.647%	0.501%	0.274%	0.071%	0.016%	0.004%

Table 77 – The analysis Cutflow for the `PFMET strategy` for SpinZero Photon Fusion samples for the 2016APV MC campaign. The table shows the number of signal events surviving each selection step across the generated monopole mass points, from 1000 to 4500 GeV. The steps include the HLT application, missing transverse momentum requirement, standard preselection, and the discriminant variable cuts on variables $f_{51} > 0.85$ and $dEdX_{\texttt{Significance}} > 9.0$. The final row corresponds to the overall signal efficiency for each mass point.

Mass [GeV]	1000	1500	2000	2500	3000	3500	4000	4500
Generated	93000	90000	99000	100000	99000	92000	100000	100000
Trigger	3266	3976	4118	3426	2423	1366	703	255
PFMET_pt > 400	1996	2369	2342	1849	1059	352	73	11
Preselections	1896	2266	2247	1799	1028	344	73	11
$f51 > 0.85$	1411	1547	1452	1140	654	229	56	10
$dEdXSig > 9.0$	1365	1491	1409	1115	647	225	53	10
signal efficiency (%)	1.468%	1.657%	1.423%	1.115%	0.654%	0.245%	0.053%	0.010%

Table 78 – The analysis Cutflow for the `PFMET strategy` for SpinHalf Photon Fusion samples for the 2018 MC campaign. The table shows the number of signal events surviving each selection step across the generated monopole mass points, from 1000 to 4500 GeV. The steps include the HLT application, missing transverse momentum requirement, standard preselection, and the discriminant variable cuts on variables $f_{51} > 0.85$ and $dEdX_{\texttt{Significance}} > 9.0$. The final row corresponds to the overall signal efficiency for each mass point.

Mass [GeV]	1000	1500	2000	2500	3000	3500	4000	4500
Generated	92000	97000	97000	100000	99000	99000	100000	72000
Trigger	3379	4440	4250	3606	2478	1489	703	221
PFMET_pt > 400	2245	2913	2722	2136	1249	458	106	13
Preselections	2142	2768	2596	2055	1200	446	103	13
$f51 > 0.85$	1582	1899	1703	1288	786	312	74	10
$dEdXSig > 9.0$	1524	1828	1650	1239	770	306	73	9
signal efficiency (%)	1.657%	1.885%	1.701%	1.239%	0.778%	0.309%	0.073%	0.013%

Table 79 – The analysis Cutflow for the `PFMET strategy` for SpinHalf Photon Fusion samples for the 2017 MC campaign. The table shows the number of signal events surviving each selection step across the generated monopole mass points, from 1000 to 4500 GeV. The steps include the HLT application, missing transverse momentum requirement, standard preselection, and the discriminant variable cuts on variables $f_{51} > 0.85$ and $dEdX_{\texttt{Significance}} > 9.0$. The final row corresponds to the overall signal efficiency for each mass point.

Mass [GeV]	1000	1500	2000	2500	3000	3500	4000	4500
Generated	50000	49090	50000	49085	50000	0	50000	45410
Trigger	1769	1935	1732	1293	907	0	308	94
PFMET_pt > 500	743	935	918	695	396	0	32	2
Preselections	703	905	873	670	384	0	30	2
f51 > 0.85	525	599	541	387	239	0	20	2
dEdXSig > 9.0	520	593	527	383	237	0	20	2
signal efficiency (%)	1.040%	1.208%	1.054%	0.780%	0.474%	nan	0.040%	0.004%

Table 80 – The analysis Cutflow for the `PFMET strategy` for SpinHalf Photon Fusion samples for the 2016 MC campaign. The table shows the number of signal events surviving each selection step across the generated monopole mass points, from 1000 to 4500 GeV. The steps include the HLT application, missing transverse momentum requirement, standard preselection, and the discriminant variable cuts on variables $f_{51} > 0.85$ and $dEdX_{\texttt{Significance}} > 9.0$. The final row corresponds to the overall signal efficiency for each mass point.

Mass [GeV]	1000	1500	2000	2500	3000	3500	4000	4500
Generated	50000	50000	49114	49113	49728	50000	46440	50000
Trigger	1817	1911	1778	1374	887	529	249	110
PFMET_pt > 500	675	849	919	684	360	125	17	3
Preselections	652	823	880	671	352	119	16	3
f51 > 0.85	458	507	571	419	224	69	10	3
dEdXSig > 9.0	453	493	558	411	220	66	8	3
signal efficiency (%)	0.906%	0.986%	1.136%	0.837%	0.442%	0.132%	0.017%	0.006%

Table 81 – The analysis Cutflow for the `PFMET strategy` for SpinHalf Photon Fusion samples for the 2016APV MC campaign. The table shows the number of signal events surviving each selection step across the generated monopole mass points, from 1000 to 4500 GeV. The steps include the HLT application, missing transverse momentum requirement, standard preselection, and the discriminant variable cuts on variables $f_{51} > 0.85$ and $dEdX_{\texttt{Significance}} > 9.0$. The final row corresponds to the overall signal efficiency for each mass point.

Mass [GeV]	1000	1500	2000	2500	3000	3500	4000	4500
Trigger	nan	0.151	0.198	0.269	0.314	0.235	0.112	0.051
PFMET_pt > 400	nan	0.582	0.592	0.621	0.605	0.522	0.373	0.340
Quality	nan	0.978	0.978	0.975	0.969	0.957	0.941	0.927
f51 > 0.85	nan	0.750	0.742	0.756	0.759	0.757	0.752	0.785
dEdXSig > 9.0	nan	0.967	0.963	0.953	0.919	0.887	0.862	0.858

Table 82 – The relative efficiency for `PFMET strategy` for Spin Zero Drell-Yan samples for the 2018 MC campaign. Efficiencies are shown for each mass point from 1000 to 4500 GeV and are computed relative to the number of events entering each selection stage and by the Equation 6.8. The steps include the HLT application, missing transverse momentum requirement, standard preselection, and the discriminant variable cuts on variables $f_{51} > 0.85$ and $dEdX_{\texttt{Significance}} > 9.0$.

Mass [GeV]	1000	1500	2000	2500	3000	3500	4000	4500
Trigger	0.123	nan	0.205	0.274	0.321	0.241	0.116	0.054
PFMET_pt $>$ 400	0.577	nan	0.597	0.613	0.596	0.511	0.375	0.303
Quality	0.974	nan	0.975	0.975	0.970	0.955	0.941	0.930
f51 $>$ 0.85	0.758	nan	0.750	0.762	0.762	0.759	0.764	0.777
dEdXSig $>$ 9.0	0.971	nan	0.963	0.950	0.913	0.876	0.870	0.836

Table 83 – The relative efficiency for `PFMET strategy` for Spin Zero Drell-Yan samples for the 2017 MC campaign. Efficiencies are shown for each mass point from 1000 to 4500 GeV and are computed relative to the number of events entering each selection stage and by the Equation 6.8. The steps include the HLT application, missing transverse momentum requirement, standard preselection, and the discriminant variable cuts on variables $f_{51} > 0.85$ and $dEdX_{\texttt{Significance}} > 9.0$.

Mass [GeV]	1000	1500	2000	2500	3000	3500	4000	4500
Trigger	0.102	0.126	0.164	0.226	0.261	0.190	0.088	0.041
PFMET_pt $>$ 500	0.446	0.469	0.491	0.509	0.494	0.404	0.262	0.241
Quality	0.966	0.975	0.971	0.963	0.947	0.932	0.920	0.870
f51 $>$ 0.85	0.750	0.720	0.721	0.754	0.759	0.762	0.768	0.810
dEdXSig $>$ 9.0	0.985	0.981	0.978	0.962	0.940	0.919	0.897	0.886

Table 84 – The relative efficiency for `PFMET strategy` for Spin Zero Drell-Yan samples for the 2016 MC campaign. Efficiencies are shown for each mass point from 1000 to 4500 GeV and are computed relative to the number of events entering each selection stage and by the Equation 6.8. The steps include the HLT application, missing transverse momentum requirement, standard preselection, and the discriminant variable cuts on variables $f_{51} > 0.85$ and $dEdX_{\texttt{Significance}} > 9.0$.

Mass [GeV]	1000	1500	2000	2500	3000	3500	4000	4500
Trigger	0.106	0.126	0.164	0.225	0.256	0.186	0.086	0.041
PFMET_pt $>$ 500	0.413	0.447	0.482	0.504	0.491	0.398	0.266	0.240
Quality	0.976	0.977	0.976	0.967	0.967	0.952	0.929	0.914
f51 $>$ 0.85	0.757	0.730	0.726	0.753	0.778	0.764	0.791	0.848
dEdXSig $>$ 9.0	0.982	0.973	0.962	0.937	0.890	0.836	0.823	0.788

Table 85 – The relative efficiency for `PFMET strategy` for Spin Zero Drell-Yan samples for the 2016APV MC campaign. Efficiencies are shown for each mass point from 1000 to 4500 GeV and are computed relative to the number of events entering each selection stage and by the Equation 6.8. The steps include the HLT application, missing transverse momentum requirement, standard preselection, and the discriminant variable cuts on variables $f_{51} > 0.85$ and $dEdX_{\texttt{Significance}} > 9.0$.

Mass [GeV]	1000	1500	2000	2500	3000	3500	4000	4500
Trigger	nan	0.028	0.025	0.020	0.014	0.008	0.004	0.002
PFMET_pt > 400	nan	0.570	0.560	0.521	0.411	0.210	0.102	0.049
Quality	nan	0.966	0.959	0.967	0.976	0.976	0.951	1.000
f51 > 0.85	nan	0.667	0.635	0.608	0.670	0.619	0.897	1.000
dEdXSig > 9.0	nan	0.952	0.966	0.966	0.985	0.990	1.000	1.000

Table 86 – The relative efficiency for `PFMET strategy` for Spin Zero Photon Fusion samples for the 2018 MC campaign. Efficiencies are shown for each mass point from 1000 to 4500 GeV and are computed relative to the number of events entering each selection stage and by the Equation 6.8. The steps include the HLT application, missing transverse momentum requirement, standard preselection, and the discriminant variable cuts on variables $f_{51} > 0.85$ and $dEdX_{\texttt{Significance}} > 9.0$.

Mass [GeV]	1000	1500	2000	2500	3000	3500	4000	4500
Trigger	nan	0.028	0.026	0.022	0.015	0.009	0.004	0.002
PFMET_pt > 400	nan	0.632	0.634	0.602	0.478	0.295	0.144	0.040
Quality	nan	0.955	0.951	0.962	0.965	0.962	0.984	0.857
f51 > 0.85	nan	0.691	0.652	0.648	0.648	0.606	0.738	1.000
dEdXSig > 9.0	nan	0.972	0.968	0.955	0.964	0.974	0.956	0.833

Table 87 – The relative efficiency for `PFMET strategy` for Spin Zero Photon Fusion samples for the 2017 MC campaign. Efficiencies are shown for each mass point from 1000 to 4500 GeV and are computed relative to the number of events entering each selection stage and by the Equation 6.8. The steps include the HLT application, missing transverse momentum requirement, standard preselection, and the discriminant variable cuts on variables $f_{51} > 0.85$ and $dEdX_{\texttt{Significance}} > 9.0$.

Mass [GeV]	1000	1500	2000	2500	3000	3500	4000	4500
Trigger	nan	0.024	0.022	0.016	0.011	0.006	0.003	0.001
PFMET_pt > 500	nan	0.444	0.501	0.530	0.428	0.224	0.082	0.031
Quality	nan	0.964	0.966	0.974	0.965	0.928	1.000	1.000
f51 > 0.85	nan	0.667	0.619	0.619	0.624	0.562	0.692	1.000
dEdXSig > 9.0	nan	0.988	0.981	0.976	0.993	0.972	0.889	1.000

Table 88 – The relative efficiency for `PFMET strategy` for Spin Zero Photon Fusion samples for the 2016 MC campaign. Efficiencies are shown for each mass point from 1000 to 4500 GeV and are computed relative to the number of events entering each selection stage and by the Equation 6.8. The steps include the HLT application, missing transverse momentum requirement, standard preselection, and the discriminant variable cuts on variables $f_{51} > 0.85$ and $dEdX_{\texttt{Significance}} > 9.0$.

Mass [GeV]	1000	1500	2000	2500	3000	3500	4000	4500
Trigger	nan	0.024	0.022	0.016	0.011	0.006	0.003	0.001
PFMET_pt > 500	nan	0.444	0.501	0.530	0.428	0.224	0.082	0.031
Quality	nan	0.964	0.966	0.974	0.965	0.928	1.000	1.000
f51 > 0.85	nan	0.667	0.619	0.619	0.624	0.562	0.692	1.000
dEdXSig > 9.0	nan	0.988	0.981	0.976	0.993	0.972	0.889	1.000

Table 89 – The relative efficiency for `PFMET strategy` for Spin Zero Photon Fusion samples for the 2016APV MC campaign. Efficiencies are shown for each mass point from 1000 to 4500 GeV and are computed relative to the number of events entering each selection stage and by the Equation 6.8. The steps include the HLT application, missing transverse momentum requirement, standard preselection, and the discriminant variable cuts on variables $f_{51} > 0.85$ and $dEdX_{\texttt{Significance}} > 9.0$.

Mass [GeV]	1000	1500	2000	2500	3000	3500	4000	4500
Trigger	0.035	0.044	0.042	0.034	0.024	0.015	0.007	0.003
PFMET_pt > 400	0.611	0.596	0.569	0.540	0.437	0.258	0.104	0.043
Quality	0.950	0.957	0.959	0.973	0.971	0.977	1.000	1.000
f51 > 0.85	0.744	0.683	0.646	0.634	0.636	0.666	0.767	0.909
dEdXSig > 9.0	0.967	0.964	0.970	0.978	0.989	0.983	0.946	1.000

Table 90 – The relative efficiency for `PFMET strategy` for Spin Half Photon Fusion samples for the 2018 MC campaign. Efficiencies are shown for each mass point from 1000 to 4500 GeV and are computed relative to the number of events entering each selection stage and by the Equation 6.8. The steps include the HLT application, missing transverse momentum requirement, standard preselection, and the discriminant variable cuts on variables $f_{51} > 0.85$ and $dEdX_{\texttt{Significance}} > 9.0$.

Mass [GeV]	1000	1500	2000	2500	3000	3500	4000	4500
Trigger	0.037	0.046	0.044	0.036	0.025	0.015	0.007	0.003
PFMET_pt > 400	0.664	0.656	0.640	0.592	0.504	0.308	0.151	0.059
Quality	0.954	0.950	0.954	0.962	0.961	0.974	0.972	1.000
f51 > 0.85	0.739	0.686	0.656	0.627	0.655	0.700	0.718	0.769
dEdXSig > 9.0	0.963	0.963	0.969	0.962	0.980	0.981	0.986	0.900

Table 91 – The relative efficiency for `PFMET strategy` for Spin Half Photon Fusion samples for the 2017 MC campaign. Efficiencies are shown for each mass point from 1000 to 4500 GeV and are computed relative to the number of events entering each selection stage and by the Equation 6.8. The steps include the HLT application, missing transverse momentum requirement, standard preselection, and the discriminant variable cuts on variables $f_{51} > 0.85$ and $dEdX_{\texttt{Significance}} > 9.0$.

Mass [GeV]	1000	1500	2000	2500	3000	3500	4000	4500
Trigger	0.035	0.039	0.035	0.026	0.018	nan	0.006	0.002
PFMET_pt > 500	0.420	0.483	0.530	0.538	0.437	nan	0.104	0.021
Quality	0.946	0.968	0.951	0.964	0.970	nan	0.938	1.000
f51 > 0.85	0.747	0.662	0.620	0.578	0.622	nan	0.667	1.000
dEdXSig > 9.0	0.990	0.990	0.974	0.990	0.992	nan	1.000	1.000

Table 92 – The relative efficiency for `PFMET strategy` for Spin Half Photon Fusion samples for the 2016 MC campaign. Efficiencies are shown for each mass point from 1000 to 4500 GeV and are computed relative to the number of events entering each selection stage and by the Equation 6.8. The steps include the HLT application, missing transverse momentum requirement, standard preselection, and the discriminant variable cuts on variables $f_{51} > 0.85$ and $dEdX_{\texttt{Significance}} > 9.0$.

Mass [GeV]	1000	1500	2000	2500	3000	3500	4000	4500
Trigger	0.036	0.038	0.036	0.028	0.018	0.011	0.005	0.002
PFMET_pt > 500	0.371	0.444	0.517	0.498	0.406	0.236	0.068	0.027
Quality	0.966	0.969	0.958	0.981	0.978	0.952	0.941	1.000
f51 > 0.85	0.702	0.616	0.649	0.624	0.636	0.580	0.625	1.000
dEdXSig > 9.0	0.989	0.972	0.977	0.981	0.982	0.957	0.800	1.000

Table 93 – The relative efficiency for `PFMET strategy` for Spin Half Photon Fusion samples for the 2016APV MC campaign. Efficiencies are shown for each mass point from 1000 to 4500 GeV and are computed relative to the number of events entering each selection stage and by the Equation 6.8. The steps include the HLT application, missing transverse momentum requirement, standard preselection, and the discriminant variable cuts on variables $f_{51} > 0.85$ and $dEdX_{\texttt{Significance}} > 9.0$.

C PFMET trigger efficiencies

This appendix presents the trigger efficiencies for the `HLT_PFMET250_HBHECleaned` (2017-2018) and `HLT_PFMET300` (2016-2016APV) paths, evaluated for all magnetic monopole production modes for some of the mass points considered: 1500 GeV, 2500 GeV, 3500 GeV, and 4500 GeV. The efficiencies were derived using simulated signal samples from the 2016, 2017 and 2018 MC campaigns through the cut-and-count method. The analysis was performed separately for the barrel region, the endcap region, and the combination of both, allowing for a detailed assessment of the trigger performance across the CMS detector. Results are shown as a function of `PFMET_pt` and include all four production mechanisms: Drell–Yan with Spin-Zero, Drell–Yan with Spin-Half, Photon Fusion with Spin-Zero, and Photon Fusion with Spin-Half.

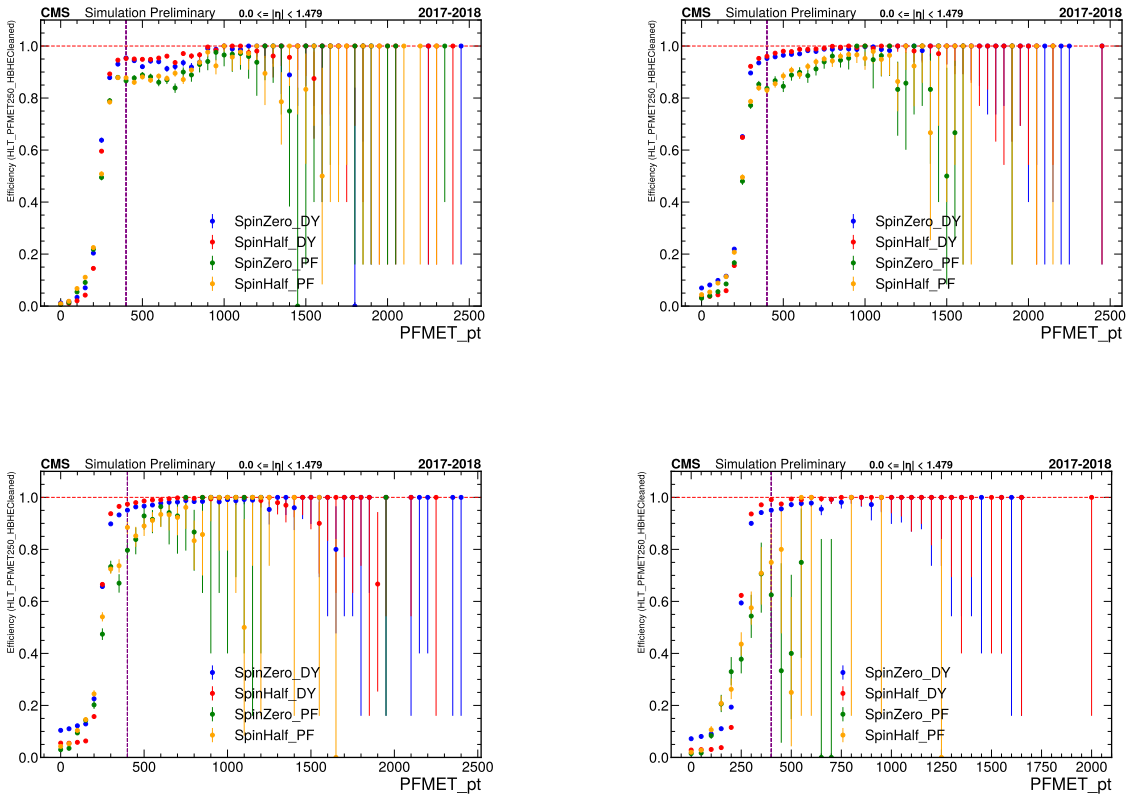

Figure 94 – Trigger efficiency of the `HLT_PFMET250_HBHECleaned` path as a function of `PFMET_pt` for simulated magnetic monopole samples with masses of 1500 GeV (top left), 2500 GeV (top right), 3500 GeV (bottom left), and 4500 GeV (bottom right). The plots combine results from the 2017 and 2018 MC campaigns and focus on the barrel region of the CMS detector. Efficiency curves are shown for four production modes: Drell–Yan Spin-0 (blue), Drell–Yan Spin-Half (red), Photon Fusion Spin-0 (green), and Photon Fusion Spin-Half (yellow).

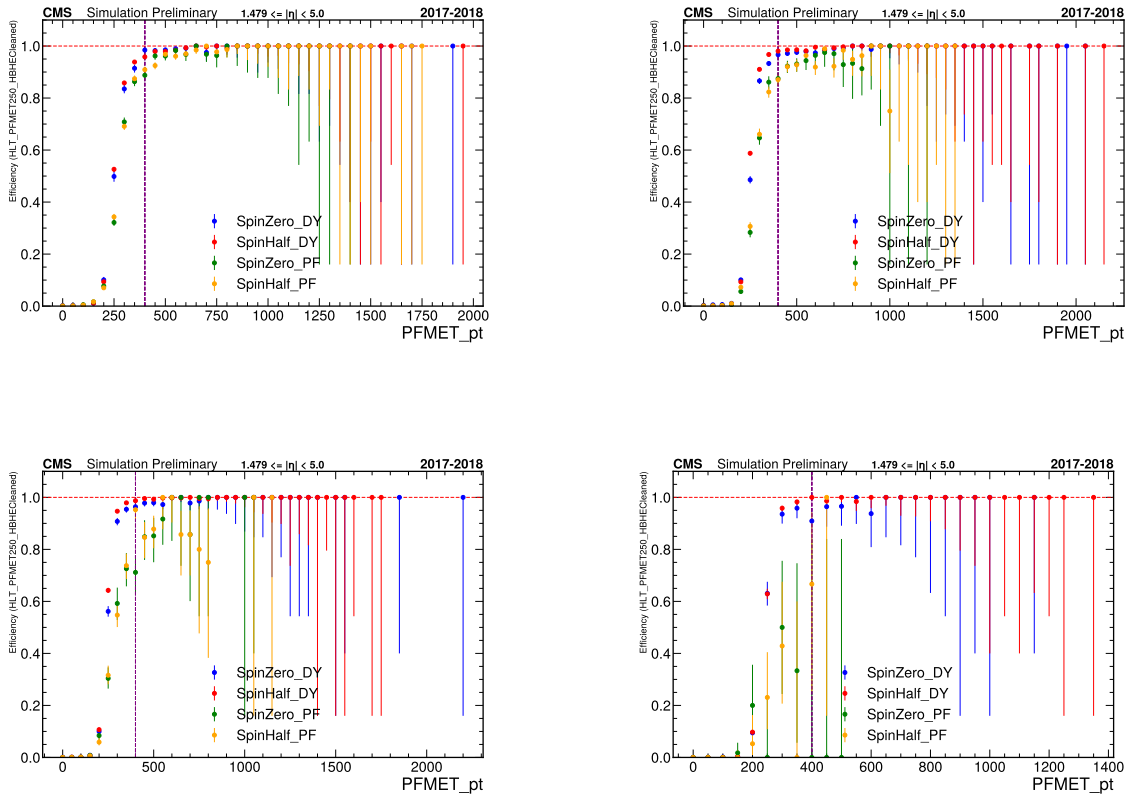

Figure 95 – Trigger efficiency of the `HLT_PFMET250_HBHECleaned` path as a function of `PFMET_pt` for simulated magnetic monopole samples with masses of 1500 GeV (top left), 2500 GeV (top right), 3500 GeV (bottom left), and 4500 GeV (bottom right). The plots combine results from the 2017 and 2018 MC campaigns and focus on the endcap regions of the CMS detector. Efficiency curves are shown for four production modes: Drell–Yan Spin-0 (blue), Drell–Yan Spin-Half (red), Photon Fusion Spin-0 (green), and Photon Fusion Spin-Half (yellow).

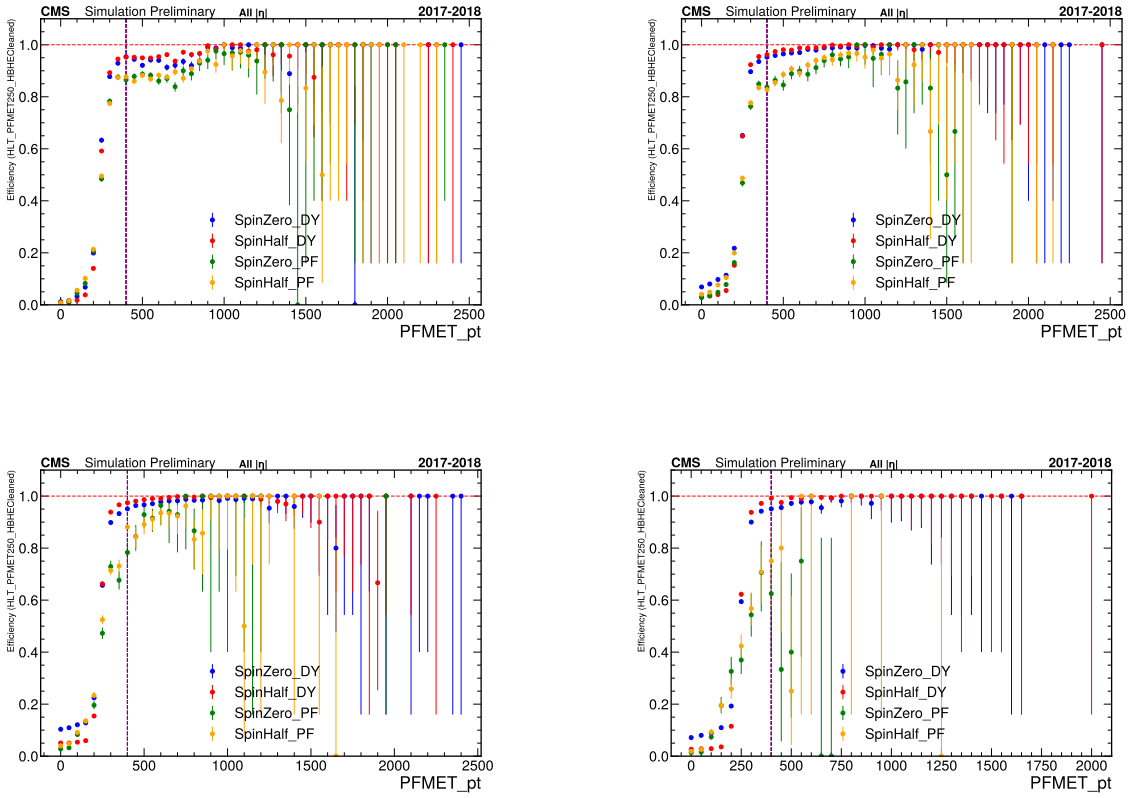

Figure 96 – Trigger efficiency of the `HLT_PFMET250_HBHECleaned` path as a function of `PFMET_pt` for simulated magnetic monopole samples with masses of 1500 GeV (top left), 2500 GeV (top right), 3500 GeV (bottom left), and 4500 GeV (bottom right). The plots combine results from the 2017 and 2018 MC campaigns and focus on the combination of barrel and endcap regions of the CMS detector. Efficiency curves are shown for four production modes: Drell–Yan Spin-0 (blue), Drell–Yan Spin-Half (red), Photon Fusion Spin-0 (green), and Photon Fusion Spin-Half (yellow).

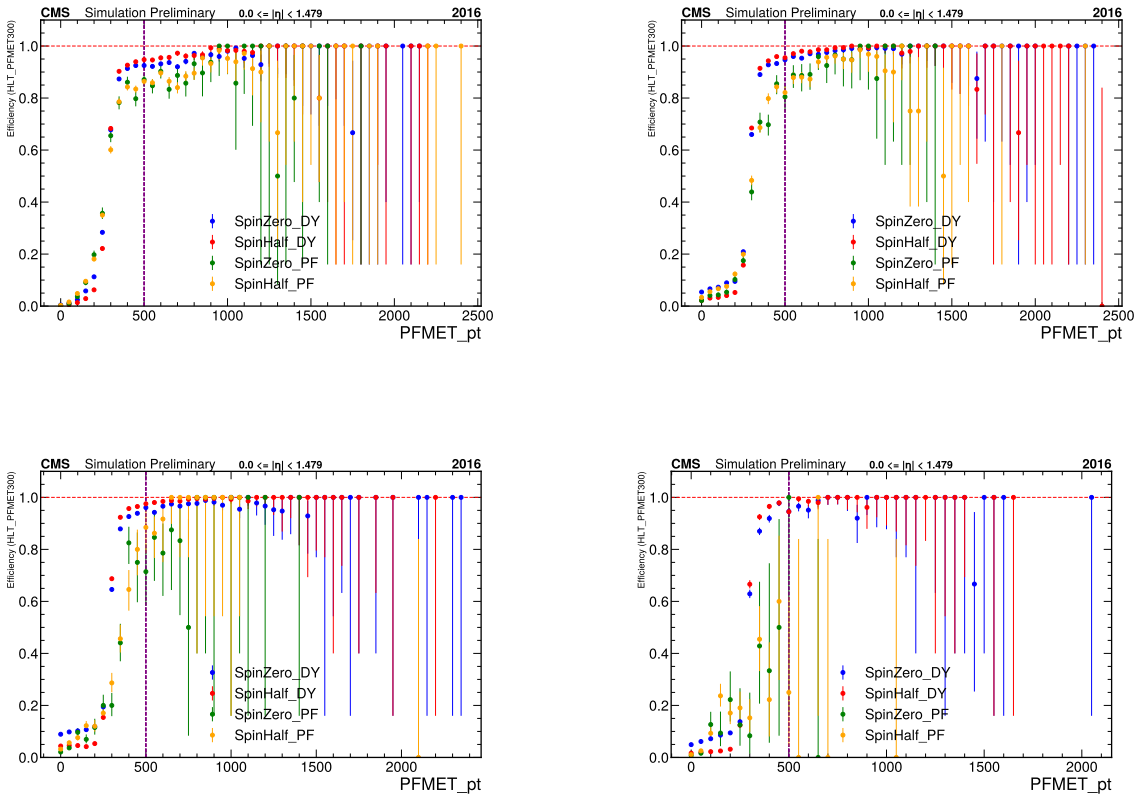

Figure 97 – Trigger efficiency of the `HLT_PFMET300` path as a function of `PFMET_pt` for simulated magnetic monopole samples with masses of 1500 GeV (top left), 2500 GeV (top right), 3500 GeV (bottom left), and 4500 GeV (bottom right). The plots combine results from the 2017 and 2018 MC campaigns and focus on the barrel region of the CMS detector. Efficiency curves are shown for four production modes: Drell–Yan Spin-0 (blue), Drell–Yan Spin-Half (red), Photon Fusion Spin-0 (green), and Photon Fusion Spin-Half (yellow).

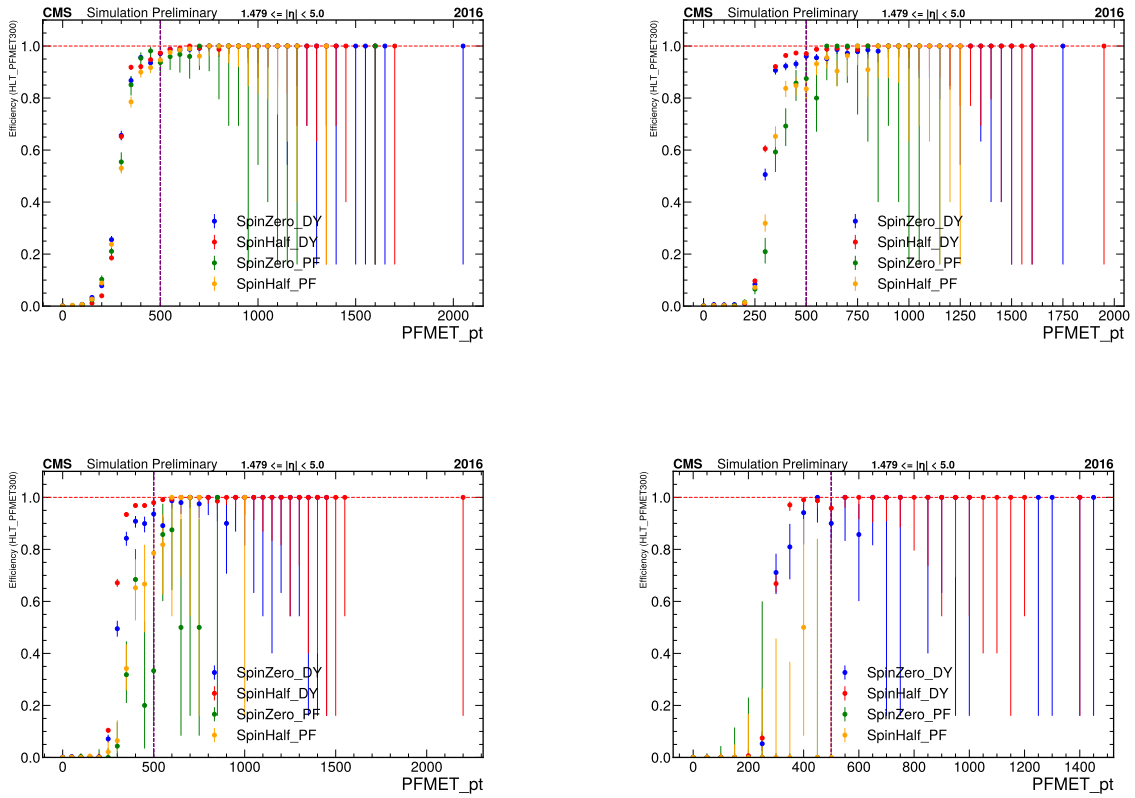

Figure 98 – Trigger efficiency of the `HLT_PFMET250_HBHECleaned` path as a function of `PFMET_pt` for simulated magnetic monopole samples with masses of 1500 GeV (top left), 2500 GeV (top right), 3500 GeV (bottom left), and 4500 GeV (bottom right). The plots combine results from the 2017 and 2018 MC campaigns and focus on the endcap regions of the CMS detector. Efficiency curves are shown for four production modes: Drell–Yan Spin-0 (blue), Drell–Yan Spin-Half (red), Photon Fusion Spin-0 (green), and Photon Fusion Spin-Half (yellow).

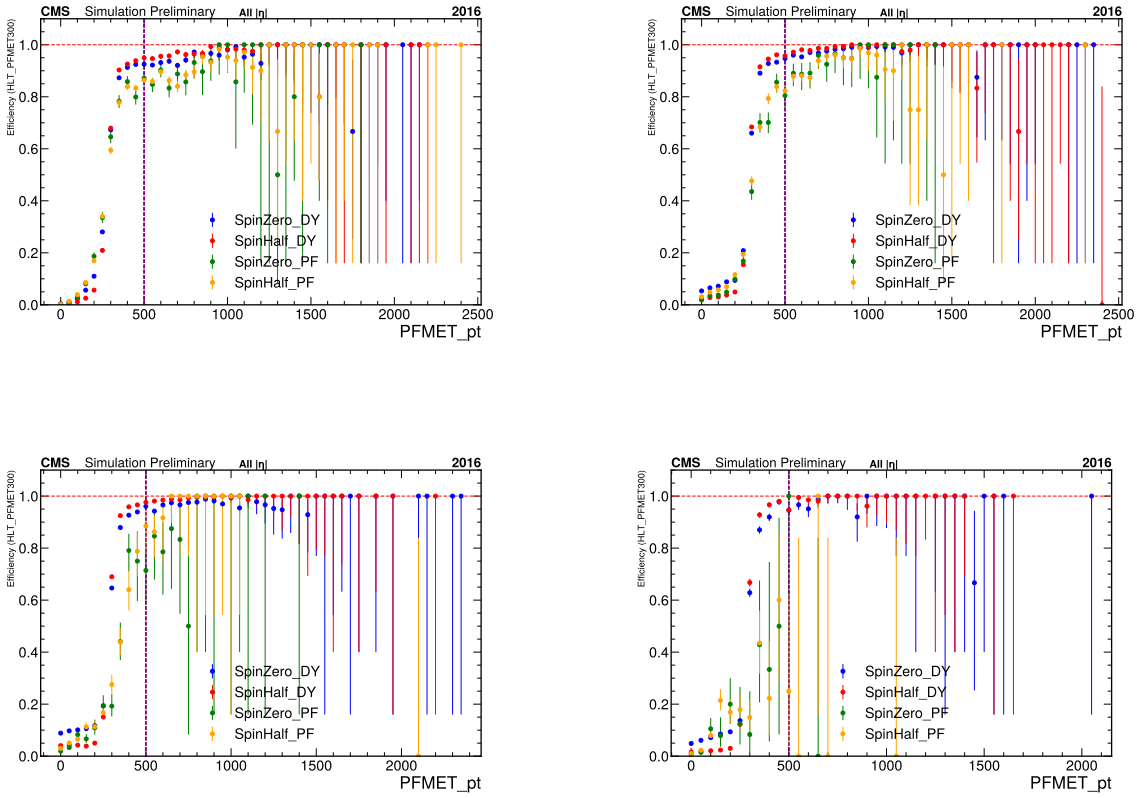

Figure 99 – Trigger efficiency of the `HLT_PFMET250_HBHECleaned` path as a function of `PFMET_pt` for simulated magnetic monopole samples with masses of 1500 GeV (top left), 2500 GeV (top right), 3500 GeV (bottom left), and 4500 GeV (bottom right). The plots combine results from the 2017 and 2018 MC campaigns and focus on the combination of barrel and endcap regions of the CMS detector. Efficiency curves are shown for four production modes: Drell–Yan Spin-0 (blue), Drell–Yan Spin-Half (red), Photon Fusion Spin-0 (green), and Photon Fusion Spin-Half (yellow).

References

[1] Sheldon L. Glashow. “Partial-symmetries of weak interactions”. Em: *Nuclear Physics* 22.4 (1961), pp. 579–588. ISSN: 0029-5582. DOI: <https://doi.org/10.1016/0029-5582(61)90469-2>. URL: <https://www.sciencedirect.com/science/article/pii/0029558261904692>.

[2] Murray Gell-Mann. “The Eightfold Way: A Theory of strong interaction symmetry”. Em: (mar. de 1961). DOI: <10.2172/4008239>.

[3] P.W. Higgs. “Broken symmetries, massless particles and gauge fields”. Em: *Physics Letters* 12.2 (1964), pp. 132–133. ISSN: 0031-9163. DOI: <https://doi.org/10.1016/0031-9163(64)91136-9>. URL: <https://www.sciencedirect.com/science/article/pii/0031916364911369>.

[4] F. Englert e R. Brout. “Broken Symmetry and the Mass of Gauge Vector Mesons”. Em: *Phys. Rev. Lett.* 13 (9 ago. de 1964), pp. 321–323. DOI: <10.1103/PhysRevLett.13.321>. URL: <https://link.aps.org/doi/10.1103/PhysRevLett.13.321>.

[5] Peter W. Higgs. “Broken Symmetries and the Masses of Gauge Bosons”. Em: *Phys. Rev. Lett.* 13 (16 out. de 1964), pp. 508–509. DOI: <10.1103/PhysRevLett.13.508>. URL: <https://link.aps.org/doi/10.1103/PhysRevLett.13.508>.

[6] G. S. Guralnik, C. R. Hagen e T. W. B. Kibble. “Global Conservation Laws and Massless Particles”. Em: *Phys. Rev. Lett.* 13 (20 nov. de 1964), pp. 585–587. DOI: <10.1103/PhysRevLett.13.585>. URL: <https://link.aps.org/doi/10.1103/PhysRevLett.13.585>.

[7] Steven Weinberg. “A Model of Leptons”. Em: *Phys. Rev. Lett.* 19 (21 nov. de 1967), pp. 1264–1266. DOI: <10.1103/PhysRevLett.19.1264>. URL: <https://link.aps.org/doi/10.1103/PhysRevLett.19.1264>.

[8] Abdus Salam. “Weak and Electromagnetic Interactions”. Em: *Conf. Proc. C* 680519 (1968), pp. 367–377. DOI: <10.1142/9789812795915_0034>.

[9] S. Navas et al. “Review of particle physics”. Em: *Phys. Rev. D* 110.3 (2024), p. 030001. DOI: <10.1103/PhysRevD.110.030001>.

[10] E. Noether. “Invariante Variationsprobleme”. ger. Em: *Nachrichten von der Gesellschaft der Wissenschaften zu Göttingen, Mathematisch-Physikalische Klasse* 1918 (1918), pp. 235–257. URL: <http://eudml.org/doc/59024>.

[11] Tancredi Carli, Klaus Rabbertz e Steffen Schumann. "Studies of Quantum Chromodynamics at the LHC". Em: *The Large Hadron Collider. Harvest of Run 1*. Ed. por Thomas Schörner-Sadenius. 2015, pp. 139–194. DOI: <10.1007/978-3-319-15001-7_5>. arXiv: <1506.03239> [hep-ex].

[12] C. S. Wu et al. "Experimental Test of Parity Conservation in Beta Decay". Em: *Phys. Rev.* 105 (4 fev. de 1957), pp. 1413–1415. DOI: <10.1103/PhysRev.105.1413>. URL: <https://link.aps.org/doi/10.1103/PhysRev.105.1413>.

[13] Sheldon L. Glashow. "The renormalizability of vector meson interactions". Em: *Nuclear Physics* 10 (1959), pp. 107–117. ISSN: 0029-5582. DOI: <https://doi.org/10.1016/0029-5582(59)90196-8>. URL: <https://www.sciencedirect.com/science/article/pii/0029558259901968>.

[14] T. Nakano e K. Nishijima. "Charge Independence for V-particles". Em: *Prog. Theor. Phys.* 10 (1953), pp. 581–582. DOI: <10.1143/PTP.10.581>.

[15] M. Gell-Mann. "The interpretation of the new particles as displaced charge multiplets". Em: *Nuovo Cim.* 4.S2 (1956), pp. 848–866. DOI: <10.1007/BF02748000>.

[16] Roel Aaij et al. "Test of lepton universality in beauty-quark decays". Em: *Nature Phys.* 18.3 (2022). [Addendum: Nature Phys. 19, (2023)], pp. 277–282. DOI: <10.1038/s41567-023-02095-3>. arXiv: <2103.11769> [hep-ex].

[17] Y. Fukuda et al. "Evidence for Oscillation of Atmospheric Neutrinos". Em: *Phys. Rev. Lett.* 81 (8 ago. de 1998), pp. 1562–1567. DOI: <10.1103/PhysRevLett.81.1562>. URL: <https://link.aps.org/doi/10.1103/PhysRevLett.81.1562>.

[18] Q. R. Ahmad et al. "Measurement of the Rate of $\nu_e + d \rightarrow p + p + e^-$ Interactions Produced by ^8B Solar Neutrinos at the Sudbury Neutrino Observatory". Em: *Phys. Rev. Lett.* 87 (7 jul. de 2001), p. 071301. DOI: <10.1103/PhysRevLett.87.071301>. URL: <https://link.aps.org/doi/10.1103/PhysRevLett.87.071301>.

[19] S. Schael et al. "Precision electroweak measurements on the Z resonance". Em: *Phys. Rept.* 427 (2006), pp. 257–454. DOI: <10.1016/j.physrep.2005.12.006>. arXiv: <hep-ex/0509008>.

[20] Nicola Cabibbo. "Unitary Symmetry and Leptonic Decays". Em: *Phys. Rev. Lett.* 10 (12 jun. de 1963), pp. 531–533. DOI: <10.1103/PhysRevLett.10.531>. URL: <https://link.aps.org/doi/10.1103/PhysRevLett.10.531>.

[21] S. L. Glashow, J. Iliopoulos e L. Maiani. "Weak Interactions with Lepton-Hadron Symmetry". Em: *Phys. Rev. D* 2 (7 out. de 1970), pp. 1285–1292. DOI: <10.1103/PhysRevD.2.1285>. URL: <https://link.aps.org/doi/10.1103/PhysRevD.2.1285>.

[22] Makoto Kobayashi e Toshihide Maskawa. “CP-Violation in the Renormalizable Theory of Weak Interaction”. Em: *Progress of Theoretical Physics* 49.2 (fev. de 1973), pp. 652–657. ISSN: 0033-068X. DOI: <10.1143/PTP.49.652>. eprint: <https://academic.oup.com/ptp/article-pdf/49/2/652/5257692/49-2-652.pdf>. URL: <https://doi.org/10.1143/PTP.49.652>.

[23] Lincoln Wolfenstein. “Parametrization of the Kobayashi-Maskawa Matrix”. Em: *Phys. Rev. Lett.* 51 (21 nov. de 1983), pp. 1945–1947. DOI: <10.1103/PhysRevLett.51.1945>. URL: <https://link.aps.org/doi/10.1103/PhysRevLett.51.1945>.

[24] Steven Weinberg. “A Model of Leptons”. Em: *Phys. Rev. Lett.* 19 (1967), pp. 1264–1266. DOI: <10.1103/PhysRevLett.19.1264>.

[25] N. Aghanim et al. “Planck 2018 results. VI. Cosmological parameters”. Em: *Astron. Astrophys.* 641 (2020). [Erratum: Astron.Astrophys. 652, C4 (2021)], A6. DOI: <10.1051/0004-6361/201833910>. arXiv: <1807.06209> [astro-ph.CO].

[26] R. N. Mohapatra e A. Y. Smirnov. “Neutrino Mass and New Physics”. Em: *Ann. Rev. Nucl. Part. Sci.* 56 (2006). Ed. por K. Anagnostopoulos et al., pp. 569–628. DOI: <10.1146/annurev.nucl.56.080805.140534>. arXiv: <hep-ph/0603118>.

[27] F. Zwicky. “Die Rotverschiebung von extragalaktischen Nebeln”. Em: *Helv. Phys. Acta* 6 (1933), pp. 110–127. DOI: <10.1007/s10714-008-0707-4>.

[28] Arindam Mazumdar, Subhendra Mohanty e Priyank Parashari. “Evidence of dark energy in different cosmological observations”. Em: *Eur. Phys. J. ST* 230.9 (2021), pp. 2055–2066. DOI: <10.1140/epjs/s11734-021-00212-y>. arXiv: <2107.02838> [astro-ph.CO].

[29] Werner Bernreuther. “CP violation and baryogenesis”. Em: *Lect. Notes Phys.* 591 (2002), pp. 237–293. arXiv: <hep-ph/0205279>.

[30] A. D. Sakharov. “Violation of CP Invariance, C asymmetry, and baryon asymmetry of the universe”. Em: *Pisma Zh. Eksp. Teor. Fiz.* 5 (1967), pp. 32–35. DOI: <10.1070/PU1991v034n05ABEH002497>.

[31] Hermann Nicolai. “Quantum Gravity: the view from particle physics”. Em: *Fundam. Theor. Phys.* 177 (2014). Ed. por Jiri Bicak e Tomas Ledvinka, pp. 369–387. DOI: <10.1007/978-3-319-06349-2_18>. arXiv: <1301.5481> [gr-qc].

[32] Ian Aitchison. *Supersymmetry in Particle Physics: An Elementary Introduction*. Cambridge University Press, 2007.

[33] Steven Weinberg. “Effective gauge theories”. Em: *Physics Letters B* 91.1 (1980), pp. 51–55. ISSN: 0370-2693. DOI: <https://doi.org/10.1016/0370-2693(80)90660-7>. URL: <https://www.sciencedirect.com/science/article/pii/0370269380906607>.

[34] W. Buchmüller e D. Wyler. "Effective lagrangian analysis of new interactions and flavour conservation". Em: *Nuclear Physics B* 268.3 (1986), pp. 621–653. ISSN: 0550-3213. DOI: <https://doi.org/10.1016/0550-3213(86)90262-2>. URL: <https://www.sciencedirect.com/science/article/pii/0550321386902622>.

[35] B. Grzadkowski et al. "Dimension-Six Terms in the Standard Model Lagrangian". Em: *JHEP* 10 (2010), p. 085. DOI: <10.1007/JHEP10(2010)085>. arXiv: <1008.4884> [hep-ph].

[36] Paul Adrien Maurice Dirac. "Quantised singularities in the electromagnetic field". Em: *Proc. Roy. Soc. Lond. A* 133.821 (1931), pp. 60–72. DOI: <10.1098/rspa.1931.0130>.

[37] P. A. M. Dirac. "The Theory of Magnetic Poles". Em: *Phys. Rev.* 74 (7 out. de 1948), pp. 817–830. DOI: <10.1103/PhysRev.74.817>. URL: <https://link.aps.org/doi/10.1103/PhysRev.74.817>.

[38] Julian Schwinger. "Magnetic Charge and Quantum Field Theory". Em: *Phys. Rev.* 144 (4 abr. de 1966), pp. 1087–1093. DOI: <10.1103/PhysRev.144.1087>. URL: <https://link.aps.org/doi/10.1103/PhysRev.144.1087>.

[39] Tanmay Vachaspati e Manuel Barriola. "A new class of defects". Em: *Phys. Rev. Lett.* 69 (13 set. de 1992), pp. 1867–1870. DOI: <10.1103/PhysRevLett.69.1867>. URL: <https://link.aps.org/doi/10.1103/PhysRevLett.69.1867>.

[40] Manuel Barriola, Tanmay Vachaspati e Martin Bucher. "Embedded defects". Em: *Phys. Rev. D* 50 (1994), pp. 2819–2825. DOI: <10.1103/PhysRevD.50.2819>. arXiv: <hep-th/9306120>.

[41] Gerardus 't Hooft. "Magnetic Monopoles in Unified Theories. Magnetic monopoles in unified gauge theories". Em: *Nucl. Phys. B* 79 (1974), pp. 276–284. URL: <https://cds.cern.ch/record/416338>.

[42] Alexander M. Polyakov. "Particle Spectrum in Quantum Field Theory". Em: *30 Years Of The Landau Institute—Selected Papers*. World Scientific, 1996, pp. 540–541.

[43] H. Georgi e S. L. Glashow. "Unity of All Elementary Particle Forces". Em: *Phys. Rev. Lett.* 32 (1974), pp. 438–441. DOI: <10.1103/PhysRevLett.32.438>.

[44] Y.M. Cho e D. Maison. "Monopole configuration in Weinberg-Salam model". Em: *Physics Letters B* 391.3 (1997), pp. 360–365. ISSN: 0370-2693. DOI: <https://doi.org/10.1016/S0370-2693(96)01492-X>. URL: <https://www.sciencedirect.com/science/article/pii/S037026939601492X>.

[45] John Ellis, Nick E. Mavromatos e Tevong You. "The price of an electroweak monopole". Em: *Physics Letters B* 756 (2016), pp. 29–35. ISSN: 0370-2693. DOI: <https://doi.org/10.1016/j.physletb.2016.02.048>. URL: <https://www.sciencedirect.com/science/article/pii/S0370269316001441>.

[46] Kimball A. Milton. "Theoretical and experimental status of magnetic monopoles". Em: *Rept. Prog. Phys.* 69 (2006), pp. 1637–1712. DOI: <10.1088/0034-4885/69/6/R02>. arXiv: <hep-ex/0602040>.

[47] Henry H. Kolm, F. Villa e A. Odian. "SEARCH FOR MAGNETIC MONOPOLES". Em: *Phys. Rev. D* 4 (1971), p. 1285. DOI: <10.1103/PhysRevD.4.1285>.

[48] P. B. Price et al. "Evidence for Detection of a Moving Magnetic Monopole". Em: *Phys. Rev. Lett.* 35 (1975), pp. 487–490. DOI: <10.1103/PhysRevLett.35.487>.

[49] TASSO Collaboration. "A search for particles with magnetic charge produced in e^+e^- annihilations at 543–1543 GeV". Em: *Zeitschrift für Physik C Particles and Fields* 38.4 (dez. de 1988), pp. 543–550. ISSN: 1431-5858. DOI: <10.1007/BF01624358>. URL: <https://doi.org/10.1007/BF01624358>.

[50] Sergey Burdin et al. "Non-collider searches for stable massive particles". Em: *Phys. Rept.* 582 (2015), pp. 1–52. DOI: <10.1016/j.physrep.2015.03.004>. arXiv: <1410.1374> [hep-ph].

[51] Thomas W. Kephart, George K. Leontaris e Qaisar Shafi. "Magnetic monopoles and free fractionally charged states at accelerators and in cosmic rays". Em: *Journal of High Energy Physics* 2017.10 (2017), p. 176. ISSN: 1029-8479. DOI: <10.1007/JHEP10(2017)176>. URL: <https://doi.org/10.1007/JHEP10(2017)176>.

[52] M. Ambrosio et al. "Final results of magnetic monopole searches with the MACRO experiment". Em: *Eur. Phys. J. C* 25 (2002), pp. 511–522. DOI: <10.1140/epjc/s2002-01046-9>. arXiv: <hep-ex/0207020>.

[53] E. Medinaceli. "Magnetic monopole search at high altitude with the SLIM experiment". Em: *Radiation Measurements* 44.9 (2009). Proceedings of the 24th International Conference on Nuclear Tracks in Solids, pp. 889–893. ISSN: 1350-4487. DOI: <https://doi.org/10.1016/j.radmeas.2009.10.091>. URL: <https://www.sciencedirect.com/science/article/pii/S1350448709002674>.

[54] M. Detrixhe et al. "Ultrarelativistic magnetic monopole search with the ANITA-II balloon-borne radio interferometer". Em: *Physical Review D* 83.2 (jan. de 2011). ISSN: 1550-2368. DOI: <10.1103/physrevd.83.023513>. URL: <http://dx.doi.org/10.1103/PhysRevD.83.023513>.

[55] A. Albert et al. "Search for magnetic monopoles with ten years of the ANTARES neutrino telescope". Em: *JHEAp* 34 (2022), pp. 1–8. DOI: <10.1016/j.jheap.2022.03.001>. arXiv: <2202.13786> [astro-ph.HE].

[56] Frederik Lauber. "Search for low relativistic magnetic monopoles at the IceCube Neutrino Observatory". Inglês. Dissertation, Bergische Universität Wuppertal, 2021. Tese de dout. Wuppertal: Bergische Universität Wuppertal, jul. de 2021. DOI: <10.25926/gph1-vf51>. URL: <https://nbn-resolving.org/urn:nbn:de:hbz:468-20211202-100837-4>.

[57] K. Ueno et al. "Search for GUT monopoles at Super–Kamiokande". Em: *Astropart. Phys.* 36 (2012), pp. 131–136. DOI: <10.1016/j.astropartphys.2012.05.008>. arXiv: <1203.0940> [hep-ex].

[58] H. Hoffmann et al. "A new search for magnetic monopoles at the CERN-ISR with plastic detectors". Em: *Lettere al Nuovo Cimento (1971-1985)* 23.10 (nov. de 1978), pp. 357–360. ISSN: 1827-613X. DOI: <10.1007/BF02776247>. URL: <https://doi.org/10.1007/BF02776247>.

[59] B. Aubert et al. "Search for magnetic monopoles in proton-antiproton interactions at 540 GeV cm energy". Em: *Physics Letters B* 120.4 (1983), pp. 465–467. ISSN: 0370-2693. DOI: <https://doi.org/10.1016/0370-2693(83)90488-4>. URL: <https://www.sciencedirect.com/science/article/pii/0370269383904884>.

[60] J.L. Pinfold et al. "A search for highly ionizing particles produced at the OPAL intersection point at LEP". Em: *Physics Letters B* 316.2 (1993), pp. 407–411. ISSN: 0370-2693. DOI: <https://doi.org/10.1016/0370-2693(93)90346-J>. URL: <https://www.sciencedirect.com/science/article/pii/037026939390346J>.

[61] D. Fryberger et al. "Search for highly ionizing particles in e^+e^- collisions at $\sqrt{s} = 29$ GeV". Em: *Phys. Rev. D* 29 (7 abr. de 1984), pp. 1524–1526. DOI: <10.1103/PhysRevD.29.1524>. URL: <https://link.aps.org/doi/10.1103/PhysRevD.29.1524>.

[62] P. Musset, M. Price e E. Lohrmann. "Search for magnetic monopoles in electron-positron collisions at 34 GeV CM energy". Em: *Physics Letters B* 128.5 (1983), pp. 333–335. ISSN: 0370-2693. DOI: <https://doi.org/10.1016/0370-2693(83)90270-8>. URL: <https://www.sciencedirect.com/science/article/pii/0370269383902708>.

[63] K. Kinoshita et al. "Search for highly ionizing particles in e^+e^- annihilations at $\sqrt{s}$ =50–52 GeV". Em: *Phys. Rev. Lett.* 60 (16 abr. de 1988), pp. 1610–1613. DOI: <10.1103/PhysRevLett.60.1610>. URL: <https://link.aps.org/doi/10.1103/PhysRevLett.60.1610>.

[64] M. Bertani et al. "Search for Magnetic Monopoles at the Tevatron Collider". Em: *Europhysics Letters* 12.7 (ago. de 1990), p. 613. DOI: <10.1209/0295-5075/12/7/007>. URL: <https://dx.doi.org/10.1209/0295-5075/12/7/007>.

[65] G. Abbiendi et al. “Search for Dirac magnetic monopoles in e+e- collisions with the OPAL detector at LEP2”. Em: *Phys. Lett. B* 663 (2008), pp. 37–42. DOI: <10.1016/j.physletb.2008.03.057>. arXiv: <0707.0404> [hep-ex].

[66] A. Aktas et al. “A Direct search for stable magnetic monopoles produced in positron-proton collisions at HERA”. Em: *Eur. Phys. J. C* 41 (2005), pp. 133–141. DOI: <10.1140/epjc/s2005-02201-6>. arXiv: <hep-ex/0501039>.

[67] B. Acharya et al. “Magnetic Monopole Search with the Full MoEDAL Trapping Detector in 13 TeV pp Collisions Interpreted in Photon-Fusion and Drell-Yan Production”. Em: *Phys. Rev. Lett.* 123.2 (2019), p. 021802. DOI: <10.1103/PhysRevLett.123.021802>. arXiv: <1903.08491> [hep-ex].

[68] Georges Aad et al. “Search for Magnetic Monopoles and Stable High-Electric-Charge Objects in 13 Tev Proton-Proton Collisions with the ATLAS Detector”. Em: *Phys. Rev. Lett.* 124.3 (2020), p. 031802. DOI: <10.1103/PhysRevLett.124.031802>. arXiv: <1905.10130> [hep-ex].

[69] B. Acharya et al. “Search for magnetic monopoles with the MoEDAL prototype trapping detector in 8 TeV proton-proton collisions at the LHC”. Em: *JHEP* 08 (2016), p. 067. DOI: <10.1007/JHEP08(2016)067>. arXiv: <1604.06645> [hep-ex].

[70] B. Acharya et al. “Search for Magnetic Monopoles with the MoEDAL Forward Trapping Detector in 13 TeV Proton-Proton Collisions at the LHC”. Em: *Phys. Rev. Lett.* 118.6 (2017), p. 061801. DOI: <10.1103/PhysRevLett.118.061801>. arXiv: <1611.06817> [hep-ex].

[71] B. Acharya et al. “Search for magnetic monopoles with the MoEDAL forward trapping detector in 2.11 fb^{-1} of 13 TeV proton-proton collisions at the LHC”. Em: *Phys. Lett. B* 782 (2018), pp. 510–516. DOI: <10.1016/j.physletb.2018.05.069>. arXiv: <1712.09849> [hep-ex].

[72] Georges Aad et al. “Search for magnetic monopoles in $\sqrt{s} = 7$ TeV pp collisions with the ATLAS detector”. Em: *Phys. Rev. Lett.* 109 (2012), p. 261803. DOI: <10.1103/PhysRevLett.109.261803>. arXiv: <1207.6411> [hep-ex].

[73] Georges Aad et al. “Search for magnetic monopoles and stable particles with high electric charges in 8 TeV pp collisions with the ATLAS detector”. Em: *Phys. Rev. D* 93.5 (2016), p. 052009. DOI: <10.1103/PhysRevD.93.052009>. arXiv: <1509.08059> [hep-ex].

[74] Chris Quigg. “LHC Physics Potential vs. Energy: Considerations for the 2011 Run”. Em: (fev. de 2011). arXiv: <1101.3201> [hep-ph].

[75] H. Bethe. "Zur Theorie des Durchgangs schneller Korpuskularstrahlen durch Materie". Em: *Annalen der Physik* 397.3 (1930), pp. 325–400. DOI: <https://doi.org/10.1002/andp.19303970303>. eprint: <https://onlinelibrary.wiley.com/doi/pdf/10.1002/andp.19303970303>. URL: <https://onlinelibrary.wiley.com/doi/abs/10.1002/andp.19303970303>.

[76] S. P. Ahlen. "Stopping-power formula for magnetic monopoles". Em: *Phys. Rev. D* 17 (1 jan. de 1978), pp. 229–233. DOI: <10.1103/PhysRevD.17.229>. URL: <https://link.aps.org/doi/10.1103/PhysRevD.17.229>.

[77] Yoichi Kazama, Chen Ning Yang e Alfred S. Goldhaber. "Scattering of a Dirac particle with charge Ze by a fixed magnetic monopole". Em: *Phys. Rev. D* 15 (8 abr. de 1977), pp. 2287–2299. DOI: <10.1103/PhysRevD.15.2287>. URL: <https://link.aps.org/doi/10.1103/PhysRevD.15.2287>.

[78] Elena Papageorgiu e Leo Stodolsky. "Identification of magnetic monopoles via electron-positron pair production". Em: *Physics Letters B* 197.1 (1987), pp. 277–280. ISSN: 0370-2693. DOI: <https://doi.org/10.1016/0370-2693(87)90383-2>. URL: <https://www.sciencedirect.com/science/article/pii/0370269387903832>.

[79] Gabriel David Palacino Caviedes. "Search for magnetic monopoles in 8 TeV centre-of-mass energy proton-proton collisions with the ATLAS detector at the LHC". Presented 09 Dec 2015. York U., Canada, 2015. URL: <https://cds.cern.ch/record/2119479>.

[80] Oliver Sim Brüning et al. *LHC Design Report*. CERN Yellow Reports: Monographs. Geneva: CERN, 2004. DOI: <10.5170/CERN-2004-003-V-1>. URL: <https://cds.cern.ch/record/782076>.

[81] Esma Mobs. "The CERN accelerator complex in 2019. Complexe des accélérateurs du CERN en 2019". Em: (2019). General Photo. URL: <https://cds.cern.ch/record/2684277>.

[82] Sara Ghasemi. "Cross-Section Measurement of $t\bar{t}\gamma$ Production in pp Collisions at $\sqrt{s} = 8$ and 13 TeV with the ATLAS Experiment". Presented 29 Nov 2019. Siegen U., 2019. URL: <https://cds.cern.ch/record/2719259>.

[83] K. Aamodt et al. "The ALICE experiment at the CERN LHC". Em: *JINST* 3 (2008), S08002. DOI: <10.1088/1748-0221/3/08/S08002>.

[84] Jaroslav Adam et al. "Enhanced production of multi-strange hadrons in high-multiplicity proton-proton collisions". Em: *Nature Phys.* 13 (2017), pp. 535–539. DOI: <10.1038/nphys4111>. arXiv: <1606.07424> [nucl-ex].

[85] A. Augusto Alves Jr. et al. "The LHCb Detector at the LHC". Em: *JINST* 3 (2008), S08005. DOI: <10.1088/1748-0221/3/08/S08005>.

[86] G. Aad et al. “The ATLAS Experiment at the CERN Large Hadron Collider”. Em: *JINST* 3 (2008), S08003. DOI: <10.1088/1748-0221/3/08/S08003>.

[87] S. Chatrchyan et al. “The CMS Experiment at the CERN LHC”. Em: *JINST* 3 (2008), S08004. DOI: <10.1088/1748-0221/3/08/S08004>.

[88] Georges Aad et al. “Observation of a new particle in the search for the Standard Model Higgs boson with the ATLAS detector at the LHC”. Em: *Phys. Lett. B* 716 (2012), pp. 1–29. DOI: <10.1016/j.physletb.2012.08.020>. arXiv: <1207.7214> [hep-ex].

[89] Serguei Chatrchyan et al. “Observation of a New Boson at a Mass of 125 GeV with the CMS Experiment at the LHC”. Em: *Phys. Lett. B* 716 (2012), pp. 30–61. DOI: <10.1016/j.physletb.2012.08.021>. arXiv: <1207.7235> [hep-ex].

[90] CMS Collaboration. *CMS luminosity - public results*. <https://twiki.cern.ch/twiki/bin/view/CMSPublic/LumiPublicResults>. Accessed: 05 Oct. 2023. 2023.

[91] Apollinari G. et al. *High-Luminosity Large Hadron Collider (HL-LHC): Technical Design Report V. 0.1*. CERN Yellow Reports: Monographs. Geneva: CERN, 2017. DOI: <10.23731/CYRM-2017-004>. URL: <https://cds.cern.ch/record/2284929>.

[92] Tai Sakuma e Thomas McCauley. “Detector and Event Visualization with SketchUp at the CMS Experiment”. Em: *J. Phys. Conf. Ser.* 513 (2014). Ed. por D. L. Groep e D. Bonacorsi, p. 022032. DOI: <10.1088/1742-6596/513/2/022032>. arXiv: <1311.4942> [physics.ins-det].

[93] A. M. Sirunyan et al. “Performance of the CMS muon detector and muon reconstruction with proton-proton collisions at $\sqrt{s} = 13$ TeV”. Em: *JINST* 13.06 (2018), P06015. DOI: <10.1088/1748-0221/13/06/P06015>. arXiv: <1804.04528> [physics.ins-det].

[94] *The CMS magnet project: Technical Design Report*. Technical design report. CMS. Geneva: CERN, 1997. DOI: <10.17181/CERN.6ZU0.V4T9>. URL: <https://cds.cern.ch/record/331056>.

[95] V Karimäki et al. *The CMS tracker system project: Technical Design Report*. Technical design report. CMS. Geneva: CERN, 1997. URL: <https://cds.cern.ch/record/368412>.

[96] Serguei Chatrchyan et al. “Description and performance of track and primary-vertex reconstruction with the CMS tracker”. Em: *JINST* 9.10 (2014), P10009. DOI: <10.1088/1748-0221/9/10/P10009>. arXiv: <1405.6569> [physics.ins-det].

[97] *The Phase-2 Upgrade of the CMS Tracker*. Rel. técn. Geneva: CERN, 2017. DOI: <10.17181/CERN.QZ28.FLHW>. URL: <https://cds.cern.ch/record/2272264>.

[98] *The CMS electromagnetic calorimeter project: Technical Design Report*. Technical design report. CMS. Geneva: CERN, 1997. URL: <https://cds.cern.ch/record/349375>.

[99] Vardan Khachatryan et al. "The CMS trigger system". Em: *JINST* 12.01 (2017), P01020. DOI: <10.1088/1748-0221/12/01/P01020>. arXiv: <1609.02366> [physics.ins-det].

[100] Albert M Sirunyan et al. "Performance of the CMS Level-1 trigger in proton-proton collisions at $\sqrt{s} = 13$ TeV". Em: *JINST* 15.10 (2020), P10017. DOI: <10.1088/1748-0221/15/10/P10017>. arXiv: <2006.10165> [hep-ex].

[101] Santeri Henrikki Laurila. *Search for Charged Higgs Bosons Decaying to a Tau Lepton and a Neutrino with the CMS Experiment*. Mai. de 2019.

[102] W. Bialas e D. A. Petyt. "Mitigation of anomalous APD signals in the CMS ECAL". Em: *JINST* 8 (2013), p. C03020. DOI: <10.1088/1748-0221/8/03/C03020>.

[103] David A. Petyt. "Anomalous APD signals in the CMS Electromagnetic Calorimeter". Em: *Nucl. Instrum. Meth. A* 695 (2012). Ed. por Philippe Bourgeois et al., pp. 293–295. DOI: <10.1016/j.nima.2011.10.025>.

[104] "LHC computing Grid. Technical design report". Em: (jun. de 2005). Ed. por I. Bird et al.

[105] Torbjörn Sjöstrand et al. "An introduction to PYTHIA 8.2". Em: *Comput. Phys. Commun.* 191 (2015), pp. 159–177. DOI: <10.1016/j.cpc.2015.01.024>. arXiv: <1410.3012> [hep-ph].

[106] M. Bahr et al. "Herwig++ Physics and Manual". Em: *Eur. Phys. J. C* 58 (2008), pp. 639–707. DOI: <10.1140/epjc/s10052-008-0798-9>. arXiv: <0803.0883> [hep-ph].

[107] J. Alwall et al. "The automated computation of tree-level and next-to-leading order differential cross sections, and their matching to parton shower simulations". Em: *JHEP* 07 (2014), p. 079. DOI: <10.1007/JHEP07(2014)079>. arXiv: <1405.0301> [hep-ph].

[108] Stefano Frixione, Paolo Nason e Carlo Oleari. "Matching NLO QCD computations with Parton Shower simulations: the POWHEG method". Em: *JHEP* 11 (2007), p. 070. DOI: <10.1088/1126-6708/2007/11/070>. arXiv: <0709.2092> [hep-ph].

[109] Johan Alwall et al. "A Standard format for Les Houches event files". Em: *Comput. Phys. Commun.* 176 (2007), pp. 300–304. DOI: <10.1016/j.cpc.2006.11.010>. arXiv: <hep-ph/0609017>.

[110] Rikkert Frederix e Stefano Frixione. "Merging meets matching in MC@NLO". Em: *JHEP* 12 (2012), p. 061. DOI: <10.1007/JHEP12(2012)061>. arXiv: <1209.6215> [hep-ph].

[111] S. Agostinelli et al. "Geant4—a simulation toolkit". Em: *Nuclear Instruments and Methods in Physics Research Section A: Accelerators, Spectrometers, Detectors and Associated Equipment* 506.3 (2003), pp. 250–303. ISSN: 0168-9002. DOI: <https://doi.org/10.1016/S0168-9002(03)01368-8>. URL: <https://www.sciencedirect.com/science/article/pii/S0168900203013688>.

[112] A. M. Sirunyan et al. "Particle-flow reconstruction and global event description with the CMS detector". Em: *JINST* 12.10 (2017), P10003. DOI: <10.1088/1748-0221/12/10/P10003>. arXiv: <1706.04965> [physics.ins-det].

[113] Giovanni Petrucciani, Andrea Rizzi e Carl Vuosalo. "Mini-AOD: A New Analysis Data Format for CMS". Em: *J. Phys. Conf. Ser.* 664.7 (2015), p. 7. DOI: <10.1088/1742-6596/664/7/072052>. arXiv: <1702.04685> [physics.ins-det].

[114] *Commissioning of the Particle-flow Event Reconstruction with the first LHC collisions recorded in the CMS detector*. Rel. técn. 2010. URL: <http://cds.cern.ch/record/1247373>.

[115] Wolfgang Adam et al. *Track Reconstruction in the CMS tracker*. Rel. técn. Geneva: CERN, 2006. URL: <https://cds.cern.ch/record/934067>.

[116] K. Rose. "Deterministic annealing for clustering, compression, classification, regression, and related optimization problems". Em: *IEEE Proc.* 86.11 (1998), pp. 2210–2239. DOI: <10.1109/5.726788>.

[117] W Adam et al. "Reconstruction of electrons with the Gaussian-sum filter in the CMS tracker at the LHC". Em: *Journal of Physics G: Nuclear and Particle Physics* 31.9 (jul. de 2005), N9–N20. ISSN: 1361-6471. DOI: <10.1088/0954-3899/31/9/n01>. URL: <http://dx.doi.org/10.1088/0954-3899/31/9/N01>.

[118] Matteo Cacciari, Gavin P. Salam e Gregory Soyez. "The anti-k_t jet clustering algorithm". Em: *JHEP* 04 (2008), p. 063. DOI: <10.1088/1126-6708/2008/04/063>. arXiv: <0802.1189> [hep-ph].

[119] *Jet algorithms performance in 13 TeV data*. Rel. técn. Geneva: CERN, 2017. URL: <https://cds.cern.ch/record/2256875>.

[120] Michelangelo Mangano. "Motivations and precision targets for an accurate luminosity determination at the LHC. Motivations and precision targets for luminosity". Em: (2011). URL: <https://cds.cern.ch/record/1357612>.

[121] H Burkhardt e P Grafström. *Absolute Luminosity from Machine Parameters*. Rel. técn. 2007. URL: <https://cds.cern.ch/record/1056691>.

[122] S van der Meer. *Calibration of the effective beam height in the ISR*. Rel. técn. Geneva: CERN, 1968. URL: <https://cds.cern.ch/record/296752>.

[123] Carlo Rubbia. *Measurement of the luminosity of p−overlinep collider with a (generalized) Van der Meer Method*. Rel. técn. Geneva: CERN, 1977. URL: <https://cds.cern.ch/record/1025746>.

[124] Joscha Knolle. "Measuring luminosity and the $t\bar{t}Z$ production cross section with the CMS experiment". Presented 25 Jun 2020. Hamburg U., 2020. URL: <https://cds.cern.ch/record/2744549>.

[125] P. Grafström e W. Kozanecki. "Luminosity determination at proton colliders". Em: *Progress in Particle and Nuclear Physics* 81 (2015), pp. 97–148. ISSN: 0146-6410. DOI: <https://doi.org/10.1016/j.ppnp.2014.11.002>. URL: <https://www.sciencedirect.com/science/article/pii/S0146641014000878>.

[126] "Measurement of the offline integrated luminosity for the CMS proton-proton collision dataset recorded in 2023". Em: (2024). URL: <https://cds.cern.ch/record/2904808>.

[127] *CMS Luminosity Based on Pixel Cluster Counting - Summer 2012 Update*. Rel. técn. Geneva: CERN, 2012. URL: <https://cds.cern.ch/record/1482193>.

[128] *CMS luminosity measurement for the 2018 data-taking period at* $\sqrt{s} = 13$ TeV. Rel. técn. Geneva: CERN, 2019. URL: <https://cds.cern.ch/record/2676164>.

[129] Paul Lujan. "Performance of the Pixel Luminosity Telescope for Luminosity Measurement at CMS during Run2". Em: *PoS* EPS-HEP2017 (2017). Ed. por Paolo Checchia et al., p. 504. DOI: <10.22323/1.314.0504>.

[130] Maria Hempel. "Development of a Novel Diamond Based Detector for Machine Induced Background and Luminosity Measurements". DESY, 2017. URL: <https://cds.cern.ch/record/2282941>.

[131] A. M. Sirunyan et al. "Performance of the CMS muon detector and muon reconstruction with proton-proton collisions at $\sqrt{s} = 13$ TeV". Em: *JINST* 13.06 (2018), P06015. DOI: <10.1088/1748-0221/13/06/P06015>. arXiv: <1804.04528> [physics.ins-det].

[132] D. Bederede et al. "SICAL — a high precision silicon-tungsten luminosity calorimeter for ALEPH". Em: *Nucl. Instrum. Meth. A* 365 (1995), pp. 117–134. DOI: <10.1016/0168-9002(95)00409-2>.

[133] I. C. Brock et al. "Luminosity Measurement in the L3 Detector at LEP". Em: *Nucl. Instrum. Meth. A* 381 (1996), pp. 236–266. DOI: <10.1016/S0168-9002(96)00734-6>.

[134] F. Abudinén et al. "Measurement of the integrated luminosity of the Phase 2 data of the Belle II experiment". Em: *Chin. Phys. C* 44.2 (2020), p. 021001. DOI: <10.1088/1674-1137/44/2/021001>. arXiv: <1910.05365> [hep-ex].

[135] Medina Ablikim et al. “Measurement of the integrated luminosity and the center-of-mass energy of the data taken by BESIII at $\sqrt{s} = 2.125$ GeV”. Em: *Chin. Phys. C* 41.11 (2017), p. 113001. DOI: <10.1088/1674-1137/41/11/113001>. arXiv: <1705.09722> [hep-ex].

[136] M. Ablikim et al. “Precision measurement of the integrated luminosity of the data taken by BESIII at center of mass energies between 3.810 GeV and 4.600 GeV”. Em: *Chin. Phys. C* 39.9 (2015), p. 093001. DOI: <10.1088/1674-1137/39/9/093001>. arXiv: <1503.03408> [hep-ex].

[137] G. Carboni et al. “Precise Measurements of Proton - Anti-proton and Proton Proton Total Cross-sections at the CERN Intersecting Storage Rings”. Em: *Nucl. Phys. B* 254 (1985), pp. 697–736. DOI: <10.1016/0550-3213(85)90242-1>.

[138] “CMS Luminosity Based on Pixel Cluster Counting - Summer 2013 Update”. Em: (2013).

[139] Roel Aaij et al. “Precision luminosity measurements at LHCb”. Em: *JINST* 9.12 (2014), P12005. DOI: <10.1088/1748-0221/9/12/P12005>. arXiv: <1410.0149> [hep-ex].

[140] Morad Aaboud et al. “Luminosity determination in pp collisions at $\sqrt{s} = 8$ TeV using the ATLAS detector at the LHC”. Em: *Eur. Phys. J. C* 76.12 (2016), p. 653. DOI: <10.1140/epjc/s10052-016-4466-1>. arXiv: <1608.03953> [hep-ex].

[141] “ALICE luminosity determination for pp collisions at $\sqrt{s} = 8$ TeV”. Em: (2017).

[142] “ALICE luminosity determination for pp collisions at $\sqrt{s} = 13$ TeV”. Em: (2016).

[143] “Luminosity determination in *pp* collisions at $\sqrt{s} = 13$ TeV using the ATLAS detector at the LHC”. Em: (jun. de 2019).

[144] Albert M Sirunyan et al. “Precision luminosity measurement in proton-proton collisions at $\sqrt{s} = 13$ TeV in 2015 and 2016 at CMS”. Em: *Eur. Phys. J. C* 81.9 (2021), p. 800. DOI: <10.1140/epjc/s10052-021-09538-2>. arXiv: <2104.01927> [hep-ex].

[145] “CMS luminosity measurement for the 2017 data-taking period at $\sqrt{s} = 13$ TeV”. Em: (2018).

[146] “CMS luminosity measurement for the 2018 data-taking period at $\sqrt{s} = 13$ TeV”. Em: (2019).

[147] J. Salfeld-Nebgen e D. Marlow. “Data-driven precision luminosity measurements with Z bosons at the LHC and HL-LHC”. Em: *Journal of Instrumentation* 13.12 (dez. de 2018), P12016–P12016. DOI: <10.1088/1748-0221/13/12/p12016>. URL: <https://doi.org/10.1088%2F1748-0221%2F13%2F12%2Fp12016>.

[148] The CMS Collaboration. *The Phase-2 Upgrade of the CMS Beam Radiation, Instrumentation, and Luminosity Detectors: Conceptual Design*. Rel. técn. Geneva: CERN, 2020. URL: <https://cds.cern.ch/record/2706512>.

[149] Albert M Sirunyan et al. "Electron and photon reconstruction and identification with the CMS experiment at the CERN LHC". Em: *JINST* 16.05 (2021), P05014. DOI: <10.1088/1748-0221/16/05/P05014>. arXiv: <2012.06888> [hep-ex].

[150] M. Dittmar, F. Pauss e D. Zurcher. "Towards a precise parton luminosity determination at the CERN LHC". Em: *Phys. Rev. D* 56 (1997), pp. 7284–7290. DOI: <10.1103/PhysRevD.56.7284>. arXiv: <hep-ex/9705004>.

[151] Georges Aad et al. "Measurement of $W^{\pm}$ and Z-boson production cross sections in pp collisions at $\sqrt{s} = 13$ TeV with the ATLAS detector". Em: *Phys. Lett. B* 759 (2016), pp. 601–621. DOI: <10.1016/j.physletb.2016.06.023>. arXiv: <1603.09222> [hep-ex].

[152] Albert M Sirunyan et al. "Measurements of differential Z boson production cross sections in proton-proton collisions at $\sqrt{s} = 13$ TeV". Em: *JHEP* 12 (2019), p. 061. DOI: <10.1007/JHEP12(2019)061>. arXiv: <1909.04133> [hep-ex].

[153] Claude Duhr e Bernhard Mistlberger. "Lepton-pair production at hadron colliders at N^{3}LO in QCD". Em: *JHEP* 03 (2022), p. 116. DOI: <10.1007/JHEP03(2022)116>. arXiv: <2111.10379> [hep-ph].

[154] *Luminosity Determination using $Z \to \ell\ell$ events at $\sqrt{s} = 13$ TeV with the ATLAS detector*. Rel. técn. All figures including auxiliary figures are available at urlhttps://atlas.web.cern.ch/Atlas/GROUPS/PHYSICS/PUBNOTES/ATL-DAPR-PUB-2021-001. Geneva: CERN, 2021. URL: <https://cds.cern.ch/record/2752951>.

[155] J. Alwall et al. "The automated computation of tree-level and next-to-leading order differential cross sections, and their matching to parton shower simulations". Em: *Journal of High Energy Physics* 2014.7 (jul. de 2014). ISSN: 1029-8479. DOI: <10.1007/jhep07(2014)079>. URL: <http://dx.doi.org/10.1007/JHEP07(2014)079>.

[156] Torbjörn Sjöstrand et al. "An introduction to PYTHIA 8.2". Em: *Computer Physics Communications* 191 (jun. de 2015), pp. 159–177. ISSN: 0010-4655. DOI: <10.1016/j.cpc.2015.01.024>. URL: <http://dx.doi.org/10.1016/j.cpc.2015.01.024>.

[157] R. L. Workman et al. "Review of Particle Physics". Em: *PTEP* 2022 (2022), p. 083C01. DOI: <10.1093/ptep/ptac097>.

[158] "Luminosity monitoring with Z counting in early 2022 data". Em: (2023). URL: <https://cds.cern.ch/record/2851655>.

[159] Aram Hayrapetyan et al. "Luminosity determination using Z boson production at the CMS experiment". Em: *Eur. Phys. J. C* 84.1 (2024), p. 26. DOI: <10.1140/epjc/s10052-023-12268-2>. arXiv: <2309.01008> [hep-ex].

[160] Albert M Sirunyan et al. “Measurement of the differential Drell-Yan cross section in proton-proton collisions at $\sqrt{s} = 13$ TeV”. Em: *JHEP* 12 (2019), p. 059. DOI: <10.1007/JHEP12(2019)059>. arXiv: <1812.10529> [hep-ex].

[161] S. Carrazza, S. Forte e J. Rojo. “Parton Distributions and Event Generators”. Em: (2013). arXiv: <arXiv:1311.5887> [hep-ph].

[162] A. V. Manohar et al. “The photon content of the proton”. Em: *Journal of High Energy Physics* 2017 (2017). arXiv: <arXiv:1708.01256> [hep-ph].

[163] “Nucl. Instrum. Meth. A545”. Em: *Nuclear Instruments and Methods in Physics Research Section A* 545 (2005), pp. 503–515.

[164] “Nucl. Instrum. Meth. A506”. Em: *Nuclear Instruments and Methods in Physics Research Section A* 506 (2003), pp. 250–303.

[165] “IEEE Transactions on Nuclear Science”. Em: *IEEE Transactions on Nuclear Science* 53.1 (2006), pp. 270–278.

[166] S. P. Ahlen. “Stopping-power formula for magnetic monopoles”. Em: *Phys. Rev. D* 17 (1978), pp. 229–233. DOI: <10.1103/PhysRevD.17.229>.

[167] S. Ahlen. “Monopole Energy Loss and Detector Excitation Mechanisms”. Em: *Magnetic Monopoles*. Ed. por J. Carrigan e W. Trower. Vol. 102. NATO Advanced Science Institutes Series. Springer US, 1983, pp. 259–290.

[168] J. B. Birks. “Scintillations from Organic Crystals: Specific Fluorescence and Relative Response to Different Radiations”. Em: *Proc. Phys. Soc. A* 64 (1951), pp. 874–877. DOI: <10.1088/0370-1298/64/10/303>.

[169] Vardan Khachatryan et al. “CMS Tracking Performance Results from Early LHC Operation”. Em: *Eur. Phys. J. C* 70 (2010), pp. 1165–1192. DOI: <10.1140/epjc/s10052-010-1491-3>. arXiv: <1007.1988> [physics.ins-det].

[170] Daniele del Re. “Timing performance of the CMS ECAL and prospects for the future”. Em: *Journal of Physics: Conference Series* 587.1 (fev. de 2015), p. 012003. DOI: <10.1088/1742-6596/587/1/012003>. URL: <https://dx.doi.org/10.1088/1742-6596/587/1/012003>.

[171] Albert M Sirunyan et al. “Search for long-lived particles using nonprompt jets and missing transverse momentum with proton-proton collisions at $\sqrt{s} = 13$ TeV”. Em: *Phys. Lett. B* 797 (2019), p. 134876. DOI: <10.1016/j.physletb.2019.134876>. arXiv: <1906.06441> [hep-ex].

[172] Syed Asghar Abbas Afsar. “Search for the Magnetic Monopole with the Compact Muon Solenoid Detector at the Large Hadron Collider”. Em: (2021). URL: <https://cds.cern.ch/record/2823358>.

[173] Albert M Sirunyan et al. "Reconstruction of signal amplitudes in the CMS electromagnetic calorimeter in the presence of overlapping proton-proton interactions". Em: *JINST* 15.10 (2020), P10002. DOI: <10.1088/1748-0221/15/10/P10002>. arXiv: <2006.14359> [physics.ins-det].

[174] "Performance of various triggers used in the Supersymmetry group in early 2018 data". Em: (2018). URL: <https://cds.cern.ch/record/2631527>.

[175] A. Hayrapetyan et al. "Performance of the CMS high-level trigger during LHC Run 2". Em: *JINST* 19.11 (2024), P11021. DOI: <10.1088/1748-0221/19/11/P11021>. arXiv: <2410.17038> [physics.ins-det].

[176] Pekka Sinervo. "Definition and Treatment of Systematic Uncertainties in High Energy Physics and Astrophysics". Em: *eConf* C030908 (2003). Ed. por L. Lyons, R. P. Mount e R. Reitmeyer, TUAT004.

[177] Albert M Sirunyan et al. "Precision luminosity measurement in proton-proton collisions at $\sqrt{s} = 13$ TeV in 2015 and 2016 at CMS". Em: *Eur. Phys. J. C* 81.9 (2021), p. 800. DOI: <10.1140/epjc/s10052-021-09538-2>. arXiv: <2104.01927> [hep-ex].

[178] "CMS luminosity measurement for the 2017 data-taking period at $\sqrt{s} = 13$ TeV". Em: (2018).

[179] "CMS luminosity measurement for the 2018 data-taking period at $\sqrt{s} = 13$ TeV". Em: (2019).

[180] A L Read. "Presentation of search results: the CLs technique". Em: *Journal of Physics G: Nuclear and Particle Physics* 28.10 (set. de 2002), p. 2693. DOI: <10.1088/0954-3899/28/10/313>. URL: <https://dx.doi.org/10.1088/0954-3899/28/10/313>.

[181] Glen Cowan et al. "Asymptotic formulae for likelihood-based tests of new physics". Em: *Eur. Phys. J. C* 71 (2011). [Erratum: Eur.Phys.J.C 73, 2501 (2013)], p. 1554. DOI: <10.1140/epjc/s10052-011-1554-0>. arXiv: <1007.1727> [physics.data-an].

[182] Aram Hayrapetyan et al. "The CMS Statistical Analysis and Combination Tool: Combine". Em: *Comput. Softw. Big Sci.* 8.1 (2024), p. 19. DOI: <10.1007/s41781-024-00121-4>. arXiv: <2404.06614> [physics.data-an].

[183] Mai Muhammed Hassan El Sawy. *Search for Magnetic Monopoles in the CMS experiment at the Large Hadron Collider (LHC)*. Mai. de 2020.

[184] Georges Aad et al. "Search for magnetic monopoles and stable particles with high electric charges in $\sqrt{s} = 13$ TeV pp collisions with the ATLAS detector". Em: *JHEP* 11 (2023), p. 112. DOI: <10.1007/JHEP11(2023)112>. arXiv: <2308.04835> [hep-ex].